Emergent properties of misfit layer compounds from first principles.

A thesis presented for the degree of Doctor of Philosophy in physics in compliance with the co-tutelle agreement between

UNIVERSITÀ DI TRENTO and SORBONNE UNIVERSITÉ

Dipartimento di fisica dell'Università di Trento Corso di Dottorato in Fisica – XXXVII Ciclo

Institut de Nanosciences de Paris École doctorale n° 564: Physique en Île-de-France

Candidate:
Ludovica Zullo

Supervisors:
Prof. Matteo Calandra
Dr. Tristan Cren

4 November 2024

Thesis defended on 4 November 2024 in front of a Board of Examiners composed by:

Reviewer	Prof. Marina Rucsandra Filip, University of Oxford
Reviewer	Prof. Claudio Attaccalite, CINAM, Aix-Marseille Université
Examiner	Prof. Claudine Katan, Institut des sciences chimiques de Rennes
Examiner	Prof. Andrea Gauzzi, Sorbonne Université
Examiner	Prof. Pierluigi Cudazzo, Università di Trento
Supervisor	Prof. Matteo Calandra, Università di Trento
Supervisor	Dr. Tristan Cren, Sorbonne Université

Abstract

Misfit layer compounds (MLCs) are heterostructures composed of rocksalt units stacked with few-layers transition metal dichalcogenides (TMDs). They host Ising superconductivity, charge density waves, and good thermoelectricity. However, research has mostly focused on specific compounds and trial-and-error synthesis, making the design of misfits' emergent properties hindered by a lack of a global picture. Our work offers an original perspective by deriving misfits' properties from those of their constituent layers. We identify the fundamental mechanism governing charge transfer and demonstrate how charge injection into the TMD layers can be effectively controlled through chemical alloying in the rocksalt unit. We show that misfits behave as a periodic arrangement of ultra-tunable field-effect transistors, allowing for massive chargings. We establish a strategy to study the electronic and vibrational properties of MLCs, highlighting the two-dimensional nature of the lattice dynamics of TMDs in these three-dimensional hetrostructures. Finally, we present an in-depth study of superconductivity in MLCs, estimating critical temperatures and comparing with existent experimental data. Our work provides a complete characterization of these heterostructures, aiming to guide the design of materials with targeted emergent properties for future device applications.

Keywords: heterostructures, transition metal dichalcogenides, charge transfer, emergent properties, superconductivity

Résumé

Les matériaux misfit lamellaires (misfit layer compounds (MLCs)) sont des hétérostructures composées de couches de dichalcogénures de métaux de transition (TMD) en sandwich avec des couches de chalcogénures rocksalt. Ces structures abritent une supraconductivité de type Ising, des ondes de densité de charge et de bonnes propriétés thermoélectriques. Cependant, la recherche s'est principalement concentrée sur des composés spécifiques et une synthèse par essais et erreurs, ce qui a entravé l'exploration des propriétés émergentes des misfits en raison d'un manque de vision global. Notre travail propose une perspective originale en dérivant les propriétés des misfits à partir de celles de leurs couches constituantes. Nous identifions le mécanisme fondamental régissant le transfert de charge et démontrons comment l'injection de charge dans les couches de TMDs peut être efficacement contrôlée par l'alliage chimique dans l'unité rocksalt. Nous montrons que les misfits se comportent comme un agencement périodique de transistors à effet de champ ultra-ajustables, permettant des effets de charges massifs. Nous établissons une stratégie pour étudier les propriétés électroniques et vibrationnelles des MLCs, mettant en évidence la nature bidimensionnelle de la dynamique du réseau des TMDs dans ces hétérostructures tridimensionnelles. Enfin, nous présentons une étude approfondie de la supraconductivité dans les MLCs, en estimant des températures critiques et en les comparant avec les données expérimentales existantes. Notre travail fournit une caractérisation complète de ces hétérostructures, visant à guider la conception de matériaux avec des propriétés émergentes ciblées pour de futures applications dans des dispositifs électroniques.

Mots clés: hétérostructures, dichalcogénures de métaux de transition, transfert de charge, propriétés émergentes, supraconductivité

Acknowledgements

I still can't believe how much pursuing this path changed my life. But I know that going through all the good and bad days has shaped me into the woman and scientist I am now, as well as the one I will become in the future.

I am sincerely grateful to my two supervisors. Matteo Calandra for being my first scientific guide in this journey. The dedication you have for science inspires me to always push further while maintaining the ship's wheel steady. Tristan Cren who immediately understood and supported me in my scientific path. Thank you for teaching me that true physics is hidden in the simplest concepts. I'd also like to thank my master's thesis advisor, Giovanni Cantele, for being the first person to have faith in my scientific career and provide consistent encouragement. I also wish to acknowledge Marie-Aude Méasson, with whom I had the privilege of collaborating and acquiring a wealth of knowledge regarding Raman spectroscopy. I would like to acknowledge the referees, professors Marina Rucsandra Filp and Claudio Attaccalite, who kindly accepted to review my thesis, and the other members of the jury, professors Claudine Katan, Andrea Gauzzi and Pierluigi Cudazzo. I am profoundly appreciative of the secretary teams of both institutions, with a special mention for Micaela Paoli, whose commitment to each individual Ph.D. is truly remarkable, Isabelle Borges, and Valérie Guezo. I want to express my gratitude for the members of my two scientific groups, the Mattheory group in Trento and the SNEQ team at the INSP. All these people warmly welcomed me, helping to keep my mental health stable during the Ph.D. between a ping-pong match and a post-work apéro. A special thanks goes to my friend and colleague Giovanni Marini. I've seen you becoming an invaluable researcher; with your contagious positive and calm mindset, you make all of us believe that everything can be fixed one step at a time. Thank you for supporting me both in my scientific and personal life.

My Ph.D. journey would not have been the same without the support from all the people I met, first in Trento and then in Paris, whom I am fortunate to call friends. Thanks to the 'Vabbuòja' team. Nicola for our deep connection, Costanza for being my trentino-sister, Manuel for all our life talks, and Gianmarco my favourite enemy-to-friend. You've become my Trento family, the one I will always come back to. Thanks to Alberto, GioNovi, Stefano, Matteo, Cecilia, Thomas, Elio, GioMattiotti, Lorenzo, Bob, Margherita, Elena, Jules, Alessio, Veronica and Kris. Thank you for all the morning coffees and afternoon spritzes, mountain

hiking, and especially for all the laughter that brought joy to my days. Thanks to my beloved Parisian friends Eliane, Pascal, Carlos, Sergei, Romeo, Laurita, Antoine, Christian, Noemi, Robin and Axel. Thank you for our Parisian nights, our visits to Amsterdam, Malta, and, most importantly, to the canteen, and for sharing with me the delight of eating haricots verts every day. Thanks to Matias to always be there for me, Hugo to keep cheering me up, and Angelique, who has been by my side since the beginning of my Parisian journey. Thanks to Arianna, my special palier friend, for all the Parisian adventures between strange food tastes and brocantes.

I want to express my profound gratitude and love to my family, Liliana, Fabrizio and Chris. You raised me with grace, and because of your sacrifice and love, I am a free woman with the ability to choose her own path. You will always be my inspiration. Andrea, thank you for treating me with respect and love. You have the ability to awaken my inner child, sharing with me the beauty of the present moment while enjoying the scenery. Sara, Ilaria, Laura and Mattia my core-friends I deeply love you and I am honoured to share my daily life with you. No distance will keep us apart. Mattia for sharing 'ugly horses' and life talks, Laura for being my personal sunshine, Sara and Ilaria, thank you for being my strong, independent, and furious women, my inspiration, and my source of happiness. Lastly, thank you Ludovica, remember who you are, I am proud of you!

Contents

Introduction

Heterostructures composed of two-dimensional (2D) materials attracted a lot of attention in recent years due to the ability to fine engineering layer-by-layer materials with remarkable physical properties. Few layers of atoms can be isolated and manipulated with the aim of discovering novel physical phenomena that are unachievable in their bulk counterparts. This field has its roots in the work of Andre Geim and Konstantin Novoselov [1], whose pioneering studies on graphene established the baseline for the investigation of other 2D materials.
In a heterostructure, 2D materials such as graphene, hexagonal boron nitride (h-BN), transition metal dichalcogenides (TMDs), and many others can be stacked or integrated to form layered assemblies. The van der Waals (vdW) forces that hold the layers together facilitate the assembly of diverse materials while maintaining high interface quality, free of the defects and dislocations that commonly plague traditional semiconductor heterostructures, resulting in superior electronic and mechanical properties. Novoselov and Geim's reviews have extensively discussed the potential of these materials [2, 3], describing the vdW heterostructures as an atomic-scale LEGO game. They claim that the strengths of new technologies based on these heterostructures can be identified in their rich tunability: the variety of choice between "bricks" such as the multitude of two-dimensional layers already synthesized, the number of sheets, the diverse stacking configurations, and many others. These features can thus be seen as control knobs for fine-tuning mechanical, optical, electrical, and superconductive properties in two-dimensional heterostructures. The quest for synthesizing and modeling new heterostructures represents a frontier in material science and application, driven by the potential to build innovative devices.

Misfit layer compounds (MLCs) are heterostructures composed of rocksalt units stacked along the out-of plane direction with few-layer transition metal dichalcogenides. Because of the different lattice parameters of their constituent layers, these compounds inherently possess a "misfit" between the layers along one of the in-plane directions, making the misfit crystal incommensurate. Despite being three-dimensional (3D) crystals, the physical properties of misfit layer compounds are intertwined with the one of their two-dimensional building blocks. MLCs are mechanically stable bulk structures with strong intralayer bonding. They also inherited the tunability of two-dimensional heterostructures, with the possibility to be cleaved, obtaining clean surfaces, thanks to the weak interlayer van deer Waals interactions.

Misfit layer compounds have been known for a long time. Due to their complex composition, these heterostructures have been a puzzle for the crystallography community, and thus their structures as a function of the RS and TMD composition have been thoroughly investigated [4,5]. However, the exploration of physical properties of misfit layer compounds is quite recent, and focused mainly on two interesting perspectives.

The first is that charge transfer occurs as a result of the interaction between the TMD layers and the rocksalt units. For example, recently [6], it has been shown that it is possible to overcome the limit of the largest carrier doping that can be achieved via field effect gating in the metallic TMD $NbSe_2$ ($n_e \approx 3 \times 10^{14}$ e^- cm^{-2} [7]) within a misfit heterostructure. Indeed, in the misfit layer compound $(LaSe)_{1.14}(NbSe_2)_2$, a massive electron transfer from the LaSe rocksalt to the $NbSe_2$ TMD occurs, leading to a rigid doping as large as $n_e \approx 6 \times 10^{14}$ e^- cm^{-2}. The capability of inducing a controlled and tunable number of carriers in few layer systems has been pivotal for the success of 2D materials [8]. Therefore, this important result opens up the prospect of employing misfit layer compounds as a new platform to achieve controllable doping of TMDs. It is, however, unclear if the electron doping in misfits can be in some way controlled by any physical parameter and, more importantly, how general this mechanism to dope few layer TMDs is.

The second point is that recently a plethora of new emergent properties have been discovered in misfit layer compounds. Indeed, they host physical properties such as Ising superconductivity [9–13] charge density waves (CDW) [14–16], topological effects [17] and many others. Emergent properties of a system are those emerging from the interactions between its individual components. These properties are not inherent to any single component but arise from the collective behaviour of the system as a whole. Designing heterostructures with desired emergent properties is, however, a challenging task of increasing interest for the condensed matter community, beyond the particular case of misfit layer compounds, to understand how the complexity of the system's interactions leads to new behaviors that cannot be easily predicted from the properties of the isolated components.

To summarize, the research in the field of misfit layer compounds has led to remarkable results, but it has mostly proceeded by isolated discoveries and trial-and-error chemical synthesis, while general rules to understand what happens when assembling different rocksalts and TMDs are missing. The need of a global picture becomes evident when considering that: first of all, many binary layers and ternary alloys composed of monochalcogenides can be assembled with practically any few layer dichalchogenide; second, the thickness of the dichalcogenide layers can be chosen at will. This makes misfit layer compounds a playground with a lot of possible combinations but also leads to many unanswered questions. For example, how does the charge transfer occur in these heterostructures? Are the TMD layers acceptors or donors? How can the charge transfer be tuned? To what extent is the electronic structure of the TMD affected when inserted in the heterostructure? Most important, what are the emergent properties of the misfit, i.e., properties of the MLC that are absent in the pristine constituents? How can

we design misfit properties from the knowledge of their building blocks?

In this Thesis, we answer these questions by performing extensive first-principles calculations of misfit layer compounds in the density functional theory (DFT) framework. More specifically, the purpose of this Thesis is to develop an approach that allows to derive the properties of misfit layer compounds starting from their individual constituents, namely rocksalts and transition metal dichalcogenides. Such a study would not have been accurate without a solid grasp of the experimental state-of-the-art in misfit layer compounds characterization; hence, I had the chance to collaborate closely with the experimental SNEQ team at the Institut des Nanosciences de Paris (INSP).
First of all, the solution to the problem of determining the features of misfit layer compounds based on those of each of their components necessarily involves understanding the charge transfer mechanism between the two components of the heterostructure. We address this problem by identifying the fundamental mechanism ruling charge transfer and demonstrating how the charge injection into the TMD layers can be efficiently controlled by chemical alloying in the rocksalt unit. Our methodology involves the accurate study of the properties of individual rocksalts and TMDs from which we are able to predict the amount of chargings as well as the direction of the charge transfer in misfit heterostructures. Second, we characterize misfit layer compounds by deriving their electronic, vibrational and emergent properties such as superconductivity with extensive ab initio calculations. We then use the knowledge gained from our global picture for the charge transfer to build a physically meaningful effective model to describe misfit layer compounds. This model allows to reduce the computational effort of simulating these large supercell heterostructures in the DFT framework. Our methodology provides a complete and new characterization of misfit layer compounds heterostructures. Most importantly, we are able to compare our findings with the state-of-the-art experimental results, showing the validity of our method in calculating the electronic and vibrational properties of these heterostructure. Finally, our method demonstrates how to exploit the distinct physics of individual constituents to design misfit layer compounds. We illustrate how to construct heterostructures that not only can inherit properties from each two-dimensional constituent but also exhibit emergent properties unique to the misfit, resulting from interactions among the constituent layers.

Topics covered in the manuscript are organized as follows. In the first chapter, we introduce misfit layer compounds composition and structural complexity, emphasizing how each subsystem contributes to the ultimate crystal structure. We provide state-of-the-art literature on experimental synthesis, characterization, and emergent physics. In the second chapter we present our DFT calculations, demonstrating the mechanism controlling the charge transfer in misfit layer compounds. In the third chapter we explore the geometrical and electronic properties of misfit layer compounds, comparing our ab initio calculations to known experimental data. In the fourth chapter, we present the field effect transistor approach designed to study misfit layer compounds. We explain how we can efficiently model a mis-

fit layer compound by a collection of field effect transistors. We demonstrate the validity of this approach by deriving electronic and vibrational properties of misfit crystals in comparison with the full misfit calculations. In the fifth chapter, we present our ab initio calculations of the superconductive properties of misfit layer compounds, evaluating superconducting critical temperatures and comparing our results with experimental data. In the end we draw our conclusions, summarizing the main achievements of this Thesis and discussing the possible future direction on this subject.

Chapter 1

Misfit layer compounds

1.1 Introduction to misfit crystals

Misfit compounds are heterostructures built as a periodic arrangement along the c axis of two different types of two dimensional (2D) materials [4, 5]. The name "misfit" originates from a peculiar feature of these materials, which is the lattice mismatch between the different types of constituent layers. The mismatch causes the crystal to be incommensurate along one of the in-plane directions, adding an additional complexity to the crystal structure.
The first successes in the synthesis of misfit layered materials was in 1987. Misfit crystals were grown by vapor transport methods, and then characterized by single crystal X-ray diffraction, which was crucial for identifying the distinctive mismatch patterns.
In this work, we focus on a class of misfit materials known as misfit layer compounds (MLCs) whose chemical formula is $(RQ)_{1+\delta}(TX_2)_m$ where RQ are rocksalt bilayers and TX_2 are few layers transition metal dichalcogenides. To describe the misfit crystal we start from its building blocks, namely RQ and TX_2 layers. We might think of these layers as two jigsaw puzzle pieces that don't fit nicely together, as depicted in Fig. 1.1.
The first piece belongs to the family of transition metal dichalcogenides (TMDs), which are two-dimensional (2D) materials with the chemical formula TX_2 having an hexagonal lattice. The three-atom-thick layer is made up of a transition metal atom T (Nb, Mo, W, Ti,...) sandwiched between two layers of chalcogen atoms X (S, Se, Te).
The second piece is a rocksalt (RS) slab RQ, where R is Pb, Bi, Sn, or rare earth metals such as La, and Q is a chalcogen atom (S, Se, or Te). The slab consists of a distorted slice of a three-dimensional rocksalt structure having a tetragonal lattice.
The misfit is then a three-dimensional (3D) "puzzle" heterostructure consisting of an intergrowth structure formed by alternating stacking along the c axis of RQ planes and m layers of TMDs, with m= $1, 2$, as depicted in Fig.1.1. The factor $1+\delta$ in the chemical formula is related to the mismatch between the TMD and the

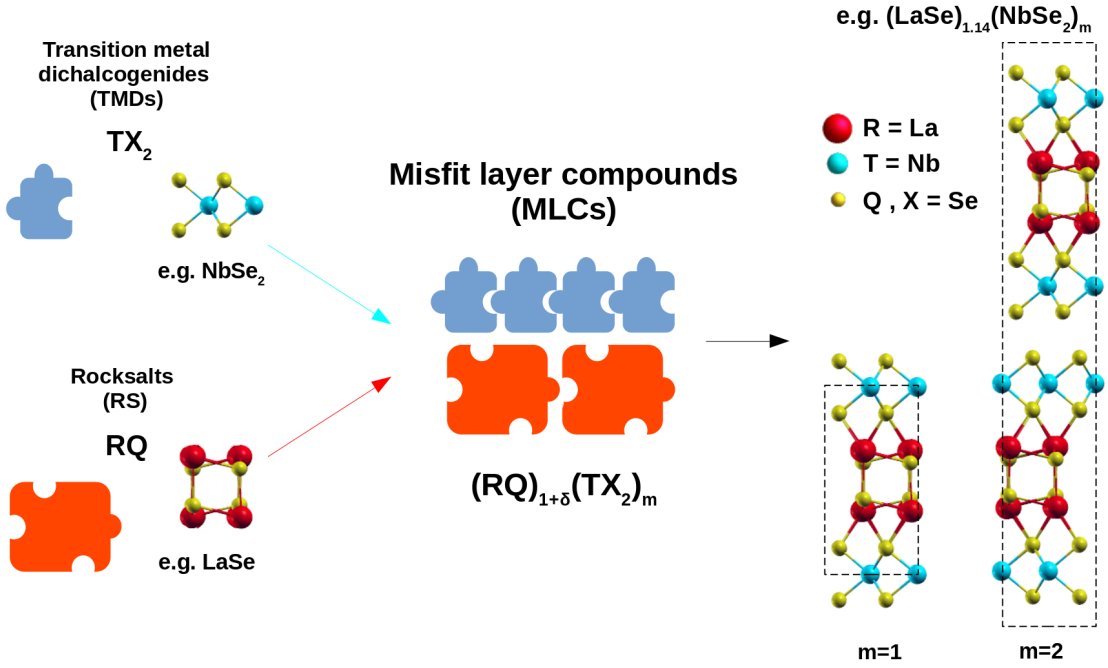

Figure 1.1: Misfit layer compounds ($(RQ)_{1+\delta}(TX_2)_m$) pictured as a jigsaw puzzle. The material building blocks, transition metal dichalcogenides (TMDs) and rocksalts (RS), are imagined as two jigsaw puzzle pieces that do not fit together. As an example, the compound $(LaSe)_{1.14}(NbSe_2)_m$ is depicted. In this misfit, the TMD is $NbSe_2$ (cyan jigsaw piece) and the RS is LaSe (red jigsaw piece). The regular alteration of these pieces forms the misfit with m=1, 2.

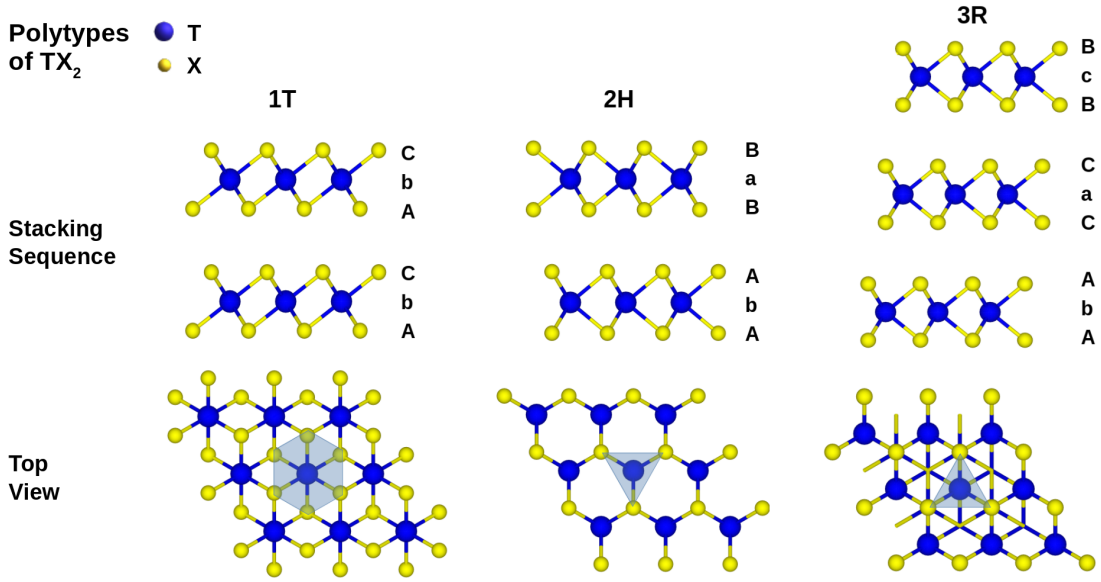

Figure 1.2: Polytypes of TMDs (1T,2H and 3R). Bottom panel: top views together with the different coordination of the T atom. Upper panel: side views with the stacking sequences. In the X-T-X sandwich, each stacking sequence is labelled with upper-case letters for the X atoms and with lower-case letters for the T atom.

rocksalt in the misfit, as explained in detail in the next sections. It is possible to synthetize misfit layer compounds with different (Q≠X) or equal (Q=X) chalcogen atoms in the TMD and rocksalt. In Fig. 1.1 we can see an example of misfit layer compound, namely $(LaSe)_{1.14}(NbSe_2)_m$, with m=1, 2, formed by $NbSe_2$ as the TMD and LaSe as the rocksalt.
The nature of bonding in MLCs stems from both the individual constituent bonds, and from their interactions. Within the misfit, the TX_2 and RQ units exhibit an inner strong iono/covalent bonding, whereas the interaction in the misfit out-of-plane direction is weaker, and its nature depends on the number of TMD layers in the crystal index m. Misfits with m=1, experience weak iono/covalent bonds between monolayers TMD and rocksalt units, while those with m=2 inherited an additional van der Waals (vdW) interaction via TMDs' stacking. Thus, clean misfit surfaces terminating in monolayer TMD can be obtained by cleaving a misfit with m=2 in the region between two TMD layers.
In misfit layer compounds each building block, called subunit or subsystem, has its own unit cell and space group. In the following, we shall identify the subsystems as (1) TMD layers and (2) RS units. We now discuss the composition of misfit layer compounds starting from the structure of their two constituents, namely transition metal dichalcogenides and rocksalts.

1.2 Subsystems of misfit layer compounds

1.2.1 Transition metal dichalcogenides

The first type of subsystem in misfit layer compounds is the two-dimensional transition metal dichalcogenide. Transition metal dichalcogenides (TMDs) are a class of two-dimensional materials that have sparked widespread interest in the scientific community due to their exceptional electrical, optical, and mechanical capabilities [18–21].
TMDs are classified as layered materials, like graphene, in which layers may be exfoliated into single or few-layer sheets. The transition metal and chalcogen atoms form a covalent in-plane bond in a single layer of TMDs, while weak van der Waals (vdW) interactions between layers occur in the out-of-plane direction. Two essential degrees of freedom, coordination geometry and stacking, significantly influence the behavior of the band structure and overall performance of TMDs in a variety of applications.
Metal atoms in TMDs are usually coordinated with chalcogen atoms in trigonal prismatic or octahedral geometry. In the trigonal prismatic coordination, six chalcogen atoms are arranged around the central transition metal atom, defining the vertices of a triangular prism. In the octahedral coordination, the transition metal atom is surrounded by six chalcogen atoms in an octahedral arrangement. The two type of coordination are shown in Fig. 1.2 (blue shaded regions). The preferred coordination of a TMD is established by the amount of ionicity of the bonding between the transition metal and chalcogen atoms [22]. Monolayer TMDs are classed based on the coordination of the T atom into two polymorphs: trigonal prismatic 1H and octahedral 1T phases. The first belongs to the D_{3h} point group, whereas the second belongs to the D_{3d} group.
Because of the distinct coordination in the monolayer, TMDs have various stacking sequences or polytypes in their bulk and multi-layer systems, which have a significant influence on their properties. Figure 1.2 shows the three most common stacking configurations for multilayer TMDs: 1T, 2H, and 3R. Within the X-T-X sandwich, each stacking sequence is labelled with upper-case letters for the X atoms and with lower-case letters for the T atom [23].
TMDs with trigonal prismatic coordination of the T atom can be arranged either in the 2H or in the 3R sequence. In the 2H polytype, the layers stack in an AbA BaB sequence with point group D_{6h}. Conversely, in the 3R polytype, the layers stack in an AbA CaC BcB sequence with point group C_{3v}. A representative TMD with trigonal prismatic coordination of the T atom is bulk 2H-$NbSe_2$. This metallic compound displays competition between charge density wave (CDW) and superconducting order [24–27].
2H and 3R TMDs can exhibit semiconducting properties with sizable bandgap like MoS_2, WS_2, $MoSe_2$, and WSe_2, making them suitable for electronic, optoelectronic and electrocatalytic applications [28–30].
TMDs in the 1T configuration have the T atom octahedral coordinated. The layers of this polytype have a point group D_{6d} and stack in a AbC sequence. 1T-TMDs generally exhibit metallic or semi-metallic behavior. This makes them suitable

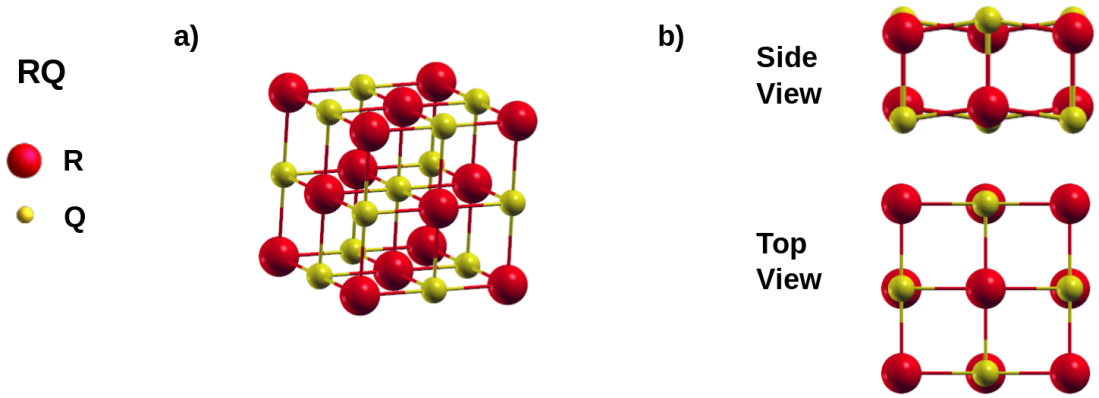

Figure 1.3: The rocksalt (RS) crystal. a) Bulk rocksalt crystal as two interpenetrated face-centered cubic (FCC) lattices of R (red) and Q (yellow) atoms. b) Side and top view of a rocksalt unit in misfit layer compounds.

for applications requiring high electrical conductivity. Examples of 1T-TMDs are VSe_2 and VS_2, which may be used as anode materials for ion-storage [31], and $TiSe_2$, which displays charge density wave (CDW) [32]. The 1T also presents a distorted counterparts which is named $1T'$ phase, where the displacement of some of the transition metal atoms results in T-T (metal-metal) bonding [33].
TMDs in misfit layer compounds exist in monolayer or bilayer form, with an ortho-hexagonal unit cell that matches the rocksalt structure, as explained in the next section.

1.2.2 Rocksalts

The second kind of subsystem in misfit layer compounds is the rocksalt unit. Rocksalt crystals are a wide variety of cubic three-dimensional materials [34,35]. These crystals are named after NaCl, a well-known substance found in many kitchens. In the chemical formula RQ, the bonds are cation-anion, where R^+ is the cation (for example, Na^+) and Q^- is the anion (for example, Cl^-) in a $1:1$ ratio.
Bulk crystals rock-salt possesses space group number 225 ($Fm\bar{3}m$). This lattice can be thought of as two interpenetrated face-centered cubic (FCC) lattices, as depicted in Fig. 1.3(a). In the crystal both cations and anions form a FCC unit cell with octahedral and tetrahedral interstitial sites. The cations occupy all octahedral sites of the anions in the in the FCC lattice, leaving all tetrahedral sites vacant and vice versa. As a result, in a rocksalt structure, each anion is octahedrally coordinated by six cations, and each cation is octahedrally coordinated by six anions. Many binary compounds crystallize in a rocksalt structure. This structure is found in the majority of alkali metal hydrides and halides.
In this work, we focus on rocksalt structure with R = Pb, Bi, Sn, or rare earth metals such as La, and Q being a chalcogen atom (Q = S, Se, Te). Rocksalts of this family exhibit different kind of behaviours. For example, LaSe and BiS are metals, while PbSe and SnS are insulators. Rocksalt chalcogenides with R = Sn are predicted to be topological insulators [36]. Other rocksalt crystals with R

a_2 (Å)		a_1 (Å) 3.15	3.15	3.17	3.31	3.326	3.327	3.33	3.374	3.437	3.54	3.7	3.8
		MoS_2	WS_2	VS_2	VSe_2	$MoSe_2$	WSe_2	NbS_2	TiS_2	$NbSe_2$	$TiSe_2$	SnS_2	$SnSe_2$
5.714	BiS	1.81	1.81	1.80	1.73	1.72	1.72	1.72	1.69	1.66	1.61	1.54	1.50
5.852	SnS	1.86	1.86	1.85	1.77	1.76	1.76	1.76	1.73	1.70	1.65	1.58	1.54
5.875	LaS	1.87	1.87	1.85	1.78	1.77	1.77	1.76	1.74	1.71	1.66	1.59	1.54
5.927	SnSe	1.88	1.88	1.87	1.79	1.78	1.78	1.78	1.76	1.72	1.67	1.60	1.56
6	LaSe	1.91	1.90	1.89	1.81	1.80	1.80	1.80	1.78	1.75	1.69	1.62	1.57
6	PbS	1.90	1.90	1.89	1.81	1.80	1.80	1.80	1.78	1.75	1.69	1.62	1.57
6.026	BiSe	1.91	1.91	1.90	1.82	1.81	1.81	1.81	1.79	1.75	1.70	1.63	1.58
6.028	PbSe	1.91	1.91	1.90	1.82	1.81	1.81	1.81	1.79	1.75	1.70	1.63	1.58

Figure 1.4: Exact mismatch ratios a_2/a_1. Lattice parameters of the considered compounds are experimental values.

= Pb undergo a topological phase transition induced by pressure and/or alloying [37]. Exceptionally high figure of merit (ZT) for thermoelectric applications is observed in single crystal and polycrystalline SnSe samples [38].
The rocksalt, as a subunit of misfit layer compounds, is in a bilayer form, depicted in Fig. 1.3(b). The rocksalt bilayer is an alternation of R and Q atoms. Each layer within the bilayer is a slice of the rocksalt structure, which is distorted to match the TMD lattice. In this configuration, the R atom has total coordination 5, including four R-Q in-plane bonds of roughly 90° and one R-Q out-of-plane bond, as seen in Fig. 1.3(b). We will denote this structure as the rocksalt unit, having an ortho-tetragonal lattice, as detailed in the next section.

1.3 Structure of misfit layer compounds

1.3.1 The mismatch

To accommodate layers with very different crystal lattices that are mismatched in one of the in-plane directions, the misfit crystal has a substantially larger unit cell than that of its components. To quantify this, we define the lattice mismatch ratio as a_2/a_1, where a_1 and a_2 are the TMD and RS lattice parameters for one of the in-plane directions. The mismatch ratio is a number that represents the in-plane incommensurability of a misfit. This ratio is in the range $\sim 1.5 - 1.9$ and sets the parameter δ in the chemical formula through the relation $1 + \delta = 2 \times (a_1/a_2)$.
The challenge of simulating a misfit layer compound in the density functional theory (DFT) framework, deals with the dimension of the crystal cell. Periodicity must be restored by defining a "commensurate approximant" of the misfit cell. The commensurate approximant is a supercell that restores periodicity in the mismatch direction. To create a commensurate approximant for DFT calculations, the lattice mismatch ratio a_2/a_1 must be known. Then we can approximate the ratio using the closest x and y integers as $a_2/a_1 \approx x/y$. Such supercell typically contains hundreds of atoms; the higher the lattice mismatch ratio, the larger the supercell required to restore periodicity.

a_2 (Å) \ a_1 (Å)	3.15	3.15	3.17	3.31	3.326	3.327	3.33	3.374	3.437	3.54	3.7	3.8
	MoS_2	WS_2	VS_2	VSe_2	$MoSe_2$	WSe_2	NbS_2	TiS_2	$NbSe_2$	$TiSe_2$	SnS_2	$SnSe_2$
5.714	BiS	1.10	1.10	1.11	1.16	1.16	1.16	1.17	1.18	1.20	1.24	1.30	1.33
5.852	SnS	1.08	1.08	1.08	1.14	1.14	1.14	1.14	1.15	1.18	1.21	1.26	1.30
5.875	LaS	1.07	1.07	1.08	1.13	1.13	1.13	1.13	1.15	1.17	1.21	1.26	1.30
5.927	SnSe	1.06	1.06	1.07	1.12	1.13	1.12	1.12	1.14	1.16	1.20	1.25	1.29
6	LaSe	1.05	1.05	1.06	1.10	1.11	1.11	1.11	1.13	1.15	1.18	1.23	1.27
6	PbS	1.05	1.05	1.06	1.10	1.11	1.11	1.11	1.13	1.15	1.18	1.23	1.27
6.026	BiSe	1.05	1.05	1.05	1.10	1.10	1.10	1.11	1.12	1.14	1.18	1.23	1.27
6.028	PbSe	1.05	1.05	1.05	1.10	1.10	1.10	1.11	1.12	1.14	1.18	1.23	1.26

Figure 1.5: Exact misfits stechiometry $1 + \delta = 2 \times a_1/a_2$. Lattice parameters of the considered compounds are experimental values.

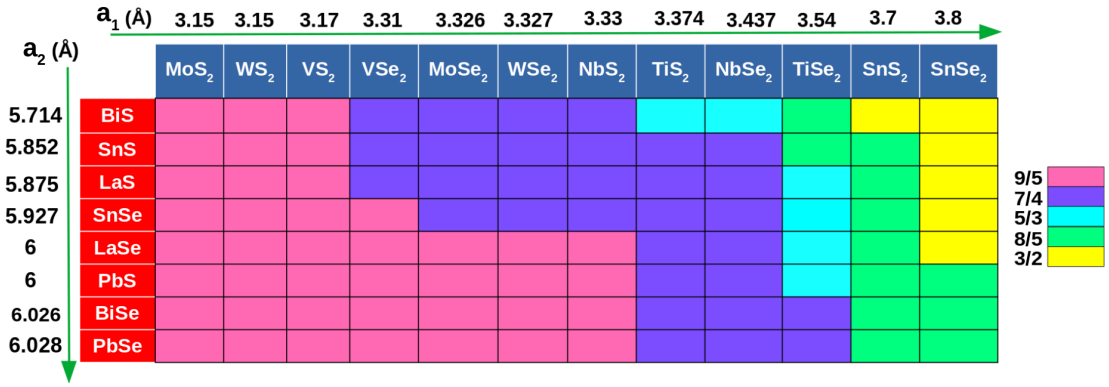

Figure 1.6: Table of the periodic approximant extracted from the rocksalt and TMDs lattice mismatch. Lattice parameters of the considered compounds are experimental values.

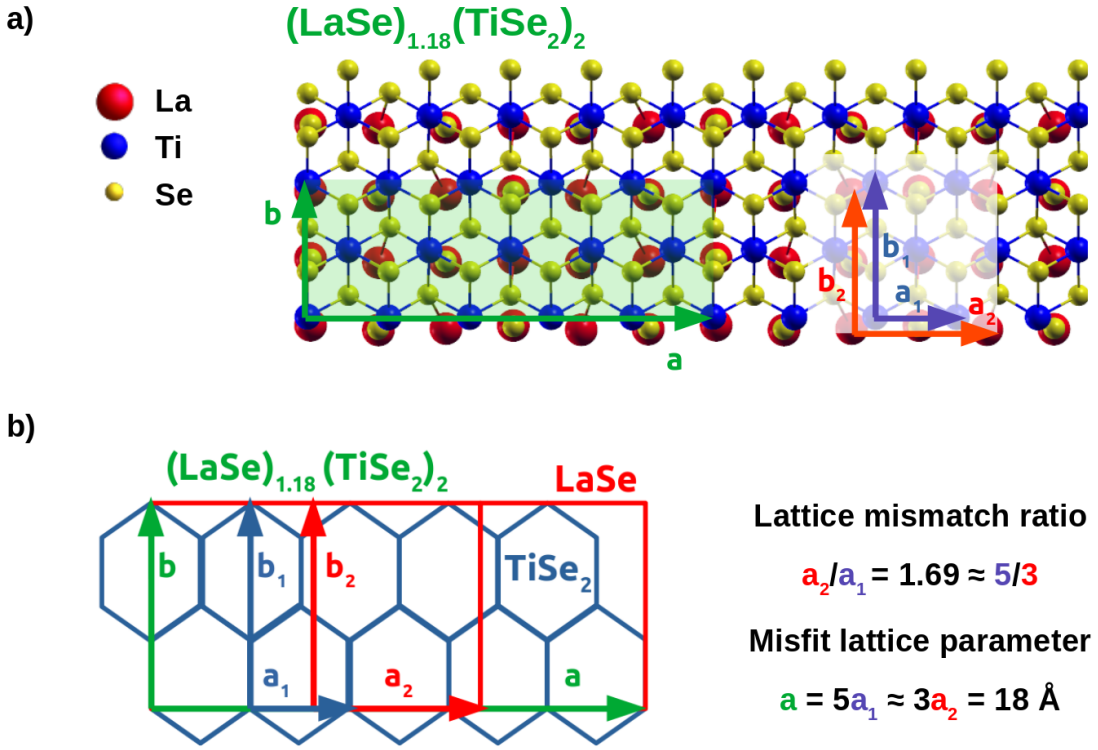

Figure 1.7: a) The in-plane cell of the misfit layer compound $LaSe_{1.18}TiSe_2$. Subsystem's axes are depicted in blue for the TMD ($TiSe_2$) and in red for the RS (LaSe). The shaded green region corresponds to the commensurate approximant of the misfit cell. b) A sketch of the in-plane cell of the misfit layer compound $LaSe_{1.18}TiSe_2$ (green). The lattice mismatch ratio is $a_2/a_1 = 1.69 \approx 5/3$, thus the commensurate approximant of the misfit cell is constructed by 5 repetitions of $TiSe_2$ (blue hexagons) and 3 repetitions of La (red rectangles) along the mismatch direction.

From the individual constituents' lattice parameters and the mismatch ratio we can derive the size of all the considered misfit supercells. Starting from the experimental lattice parameters of each isolated, considered rocksalts and TMDs, the schema of the exact mismatch ratios a_2/a_1 and the exact misfits stechiometry $1+\delta = 2 \times a_1/a_2$ is reported in Fig. [1.4] and [1.5], respectively. We can visualize the periodic approximant of the misfit supercell required for a DFT simulation from Fig. 1.6.

To get an idea of the construction of the commensurate approximant of the misfit cell, we report the example of the in-plane cell of the misfit layer compound $LaSe_{1.18}TiSe_2$ in Fig. 1.7(a). Isolated $TiSe_2$ has an hexagonal cell with in-plane lattice vectors a_1=b_1=3.54 Å , while LaSe has a tetragonal cell with in-plane lattice vectors a_2=b_2=6 Å . Taking a as the mismatch direction, the mismatch ratio reads: $a_2/a_1 = 1.69 \approx 5/3$. This indicates that in order to generate a misfit crystal with these two layers, 5 repetitions of the $TiSe_2$ lattice parameter and 3 repetitions of the LaSe lattice parameter along a are needed. A sketch of the in-plane misfit cell of $LaSe_{1.18}TiSe_2$ is shown in green in Fig. 1.7(b). In this image, 5 blue hexagons indicate the repeats along the mismatch direction of $TiSe_2$, whereas 3

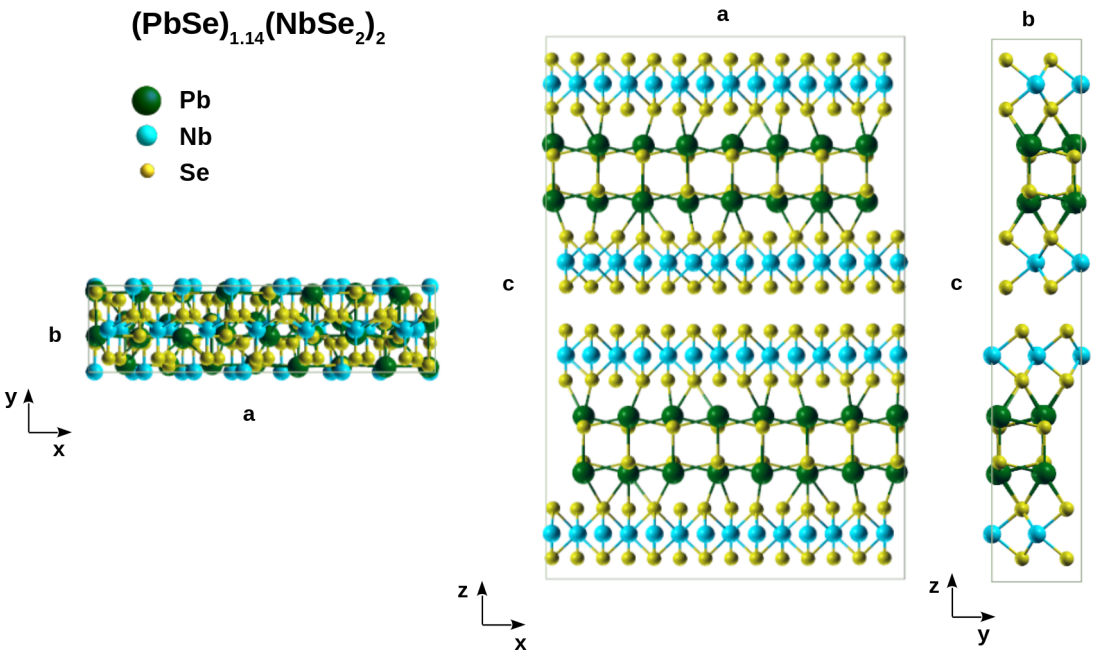

Figure 1.8: An example of a top and side view of a misfit lattice: $(PbSe)_{1.14}(NbSe_2)_2$. In this misfit, layers of the TMD 2H-$NbSe_2$ are stacked with RS units of PbSe.

red rectangles represent those of La. To match one another, the individual cells of $TiSe_2$ (blue) and LaSe (red) are orthorhombic, as detailed in the following, with lattice parameters $a_1 = 3.54$ Å , $a_2 = 6$ Å and b_1=b_2=6 Å . In this way the misfit crystal is commensurate along the b direction, with lattice parameter b=b_1=b_2=6 Å . The lattice parameter a along the incommensurate direction can be approximated by a ≈ xa_1=ya_2=5a_1=3a_2=18 Å .

1.3.2 Lattice and stacking

Misfit layer compounds are complex heterostructures whose chemical and physical behaviour is intimately linked to the structural composition and interactions of their constituents [4, 5, 39]. Individual subunits of the misfit crystal exhibit incommensurate modulation due to the lattice mismatch. Indeed, atoms in each subsystem experience a mutual perception of the other subsystems' periodic potentials, resulting in a displacement from their average positions. In diffraction experiments, such reciprocal modulation produces new satellite reflections as well as the reflections of the two subsystem lattices which provide valuable information about the presence of a misfit structure.
As we will show in the following chapters, the mutual modulation along the incommensurate axis in the misfit depends greatly on the ionic radius of the R atom in the rocksalt units, which modifies the distances within the adjacent TMD layers. Each of the individual subsystem has its own space group and symmetries. In order to fully describe the misfit crystal, a theory based on the notion of incommensurately modulated crystals has been proposed [40–42]. In this framework,

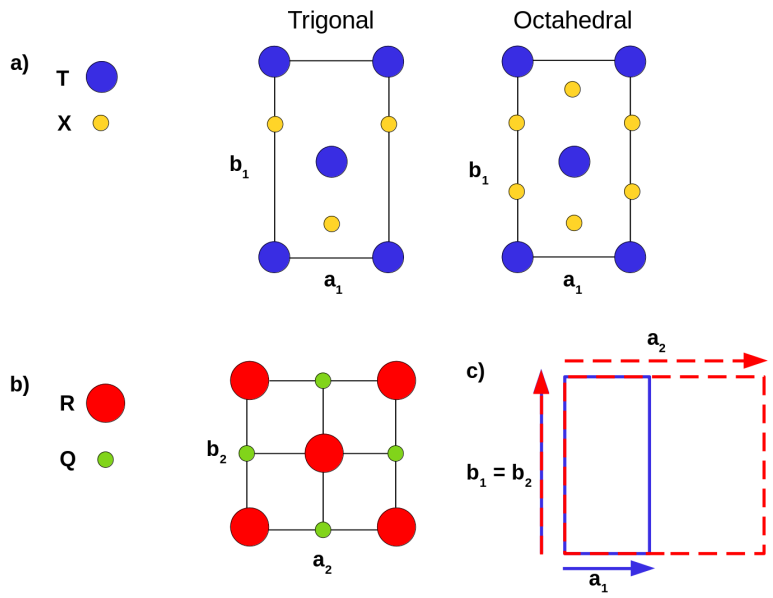

Figure 1.9: In-plane subsystems' cell and coordination in the misfit crystal. a) Top view of TMDs' ortho-hexagonal unit cell. The difference between the T atoms in trigonal prismatic coordination and those in octahedral coordination is shown. b) Top view of rocksalt's ortho-tetragonal unit cell. c) Schematic diagram of the embedding of the two subsystems' in-plane lattices in the misfit crystal.

the real structure replaces the three-dimensional space groups of subsystem average structures with the $(3+1)$D superspace groups of modulated misfit structure. The misfit crystal holds a cell with commensurate axes **b** and **c**, whereas **a** is the incommensurate direction where the two subsystems have a lattice mismatch, also known as the "mismatch" axis. In Fig. 1.8 an example of misfit lattice is show for the compound $(PbSe)_{1.14}(NbSe_2)_2$.

In order to define the misfit 3D lattice, we start with the in-plane unit cell. We label the in-plane lattice parameters of the individual subsystems as a_1, b_1 for the TMD and a_2, b_2 for the RS (Fig. 1.9).
Within the misfit, both the TMD and the RS comprise orthorhombic cells to match each other in-plane lattice parameters in the commensurate direction **b**.
In the misfit, the TMD forms an ortho-hexagonal in-plane unit mesh (a_1,$a_1\sqrt{3}$) whose shape is determined by the coordination of the T atom, as seen in Fig. 1.9(a). As a result, the rocksalt unit has an in-plane ortho-tetragonal cell (Fig. 1.9(b)), with a_2=b_2, generated via a deformation in the **b** direction to match the ortho-hexagonal TMD cell. Thus, the in-plane cell of the misfit is commensurate along the **b** axis with lattice parameter b=b_1=b_2. Along the mismatch axis **a**, $a_1 \neq a_2$, and thus the system is incommensurate in that direction. A sketch of the in-plane unit cell of the misfit is depicted in Fig. 1.9(c).
In the out-of-plane direction of the misfit, the TMD and the rocksalt share the **c** axis. Fig. 1.10 illustrates that the misfit cell is often orthorhombic or monoclinic, depending on the coordination of the T atom in the TMD.
In compounds with the TMD subsystems in trigonal prismatic coordination, the

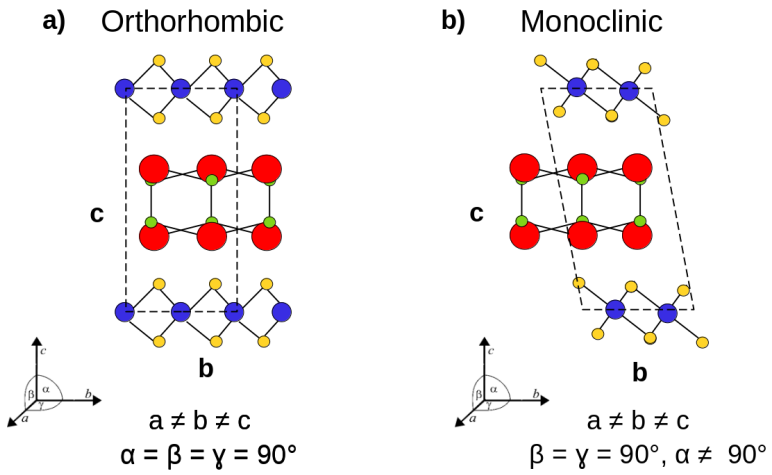

Figure 1.10: Side view of misfit cell depicted for different coordination of the T atom in the TMD: a) orthorhombic and b) monoclinic.

angle α equals 90 °(see Fig. 1.10(a)). This is due to the symmetry of a single TX_2 sandwich, where the mirror plane connects the X atoms of both planes sandwiching T. In this case, the misfit cell is orthorhombic with axes shown in Fig.1.10(a). On the contrary, octahedral sandwiches have rows of chalcogen that are displaced by 1/6b. The resultant structure is monoclinic, with an angle given by $\alpha - 90 = cos(b/6c)$ (Fig.1.10(b)).

TMDs and rocksalts are stacked along the out-of-plane direction of the misfit. The rocksalt subunit (red) is alternated with a monolayer TMD for m=1 and with a bilayer TMD for m=2 (blue), as sketched in Fig 1.11(a).

Misfits can be stacked in four primary sequences based on the centering of each subsystem. Symmetry allows each subsystem's structure to be either C-centered or F-centered. The C-centered configuration is the inner ortho-hexagonal or ortho-tetragonal lattice of the TMDs and RS, respectively, with one layer per unit cell. The F-centered layout includes extra centering in $(0, 1/2, 1/2)$ and $(1/2, 0, 1/2)$, as well as two layers per unit cell and a doubling of the c axis.

This centering results in four primary stackings in a misfit layer compound (shown in Fig.1.11(b) for the case m=1 with the trigonal coordination of the T atom in the TMDs sandwich), denoted as CC, FF, CF, and FC. In the CC and FF stackings, both the subsystems' lattices are in the same centering configuration (C or F), therefore the relation between the out-of-plane axis is $\mathbf{c_1}=\mathbf{c_2}$. The misfit out-of-plane direction $\mathbf{c}$ for the FF stacking is double that of the CC stacking. In the CF and FC stackings, the first subsystem has opposite centering with respect to the second. In the CF stacking, the RQ lattice is C-centered, the TX_2 lattice is F-centered ($\mathbf{c_2}=2\mathbf{c_1}$), and the reverse applies in the FC stacking ($\mathbf{c_1}=2\mathbf{c_2}$). Misfit layer compounds with m=2 exhibit the same kind of stackings. However, in this scenario, the various aforementioned polytypes of TMDs must be considered in the misfit stacking.

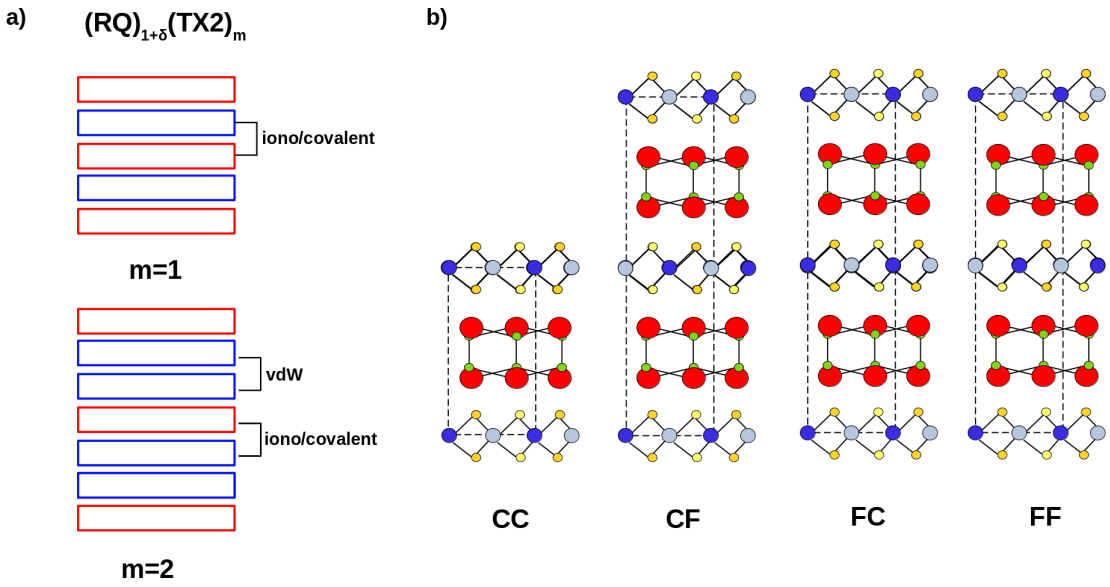

Figure 1.11: Misfit layer compounds stacking sequences. a) MLCs stacking as a function of the m-layers of the TMD subsystem, with m=1, 2. b) MLCs stacking configurations projected along the [100] axis. Example of the possible stackings for m=1 and the TMD in the trigonal prismatic coordination. Atoms of the same type at heights differing by $a/2$ are labeled by lighter and darker circles.

1.4 Experimental synthesis

The synthesis of MLCs is a key step since they must be thermodynamically stable when compared to competing phases. In this section we discuss the methods that have been developed to synthetize these complex structures [4, 5, 39].
The most widespread method to synthetize high quality misfit crystals is chemical vapor transport (CVT). CVT is a technique where the desired elements or compounds are transported in the vapor phase and deposited onto a substrate or within a reaction chamber [43, 44]. This approach requires a multi-zone furnace able to maintain a temperature gradient. The target substance is treated with a volatile transport agent to form a gaseous intermediate complex. The most commons transport agent iodine and chlorine. If treated at lower temperatures, the gas's thermodynamic energy is inadequate to form an intermediate complex, causing it to breakdown into the target material and transport agent. The gaseous intermediate follows the temperature gradient throughout the reaction vessel. The target material crystallizes in the portion of the reaction vessel with a lower temperature, while the transport agent stays in the gas phase and can react with the remaining material. Repeating this technique creates bigger crystals of the target substance. Creating misfit compounds throughout CVT requires assessing material stability at furnace specific temperatures and developing methods to introduce it into the gas phase.
The second most common technique to synthetize misfit layer compounds is chemical vapour deposition (CVD) [45] and physical vapour deposition (PVD) [46]. CVD is a versatile method where gaseous precursors decompose on a heated sub-

strate to form the desired compound. This technique allows for the deposition of thin films with precise control over thickness, composition, and crystallinity. The deposition process involves injecting precursor materials into a growth chamber, where they react with one other. This method enables direct material developing from the gas phase and chemical control by adjusting reagent vaporization and flow rates. In PVD the process is similar to CVD, but includes vaporizing and recondensing the target substance without a chemical reaction, evaporating target components with an electron beam. The step-by-step deposition is a controllable process that allows to create one layer at a time. The main challenges in employing CVD and PVD techniques are calibrating atomic fluxes and the sluggish growth rate necessary for synthetic control.

Another layer-by-layer growth method is molecular beam epitaxy (MBE) [47]. A substrate is cleaned and placed in an ultra-high vacuum (UHV) chamber to prevent contamination. Solid-source materials are deposited as molecule beams on the heated substrate, where they rearrange to form thin crystalline layers. Because the chamber is under UHV, the mean free path of the particles is long, allowing the beams to travel without colliding with other particles. The substrate temperature and beam fluxes are precisely controlled to manage the growth rate and layer quality. By changing the source materials and altering the deposition conditions, multiple layers with varied compositions may be produced successively, resulting in complex multilayer architectures. A unique type of MBE is van der Waals epitaxy (VDWE), in which a transition metal dichalcogenide is deposited on another or the same TMD to form the vdW gap [48]. Building a misfit involves depositing a three-dimensional compound onto a two-dimensional layer (or vice versa), which implies both types of epitaxies and is known as quasi van der Waals epitaxy [49].

Finally, other techniques as solid-state reactions and solvothermal and hydrothermal synthesis can be employed to build a misfit. Solid-state reactions consist of the direct combining of elemental or compound precursors at high temperatures [50]. This process normally involves carefully combining the precursors, and subsequent heating at temperatures ranging from 500°C to 1000°C, depending on the target item. Solid-state reactions have advantages since they are simple and produce reasonably pure products. However, they frequently need extended reaction periods and may produce products with greater grain sizes and reduced homogeneity. Solvothermal and hydrothermal synthesis include chemical reactions in a solvent at high temperatures and pressures, generally in an autoclave [51]. Hydrothermal synthesis employs water as a solvent, whereas solvothermal synthesis can use a variety of organic solvents. They are especially beneficial for synthesizing compounds that are difficult to get through high-temperature solid-state methods, but may result in lower yields than other approaches.

Once the MLC crystals have been synthesized, they must be subjected to an accurate characterisation methodology to ensure proper growth and purity of the sample. Single crystal X-ray diffraction (XRD) is the primary technique employed to characterise misfit layer compounds. The diffraction pattern provides information about the crystal structure, including lattice parameters, phase composition, and

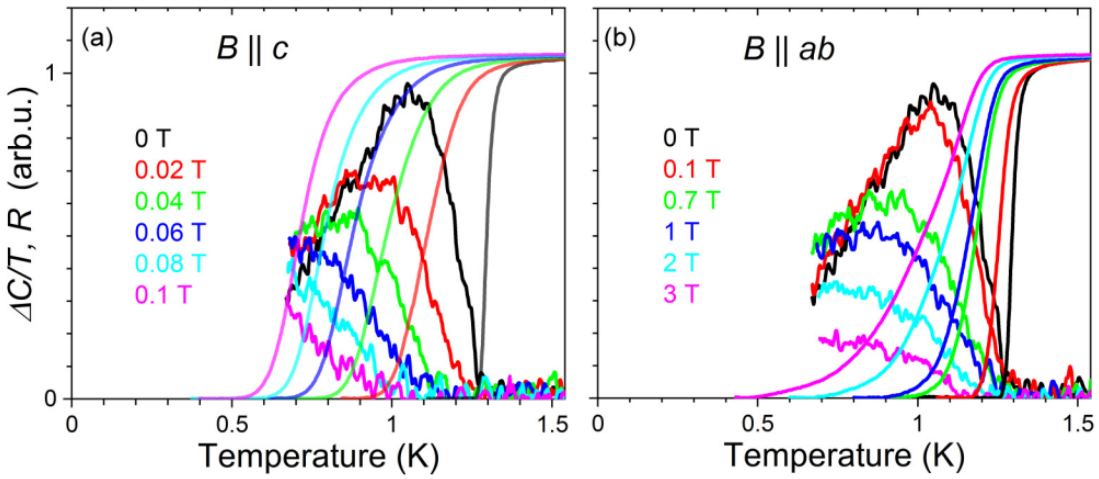

Figure 1.12: Superconducting transitions of $(LaSe)_{1.14}(NbSe_2)$ obtained by resistive and heat capacity measurements from Ref. [9]. Temperature and field sweeps of the specific heat were measured using an ac calorimeter in a He-3 cryostat [54, 55]. The superconducting transitions are displayed for the indicated fields B parallel to the c axis (a), and parallel with the ab plane (b).

crystallinity [52]. It also give informations on disorder, twinning and the eventual occurrence of orientation variants. For electron diffraction thin samples of single crystals are prepared by repeated cleavage or splicing. First of all, the intensity measurements of the two subsystems are carried out individually; the common reflections can be adopted to scale the two sets of data. With the electron beam perpendicular to the layers, reflections from both subsystems are obtained, as well as satellite reflections caused by mutual modulation of the two layers, which serve as the misfit crystal's fingerprint. High resolution imaging may also capture rows of atoms with quasi-periodic intensity modulation in the misfit direction. Finally, Raman spectroscopy can give precise insights on the bonding and structure of MLC layers [53], as well as the ability to identify phases by detecting distinctive Raman signatures. In MLCs, the mismatch between layers often leads to unique spectral features that can be analyzed to understand the precise stacking order in the crystal.

1.5 Phenomenology and emergent properties

Misfit layer compounds are a fertile ground for discovering and studying fascinating physical phenomena. The ability to fine-tune their properties through chemical composition and stacking order, makes them versatile materials for both fundamental research and technological applications.
A key-feature of MLCs is the charge transfer mechanism that occurs in the bulk as a result of the interaction between the TMD layers and the rocksalt units. Indeed, as will be detailed in the next chapter, the rocksalt unit acts as an electron reservoir, donating electrons to the TMD layers, which are highly doped.

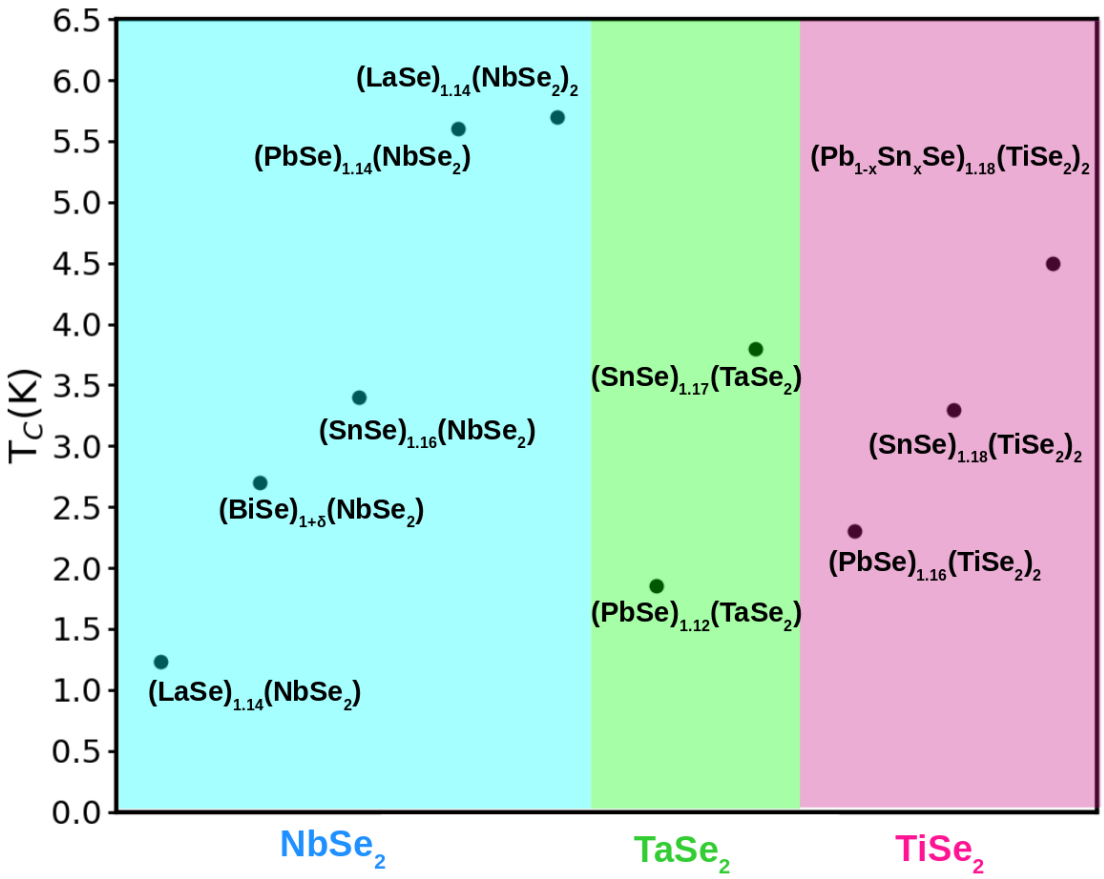

Figure 1.13: A diagram of the superconducting misfit layer compounds with X=Se. The y-axis shows critical temperatures (T_C) in Kelvin (K). Shaded regions in the figure categorize misfit layer compounds based on the kind of TMD in the structure, namely $NbSe_2$ (cyan), $TaSe_2$ (green) and $TiSe_2$ (pink).

MLCs exhibit a range of emergent properties that arise from the interaction between the individual constituents, leading to phenomena that can only partially or cannot be explained in terms of separate subsystems.
Superconductivity was discovered in several MLCs, both with inherently superconducting TMD layers, such as NbX_2 and TaX_2 (with X=S,Se), and with TMDs in which parameters like pressure or doping can induce superconductivity, such as TiX_2 with X=S,Se.
Misfit layer compounds where the TMD is $NbSe_2$ stacked with diverse rocksalt monochalcogenides display an extreme in-plane upper critical magnetic field that substantially violates the Pauli paramagnetic limit. This can be linked to a particular kind of superconductivity, the so-called "Ising superconductivity". This type of superconductivity occurs, in most cases, in monolayers that lack crystal inversion symmetry and have significant spin-orbit coupling, such as $NbSe_2$. The combination of these effects produces an effective spin-orbit magnetic field. This fixes electron spins out of plane (thus the term "Ising") with opposing signs for opposite momenta at the points K and $K^{'}$ of the hexagonal Brillouin zone of the monolayer (spin-momentum locking). The locking of spin and momentum in the superconducting pairing prevents spin pair splitting, enhancing the in-plane critical magnetic field. Examples of misfit layer compound displaying Ising superconductivity are $(LaSe)_{1.14}(NbSe_2)_m$ with m=1, 2 [9], $(PbSe)_{1.14}(NbSe_2)$ [56], $(SnSe)_{1.16}(NbSe_2)$ [57] and $(BiSe)_{1+\delta}(NbSe_2)$ [58] with critical temperatures ranging from 1.23 to 5.7 K. As an example, superconducting transitions of $(LaSe)_{1.14}(NbSe_2)$ obtained by resistive and heat capacity measurements is shown in Fig. 1.12.
Enhancement of superconducting critical temperature with respect to the TMD bulk counterpart is observed in MLCs with $TaSe_2$. Anisotropic superconductivity with higher in-plane critical field was detected in $(SnSe)_{1.17}(TaSe_2)$ [23] and $(PbSe)_{1.12}(TaSe_2)$ [59] with T_c of 3.8 and 1.85 K respectively.
Finally, MLCs with $TiSe_2$ exhibit doping-induced superconductivity, as it happens in bulk Cu-intercalated $TiSe_2$ [60]. Critical temperatures ranging from 2.3 to 4.5 K are reported for MLCs $(PbSe)_{1.16}(TiSe_2)_2$ [10], $(SnSe)_{1.18}(TiSe_2)_2$ [61] and $(Pb_{1-x}Sn_xSe)_{1.16}(TiSe_2)_2$ [17].
Figure. 1.13 shows a summary of the experimental data on superconductivity in misfit layer compounds with X=Se. The y-axis shows critical temperatures (T_C) in Kelvin (K). Shaded regions in the figure categorize misfit layer compounds based on the kind of TMD in the structure, namely $NbSe_2$ (cyan), $TaSe_2$ (green) and $TiSe_2$ (pink).
Modulation of the TMD lattice under the influence of the rocksalt substrate can trigger charge density wave (CDW) states in MLCs. Compounds with $TiSe_2$ [14] and VSe_2 [15, 62] show variation in the CDW pattern. The presence of a 2×2 CDW in $(LaSe)_{1.14}(NbSe_2)_2$ misfit layer compound was under debate. This topic will be extensively treated in the next chapters by presenting our combined study based on Raman spectroscopy and ab initio calculations on $(LaSe)_{1.14}(NbSe_2)_2$ lattice dynamics. Strain due to the lattice mismatch and charge transfer in MLCs can modify magnetic phases by altering the exchange interactions between magnetic moments [63–65].

The MLCs's superlattice structure enables selective scattering of phonons at interfaces, lowering lattice thermal conductivity while having no effect on electrical conductivity, making them excellent thermoelectic materials [66]. The thermoelectric performance is extremely anisotropic, with substantially larger power factors along the in-plane axis than in the cross-plane direction. For example, $(SnS)_{1.2}(TiS_2)_2$ has an in-plane power factor that is more than ten times larger than the cross-plane value [67]. Substitutions and intercalations in the constituent layers, as in the case of $(SnS)_{1.2}(TiS_2)_2$ with element like Co and Cu, can optimize the carrier concentration and further enhance the Seebeck coefficient [67]. Finally, some misfit sulfides and oxides have thermoelectric figures of merit ZT that can reach promising values around 1 at elevated temperatures, making them appealing for waste heat recovery applications.

1.6 Summary

In the first chapter, we introduced the materials under consideration in this thesis, namely misfit layer compounds (MLCs).
These heterostructures are characterized by their composite structure, which consists of alternating layers of distinct compounds with mismatched lattices, namely transition metal dichalcogenide (TMD) layers and rocksalt units.
We thoroughly investigated the composition and structural complexity of MLCs, emphasizing how each subsystem contributes to the ultimate crystal structure.
We provided an in-depth examination of the subsystem geometries, we discussed the mismatch, which gave rise to the word misfit, and defined the misfit crystal lattice.
We provided a comprehensive review of the state-of-the-art synthesis methods used to create these complex structures. This included techniques such as molecular beam epitaxy (MBE), chemical vapor deposition (CVD) to produce high-quality MLCs with precise control over layer composition and thickness.
Furthermore, we discussed the experimental fingerprints of misfit crystals, focusing on the tools and techniques used to characterize these materials.
Finally, we presented MLCs and their emergent properties, which don't arise from the individual subsystems alone but from their intricate interplay within the composite structure.
We examined several examples of such emergent phenomena, providing detailed case studies of MLCs exhibiting superconductivity, charge density waves, magnetism, and thermoelectricity.

Chapter 2

Work function and band alignment of TMD monolayers and rocksalt units

2.1 The work function

In solid state physics, the work function is defined as the lowest energy needed to remove an electron from the material and send it to the vacuum with zero kinetic energy [68, 69].
To establish the work function formula, first we recall the main characteristics of a material's electronic structure by glancing at the diagram in Fig. 2.1. In an insulator or semicontuctor, the highest occupied state is known as the valence band maximum (VBM), while the lowest unoccupied state is known as the conduction band minimum (CBM). The single-particle energy gap E_g is the energy difference between these band edges. In a metal, the gap is zero and the Fermi energy (E_F) refers to the energy of the highest occupied state that separates occupied and unoccupied states. An energy barrier at the material's surface prevents the electrons from escaping to the vacuum. The barrier culminates at the vacuum level E_{VAC} which corresponds to the energy level of an electron at rest within a few nanometers outside the solid, with zero kinetic energy relative to the surface. Therefore, we can formally define the energy difference between the Fermi energy E_F and the energy at the vacuum level E_{VAC} as the work function W, the minimum energy necessary to remove an electron from the system to the vacuum level:

$$W = E_{VAC} - E_F. \tag{2.1}$$

In the case of an insulator, where the Fermi level lies inside the gap, one can define the ionization potential (IP) as the energy difference between the valence band maximum and the energy at the vacuum level:

$$IP = E_{VAC} - VBM, \tag{2.2}$$

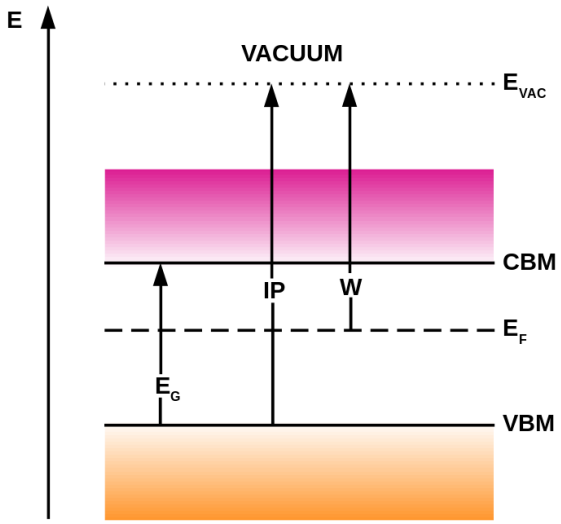

Figure 2.1: A sketch of an energy diagram for a semiconductor with flat bands at the surface. Band edges (VBM, CBM), vacuum level E_{VAC}, work function W, energy gap E_G, ionization potential IP are defined.

thus, in a metal, IP=W.
The work function is a simple, experimentally accessible quantity. There are several ways for measuring the work function, but photoelectric emission is the most commonly used [70]. By shining a monochromatic light of known frequency on the target, it is possible to measure the maximum kinetic energy of the emitted photoelectrons. Thus, the W formula may be derived from the concept of energy conservation. When an electron is removed from a solid surface by absorbing a photon of light, the energy of the photon must be equal to the sum of the work function and the kinetic energy of the electron:

$$h\nu = E_K + W \tag{2.3}$$

where h is the Plank's constant, ν is the frequency of the photon and E_K is the kinetic energy of the emitted electron.
The work function of a material is intricately tied to its composition and surface properties. Understanding the influence of factors such as crystal structure, surface orientation, cleanliness, adsorbates, and temperature is essential for accurately predicting and controlling the work function [71]. As detailed later, density functional theory (DFT) simulations provide a solid platform for studying work functions, taking into account the atomic lattice, exchange-correlation effects, and surface reconstructions [72].

2.2 The band alignment

Band alignment in solid-state physics refers to the relative placement of distinct materials' energy bands when they are brought into contact, such as at a heterojunction or interface. This alignment is crucial for determining the physical

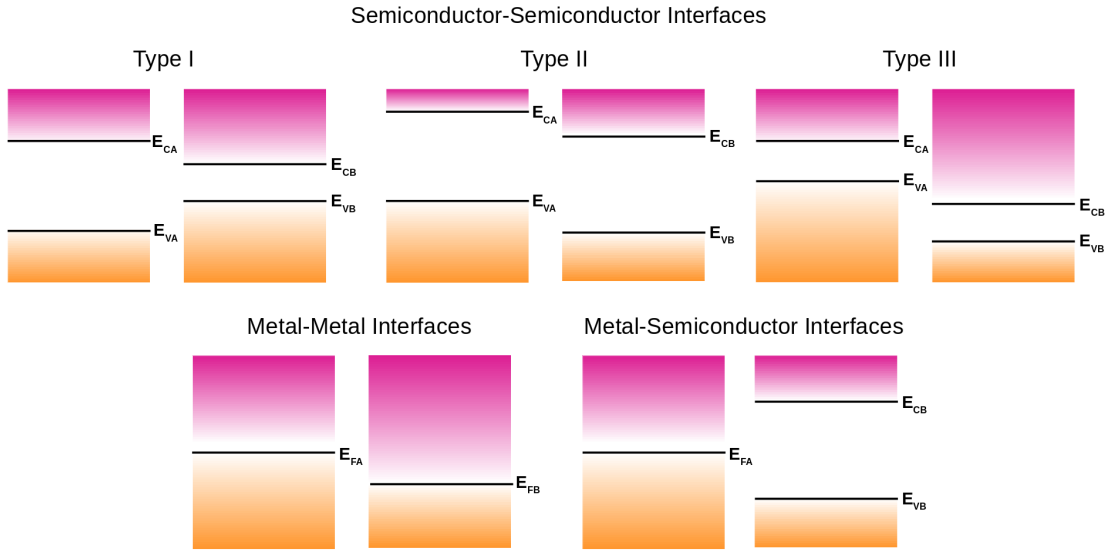

Figure 2.2: A sketch of interfaces classification. Orange and pink represent occupied and vacant bands, respectively. The labels relate to band edges with energy E_{VX}/E_{CX} for VMB and CBM in a semiconductor, and E_{FX} for a metal, where X=A,B stands for material A and B.

properties and behavior of the joined materials, since it influences how charge carriers (electrons and holes) flow over the interface. Proper alignment allows for effective charge transfer and separation, which is critical for the performance of electrical and optoelectronic devices. Poor band alignment, on the other hand, might have negative consequences, such as increased charge carrier recombination or energy barriers that obstruct carrier flow, lowering device efficiency and functionality. Understanding and managing band alignment is therefore essential for developing high-performance solid-state physics devices.
To gain a deeper understanding of the band alignment across different scenarios, we recall that the material interfaces may be classified into three types: semiconductor-semiconductor, metal-metal, and metal-semiconductor.
A sketch of interfaces classification is shown in Fig. 2.2.
The semiconductor-semiconductor interfaces are determined by the relative locations of each material's VBM and CBM. When two insulators with differing band gaps come into contact, their valence and conduction bands must align to ensure that the vacuum level remains constant throughout the interface.
It is further possible to divide the semiconductor-semiconductor interfaces in three categories: type I,II and III. Straddling alignment, also known as type I alignment, occurs when the conduction band minimum (CBM) and valence band maximum (VBM) of one material are both inside the other material's bandgap. In staggered alignment, referred to as type II alignment, the CBM and VBM of the first material are higher in energy than those of the other material. In broken gap alignment, or type III alignment, the CBM of one material lies below the VBM of the other material.
At metal-metal interfaces, the Fermi levels of the two metals must align, resulting

in a contact potential difference between the metals that allows electron transport and thermal equilibrium.
In a metal-semiconductor interface, the Fermi levels of the two materials must align, causing band bending in the insulator to compensate for the difference in work functions. The band alignment dictates the so-called Schottky barrier height, which governs electron injection from the metal into the insulator. The barrier height creates a depletion region, allowing current to flow in one direction while preventing it in the other. On the other hand, if the height of the barrier is very small or negligible (ohmic contacts), the current has no preferential direction.
To complete this picture, it has to be pointed out that in the aforementioned cases, we only considered a rigid shift of the bands when two materials are in contact to reach an equilibrium state. Thus, we neglected the band bending effect.
Band bending is the process by which a material's band structure bends up or down near a junction or contact [73]. Schottky and Mott developed the band bending concept to account for the right behavior of a metal-semiconductor interface [74, 75]. This process is represented in Fig. 2.3.
When metal and semiconductor are in contact, electrons flow between them due to the difference in work function. For example, if the metal work function (W(M)) is higher than that of the semiconductor (W(S)), electrons flow from the semiconductor to the metal. This process continues until the Fermi levels of the metal and semiconductor are aligned. In this case, electrostatic induction causes the metal to be negatively charged at the metal/semiconductor interface, while the semiconductor becomes positively charged. The electric field between the metal and the semiconductor at the interface cannot be efficiently screened in the semiconductor, resulting in a lower concentration of free charge carriers at the semiconductor surface compared to that of the bulk.
Thus, a space charge region is formed: in the considered case, if W(M)>W(S), the electrons are depleted in the space charge area, which is known as the "depletion layer", characterized by an excess of positive charges.
In the opposite case, if W(M)<W(S), the electrons are accumulated in the space charge area, which is known as the "accumulation layer", characterized by an excess of negative charges.
The charge transfer between the metal and the semiconductor results in band bending: in the space charge region, the band edges in the semiconductor are continuously shifted due to the electric field between the semiconductor and the metal until equilibrium is reached.
When W(M)>W(S), the semiconductor band edges bend upward towards the metal-semiconductor interface. The opposite process happens when W(M)<W(S), and the semiconductor band edges bend downward toward the interface.
The degree of bending of the semiconductor's energy band at the interface is equal to the difference in work function between metal and semiconductor. Therefore, we can define the band bending potential as:

$$V_{BB} = |W(M) - W(S)| \tag{2.4}$$

whose behaviour is shown for the two cases in Fig. 2.3.
In conclusion, we presented a wide range of interfaces based on material features.

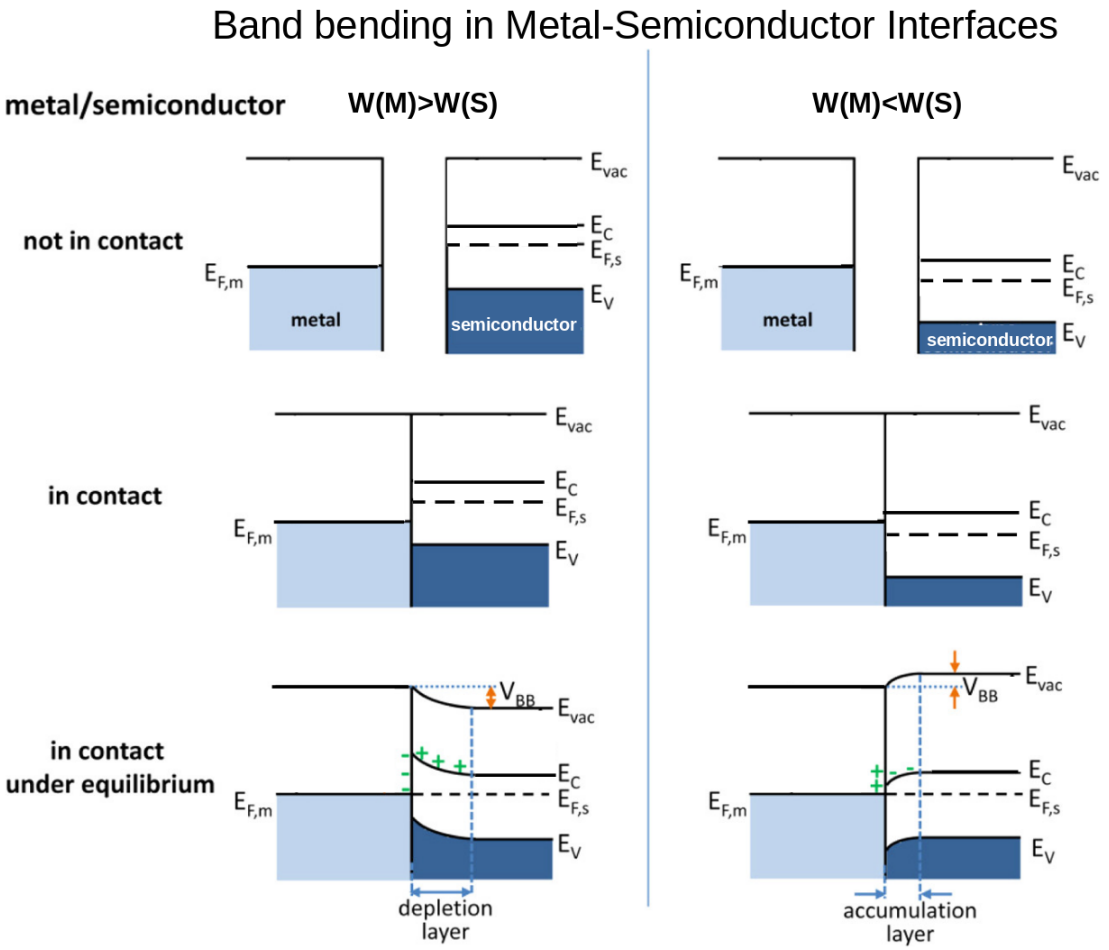

Figure 2.3: Band bending in metal-semiconductor interfaces. Light-blue and blue represent occupied states for metal and semiconductor, respectively. The labels refer to band edges with energy E_V/E_C for VMB and CBM in a semiconductor. $E_{F,x}$ stands for Fermi level, where X=m,s represents metal or semiconductor. E_{vac} labels the vacuum level. W(X), where X=M,S, represents the work function of the metal and semiconductor. The diagrams show two different cases, namely when W(M)>W(S) and vice versa (W(M)<W(S)) and the respective behaviour of the band bending potential V_{BB}. Image adapted from Ref. [73], distributed under a CC BY-SA 3.0 licence

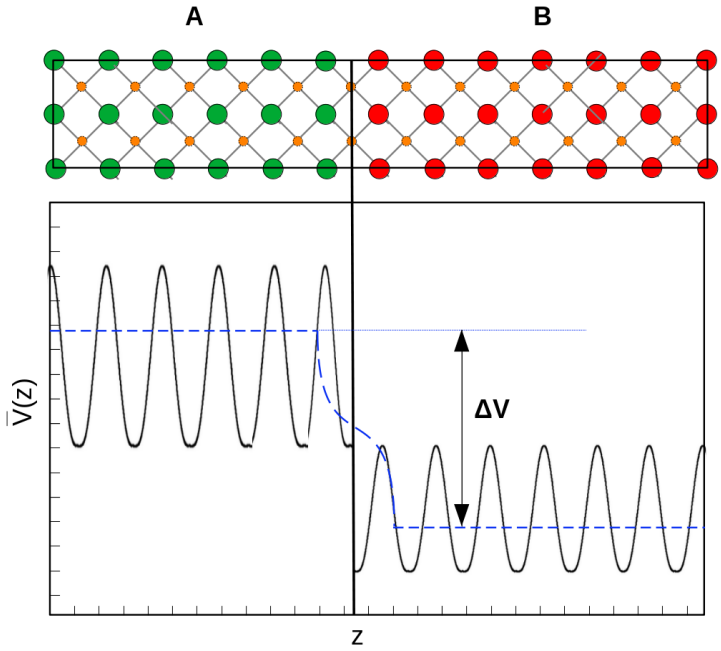

Figure 2.4: Schematic example of potential line up. The plot represents the planar average of the electrostatic potential ($\overline{V}$(z)) as a function of the out-of-plane coordinate (z) at the interface (black vertical solid line) between two materials A and B. Blue dashed lines represent the macroscopic average of $\overline{V}$(z) in each material ($\overline{\overline{V}}(z)$). The difference in macroscopic average of electrostatic potentials between A and B is denoted as ΔV.

The band alignment provides a global visualization picture of the different interfaces and serves as a starting point for developing novel devices.
In the following we discuss the band alignment determination in the DFT framework.

2.2.1 Band alignment and work function determination in density functional theory

To present the work function and band alignment determination in the context of density functional theory (DFT), we discuss the potential line up problem at interfaces.
The potential line up problem in density functional theory calculations arises when trying to align the electrostatic potentials of different materials or surfaces to determine band alignment and work functions [76].
The band alignment (or band offset) determination entails bringing two materials (which will be denoted as A and B) with different band edges together at an interface. The band structure of A and B may be determined in relation to a reference level, typically, as will be later detailed, an average of the electrostatic potential, $\overline{V}$(X), where X=A,B. The band offset problem is solved by calculating the difference in average electrostatic potentials between A and B, denoted as ΔV.
We need then to establish the locations of the average electrostatic potentials

inside A and B on an absolute energy scale, such as relative to the vacuum level. The long-range nature of the Coulomb interaction, however, means that there is no absolute reference for the average potential in an infinite solid. This causes the average potential of an infinite system to be ill-defined, and the band-line up cannot be solved if the features of the atomic structure near the interface impact potentials farther away.
As shown in Fig. 2.4, to solve the problem of the potential line up [77–79], we define the electrostatic potential in the space as:

$$V(\mathbf{r}) = \frac{1}{4\pi\epsilon_0} \int_R d^3r' \, \frac{n(\mathbf{r}')}{|\mathbf{r} - \mathbf{r}'|} \tag{2.5}$$

where n($\mathbf{r}$) is the charge density and R is the volume in which the charge density is non-zero. The oscillations of the electrostatic potential V($\mathbf{r}$) in the direction perpendicular to the interface may be expressed as a planar average of the electrostatic potential $\overline{V}$(z):

$$\overline{V}(z) = \frac{1}{S} \int_S dxdy \; V(\mathbf{r}) \tag{2.6}$$

where S is the surface area of the unit cell in the interface plane. The spatial distribution of electrons and ionic cores causes periodic oscillations in the potential along the z axis. These oscillations are eliminated by a macroscopic averaging technique, resulting in a constant value in the bulk. The macroscopic average of the electrostatic potential along z is

$$\overline{\overline{V}}(z) = \frac{1}{L} \int_{-\frac{L}{2}}^{\frac{L}{2}} dz \; \overline{V}(z) \tag{2.7}$$

where L is the length of the period of oscillation along z. The potential alignment is established by the difference in electrostatic potential energy between the materials A and B. The planar-averaged electrostatic potential converges to its bulk value within two atomic layers of the interface, a phenomenon seen in various interface systems. This quick convergence illustrates that band alignment is an interface feature. Once the potential alignment between the two materials is known, the bulk band structures can be aligned. For instance, in case of semiconductor-semiconductor interface, the valence-band offset (ΔE$_V$), is defined as the position of the VBM (E$_{VBM}(X)$) with respect to the average electrostatic potential in material X with X= A or B:

$$\Delta E_V = (E_{VBM}(B) - E_{VBM}(A)) + \Delta V \tag{2.8}$$

where ΔV= $\overline{\overline{V}}(B) - \overline{\overline{V}}(A)$ is the potential line up. The conduction-band offset (ΔE$_C$) can be thus derived from the gap value of A and B. A positive valence-band offset at interface between A and B suggests that material B has a higher VBM with respect to the material A.
To reframe this issue in terms of work function determination, assume two metals,

A and B. The work function of the two materials differs as follows:

$$\begin{aligned}\Delta W &= W(A) - W(B) = \\ &= (E_{VAC} - E_F(A)) - (E_{VAC} - E_F(B)) = \\ &= E_F(B) - E_F(A)\end{aligned} \tag{2.9}$$

thus, if $\Delta W > 0$ this means that $E_F(B) > E_F(A)$, where E_F and E_{VAC} are absolute energies, resulting in a charge transfer from B to A.
The above equation cannot be solved because absolute energies cannot be determined using DFT for two reasons. First, the Fourier transform of the Hartree potential is a hill-defined quantity in DFT, since its $\mathbf{q} = \mathbf{0}$ and $\mathbf{G} = \mathbf{0}$ components are arbitrarily set to zero. Second, due to the use of pseudopotentials, the energies are always defined minus a constant.
Although the absolute energies cannot be established, the work function may be efficiently calculated using the DFT framework by means of the macroscopic average of the electrostatic potential [80]. Consider two slabs A and B after taking the macroscopic average of their electrostatic potentials. This quantity is assessed in the vacuum zone, which is farther away from the slab along z. The work function is thus determined by the location of the Fermi level E_F in relation to the average electrostatic potential in the vacuum region. This approach allows to calculate the difference in work function between two slabs A and B to determine the direction of the charge transfer, if any.

The macroscopic average approach is not suitable to 2D materials with slab thicknesses of only a few Angstroms. Indeed, as shown in Fig. 2.5, the planar average of the electrostatic potential $\overline{V}(z)$ has only a slightly dispersed peak in the region corresponding to the layer's location along the out-of-plane direction. Thus, it is not possible to define any macroscopic average of $\overline{V}(z)$.
To simulate a 2D material in the DFT framework, extra vacuum space is added to the simulation box to guarantee that the layers' periodic replicas do not interact with one another. If the vacuum space is thick enough, the value of the planar average of the electrostatic potential in the vacuum region far from the layers' location is constant (V_{VAC}).
To ensure that the electrostatic potential saturates to a certain value in the vacuum zone between two periodic replica of the material, convergence tests can be performed as a function of the vacuum space. For a monolayer, typical convergence values for the size of the vacuum space range between 5 and 15 Å .
Thus, in order to calculate the work function of a 2D material, it is sufficient to determine two quantities. The first one is the value of the planar average of the electrostatic potential in the vacuum region far from the layers' location (V_{VAC}). The second one is an energy reference (E_F), namely the Fermi energy (E_F) for a metal and the valence band maximum (VBM) for an insulator or semiconductor. Then, as shown in Fig. 2.5, the work function (W) reads:

$$W(X) = V_{VAC}(X) - E_{REF}(X) \tag{2.10}$$

where X is the 2D material under consideration.
In the next section, we will show how to use this technique to make a screening

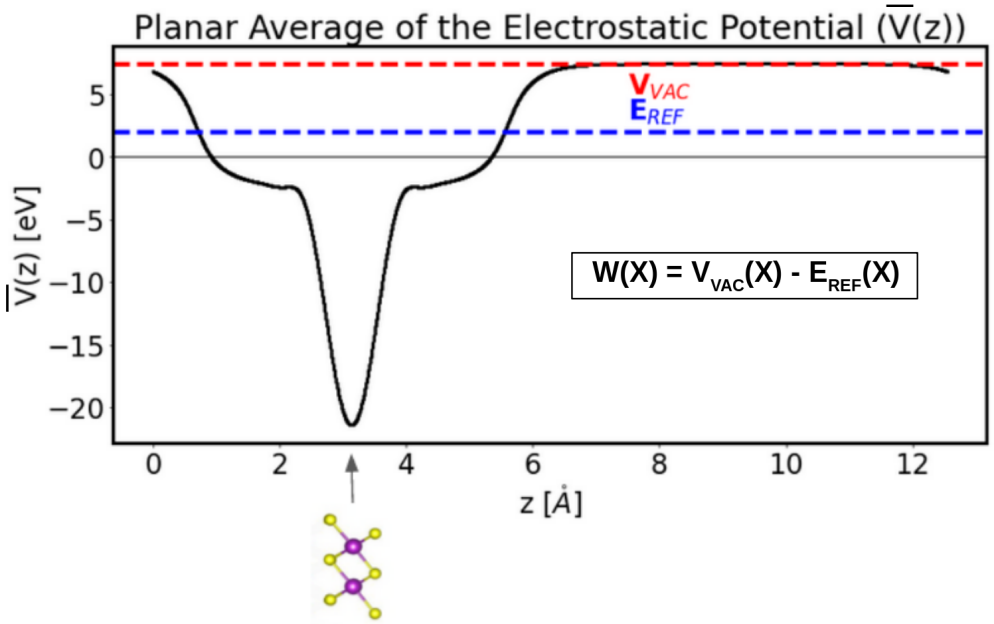

Figure 2.5: The calculation of the planar averaged electrostatic potential $\overline{V}$(z) along the out-of plane direction (z). The negative peak represents the spacial region in which the layer is located. V_{VAC} is the value of the planar averaged electrostatic potential in the vacuum region (red line). E_{REF} (blue line) corresponds to E_F (VBM) for metals (insulators/semiconductors). The work function is $W(X) = V_{VAC}(X) - E_{REF}(X)$ where X is the material under consideration.

of misfit layer compounds to determine the charge transfer mechanism in these materials.

2.3 Work function determination and band alignment of TMD monolayers and rocksalt units

To address the challenge of creating a misfit layer compound with desired physical properties, we must first provide a basic description of the essential physical mechanism, the charge transfer among constituents.
The key quantities ruling the charge transfer in these systems are the work function difference among RS and TMDs and the consequent band alignment, the lattice mismatching ratio a_2/a_1 and, finally, the degree of hybridization when the two subsystems are in contact.
As we will show in the next chapter, a computational screening of misfits starting from their building blocks serves as a preliminary analysis to get insight into their physics with cheap simulations before constructing each individual compound.
To give an idea of the scale of a misfit simulation, consider a misfit layer compound with LaSe as a rocksalt ($a_2 = 6$ Å) and $NbSe_2$ as a TMD ($a_1 = 3.437$ Å). The lattice mismatch ratio a_2/a_1 is $6/3.437 \simeq 1.75$, which may be approximated as $x/y = 7/4$. This ratio suggests that to produce the periodic approximant of the misfit, we require a supercell including 4 repetition of LaSe and 7 repetition

of $NbSe_2$ along the mismatch axis. The resultant supercell lattice parameter will be $|\mathbf{a}|=a=xa_1=ya_2=7a_1=4a_2 = 24$ Å.
Thus, for example, a huge supercell of 232 atoms and a total of 1944 electrons is needed to simulate the bulk misfit layer compound $(LaSe)_{1.14}(NbSe_2)_2$. DFT simulation of such a huge supercell requires heavy computation.
As we will show in the next chapter, we are able to simulate such a system. However, this preliminary analysis demonstrates that in order to obtain a global picture of the charge transfer process in misfit layer compounds, we require a feasible preliminary computational screening of all misfit crystals.
We present our screening technique, which is based on the misfit individual subsystems' work function and band alignment determinations.

In order to gain insight into the charge transfer among the RS and TMD layers in the MLC, we perform extensive calculations of the work functions of 8 isolated rocksalt units and 12 isolated TMDs monolayers. In the following, we will call each rocksalt unit and TMD monolayer duo the RS/TMD couple. By systematically evaluating the work functions, we aim to elucidate the intrinsic process that govern charge transfer in these heterostructures, thereby providing a deeper understanding of their potential applications [81].
The choice of considering TMD single layers is motivated by several factors. As detailed in chapter 1, MLCs with m = 1 comprises monolayers TMD alternated with rocksalt units. We can also recover the behaviour of the TMD work functions in the case of MLCs with m = 2, which are composed of alternating TMD bilayers and rocksalt units. Indeed, previous studies have shown that the work functions of bilayer TMDs are fairly close to those of single layers. [82]. This observation supports the validity of our approach, as it implies that the electronic properties of single layer TMDs can serve as reliable proxies for their bilayer counterparts.
Furthermore, it is interesting to focus on TMD monolayers since surfaces of MLCs with m=2, obtained by cleaving the bulk in the plane perpendicular to the van der Waals interaction region, terminate with a TMD monolayer that can be investigated experimentally by scanning tunnel microscopy (STM) as well as angle-resolved photoemission spectroscopy (ARPES), as detailed in the next chapter.
To make a computational screening of MLCs heterostructures from their elemental constituents, we use the previously described approach to determine the work function of 2D materials. The procedure, depicted in Fig.2.5 is the following: we estimate for each system the energy reference E_{REF}, namely Fermi energy for metals (E_F) or valence band maximum (VBM) for insulators and semiconductors. Then we use Eq. 2.10 to define the work function W(X), where X=TMDs,RS.
In this equation, V_{VAC} is the value of the electrostatic potential along z, averaged in the plane, and evaluated in the vacuum region. If $\Delta W=W(A)-W(B)> 0$ then $E_{REF}(B)>E_{REF}(A)$ and electrons will flow from the material B to the material A.
Numerical values of work functions are calculated in the Perdew-Burke-Ernzerhof (PBE) scheme [83] with the Quantum ESPRESSO (QE) package [84]. We employ pseudopotentials (pseudo efficiency) each with a proper converged kinetic energy

TX_2/RQ	W (eV)
LaS	2.46
BiS	3.88
PbS	4.48
SnS	4.48
LaSe	2.84
BiSe	3.94
PbSe	4.08
SnSe	3.74
NbS_2	6.02
TiS_2	5.72
MoS_2	5.88
WS_2	5.65
SnS_2	6.98
VS_2	5.33
$NbSe_2$	5.37
$TiSe_2$	4.92
$MoSe_2$	5.31
WSe_2	5.06
$SnSe_2$	6.04
VSe_2	4.77

Table 2.1: Individual subsystems' work function determination. Rows represent TMD monolayers in blue and RS units in red, respectively. For each compound the work function (W) used to construct the band alignment plot in Fig. 2.6 is reported.

cutoff for plane-wave basis set. The Brillouin zone integration is performed with a Monkhorst-Pack grid [85] of 21 × 21 k-points and using a Gaussian broadening of 0.01 Ry, proven to be sufficient to accurately determine the electronic properties of all systems under consideration. The in-plane lattice parameter of all the considered structures is fixed at the experimental one of each subsystem, namely the Q-layer rocksalts and the monolayer TMDs (see Fig. 1.6). The internal coordinates are fully optimised by means of the Broyden-Fletcher-Goldfarb-Shanno (BFGS) algorithm, with a convergence threshold of 10^{-4} Ry on the total energy difference between consecutive structural optimisation steps and of 10^{-3} Ry/Bohr on all forces components.
It is worth noting that the GW approximation leads to work functions that are, at most, 0.5 eV larger than the PBE case in TMDs [82]. Moreover, we verified on some rocksalt bilayers (LaSe, PbSe) that HSE06 [86] does not change quantitatively and qualitatively the picture.
The results of the TMDs and rocksalts are summarized in Tab.2.1.
We used the work function calculation to build the so-called band alignment plot, shown in Fig. 2.6. This picture shows the relative placements of energy bands (such as conduction and valence bands) across different materials or interfaces. The vertical axis shows electron energy levels, such as the conduction band edge

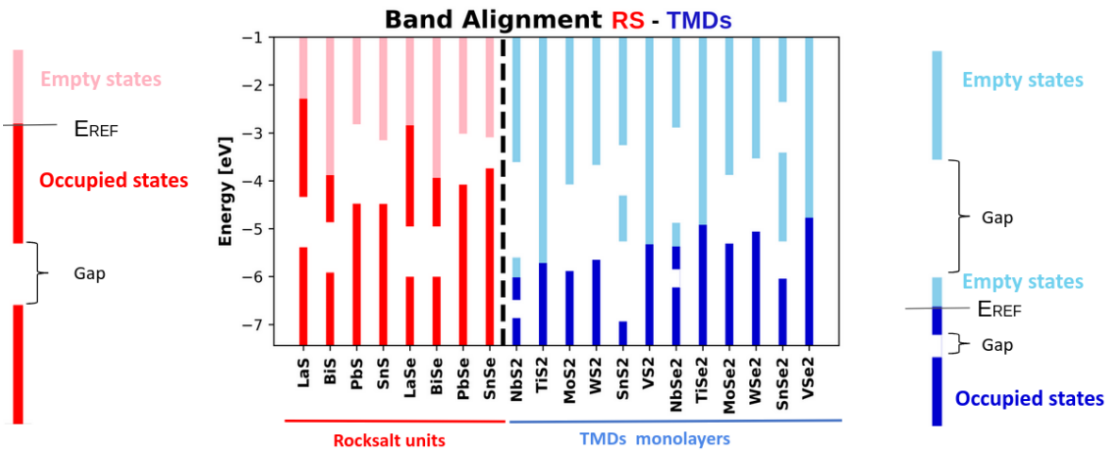

Figure 2.6: Band alignement of isolated bilayer rocksalt (red) and single layer transition metal dichalcogenides (blue). Dark (light) bars represent the position of the E F /valence band maximum (E_F /conduction band minimum) for metals/insulators. White spaces in the bars stand for gaps in the single particle spectrum. The energy zero is set to the vacuum level.

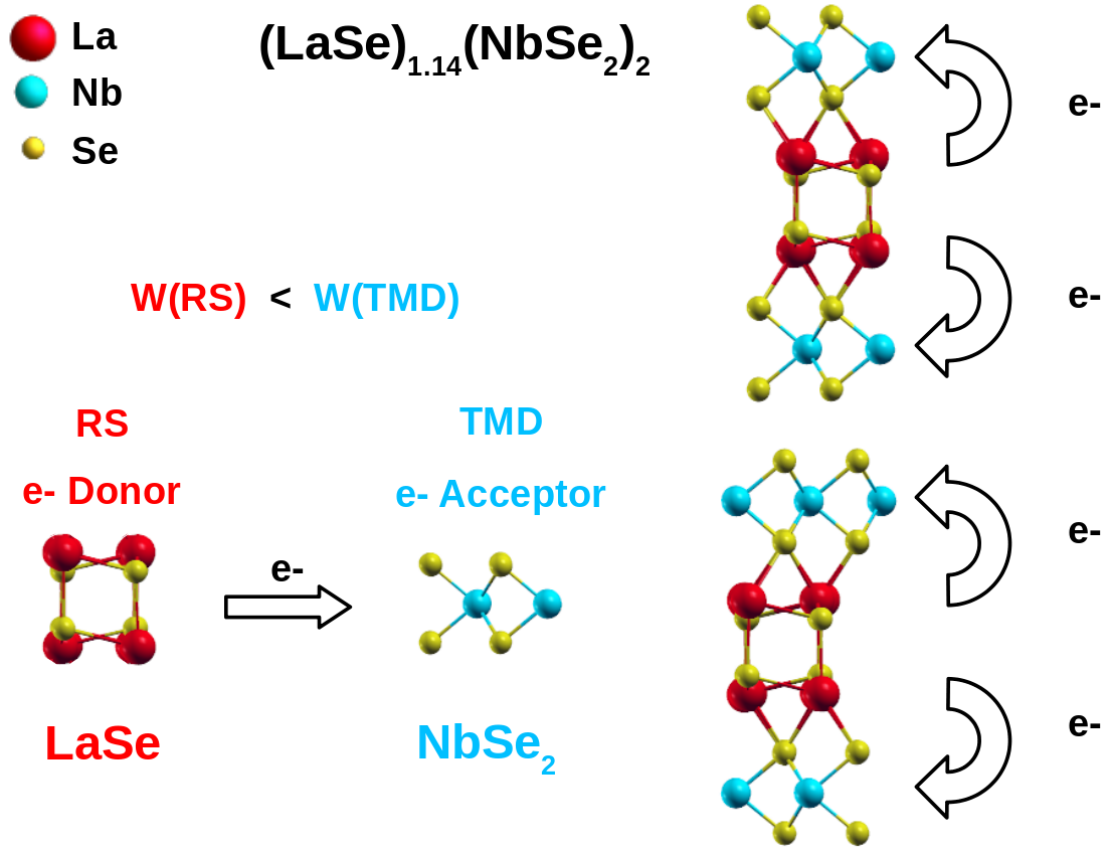

Figure 2.7: The charge transfer mechanism in misfit layer compounds. The image depicts the preferred direction of electrons (e^-) in a misfit. For example, the compound $(LaSe)_{1.14}(NbSe_2)_2$ is shown. In this misfit, the TMD is $NbSe_2$ and the RS is LaSe. W(X) represents the work function of the rocksalt (X=RS) and the TMD (X=TMD), respectively.

(CBM), valence band edge (VBM) for insulators (semiconductors), or Fermi level (E_F for metals). The horizontal axis represents the different materials. In Fig. 2.6, the rocksalt units are colored red, while the TMD monolayers are blue. Dark bars represent the Fermi level (E_F) in metals and the valence band maximum in insulators. In contrast, bright bars represent the location of the conduction band minimum in insulators. In addition to these bars, the withe spaces indicate gaps in the single particle spectrum, namely energy regions where no electron states are accessible. White gaps also divide groups of distinct bands within the valence/conduction bands. To provide a consistent reference point for these energy levels, the energy zero is set to the vacuum level.

The band alignment plot can help predict the charge transfer in misfit heterostructures. First and foremost, the band alignment plot shows that the work function of the rocksalt units is always lower than that of the TMDs. This indicates that electrons are more easily extracted from a rocksalt unit than from a TMD. Therefore, as sketched in Fig. 2.7, there is a preferential direction of charge transfer in misfit layer compounds from the RS to the TMD. The rocksalt units serve as an electron reservoir for the TMDs, allowing for efficient electron transfer between the two materials. This holds valid for all rocksalt/TMD couples, demonstrating that hole charge transfer from rocksalts to TMDs is unlikely. This is an important finding since the charge transfer phenomenon was a well-known physical mechanism in MLCs, reported in a variety of specific compounds of the family, but there was a lack of understanding concerning its microscopical mechanism.

Second, we can exploit the different work function of rocksalts to tune the charge transfer in the misfit. This can be accomplished by analyzing the differences in work function between each RS/TMD couple. As an example, take LaSe as the rocksalt and $TiSe_2$ as the TMD. The difference in work function between these two compounds is $\Delta W = W(TiSe_2) - W(LaSe) = 4.92 - 2.84 = 2.08$ eV. Changing the rocksalt with PbSe, for example, results in a work function difference of $\Delta W = W(TiSe_2) - W(PbSe) = 4.08 - 2.84 = 1.24$eV. Thus, because $W(LaSe) > W(PbSe)$, the doping level of $TiSe_2$ in a misfit layer compound with LaSe would be higher than with PbSe. Furthermore, we can imagine that it is possible to engineer a misfit in such a way that the doping level is rigidly adjustable through appropriate alloying of the RS unit. In the present case, the $TiSe_2$ doping could be controlled by an intermediate amount of La and Pb through La-Pb alloying in the rocksalt without requiring any external tuning.

The net amount of charge transfer depends, however, not only on the work function difference but also on the mutual concentration of the RS and TMD that is related to the mismatching ratio. To explain this more clearly, each RS can transfer a given amount of charge to the TMD layer, if the mismatching ratio is close to one. However, if the mismatching ratio increases, the relative concentration of RS atoms per TMD cell decreases and so does the charge transfer. By looking at Fig. 1.4 in the first chapter, it is clear that the mismatching ratio varies mostly due to the change in the TMD lattice parameter.

Finally, it should be noted that our technique is a preliminary screening that is only valid in the rigid doping regime. Any electronic-state hybridization at the

interface that influences the shape of the bands, and hence can have an impact on the charge transfer, cannot be captured by these calculations, requiring in-depth study of the complete misfit. We will discuss the degree of hybridization when the two subsystems are in contact in the next chapter.
In conclusion, this plot can therefore be used as guidance for selecting the proper RS/TMD couple. By comparing the work function and relative band positioning of different RS/TMD combinations on the plot, it is possible to target the charge transfer in the misfit. As we will show in the next chapter, the work function based approach works quite well in predicting charge transfer in the misfit.

2.4 Summary

In the second chapter, we unveil the mechanism controlling the charge transfer in misfit layer compounds.
By presenting the concepts of work function and band alignment, we emphasize the necessity of accurately assessing these quantities in heterostructures and interfaces.
The work function is a fundamental property of materials, representing the minimum energy required to remove an electron from a material and send it to the vacuum with zero kinetic energy.
Band alignment describes how different materials' energy band are positioned in relation to one another at an interface. We closely examine the various forms of band alignment, including metal-metal, metal-semiconductor, and semiconductor-semiconductor, and explained the band bending effect.
We then introduce the macroscopic average method within the framework of density functional theory (DFT), a powerful computational approach to determine the work function and band alignment.
We then specialized work function determination for 2D materials. Finally we present our results by applying the aforementioned concepts in misfit layer compounds.
We show our straightforward computational screening of MLCs based on the work function of each individual subsystem.
We calculate the work functions of isolated rocksalt units and TMD single layers to understand the charge transfer processes in misfit heterostructures.
We build the band alignment plot that, as we will show in the next chapter, qualitatively and quantitatively predicts the charge transfer in these structures.
The results show that the work function of the rocksalt units is always lower than that of the TMDs. Therefore, a preferred direction for electron transfer in misfit layer compounds exists: from the RS, which works as an electron donor, to the TMD, which is electron-doped.
Finally, we discuss how this method provides a general picture of the charge transfer mechanism in misfit layer compounds.
These findings serve as a guide for selecting the suitable RS/TMD couple to build a misfit layer compound, avoiding heavy calculations, and also provide significant information for experimental synthesis.

Chapter 3

Ab initio geometrical and electronic properties of misfit layer compounds

3.1 Experimental structure determination of bulk misfit layer compounds

In this chapter, we discuss the geometrical and electronic properties of misfit layer compounds, presenting the results of our ab initio calculations. We begin by introducing the experimental state-of-the-art procedure for structural determination of misfit layer compounds. Vapor transport techniques coupled with single crystal X-ray diffraction are one of the most used and effective methods for synthesizing and characterizing misfit layer compounds. In particular, when dealing with structure determination, the refining process in X-ray diffraction is a vital stage in determining the exact structure of misfit crystals. This technique involves adjusting a model of the crystal structure to fit the observed diffraction data. To better explain the refinement process, we recall the step-by-step X-ray diffraction procedure in the case of single crystal XRD. X-ray beams are aimed at single crystals, and the resulting diffraction pattern is recorded. This pattern includes information on the atomic arrangement of the crystal. In the pattern, the position of the spots is determined by the angles at which they occur. Each spot corresponds to a specific set of crystallographic planes, described by Miller indices (hkl), which are assigned via the indexing procedure. In the indexing process, the unit cell dimensions and the symmetries of the crystal are determined from the diffraction pattern. Based on the previously determined space group and chemical composition, an initial structural model including the atomic positions within the unit cell is constructed.
Then, the refining process is applied: by a fitting approach, the structural model's parameters are iteratively adjusted to minimize the discrepancy between observed and estimated diffraction intensities. To correctly establish the crystal composition of misfit layer compounds, the individual subunit lattices and symmetries must be refined using X-rays. Then, the common part, namely the misfit crystal,

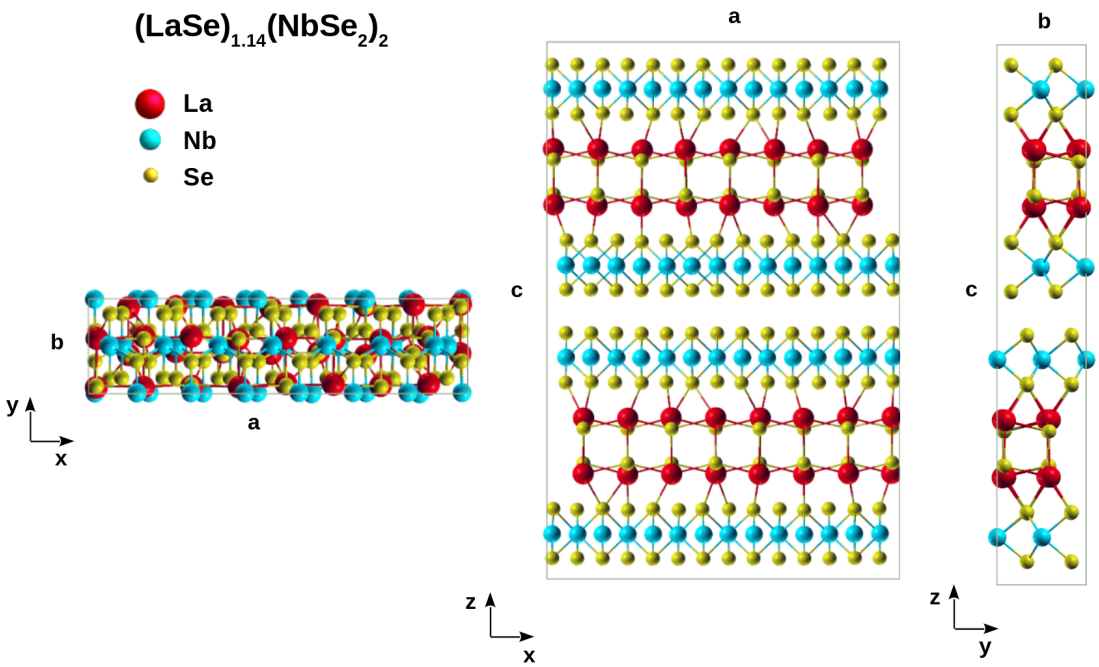

Figure 3.1: $(LaSe)_{1.14}(NbSe_2)_2$ misfit layer compound. In this misfit, layers of the transition metal dichalcogenide 2H-$NbSe_2$ are stacked with rocksalt units of LaSe.

is determined by refining the relative positions of each subunit.

For example, we report the experimental structural determination of misfit layer compound $(LaSe)_{1.14}(NbSe_2)_2$, as described in Ref. [87].

As shown in Fig. 3.1, $(LaSe)_{1.14}(NbSe_2)_2$ crystal is composed of a regular alternation of 2H-$NbSe_2$ bilayers with trigonal prismatic coordination and of LaSe rocksalt bilayers.

To grow the crystal, the elements La, Nb, Se were sealed in an evacuated silica tube in a 1 : 2 : 5 stoichiometry. Then, the tube was heated to 1050 °C for 15 days and afterwards slowly cooled to room temperature. After that, the single misfit crystal was extracted and mounted on the diffractometer.

The structural determination was separated into three stages. To begin, each subsystem was described by recording two different sets of reflections (hkl) from LaSe and $NbSe_2$ on the same crystal. The 0kl common reflections were excluded at this step. The resultant identified space groups were C111 for LaSe and $C222_1$ for $NbSe_2$, respectively. Compared to bulk 2H-$NbSe_2$, the lattice of $NbSe_2$ layers is not perfectly hexagonal and is slightly compressed along the x axis, as shown in Fig. 3.2(b). As a consequence, the $NbSe_2$ sublattice is described by a centered orthorhombic cell with in-plane lattice vectors a_1=3.437 Å and $a_1 \approx$ 6 Å. As shown in Fig. 3.2(b), each Nb, Se(1) (lower selenium), and Se(2) (upper selenium) is in Wyckoff position 8(c), 4 atoms of Nb, Se(1), and Se(2) for each layer of the $NbSe_2$ bilayer.

The LaSe sublattice has also an orthorhombic symmetry, in this case with similar in-plane lattice parameters $a_2 \approx b_2\approx$ 6 Å. As shown in Fig. 3.2(a), the bilayer LaSe is composed of 8 atoms, 4 La and 4 Se, whose positions are independent and

LaSe	Distance Å (Exp. From [87])	Distance Å (Th. From [6])
La(1)-Se_{avg}	3.11	3.09
La(2)-Se_{avg}	3.05	3.10
La(3)-Se_{avg}	3.04	3.10
La(4)-Se_{avg}	3.05	3.08
$NbSe_2$	**Distance Å (Exp. From [87])**	**Distance Å (Th. From [6])**
$(Nb\text{-}Se)_{avg}$	2.593	2.60
$(Se\text{-}Se)_{intra}$	3.317	3.31-3.36
$(Se\text{-}Se)_{inter}$	3.533	3.51-3.53

Table 3.1: Interatomic distances in $(LaSe)_{1.14}(NbSe_2)_2$. Comparison between experimental data taken From. [87] and theoretical values obtained by ab initio simulations From [6].

labeled as La(X) and Se(x) with X = $1, 2, 3, 4$.
The common portion was then identified by collecting common 0kl reflections and refining the relative positions of the LaSe and $NbSe_2$ sublattices in the yz plane. This was done by fixing the lattice parameter of $NbSe_2$ in the yz plane and refining the position of the LaSe part accordingly. With this choice, the lattice mismatch direction is the x axis (h00). The final interatomic distances of $(LaSe)_{1.14}(NbSe_2)_2$ are summarized in Tab. 3.1. Fig. 3.2 shows a sketch of the misfit subunits to clarify the atom labels. In Tab. 3.1, the distance labeled as La(X)-Se_{avg} with X=$1, 2, 3, 4, 5$ is the average interatomic distance between each La atom and its 5 coordinated Se (namely 4 in-plane bonds Se_a, Se_b, Se_c, Se_d, and 1 out-of-plane bond Se_e, as detailed in Fig. 3.2(a)). Instead, for the $NbSe_2$ subsystem, the label $(Nb\text{-}Se)_{avg}$ stands for the average interatomic distances of the Nb-Se bond within each layer. The experimental intralayer $(Se\text{-}Se)_{intra}$ and interlayer $(Se\text{-}Se)_{inter}$ distances are also reported (see Fig. 3.2(b)).

3.2 Ab initio construction of the bulk cell and comparison with experiments

We now discuss the comparison of these experimental values with ab initio calculations taken from Ref. [6], which is the starting point for DFT calculations of misfit layer compounds performed in this thesis.
The starting structure for geometrical optimization was built by considering the experimental one of Ref. [87]. In order to reproduce the aforementioned experimental refinement process, the LaSe and $NbSe_2$ parts were initially considered separated and then combined together as described in the following.
To construct a commensurate approximant of the misfit cell for first principles calculations, two supercells of $NbSe_2$ and LaSe, respectively, were built starting from their individual unit cells. This was done according to the lattice mismatch

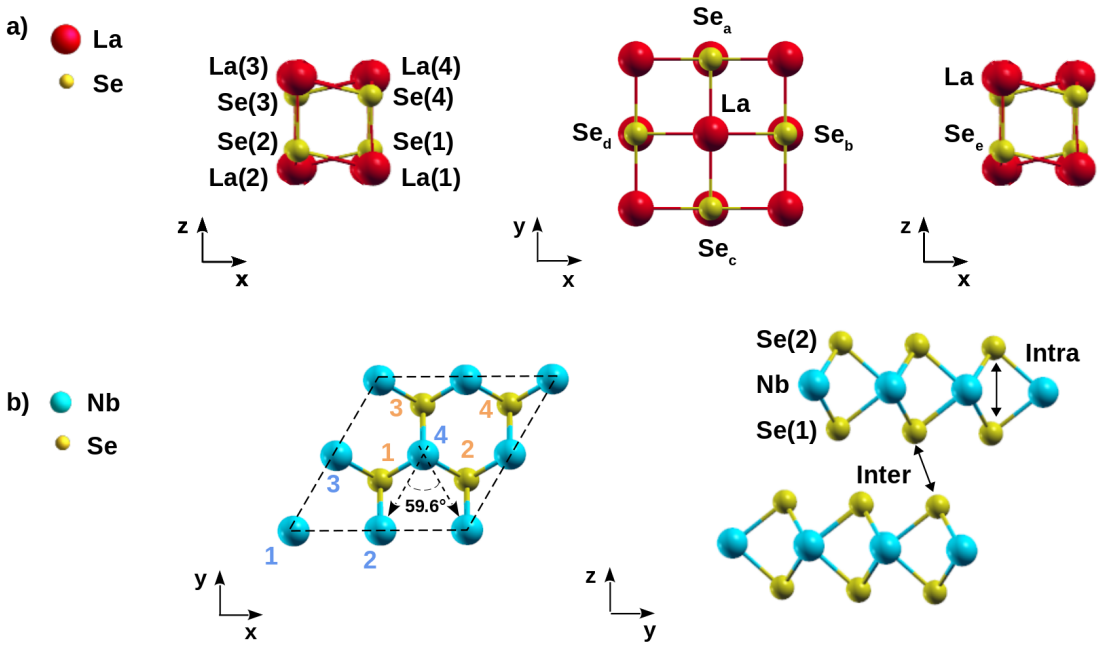

Figure 3.2: Atomic positions of $(LaSe)_{1.14}(NbSe_2)_2$ subunits. a) Atomic positions of LaSe. The LaSe bilayer is composed of 8 atoms (4 La and 4 Se). The positions are independent and labeled as La(X) and Se(X) with X = 1, 2, 3, 4. Each La atom has 5 coordinated Se, namely 4 in-plane Se_a, Se_b, Se_c, Se_d and 1 out-of-plane Se_e. b) Atomic positions of $NbSe_2$. Within the bilayer, each Nb, Se(1) and Se(2) atom is in the Wyckoff position 8(c) (with 4 atoms of Nb, Se(1) and Se(2) each layer, as shown in the left). On the right, intralayer and interlayer distances of the $NbSe_2$ bilayer are shown.

ratio, that is $a_2/a_1 = 6/3.437 = 1.75 \approx 7/4$.
For the $NbSe_2$ subsystem, a $7 \times \sqrt{3} \times 1$ supercell of the three atoms unit cell belonging to the space group $C222_1$ was generated (a slightly distored hexagonal unit cell along one direction, as discussed previously). For the LaSe part C111 symmetry was adopted and a $4 \times 1 \times 1$ supercell of the LaSe unit cell was generated. Then the two parts were combined with the LaSe centred in between the $NbSe_2$ bilayers. The assembled bulk system is composed of 232 atoms with P1 symmetry and lattice parameters $a=7a_1=4a_2=24.060$ Å , $b=b_1=b_2=6.019$ Å and the c parameter is fixed to the experimental one, $c=36.531$ Å (see Fig. 3.1).
The average interatomic distances obtained after the geometry optimization are reported in Tab. 3.1 in comparison with the experimental data of Ref. [87]. As we can see, the theoretical optimization procedure is in good agreement with the experimental data, reproducing the average interatomic distances within $\sim 2\%$ for the La-Se bond and $\sim 0.3\%$ for the Nb-Se bond.
Iono-covalent bonds form at the contact between $NbSe_2$ and LaSe with a substantial deformation of the LaSe layer and a significant deviation from an ideal rocksalt structure in which the bond length is equal in every direction. This huge modification of the LaSe interface signals a large charge transfer between LaSe and $NbSe_2$ bilayers, as detailed in the next sections.
The average value of the Nb-Se bond length does not deviate from the experimental value of 2.60 ± 0.01 Å measured by X-ray in bulk 2H-$NbSe_2$ [88]. The intralayer distance of each $NbSe_2$ layer ($(\text{Se-Se})_{intra}$) is instead affected by the presence of the rocksalt. Within the misfit supercell, the Se(1)-Se(2) interatomic distance along the **c** axis varies in a range of $3.31 - 3.36$ Å. This is due to the out-of-plane bonds between LaSe and $NbSe_2$, which are influenced by the mutual locations of La and Nb in the misfit crystal. Thus, $(\text{Se-Se})_{intra}$ shrinks by a factor $\sim 1\%$ with respect to the experimental value of 3.36 ± 0.02 Å measured by X-ray in bulk 2H-$NbSe_2$ [88]. On the contrary, the van der Waals interface between the two $NbSe_2$ layers is weakly affected by the presence of the rocksalt. Indeed, the interlayer distance ($(\text{Se-Se})_{inter}$) between two $NbSe_2$ layers within a bilayer is equal to the experimental value of bulk 2H-$NbSe_2$ (3.52 ± 0.02 Å in Ref. [88]) varying in a range of $3.51 - 3.53$ Å. This explains why the cleavage of the sample leads to a monolayer $NbSe_2$ terminated surface that can be probed by scanning tunneling microscopy (STM) and angle-resolved photoemission spectroscopy (ARPES), as shown in Ref. [6]. The cleavage between two layers forming a bilayer $NbSe_2$ does not influence the doping level; thus, what can be probed by surface techniques is well representative of the bulk.

3.3 Ab initio construction of misfit layer compound surfaces

In this paragraph, we explain the method that we use for the ab initio construction of misfit layer compound surfaces.
As mentioned in the first chapter, clean misfit surfaces can be obtained by cleav-

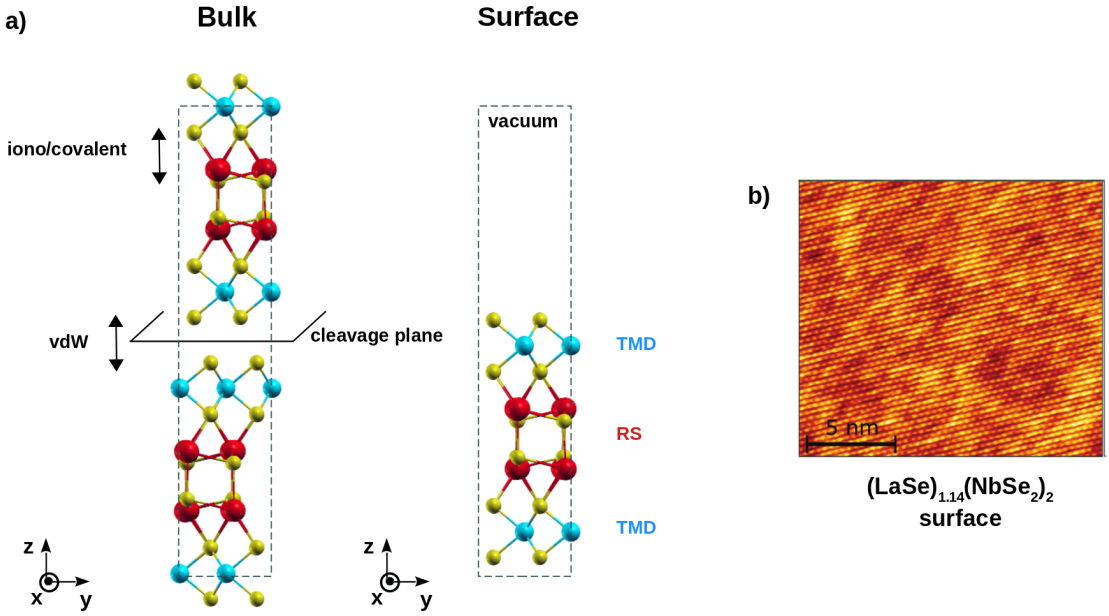

Figure 3.3: Misfit layer compounds surface. (a) A sketch of the cleavage plane in bulk misfit and of the misfit surface modeled for ab initio calculations. (b) STM topography of a cleaved $(LaSe)_{1.14}(NbSe_2)_2$ sample measured at 4.2 K adapted from Ref. [6].

ing bulk misfits with m=2 along the out-of-plane axis. Figure 3.3(a) shows that the cleavage plane cuts the crystal at the region of the weak van der Waals bonding between two layers of the TMD bilayers. Therefore, these surfaces terminate with TMD monolayers. Fig. 3.3(b) shows an STM topography of a cleaved $(LaSe)_{1.14}(NbSe_2)_2$ sample measured at 4.2 K from Ref. [6]. The triangular atomic lattice indicates that the sample is terminated by a $NbSe_2$ monolayer.
For ab initio calculations, misfit surfaces can be modeled as slabs: an alternate stacking sequence of one rocksalt bilayer sandwiched between two TMD monolayers along the c-axis (TMD-RS-TMD stacking sequence), as seen in Fig. 3.3(a). This sequence assures the neutrality of the cell, with the same charge transfer of the bulk. Vacuum space has to be added to the cell to prevent the periodic replicas of the slab from interacting with one another.
In our work [81], we consider several possible combinations of rocksalts and TMDs to build misfit layer compounds. The selection of specific materials is related to the band alignment plot presented in the second chapter (see Fig. 2.6), and will be clarified case by case in the following sections.
We now briefly illustrate how the misfit slab supercell is built (Appendix A.1 provides a more extensive, case-by-case description). For all the considered structures, we first optimize each subsystems separately. Then, we assemble the misfit surfaces by stacking the subsystems in the TMD-RS-TMD sequence. Finally we perform geometrical optimization of the misfit crystal.
We adopt the convention of using the value of δ as obtained from the lattice parameters a_1 and a_2 of the pristine TMD and RS respectively, before assembling them in a MLC structure, as reported in the tables in Fig. 1.4 and 1.5 in Chapter 1. In order to build commensurate misfit supercells, from these analysis we

TMD	a_1 [Å]	b_1 [Å]	RS	a_2 [Å]	b_2 [Å]
$SnSe_2$	3.8	6.5818	LaSe	5.7	6.5818
$TiSe_2$	3.6	6.0191	LaSe	6	6.0191
$NbSe_2$	3.437	6.0191	LaSe	6	6.0191
$NbSe_2$	3.434	6.0102	BiSe	6.0102	6.0102
$NbSe_2$	3.439	5.99	PbSe	6.02	5.99
$NbSe_2$	3.38	5.94	SnSe	5.92	5.94

Table 3.2: In-plane lattice parameters of each subsystem: a_1 and b_1 for the TMDs (cyan) and a_2 and b_2 for rocksalts (red) used to build misfit supercells.

Mismatch ratio	Misfit	a [Å]	b [Å]	c [Å]
3/2	$(LaSe)_{1.27}(SnSe_2)_2$	11.4	6.5818	30
5/3	$(LaSe)_{1.18}(TiSe_2)_2$	18	6.0191	30
7/4	$(LaSe)_{1.15}(NbSe_2)_2$	24.060	6.0191	36.531
7/4	$(BiSe)_{1.14}(NbSe_2)_2$	24.041	6.0102	30
7/4	$(PbSe)_{1.14}(NbSe_2)_2$	24.08	5.99	30
7/4	$(SnSe)_{1.16}(NbSe_2)_2$	23.68	5.94	32.34

Table 3.3: Mismatch ratios and lattice parameters, summarized for each misfit supercell under consideration.

extract the approximant used in the calculations (see Fig. 1.6).

We consider the following cases: misfits with bilayers $TiSe_2$ and $SnSe_2$, both found in the 1T phase, stacked with bilayers LaSe, and misfits belonging to the $(RQ)_{1+\delta}(NbSe_2)_2$ series with $NbSe_2$ in the 1H phase stacked with different rocksalts, namely RQ=LaSe, BiSe, PbSe and SnSe. Thus, we focus on three different TMDs, namely $NbSe_2$, $TiSe_2$ and $SnSe_2$.
For the TMD part, we use orthohorombic cells with the transition metal atom in trigonal coordination for the case of $NbSe_2$, and in octahedral coordination in the cases of $TiSe_2$ and $SnSe_2$. We optimize the in-plane lattice parameters to match that of the chosen rocksalts for each corresponding mismatch ratio. Then, starting from these cells, we build supercells according to the misfit proportions, namely a 7×1 for the $NbSe_2$, a 5×1 for the $TiSe_2$ and a 3×1 for the $SnSe_2$.
For the rocksalt part, we use centered orthohorombic cells and optimize the in-plane lattice parameters in order to obtain commensurability with the considered TMD according to each mismatch ratio. Then, starting from these cells, we build supercells according to the misfit proportions, namely a 4×1 of LaSe, BiSe, PbSe and SnSe to match with $NbSe_2$, a 3×1 of LaSe to match with $TiSe_2$ and a 2×1 of LaSe to match with $SnSe_2$.
Tab. 3.2 summarizes the lattice parameters for each isolated subunit. In this process of refinement, lattice parameters in the mismatch direction are slightly

strained in order to build a commensurate misfit structure. We lower the amount of strain required to match the RS lattices, maintaining the lattice parameter of the TMDs as near as possible to the experimental value of isolated TMDs. The amount of strain applied to each subsystem is detailed in Appendix A.1.
Finally, the common part is composed by stacking the TMD and rocksalt supercells in TMD-RS-TMD sandwich sequences. Each misfit slab comprises vacuum space (optimized form 15 to 18 Å, depending on the system) to prevent interactions between periodic replicas. Tab. 3.3 summarizes each examined misfit supercell, including its mismatch ratio, compound name, and lattice parameters. Finally, we perform geometry optimization of each misfit supercell, as detailed in Appendix A.1. In the tables Tab. A.1, A.2 and A.3, we report the optimized atomic positions expressed in crystalline coordinates for each of the misfit slabs.
We will now describe the approach used to compute the electronic properties and charge transfer of misfit surfaces. After explaining this, we will provide our findings on the geometrical and electronic properties of the considered misfit layer compounds.

3.4 Band unfolding and charge transfer determination

In this part, we discuss the approach used in our study [81] to compute the band structure of misfit layer compounds. Specifically, we introduce the band unfolding technique, which allows us to interpret the misfit band structure in terms of isolated TMD layers and the method we used to determine the charge transfer from the rocksalts to the TMDs.
As previously stated, a supercell of the commensurate approximant of the misfit cell is created to provide an appropriate input for ab initio computations of misfit layer compounds. Although the misfit supercell energy bands are directly accessible from DFT calculations, they are quite intricate and thus tricky to interpret due to the large size of the unit cell. In addition, we are particularly interested in determining how to tune the doping of TMDs in MLCs; consequently, it is critical to identify the contribution of TMDs to the electronic properties of misfits. Thus, we aim to extract TMD characteristics from misfits computations, which is doable given the relationship between the misfits' eigenvalues and those of the TMDs.
To do so, we employed the unfolding technique as implemented in the software BandsUP [89], based on the effective band structure method [90]. The EBS method allows to recover the behaviour of a primitive cell, no matter the complexity of the supercell [90]. To elucidate its working protocol, we will now provide a quick overview of this method for the unfolding procedure as implemented in Ref. [89].
A supercell (SC) is a mathematical construct created by stacking primitive cells (PC) along one or more spatial directions. The reciprocal space can be defined using the wave vectors of the Brillouin zone of the PC ($\mathbf{k}$) or the ones of the SC ($\mathbf{K}$). Unfolding allows for the reconstruction of the PC's eigenvalues $\epsilon(\mathbf{k})$ from the

estimated eigenvalues of the SC, $\epsilon(\mathbf{K})$. The direct and reciprocal lattice vectors of a SC ($\mathbf{A}_i$ and $\mathbf{B}_i$, with i=1, 2, 3) can be expressed in terms of the PC ones ($\mathbf{a}_i$ and $\mathbf{b}_i$, with i=1, 2, 3) thought the relations:

$$\underline{\mathbf{A}} = \underline{\mathbf{M}} \cdot \underline{\mathbf{a}} \; ; \; \underline{\mathbf{B}} = \underline{\mathbf{M}}^{-1} \cdot \underline{\mathbf{b}} \tag{3.1}$$

where $\underline{\mathbf{M}}$ is the 3×3 transformation matrix and $\underline{\mathbf{M}}^{-1}$ its inverse. We distinguish between two types of Brillouin zones: primitive (PBZ) and supercell (SBZ). The relation between the two volumes of the PBZ and SBZ is $\mathrm{V}_{SBZ}=\mathrm{v}_{PBZ}/\det(\underline{\mathbf{M}})$, which means SBZ has a smaller volume than PBZ. The reciprocal lattice vectors associated with the the SBZ and PBZ are:

$$\mathbf{g}_n = \sum_i p_i \mathbf{b}_i \; ; \; \mathbf{G}_n = \sum_i q_i \mathbf{B}_i \tag{3.2}$$

where $p_i, q_i \in \mathbb{Z}$. $\mathbf{G}_n$ and $\mathbf{g}_n$ froms two infinite sets, where any $\mathbf{g}$ vector is also a $\mathbf{G}$ vector. A wave vector $\mathbf{k}$ (in PBZ) is said to fold into a wave vector $\mathbf{K}$ (in SBZ) if there exists a reciprocal lattice vector $\mathbf{G}_0$ such that:

$$\mathbf{K} = \mathbf{k} - \mathbf{G}_0. \tag{3.3}$$

Conversely, a wave vector $\mathbf{K}$ (of the SBZ) unfolds into $\mathbf{k}$ of the PBZ if:

$$\mathbf{k}_i = \mathbf{K} + \mathbf{G}_i \; , \; i = 1, ..., N_{\mathbf{K}} \tag{3.4}$$

This means that while in Eq. 3.3 the vectors $\mathbf{K}$ and $\mathbf{G}_0$ are unique for a given vector $\mathbf{k}$ (thus, each $\mathbf{k}$ is mapped into a precise vector $\mathbf{K}$ in the folding), in Eq. 3.4, a given vector $\mathbf{K}$ can be obtained from a number $N_{\mathbf{K}}$ of different pairs ($\mathbf{k}_i$,$\mathbf{G}_i$) in the unfolding.

Standard electronic structure calculation methods can be applied to a periodic solid using either a PC or a SC representation. By solving the associated Schrödinger equation of the electronic system one can readily obtain both the eigenvectors that are a complete set of Bloch functions $|\psi^{PC}_{\mathbf{k},n}\rangle$ and $|\psi^{SC}_{\mathbf{K},m}\rangle$ where n, m stands for the band indices, and the dispersion relations E($\mathbf{k}$) and E($\mathbf{K}$) and which are well-defined quantities in both representations. The zone folding and unfolding geometric relations lead to the property that any SC eigenvector $|\psi^{SC}_{\mathbf{K},m}\rangle$ can be expressed as a linear combination of PC eigenvectors $|\psi^{PC}_{\mathbf{k}_i,n}\rangle$ (where $\mathbf{k}_i$ are are a set of wave vectors of the PBZ) trough:

$$|\psi^{SC}_{\mathbf{K},m}\rangle = \sum_{i=1}^{N_{\mathbf{K}}} \sum_n F(\mathbf{k}_i, n; \mathbf{K}, m) \, |\psi^{PC}_{\mathbf{k}_i,n}\rangle \, . \tag{3.5}$$

The unfolding procedure recovers the PC eigenvectors $|\psi^{PC}_{\mathbf{k}_i,n}\rangle$ and their contributions $F(\mathbf{k}_i, n; \mathbf{K}, m)$ to the SC eigenstates $|\psi^{SC}_{\mathbf{K},m}\rangle$ from the calculations of SC

alone. This last step can be accomplished by projecting $|\psi^{SC}_{\mathbf{K},m}\rangle$ on all the PC Bloch states $|\psi^{PC}_{\mathbf{k}_i,n}\rangle$ of a fixed $\mathbf{k}_i$ and calculating the spectral weight $P_{\mathbf{K},m}(\mathbf{k}_i)$. The probability of $|\psi^{SC}_{\mathbf{K},m}\rangle$ having the same character as a PC Bloch state of wave vector $\mathbf{k}$ is given by the spectral weight $P_{\mathbf{K},m}(\mathbf{k})$:

$$P_{\mathbf{K},m}(\mathbf{k}) = \sum_n |\langle \psi^{SC}_{\mathbf{K},m} | \psi^{PC}_{\mathbf{k},n} \rangle|^2 = \sum_{\mathbf{g}} |C^{SC}_{\mathbf{K},m}(\mathbf{g}+\mathbf{k}-\mathbf{K})|^2. \tag{3.6}$$

The second equality in Eq. 3.6 is derived in the Appendix of Ref. [90]. This equality shows that the spectral weight can be entirely obtained from the coefficients $C^{SC}_{\mathbf{K},m}$ of the periodic part of the plane waves that span the eigenstates of the SC, which means that the knowledge of the PC eigenstates is not required. The spectral function $A(\mathbf{k};\epsilon)$ is then defined as:

$$A(\mathbf{k};\epsilon) = \sum_m P_{\mathbf{K},m}(\mathbf{k})\delta(\epsilon - \epsilon_m(\mathbf{K})) \tag{3.7}$$

where the only pairs ($\mathbf{k}$,$\mathbf{K}$) that need to be included in the sum are those in which $\mathbf{K}$ unfolds onto $\mathbf{k}$.

The last step is then using the spectral function to obtain the EBS by the so-called cumulative sum. The procedure as implemented in BandsUP is accomplished by working with the infinitesimal version of the cumulative probability function $S_{\mathbf{k}}(\epsilon)$ to calculate the cumulative sum. The number of PC bands, at the PC wave vector, crossing the energy interval $(\epsilon, \epsilon + d\epsilon)$ is $dS_{\mathbf{k}}(\epsilon) = A(\mathbf{k};\epsilon)d\epsilon$. It is possible to map the region of interest in the ($\mathbf{k}$;ϵ) space onto a ($\mathbf{k}_j$;ϵ_j) grid with energy intervals of size $\delta\epsilon$, and assign a weight $\delta N(\mathbf{k}_j;\epsilon_j)$ to each point. The quantity:

$$\delta N(\mathbf{k}_j;\epsilon_j) = \int_{\epsilon_j-\delta\epsilon/2}^{\epsilon_j+\delta\epsilon/2} dS_{\mathbf{k}_i}(\epsilon) = \sum_m P_{m,\mathbf{K}}(\mathbf{k}_i) \int_{\epsilon_j-\delta\epsilon/2}^{\epsilon_j+\delta\epsilon/2} \delta(\epsilon - \epsilon_m(\mathbf{K}))\, d\epsilon \tag{3.8}$$

gives the number of PC bands crossing the grid ($\mathbf{k}_j$;ϵ_j). Finally, δN is averaged over wave vectors $\mathbf{k}_i$, related by symmetry operations of the PBZ.

In practice, the unfolding procedure as implemented in BandsUP follows four steps. First, a self-consistent run of the SC. Then from the knowledge of the lattice vectors of the PC and the SC ($\mathbf{a}_i$,$\mathbf{A}_i$) and the provided list of k-points of the PBZ, the corresponding weighted k-points are calculated for the SBZ. These are used to calculate the band structure of the supercell and finally to generate a plottable file. A final plot looks like the one shown in Fig. 3.4(a), the color scale follows the spectral weight of the band, representing δN. This colormap is the band structure of the misfit surface SC $(LaSe)_{1.15}(NbSe_2)_2$ unfolded onto the PC of the isolated monolayer $NbSe_2$. The blue dashed line corresponds to the Fermi level E_F of the misfit compound.

From this plot we can derive the charge transfer from the rocksalt to the TMD in the misfit as follows. In Fig. 3.4(a), we compute the band structure of the selected monolayer TMD (red solid line), namely $NbSe_2$. The red dashed line

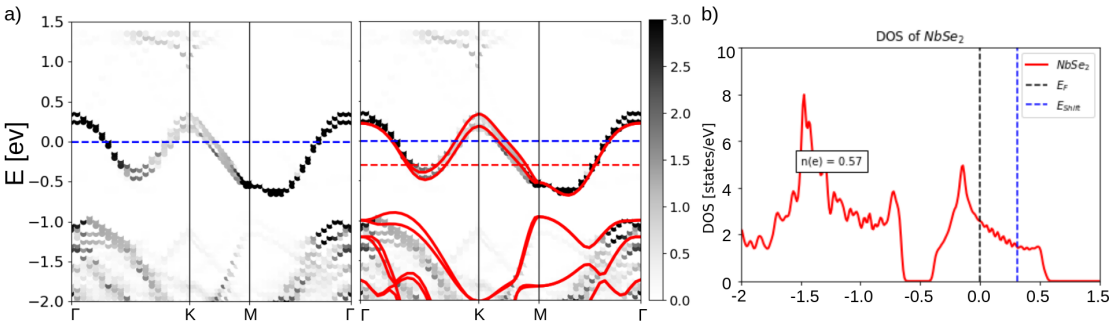

Figure 3.4: (a) Band unfolding onto the $NbSe_2$ single layer Brillouin zone of $(LaSe)_{1.15}(NbSe_2)_2$ surface. The band structure for the isolated single layer $NbSe_2$ (red line) is superimposed and aligned to the Nb d-band in the misfit. The blue dashed line corresponds to the Fermi level E_F of the misfit compound, while the red one to the Fermi level of the isolated $NbSe_2$ layer. (b) Density of states of the isolated $NbSe_2$ single layer. The blue dashed line corresponds to the Fermi level E_F of the misfit compound, while the black one to the Fermi level of the isolated $NbSe_2$ layer. The label n(e) refers to the number of electrons transferred from LaSe to $NbSe_2$.

corresponds to the TMD's Fermi level E_F. We superimpose it to the unfolded band structure of the misfit onto the PBZ of the TMD. Then, we manually shift the band structure of the TMD until it aligns to the unfolded one. In this way, the difference between the blue and the red dashed lines is the Fermi level shift of the TMD within the misfit, caused by the charge transfer from the rocksalt. We next compute the density of states (DOS) of the examined isolated monolayer TMD (as shown in Fig. 3.4(b) for $NbSe_2$). The number of electrons transferred to the TMD per formula unit is calculated by integrating the DOS between the Fermi level of the isolated TMD (black dashed line in Fig. 3.4(b)) and the Fermi level of the misfit (blue dashed line in Fig. 3.4(b)).
As shown in the example, the Fermi level of $NbSe_2$ is shifted by 0.31 eV, corresponding to a doping of 0.57 e^-/Nb atoms, or $n_e \approx 6 \times 10^{14}$ cm^{-2}, in agreement with the experimental reported value [6].
The aforementioned procedure is used in all of the computations of electronic properties of misfit surfaces detailed in the following sections.

3.5 Electronic structure of the surfaces of $(LaSe)_{1+\delta}(TX_2)_2$ misfit series

We start presenting our ab initio calculations of the electronic properties of misfit surfaces with the rocksalt LaSe [81]. As described in the previous section, we build three misfit slabs of with different TMDs, namely $NbSe_2$, $TiSe_2$ and $SnSe_2$. The choice of LaSe as the rocksalt is motivated by the band alignment plot presented in the second chapter (see Fig. 2.6).
According to our calculations shown in Tab. 2.1, among the rocksalt monochalcogenides RQ with Q=Se, the LaSe compound has the lowest work function

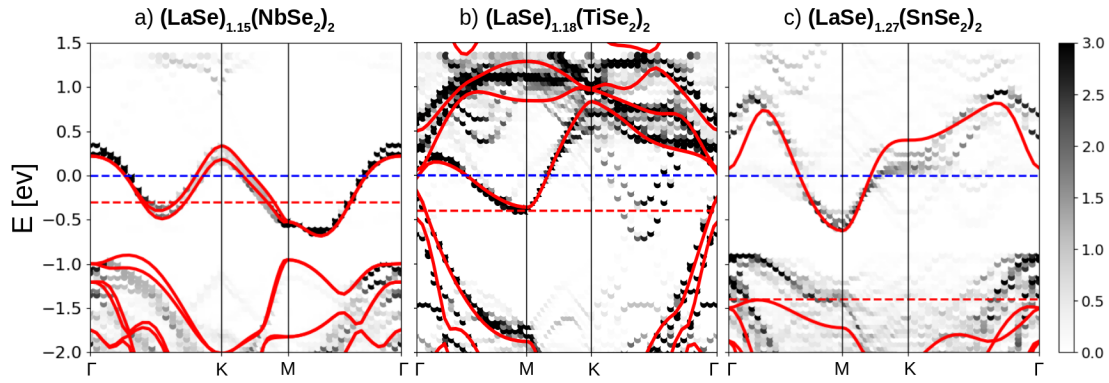

Figure 3.5: Band unfolding onto the TX_2 single layer Brillouin zone of the $(LaSe)_{1+\delta}(TX_2)_2$ surface misfit series with different TMDs. (a) $(LaSe)_{1.15}(NbSe_2)_2$, (b) $(LaSe)_{1.18}(TiSe_2)_2$, (c) $(LaSe)_{1.27}(SnSe_2)_2$. The band structure of each isolated single layer TX_2 (red line) is superimposed and aligned respectively to the (a) Nb d-band, (b) Ti d-band and (c) Sn s-band in the misfit. The blue dashed line corresponds to the Fermi level E_F of the misfit compound, while the red one to the Fermi level of the isolated TX_2 layer.

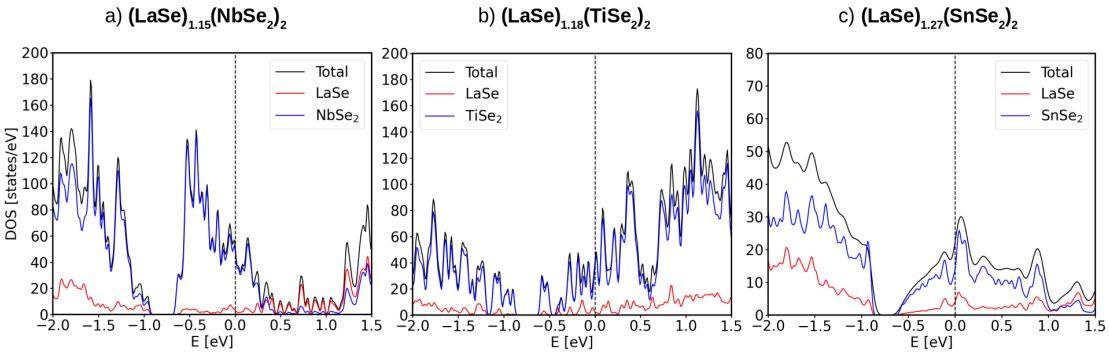

Figure 3.6: Density of states (DOS) of the $(LaSe)_{1+\delta}(TX_2)_2$ surface misfit series with different TMDs. (a) $(LaSe)_{1.15}(NbSe_2)_2$, (b) $(LaSe)_{1.18}(TiSe_2)_2$, (c) $(LaSe)_{1.27}(SnSe_2)_2$. In each plot, the black line corresponds to the total DOS of the misfit, while the red line to the partial DOS of the LaSe layers. The blue lines correspond respectively to the partial DOS of (a) $NbSe_2$, (b) $TiSe_2$ and (c) $SnSe_2$. The black dashed line corresponds to the Fermi level E_F of each misfit compound.

(W(LaSe)=2.84 eV). In the LaSe ionic bond, selenium atoms have valence of 2^- , while La atoms have a higher valence of 3^+. The excess electron makes this compound a metal [91]. This extra electron can be thus easily extracted from the rocksalt and donated to the TMD in a misfit. Indeed, as shown in Chapter 2, there is a preferential direction for the charge transfer in misfit layer compounds, which is caused by the huge work function difference between the rocksalts and the TMDs. TMDs globally possess work functions substantially larger than those of the RS compounds, thus the direction of the charge transfer will always be from the rocksalt to the TMD. We pick LaSe as the rocksalt to take advantage on the potential of creating misfits with high levels of doping. Therefore, we choose three kinds of TMDs, with different properties, to examine how the doping from the LaSe layers impacts their band structure: a metal ($NbSe_2$), a semimetal ($TiSe_2$), and an insulator ($SnSe_2$).

By looking at the band alignment plot (Fig. 2.6), we can immediately infer that in a LaSe/TX_2 interface (with TX_2=$NbSe_2$, $TiSe_2$ and $SnSe_2$), in order to reach equilibrium, the Fermi level of LaSe will shift down in energy. On the other side, the Fermi level of the different TMDs will rise up in energy: potentially, if LaSe donates the entire last valence electron, this energy shift is huge. The net amount of charge transfer depends, however, not only on the work function difference but also on the mutual concentration of the RS and TMD in each misfit that is related to the mismatching ratio. To explain this more clearly, each RS can transfer a given amount of charge to the TMD layers, if the mismatching ratio is close to one. However, if the mismatching ratio increases, the relative concentration of RS atoms per TMD cell decreases and so does the charge transfer. By looking at Fig. 1.6, it is clear that the mismatching ratio varies mostly due to the change in the TMD lattice parameter. In the case of LaSe and the selected TMDs, this ratio is 3/2 for $SnSe_2$, 5/3 for $TiSe_2$ and 7/4 for $NbSe_2$.

The considered misfits for the LaSe-TX_2 series are therefore: $(LaSe)_{1.15}(NbSe_2)_2$, $(LaSe)_{1.18}(TiSe_2)_2$ and $(LaSe)_{1.27}(SnSe_2)_2$.

We calculate the band structure of misfit layer compound surfaces $(LaSe)_{1+\delta}(TX_2)_2$. To do so, we unfold the band structure of the misfit supercell onto the primitive cell of each considered TMD monolayer.

These misfit slabs are constructed and optimized using the process outlined in the preceding section. Details of electronic structure calculations are reported in Appendix A.2.

Spin orbit coupling (SOC) is included in the electronic structure calculations of misfit compound containing $NbSe_2$ and $TiSe_2$. In the case of $TiSe_2$, we employ PBE+U method described in Refs. [92,93] in order to take into account the strong correlation effects due to the localized d orbitals of Ti. The Hubbard correction is set to U= 3.25 eV, consistently with previous work on bulk $TiSe_2$ where a good agreement with ARPES spectra was demonstrated [94]. The results of the calculations are shown in Fig. 3.5.

When comparing the band structure of misfit layer compound $(LaSe)_{1.15}(NbSe_2)_2$ to that of the superimposed and aligned isolated single layer $NbSe_2$ (red line in Fig. 3.5(a)), we can see that the Nb d-band of $NbSe_2$ shows no deformation upon

doping. The Fermi level of $NbSe_2$ is thus rigidly shifted up in energy of 0.31 eV. This shift corresponds to a doping of 0.57 e^-/Nb atoms, or $n_e \approx 6 \times 10^{14}$ cm^{-2}. Our band structure calculation and doping value is in agreement with a previous study of the group [6], in which DFT calculations are combined with STM and ARPES experiments.
A similar scenario occurs in the case of $(LaSe)_{1.18}(TiSe_2)_2$: if we superimpose and align the band structure of an isolated TiSe2 layer (red line in Fig. 3.5(b)) and then compare it with the band structure of the misfit, again no deformation of the band structure occurs. The Fermi level of $TiSe_2$ is, thus, rigidly shifted up in energy of 0.4 eV. This shift corresponds to a doping of 0.53 e^-/Ti atoms, or $n_e \approx 5 \times 10^{14}$ cm^{-2}.
In these two cases, rigid band approximation holds. In the case of $NbSe_2$, the only differences between the isolated monolayer and the misfit occur at zone center where an LaSe band slightly hybridizes with the single layer $NbSe_2$ band. Instead in the case of $TiSe_2$, two parabolic La bands cross the Fermi level along the Γ-K direction.
However, these La bands at the Fermi level have a small contribution to the density of states. Indeed, the amount of La electrons at the Fermi level remains negligible, as demonstrated by the density of states projected over LaSe and $NbSe_2$ layers (Fig. 3.6(a)) and over LaSe and $TiSe_2$ atomic states (Fig. 3.6 (b)), respectively.
The last example of the LaSe series is $(LaSe)_{1.27}(SnSe_2)_2$, whose band structure is shown in Fig. 3.5(c). We consider the layered indirect gap semiconductor 1T-$SnSe_2$ that can be exfoliated and synthesized in single layer form [95]. The electronic structure of single-layer $SnSe_2$ is shown in 3.5(c) (red line). The conduction band is formed by an isolated band with a Van Hove singularity point at K. A maximum in the density of states occurs at the energy corresponding to the band flattening. If the Fermi level is tuned at the inflection point, this would be beneficial for superconductivity, as we will discuss in Chapter 4. In this case, the rigid band approximation is clearly not applicable. We compare the electronic structure of this MLC with the one of an isolated layer $SnSe_2$ (red line in Fig. 3.5(c)). There is substantial band distortion of the s-band of Sn with respect to the isolated single layer. However, if we look at the density of states of this compound in Fig. 3.6(c), we notice that even in this case, the amount of LaSe electrons is low at the Fermi level. It must be pointed out that the amount of charge transfer between the LaSe and the $SnSe_2$ is huge. This involves a 1.4 eV Fermi level shift of $SnSe_2$, corresponding to a charge transfer of 0.77 e^-/Sn atoms, or $n_e \approx 6 \times 10^{14}$ cm^{-2}. This very large doping is due to the large work function difference between LaSe and $SnSe_2$ and the favorable mismatch ratio of 3/2 where there are 2 LaSe units per 3 $SnSe_2$ ones. Thus, we attribute the band bending occurring at the K high-symmetry point to the huge charging of the monolayer. With this amount of charge, the intralayer spacing between the two Se atoms increases by $\sim 5\%$, passing from 3.19 Å in the isolated monolayer to $SnSe_2$ to 3.34 Å within the misfit. In Chapter 4, we will present an alternative way to model this misfit.
In conclusion, our findings demonstrate that by choosing a rocksalt with low work

function, it is possible to build misfits with huge doping. We show that, the amount of charge transfer from the rocksalt to the TMD is limited by the lattice mismatch ratio. Thus, the charge transfer of a specific rocksalt can be predicted and controlled by engineering a misfit with the appropriate mismatch ratio.
We also discuss the rigid doping approximation of the misfits band structure. We find that in the particular case of LaSe, the electronic states of the rocksalt, even if present in a negligible number at the Fermi level, do not have a great influence on modifying the band structure of the TMD. However, in the case of $SnSe_2$, the structural modification induced by doping causes band bending. These results open a question: what happens in terms of charge transfer and rigid doping of the same TMD by changing the rocksalt? We address this question in the following section.

3.6 $(RQ)_{1+\delta}(NbSe_2)_2$ surface misfit series

In the previous section, we presented our study of misfit layer compounds by fixing the rocksalt (LaSe) and changing the TMDs (with TX_2= $NbSe_2$, $TiSe_2$ and $SnSe_2$).
In this section, we want to address the problem of tuning the charge transfer by appropriately choosing the rocksalt, in order to demonstrate the global picture based on work functions. We thus perform explicit calculations for several misfit surfaces terminated by a single layer of $NbSe_2$, but having different RS units as building blocks and sharing comparable mismatching ratios very close to 7/4 (these compounds belong to the ninth column in Fig. 1.6 in Chapter 2). In our work [81], we specifically consider the $(RQ)_{1+\delta}(NbSe_2)_2$ misfit series, where we fix the TMD as $NbSe_2$, and we change the rocksalt with RQ= LaSe, BiSe, PbSe, and SnSe.
To begin, we will examine how the presence of various rocksalts in the misfit surface affects the geometry of the $NbSe_2$ layer, as well as how each specific rocksalt is altered within the misfit. For this purpose, we calculate the interatomic distances of each subsystem in the $(RQ)_{1+\delta}(NbSe_2)_2$ series (with RQ=LaSe, BiSe, PbSe and SnSe). The results are summarized in Tab. 3.4.
The average value of the Nb-Se bond in all the considered misfits of the $(RQ)_{1+\delta}(NbSe_2)_2$ series (with RQ=LaSe, BiSe, PbSe and SnSe) is 2.59 Å. This length does not deviate from the experimental value of 2.60 ± 0.01 measured by X-ray in bulk 2H-$NbSe_2$ [88]. However, in each $NbSe_2$ monolayer, the out-of plane intralayer distance values $(Se\text{-}Se)_{intra}$ change along the supercell. This effect is caused by the mutual modulations between the TMD and the different rocksalts. Indeed, each monolayer in the slab has two selenimu planes: one is in contact with the rocksalt substrate, with which it forms iono/covalent bonds, and the other is adjacent to the vacuum on the other side. Thus, the intralayer distance assumes different values, shrinking or expanding with respect to the experimental value of 3.36 ± 0.02 measured by X-ray in bulk 2H-$NbSe_2$ [88], as reported in Tab. 3.4. Additionally, when $NbSe_2$ monolayers come into contact with the different rocksalts, their interlayer distance can be altered by up to 2% compared to the

TMD	Intralayer distances [Å]	RS	In-plane R-Q bonds [Å]	Intralayer distances [Å]
$NbSe_2$	3.30-3.38	LaSe	3.04-3.15	3.07-3.09
$NbSe_2$	3.34-3.37	BiSe	2.98-3.09	2.86-2.89
$NbSe_2$	3.35-3.37	PbSe	3.01-3.04	2.88-2.89
$NbSe_2$	3.39-3.41	SnSe	2.94-3.0	2.78-2.79

Table 3.4: Summary of the geometry optimization of the misfit surfaces of the $(RQ)_{1+\delta}(NbSe_2)_2$ series (with RQ=LaSe, BiSe, PbSe and SnSe). In the table, the intralayer distances of $NbSe_2$ in misfit layer compounds with different RQ layers are reported. For the rocksalts, we report the in-plane R-Q bond length and interlayer distances of the different considered compounds.

experimental value of the isolated compound. This is due to the combined action of the mutual modulation of the subsystems, together with the new bonds forming between the TMD and the different rocksalts and the substantial charge transfer between the subunits of misfit surface.
We summarize in Tab. 3.4 the R-Q in-plane and out-of-plane distances for each rocksalt. Every compound exhibits significant deformation relative to the bulk rocksalt structure. This is caused by a variety of circumstances. First and foremost, the induced strain employed to fit the TMD lattices alters the in-plane R-Q distances. Second, inside the misfit surface, the R atom can change coordination. In a bilayer rocksalt, each R atom has a coordination of 5, which increases to 6 if bonds form between the R atoms and the chalcogen of the TMD, altering also the R-Q bond length. In addition, the two neighboring TMD layers exert pressure on the rocksalt bilayer, and the R-Q distances fluctuate as the two subsystems modulate each other. This changes the out-of-plane distances. Finally, by looking at the trend of the intralayer distances in Tab. 3.4, we can tell that by going from LaSe to SnSe, the $NbSe_2$ is more and more strained, while the rocksalt is compressed. As shown in the following, the deformation is indicative of the amount of charge transfer between the rocksalt and the TMD.
In order to quantify the charge transfer between $NbSe_2$ and the different rocksalts, we need to calculate the electronic properties of these misfits. We now present our band structure calculations of misfit layer compound surfaces $(RQ)_{1+\delta}(Nb_2)_2$, with RQ= LaSe, BiSe, PbSe and SnSe. We unfold the band structure of the misfit supercell onto the primitive cell of the isolated $NbSe_2$ monolayer.
Details of these calculations are reported in Appendix A.2. To carefully take into account the spin orbit coupling (SOC) of $NbSe_2$, which splits the two degenerate bands at the Fermi level, SOC is included in all the electronic structure calculations. The results of band unfolding are shown in Fig. 3.7.
As it can be seen in Fig. 3.7, the $NbSe_2$ electronic structure in going from $(PbSe)_{1.14}(NbSe_2)_2$ to $(LaSe)_{1.15}(NbSe_2)_2$ is n-doped rigidly. The charge transfer simply induces a Fermi level up-shift, form 0 to 0.31 eV. As already reported, LaSe transfers 0.57 e^-/Nb atom, while BiSe transfers 0.19 e^-/Nb atom. Instead,

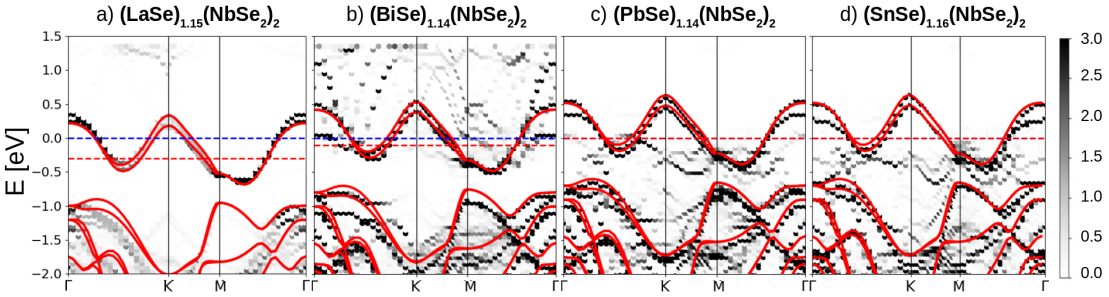

Figure 3.7: Band unfolding onto the $NbSe_2$ single layer Brillouin zone for the $NbSe_2$ surface misfit series with different rocksalt Q-layers having comparable mismatching ratio close to 7/4. (a) $(LaSe)_{1.15}(NbSe_2)_2$, (b) $(BiSe)_{1.14}(NbSe_2)_2$, (c) $(PbSe)_{1.14}(NbSe_2)_2$, (d) $(SnSe)_{1.16}(NbSe_2)_2$. The band structure for the isolated single layer $NbSe_2$ (red line) is superimposed and aligned to the Nb d-band in the misfit. The blue dashed line corresponds to the Fermi level E_F of the misfit compound, while the red one to the Fermi level of the isolated $NbSe_2$ layer. In the last two panels the dashed red line is superimposed to the dashed blue one.

in the compounds with PbSe and SnSe there is no charge transfer. As it can be seen in Fig. 3.7, the behavior of the misfit $NbSe_2$ 7/4 serie is almost completely characterized by the work function differences. Indeed as W(LaSe) < W(BiSe) < W(SnSe) < W(PbSe) (see Tab. 2.1 in Chapter 2), the charge transfer decreases by progressively decreasing the difference W($NbSe_2$) - W(RS), as expected. In both LaSe and BiSe ionic bonds, the selenium atoms have a valence of 2^-, while the La and Bi atoms have a higher valence of 3^+. Thus, LaSe and BiSe are metallic compounds in which an extra electron can be exchanged from the rocksalt to $NbSe_2$ in the misfit. The lattice mismatch ratio for all compounds is 7/4, indicating that the misfit contains the same fraction of LaSe and BiSe. However, the charge transfer is different: LaSe transfers more electrons than BiSe. The work function, W(LaSe) < W(BiSe), makes it simpler for LaSe to donate electrons to $NbSe_2$ compared to BiSe.
Both PbSe and SnSe are insulators. In their ionic bonds, the selenium atoms have a valence of 2^- that is perfectly compensated by the valence 2^+ of the Pb and Sn atoms. The work function difference between $NbSe_2$ and PbSe is too small for the rocksalt to transfer any of its electrons. The work function of BiSe is slightly larger than the one of SnSe; however, BiSe seems to transfer few more electrons than SnSe. The differences are due to fine details in the electronic-states hybridization.
From these and the previous analysis two questions arise: how general is this rigid doping effect and how to exploit rocksalts with different work function to effectively tune the doping of TMDs? We now show that it is possible to engineer the misfit in such a way that the doping level is rigidly adjustable through appropriate alloying of the RS Q-layer.

3.7 Tunable doping by La-Pb alloying in misfit layer compound surfaces

Ternary alloys of two monochalcogenides within a single RS Q-layer (e.g., $La_xSr_{1-x}S$) have been already synthesized [96], leading to misfit layer compounds having chemical formulas of the kind $(R_xM_{1-x}Q)_{1+\delta}(TX_2)_m$. To build this kind of misfits, we keep the mismatch ratio of the compound with x=1 (rocksalt with RQ), and then we pregressively substitute some of the R atoms with M atoms with concentration $1-x$ ($R_xM_{1-x}Q$) until reaching x=0 (rocksalt with MQ). The idea is to adjust TMD doping by alloying in rocksalt. The band alignment diagram (Fig. 2.6 in Chapter 2) can help us picking the right R and M atoms. For example, we choose $TiSe_2$ as the TMD and examine all potential rocksalts containing Se. As seen in Fig. 3.8, LaSe have a significant work function difference with $TiSe_2$, while the work function difference between PbSe and $TiSe_2$ is smaller. As already reported in the $(LaSe)_{1+\delta}(TX_2)_2$ series, $TiSe_2$ is rigidly doped by LaSe of a huge amount of 0.53 e^-/Ti atoms. Thus, we wonder if it is possible to tune rigidly the doping by La-Pb alloying in misfit surfaces. For this reason, in our work [81], we consider MLCs having the following stoichiometry $(La_xPb_{1-x}Se)_{1.18}(TiSe_2)_2$ as a function of x and lattice mismatch ratio 5/3. A comparison between these systems and the previous results for the $NbSe_2$ series allows us to draw conclusions that are less dependent on the chosen TMD. From the previous reasoning, we expect that the La concentration (x) allows tuning of the carrier concentration in the $TiSe_2$ layers within the misfits, with x = 1 (x = 0) corresponding to the highest (lowest) n-doping. In Fig. 3.9(a), we show the calculated band structure of the $(La_xPb_{1-x}Se)_{1.18}(TiSe_2)_2$ misfit for x = 1.0, 0.34, and 0.0 compared with that of an isolated $TiSe_2$ single layer. For all concentrations, we employed the band unfolding technique within the PBE+U scheme with U=3.25 eV, which has previously been shown to accurately capture the strong correlation effects caused by Ti's localized d orbitals in the misfit with LaSe. To justify the employment of the Hubbard correction, in Fig. A.2 of Appendix A.2, we also show the same calculations of $(La_xPb_{1-x}Se)_{1.18}(TiSe_2)_2$ in the PBE scheme for more $x = 1.0, 0.67, 0.5, 0.34, 0.0$. The main difference between these two approaches resides in the energy dispersion around the Fermi level, especially the overlap/gap between the Se-4p valence band in Γ and the Ti-3d conduction band in M. Indeed, as shown in Ref. [94], the introduction of Hubbard interaction leads to a better comparison with ARPES experiments in which shows that monolayer 1T-$TiSe_2$ is a perfectly compensated semimetal. We also add the SOC effect in this calculations. However, as detailed in Appendix A.2, relativistic effects are negligible for the electronic properties of $(La_xPb_{1-x}Se)_{1.18}(TiSe_2)_2$ (see Fig. A.1 in Appendix A.2 for the concentrations $x = 1.0, 0.67, 0.5, 0.34, 0.0$ in the PBE+U scheme without SOC). Inspecting our calculations in Fig. 3.9(a), we can immediately state that by increasing x, the doping is increased. Most importantly, the Ti d-band displays no deformation upon doping. At the highest doping level (x = 1, corresponding to a charge transfer of 0.53 electrons per Ti) we already discussed that two parabolic La bands cross the Fermi level along the Γ-K direction. These

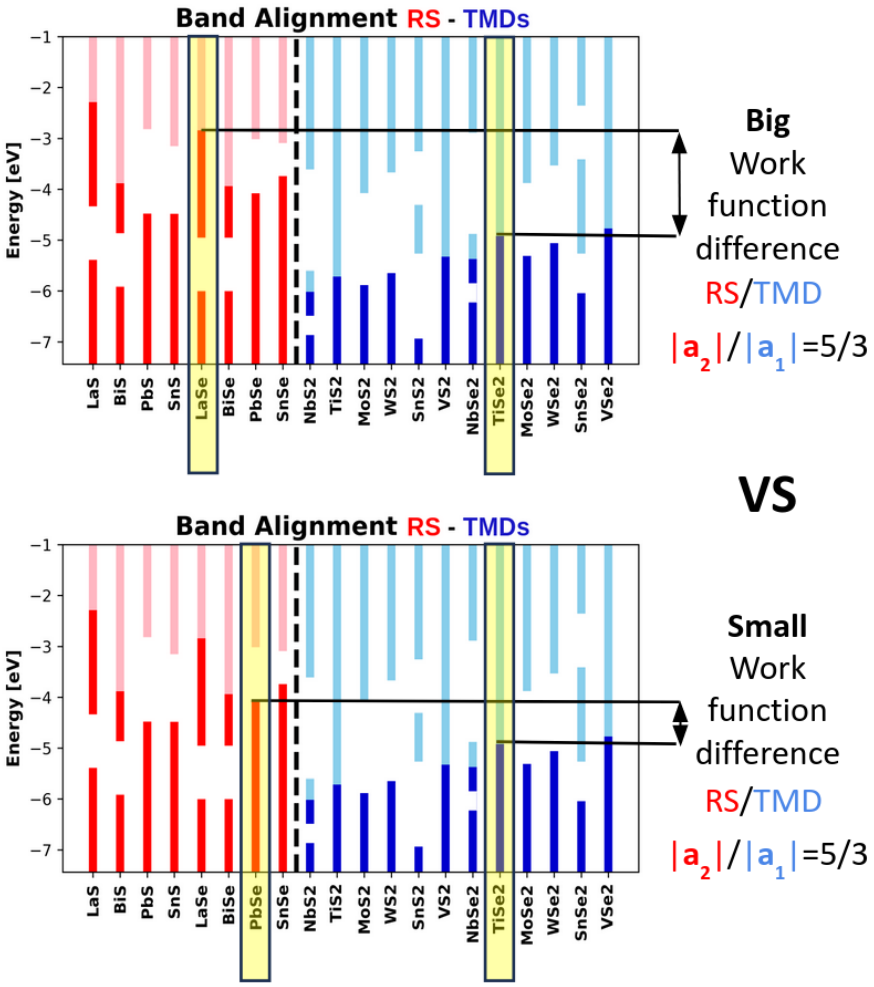

Figure 3.8: Band alignement of isolated bilayer rocksalt (red) and single layer transition metal dichalcogenides (blue). Dark (light) bars represent the position of the E_F/valence band maximum (E_F /conduction band minimum) for metals/insulators. White spaces in the bars stand for gaps in the single particle spectrum. The energy zero is set to the vacuum level. In this example, we select the TMD $TiSe_2$ and evaluate its work function difference with two different rocksalts, namely LaSe and PbSe.

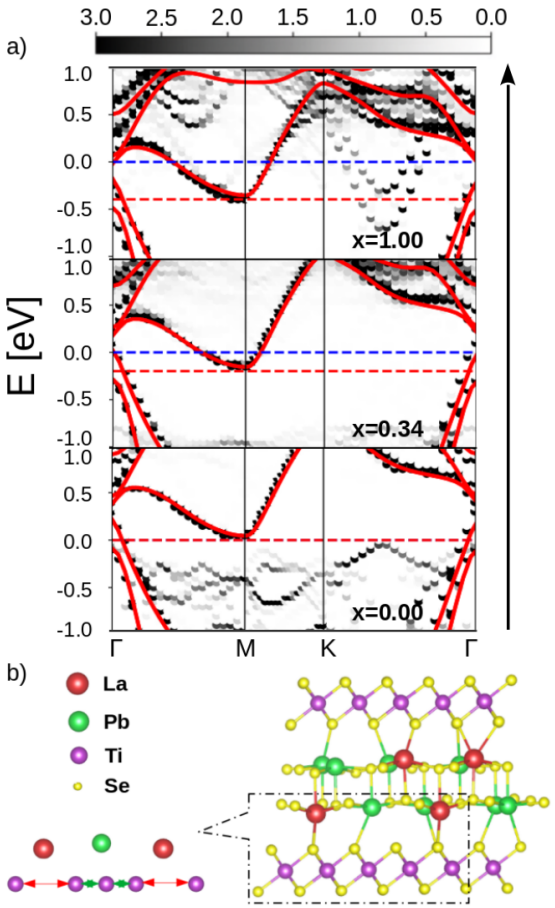

Figure 3.9: a) Band unfolding onto the single layer $TiSe_2$ Brillouin zone of the misfit compound surfaces $(La_xPb_{1-x}Se)_{1.18}(TiSe_2)_2$ for $x = 1.0, 0.34, 0.0$. The band structure of the isolated single layer $TiSe_2$ (red line) is superimposed and aligned to the bottom of the Ti d-band in the misfit. The blue dashed line corresponds to the Fermi level E_F of the misfit compound, while the red one to the Fermi level of the isolated $TiSe_2$ layer (in the lowest panel they coincide). b) Lattice deformation of the $TiSe_2$ layers generated by the partial substitution of Pb atoms in $(La_xPb_{1-x}Se)_{1.18}(TiSe_2)_2$. The magnified portion shows a bond length alternation in the $TiSe_2$ lattice with two different distances d_1 (red) and d_2 (green).

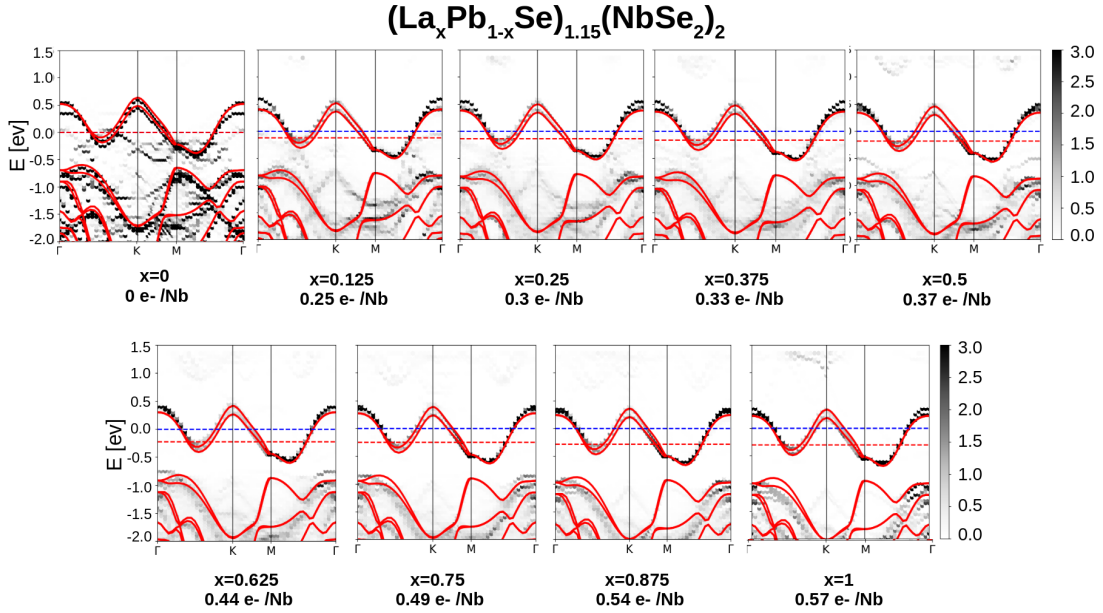

Figure 3.10: Band unfolding onto the single layer $NbSe_2$ Brillouin zone of the misfit compound surfaces $(La_xPb_{1-x}Se)_{1.15}(NbSe_2)_2$ for x= 1, 0.875, 0.75, 0.625, 0.5, 0.375, 0.25, 0.125 and 0. The band structure of the isolated single layer $NbSe_2$ (red line) is superimposed and aligned to the bottom of the Ti d-band in the misfit. The blue dashed line corresponds to the Fermi level E_F of the misfit compound, while the red one to the Fermi level of the isolated $NbSe_2$ layer (in the first panel they coincide).

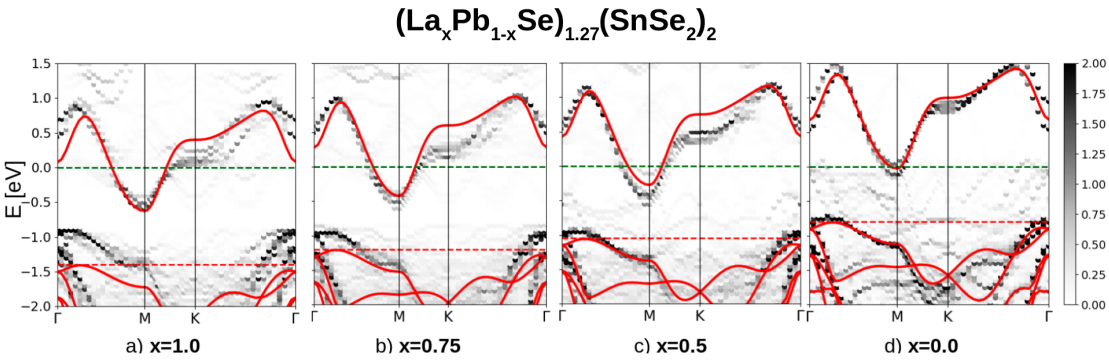

Figure 3.11: Band unfolding onto the single layer $SnSe_2$ Brillouin zone of the misfit compound surfaces $(La_xPb_{1-x}Se)_{1.27}(SnSe_2)_2$ for x= 1, 0.75, 0.5, and 0. The band structure of the isolated single layer $SnSe_2$ (red line) is superimposed and aligned to the bottom of the Ti d-band in the misfit. The blue dashed line corresponds to the Fermi level E_F of the misfit compound, while the red one to the Fermi level of the isolated $SnSe_2$ layer.

bands disappear by decreasing x (see more values of x in Fig. A.1 in Appendix A.2). Remarkably, the electronic structure of $(PbSe)_{1.18}(TiSe_2)_2$ is almost indistinguishable from that of the isolated $TiSe_2$ layer. The Fermi level of the TMD in the misfit (blue) is shifted with respect to the single layer one (red) of an amount which is directly related to the presence of Pb in the rocksalt. Following the direction of the arrow in Fig. 3.9(a), the doping is increased rigidly much like in a field effect transistor (FET) configuration. This is a crucial result since it means that the doping of the TMD in misfit layer compounds is tunable by chemical insight.

We will now discuss how the geometry of the TMD layer is modified by the action of an alloyed rocksalt substrate.

Despite the similarity in the electronic structure, we find that $(PbSe)_{1.18}(TiSe_2)_2$ does not display a 2×2 CDW as it happens in the case of the supported $TiSe_2$ single layer [97–99]. This result is in agreement with resistivity data on this MLC [10] where no CDW was detected.

We attribute the suppression of the CDW to the strong bonding between $TiSe_2$ and the the RS Q-layer. We find that in $(La_xPb_{1-x}Se)_{1.18}(TiSe_2)_2$, for $x \neq 0, 1$, the Ti-Ti distances are modulated by the presence of Pb atoms in the host LaSe lattice (i.e. the Ti-Ti distance becomes shorter if the Ti atoms are close to a Pb atom).

The reason is mostly sterical as the La atomic radius is larger than the one of Pb, therefore Pb atoms are more strongly bounded to the RS layer and a consequent deformation of the LaSe rocksalt host occurs (as shown in Fig. 3.9(b), followed by a modulation of the Ti-Ti distances). We verified that, even starting from 2×2 distorted $TiSe_2$ layers in the misfit, the structural optimization suppresses the CDW and leads to other distortion patterns that essentially follow the Pb atoms superstructure. Our analysis shows that altering the chemical composition of the rocksalt has a double effect: on the one hand, it allows to precisely tune the rigid doping of the TMD, on the other hand it suppresses the 2×2 CDW of the $TiSe_2$ bilayer and introduces an additional modulation related to the alternation of La and Pb.

To further confirm the claim that the doping in misfits can be tuned chemically, we decide to change the TMD by choosing $NbSe_2$. As already shown in Fig. 3.7, $NbSe_2$ is highly doped by LaSe of 0.57 e^{-1}/Nb atoms, while in misfit with PbSe, the band structure of $NbSe_2$ inside the misfit is comparable to that of an undoped isolated monolayer. Thus, we consider misfit layer compounds with formula $(La_xPb_{1-x}Se)_{1.15}(NbSe_2)_2$ as a function of x and lattice mismatch ratio 7/4. As shown in Fig. 3.10, we calculate the electronic band structure of these compounds for x= 1, 0.875, 0.75, 0.625, 0.5, 0.375, 0.25, 0.125 and 0. We employed SOC in all the unfoldings to account for the band splitting of the Nb's d-bands at the Fermi level (in Appendix A.2, a comparison with the case without SOC for some of the concentrations is shown in Fig. A.3). For all the concentrations, we report (in black) the amount of charge transferred from the rocksalt to $NbSe_2$. We can clearly see the evolution of the electrons per Nb atoms as a function of the concentration of the La atoms (x). The bands of $NbSe_2$ inside the misfit are

essentially identical to those of an isolated single layer $NbSe_2$, with a rigid upward shift when going from the misfit with 100% of Pb atoms (x = 0) to the one with 100% of La atoms (x = 1). This analysis reinforce our claim on the chemically tunable doping in misfit layer compounds.
Finally we tested the alloying in the rocksalt in the case of $SnSe_2$, constructing misfit surfaces of the kind $(La_xPb_{1-x}Se)_{1.27}(SnSe_2)_2$ as a function of x and lattice mismatch ratio 3/2. In Fig. 3.11, we show the band unfolding onto the single layer $SnSe_2$ Brillouin zone of the misfit compound $(La_xPb_{1-x}Se)_{1.27}(SnSe_2)_2$ for x= 1, 0.75, 0.5, and 0. We find that La-Pb alloying allows perfect control of the doping level due to the large work function difference between LaSe and $SnSe_2$ and an insulator-to-metal transition occurs in $SnSe_2$. In this case, as we explained for the case of $(LaSe)_{1.27}(SnSe_2)_2$, that corresponds to x=1, the large doping of La atoms causes the increase of the $SnSe_2$ intralayer distance, thereby modifying the curvature of the Sn s-band of $SnSe_2$. Indeed, when the doping lowers, this band distortion gradually reduces until it disappears in the case of a rocksalt with 100% of Pb atoms (x = 0).
The results obtained for the $(La_xPb_{1-x}Se)_{1+\delta}(TX_2)_2$ series show that it is possible to reach a complete control on the doping via chemical intuition in misfit layer compounds, further validating our approach based on work function. We can think about misfits like a periodic arrangement of ultratunable field effect transistors, where charging can be reached and controlled efficiently by the La-Pb alloying in the rocksalt. In the next section we will show how to exploit these findings to models misfit layer compounds.

3.8 Summary

In Chapter 3, we describe the ab initio geometrical and electronic properties of misfit layer compounds. We start by comparing the experimental structure determination of bulk misfit layer compounds with the ab initio process. As an example, we characterize the geometrical properties of bulk $(LaSe)_{1.14}(NbSe_2)_2$ with a detailed analysis of ab initio calculations by carefully taking into account the geometrical modifications of LaSe and $NbSe_2$ within the misfit in comparison with experimental data [5, 6].
We then explain our procedure to build misfit surfaces and introduce the band unfolding technique as implemented in the BandsUP software [89, 90] that we use to calculate the misfit supercell band structure in terms of that of the TMD primitive cell.
Finally, we present our ab initio calculations of the electronic structure and geometrical properties of selected misfit layer compound surfaces [81]. First, we select LaSe as the rocksalt, which has the lowest work function among the Se compounds. We choose three kinds of TMDs with different properties, namely a metal ($NbSe_2$), a semimetal ($TiSe_2$), and an insulator ($SnSe_2$), to examine how the high doping from the LaSe layers impacts their band structure within the misfit. Then, we address the problem of tuning the charge transfer by appropriately choosing the rocksalt in order to demonstrate the global picture based on work

functions presented in Chapter 2. We specifically consider the $(RQ)_{1+\delta}(NbSe_2)_2$ misfit series, where we fix the TMD as $NbSe_2$, and we change the rocksalt with RQ = LaSe, BiSe, PbSe, and SnSe. We show that the behavior of this misfit series is almost completely characterized by the work function difference; thus, it is possible to tune the doping of the TMD in the misfit by chemical intuition. Lastly, we presented our results on the $(La_xPb_{1-x}Se)_{1+\delta}(TX_2)_2$ series with TX_2 = $NbSe_2$, $TiSe_2$, and $SnSe_2$. Our findings show that it is possible to think about misfits like a periodic arrangement of ultratunable field effect transistors, where charging can be reached and controlled efficiently by the La-Pb alloying in the rocksalt.

Chapter 4

Modeling misfit layer compounds as a collection of field effect transistors

4.1 Gated two-dimensional materials in the field effect transistor setup

In the previous chapter, we demonstrated that misfit layer compounds are highly tunable systems, where charge transfer from the rocksalts to the transition metal dichalcogenides can be tailored by chemical alloying. In this chapter, we will explain how to model misfit layer compounds as a collection of field effect transistors. First and foremost, we introduce the field effect transistor setup (FET setup) as developed in Ref. [100, 101], tailored for the case of two-dimensional heterostructures in field-effect configuration. Then, as detailed in the following, we will explain how, by working within the FET setup, we are able to model misfits as a periodic arrangement of FETs.

We consider a 2D material that is periodic only on the in-plane axes x and y and has a finite thickness along the out-of-plane direction z. Thus, it is possible to identify the positions of the cells from the in-plane primitive lattice vectors $\mathbf{a}$ and $\mathbf{b}$ as $\mathbf{R}_p = \mathrm{u}\mathbf{a}+\mathrm{v}\mathbf{b}$, where u and v are two integers. In reciprocal space, the crystal is described by reciprocal vectors $\mathbf{G}_p$, generated by two in-plane primitive reciprocal lattice vectors $\mathbf{a}^*$ and $\mathbf{b}^*$.

The ground state properties of the system within the DFT framework are determined by the ground-state electronic density n. In the case of a 2D materials, we can separate the contribution of the in-plane electron coordinate $\mathbf{r}_p$ and the out-of-plane z coordinates of the Bloch wave functions, solutions of the Kohn-Sham (KS) equations:

$$\psi_{\mathbf{k},s}(\mathbf{r}_p, z) = \mathbf{w}_{\mathbf{k},s}(\mathbf{r}_p, z)e^{i\mathbf{k}\cdot\mathbf{r}_p} \tag{4.1}$$

where $\mathbf{k}$ is the in-plane wave vector and the band index s define an electronic state. Thus, the ground-state electronic density is:

$$n(\mathbf{r}_p, z) = 2\sum_{\mathbf{k},s} f(\epsilon_{\mathbf{k},s})|\psi_{\mathbf{k},s}(\mathbf{r}_p, z)|^2. \tag{4.2}$$

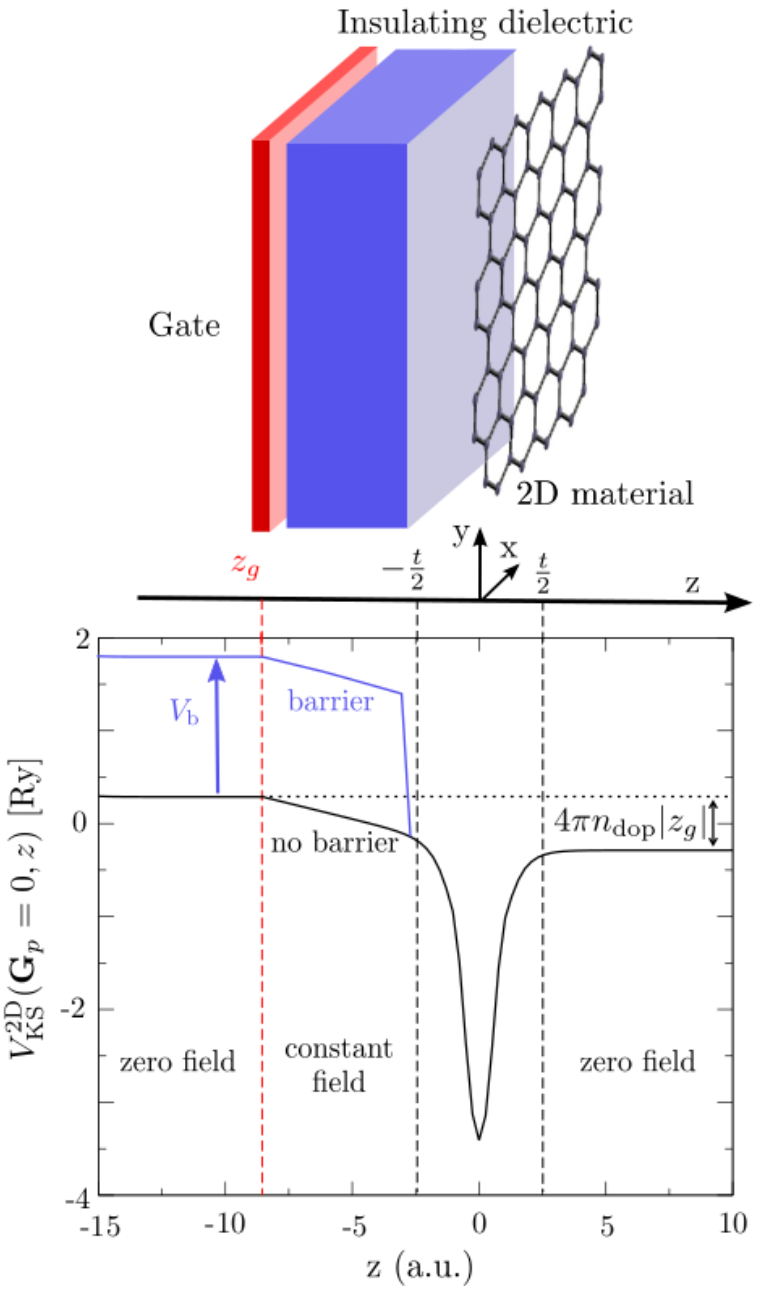

Figure 4.1: The sketch shows a minimal model of the FET setup containing the 2D material and a gate separated by an insulating dielectric. The plot shows the out-of-plane behavior of the corresponding Kohn-Sham (KS) potential for a hole-doped single-layer 2D material (graphene) in the FET setup. A charged plane simulates the gate. On the left of the material, the KS potential is represented in black, when only vacuum separates the gate and the material. In blue, a potential barrier is added to simulate the dielectric material. Figure taken from Ref. [101].

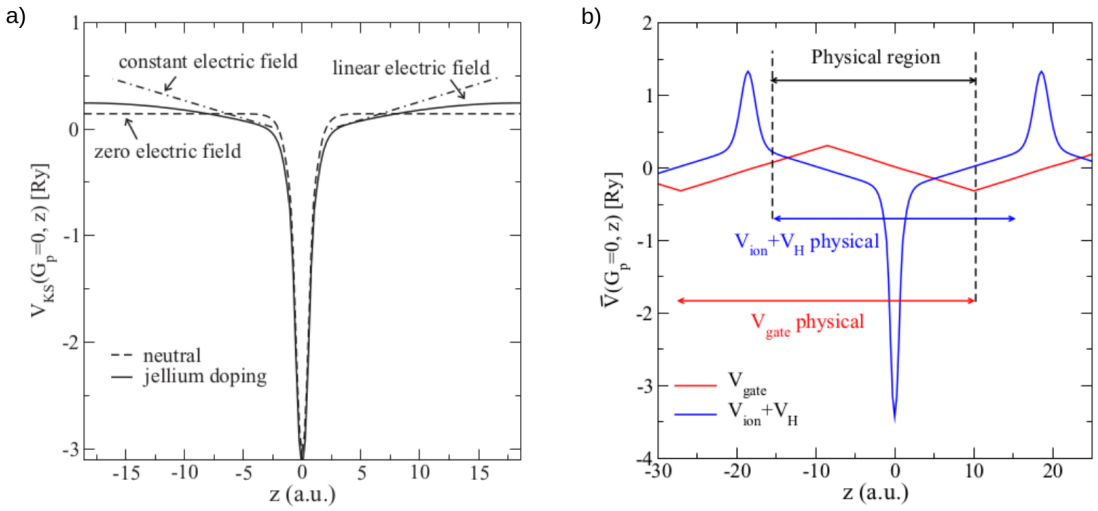

Figure 4.2: a) Planar-averaged KS potential in the out-of-plane direction as simulated in DFT with 3D PBC for neutral (dashed line) and doped (plain line) graphene. In the case of doped graphene, the quadratic behavior of the KS potential indicates the presence of a jellium background and a linear electric field. The dot-dashed line represent the behavior one would expect from an isolated monopole with the same surface charge density as the 2D material $V_{mono}=-2\pi e^2 n_{dop}|z|$. b) Determination of the physical region. In the upper panel, the gate potential and the material's potential $<\overline{V}_{ion}+\overline{V}_H>_p(z)$ are shown, and the region where they make sense physically is indicated. The physical region is the overlap between those regions. In the plot, c$\approx$ 37 a.u. and $z_g\approx -8.5$ a.u. Figure taken from Ref. [101].

The KS potential of the 2D system V_{KS}^{2D} is the sum of the external potential V_{ext}^{2D} (which, for now, consists of the potential generated by the ions V_{ion}^{2D}), the Hartree potential V_H^{2D} , and the exchange-correlation potential V_{XC}^{2D}:

$$V_{KS}^{2D}(\mathbf{r}_p, z) = V_{ext}^{2D}(\mathbf{r}_p, z) + V_H^{2D}(\mathbf{r}_p, z) + V_{XC}^{2D}(\mathbf{r}_p, z). \tag{4.3}$$

All the quantities in Eq. 4.1, 4.2 and 4.3 are periodic with the 2D periodicity of the crystal:

$$f(\mathbf{r}_p + \mathbf{R}_p, z) = f(\mathbf{r}_p, z) \tag{4.4}$$

thus, the 2D Fourier transform reads:

$$f(\mathbf{G}_p, z) = \frac{1}{S} \int_S f(\mathbf{r}_p, z) e^{-i\mathbf{G}_p \cdot \mathbf{r}_p} d\mathbf{r}_p \tag{4.5}$$

where the integral is over the area of the unit cell S. In-plane averages are defined as f($\mathbf{G}_p$ = 0,z) = $\langle f \rangle_p$(z), and are also extend in the out-of-plane direction. A relevant length scale for the out-of-plane extension of the 2D material would be the electronic density's thickness t, defined such that:

$$\int_{-t/2}^{t/2} \langle n \rangle_p(z)\ dz \approx n_0, \tag{4.6}$$

where $n_0 \times S$ is the number of valence electrons per unit cell in the system, equal to the sum of the ionic charges $\sum_\alpha Z_\alpha$ in the neutral case, where α labels the atoms in the unit cell. We now consider what must be done to simulate this 2D material in the FET setup. We consider a single-gate configuration, as shown in Fig. 4.1. A planar gate is placed parallel to 2D material and a voltage difference is applied between the two. An insulating material (gate dielectric) separates the 2D material and the gate, such that no current can flow between them and opposite surface charges accumulate on both sides.

The key feature of the FET setup is its asymmetry in terms of electric field. Between the gate and the 2D material, the electric field is finite. On the other side of the 2D material and of the gate, the electric field is zero. In the out-of-plane direction, it is essential to simulate the correct 2D potentials in a region at least as large as the thickness t.

Instead of modeling every ion and electron outside this region, it is possible to simulate the effects of those components on the 2D material. The main purpose of the FET setup is to charge the 2D material. Considering an electron density such that:

$$\int \langle n \rangle_p(z)\ dz = n_0 = \sum_\alpha \frac{Z_\alpha}{S} + n_{dop}, \tag{4.7}$$

where Z_α is the number of pseudo charges of atom α, S is the surface of the 2D unit cell, and $n_{dop} \times S$ is the surface of the 2D unit cell, and density of the 2D material is obtained by integrating the sum of the charge distributions associated with the ions and electrons:

$$\int \langle \rho_{ion} + \rho_{elec} \rangle_p(z)\ dz = -e n_{dop}, \tag{4.8}$$

where the charge densities ρ are related to the corresponding electrons or ions density as $\rho_{ion} = en_{ion}$ and $\rho_{elec} = -en$. In the FET setup of Fig. 4.1, the doping comes from the presence of accumulated counter charges in the gate. A charged plane of opposite surface charge density $+en_{dop}$ is added at $z_g < -t/2$, playing the role of the gate:

$$\rho_{gate}(z) = +en_{dop}\delta(z - z_g), \tag{4.9}$$

$$V^{2D}_{gate}(z) = +2\pi e^2 n_{dop}|z - z_g|. \tag{4.10}$$

Finally the system is now neutral as:

$$\int \langle \rho_{ion} + \rho_{elec} \rangle_p(z) + \rho_{gate}(z)\ dz = 0 \tag{4.11}$$

and the potential of the gate is included in the external potential:

$$V^{2D}_{ext}(\mathbf{r}_p, z) = V^{2D}_{gate}(z) + V^{2D}_{ion}(\mathbf{r}_p, z). \tag{4.12}$$

The resulting planar-averaged KS potential V^{2D}_{KS} is the black line in Fig. 4.1, in the case of a hole-doping monolayer material. At this point, it has the features expected from a FET setup with vacuum as the insulating dielectric.
The general characteristics of this potential are easily deduced from a simple parallel plate capacitor model: (i) outside the system, the electric field is zero and the potential is constant; (ii) between the 2D material and the gate, the electric field is constant and the potential is linear with a slope of $4\pi e^2 n_{dop}$; (iii) this electrostatic configuration translates into an out-of-plane dipolar moment, which induces a shift in the KS potential:

$$\langle V^{2D}_{KS} \rangle_p(+\infty) - \langle V^{2D}_{KS} \rangle_p(-\infty) = 4\pi e^2 n_{dop}|z_g|, \tag{4.13}$$

as represented in Fig. 4.1.
The other element to consider to have a minimal working model for the FET setup is the dielectric separating the gate and the material. Its necessity is obvious in the case of electron-doping. In that situation, the polarity of the system pictured in Fig. 4.1 is reversed. This means that the gate lies at a lower potential than the 2D material. In such a simulation, there would then be some leaking of electrons towards the gate. This is not physical. In a FET setup, this is prevented by the presence of an insulator between the gate and the material. From a more mechanical point of view, the necessity of the dielectric is in fact more general. Indeed, both for hole and electron doping, there is an attractive force between the gate and the material, which is simply the electrostatic attraction between two oppositely charged plates:

$$|\mathbf{F}_{gate-material}| = S \times 2\pi e^2 n^2_{dop}. \tag{4.14}$$

In this context, the dielectric provides a counteracting repulsive force. To emulate both the insulating and repulsive roles of the dielectric, a potential barrier is added in between the material and the gate:

$$V^{2D}_{barrier}(z) = \begin{cases} V_b & \text{if } z < z_b. \\ 0 & \text{otherwise,} \end{cases} \tag{4.15}$$

where $z_g < z_b < 0$. This potential can be included in the 2D external potential V_{ext}^{2D}. Adding such a barrier results in the potential represented by a blue line in Fig. 4.1. This barrier potential essentially forbids (or makes highly unlikely) the presence of electrons for $z < z_b$, thus preventing electrons from leaking towards the gate. Since the electrons cannot go past the barrier, and since the ions are strongly attracted by the electrons, the barrier repels the 2D material as a whole. The equilibrium position of the material with respect to the barrier can be determined by relaxation of the forces in the system.
Finally, we briefly discuss how to tackle with periodic replica of the system to correctly recover the behaviour of the potential of a 2D material in the FET setup [101]. The standard method in plane-wave DFT packages amounts to the use of a jellium background. Each slab is then globally neutral, containing the doped material and a uniform distribution of compensating charges. In between the periodic images, the resulting potential is quadratic in z, with extrema at mid-distance between layers. This potential does fulfill the periodic boundary conditions (PBC) and does not diverge. However, it is quite different from the potential one would expect for a charged, isolated 2D material. In the FET setup for gated 2D materials, the 3D PCB issue is solved by using the Coulomb cutoff technique.
The general idea is to cut all the potentials off between the periodic images along the z-axis. In effect, all physical links between periodic images are severed because the potential generated by one periodic image does not reach the others. Each slab is effectively isolated. In this way, there is no physical 3D periodic system anymore. There is a 2D periodic system, copied and repeated in the third dimension in order to build potentials that mathematically fulfill 3D periodic boundary conditions. However, at half the distance between the periodic images, the potential is null.
Each long-range potential (V_H,V_{ion},V_{gate}) in the original 3D code is generated by a certain distribution of charges via the Coulomb interaction ($v_c(\mathbf{r})$=$\frac{e^2}{\mathbf{r}}$). To build the corresponding cutoff potentials in the code ($\overline{V}_H$,$\overline{V}_{ion}$,$\overline{V}_{gate}$), the following cutoff Coulomb interaction is used:

$$\overline{v}_c(\mathbf{r}) = \frac{e^2\theta(l_z - |z|)}{|\mathbf{r}|}) \tag{4.16}$$

where $\mathbf{r} = (\mathbf{r}_p, z)$ is a generic three-dimensional space variable. An arbitrary charge density ρ then generates the following potential:

$$\overline{V}(\mathbf{r}) = \int \frac{e\rho(\mathbf{r}')}{|\mathbf{r} - \mathbf{r}'|}\theta(l_z - |z|)\ d\mathbf{r}'. \tag{4.17}$$

Roughly speaking, considering a single charged plane, we generate its potential only within a certain slab of thickness $2l_z$ centered on the charge distribution. Within this slab, we have that $\overline{V}(\mathbf{r}) = \mathrm{V}^{2D}(\mathbf{r})$. Outside of this slab, the potential is zero. Each periodic image of each charge distribution (ρ_{ion}, ρ_{elec}, ρ_{gate}) generates its own potential within its own slab. To fulfill 3D PBC, the simpler way is to cut off midway between the periodic images:

$$l_z = \frac{c}{2}. \tag{4.18}$$

Since the potentials V_{ion}^{2D}, V_{H}^{2D}, and V_{gate}^{2D} are symmetric with respect to the plane of the associated subsystem (ions, electrons, gate), they have the same value on both sides of the corresponding slab. $\overline{V}_{ion}^{2D}$, $\overline{V}_{H}^{2D}$, and $\overline{V}_{gate}^{2D}$ are each continuous and periodic, and so is their sum $\overline{V}_{KS}^{2D}$. However, since the slabs of each subsystem do not coincide, the KS potential is only physical within the overlap of the subsystems' slabs. This overlap region defines a "physical region", as illustrated in Fig. 4.2, where all the potentials make sense. Outside of this region, there are some spurious unphysical variations of the KS potential. Those spurious variations are a necessary consequence of fulfilling 3D PBC. Nevertheless, everything happens, as demonstrated in Ref. [101], within the physical region associated to the KS potential. To simulate the system, is just needed to make sure that the 2D material lies in this physical region.
In conclusion, the FET setup method is a powerful tool to investigate the properties of gated 2D materials. It has been already employed to many applications involving TMDs. For example, for the investigation of how field-effect doping affects the structural properties, the electronic structure, and the Hall coefficient of few-layers transition-metal dichalcogenides [100] and to study phonon mediated superconductivity in field-effect doped molybdenum dichalcogenides [102].
In the next sections, we will show how to apply this methodology to predict the electronic and vibrational properties of misfit layer compounds. The applications of this technique extend far beyond simulations of gated 2D materials. For example, whenever a subset of a material can be assimilated to a charged plate, this approach can be successfully adopted (see Fig. 4.3).

4.2 Misfit layer compounds as a collection of field effect transistors

In Chapter 2 we demonstrate that, inside the misfit, the rocksalt subunit acts as a donor, transferring electrons to the TMD layers.
In Chapter 3 we used the physical insight gained from the work function analysis to calculate the electronic properties of misfit layer compound surfaces. The results show that it is possible, via Pb/La alloying in the RS layers, to set the Fermi level at will. For example, in the case of $(LaSe)_{1.27}(SnSe_2)_2$ it is possible to tune the doping of $SnSe_2$ to reach the Van Hove singularity.
Starting from these findings, we want to model the misfit as a collection of field effect transistors. Because the rocksalt serves as an electron reservoir, it may be assimilated to a capacitor plate in a field effect transistor scheme. By means of the field effect transistor setup, presented in the previous section, it is then possible to model the effect of the misfit structure onto the TMD layers. As we can see from Fig. 4.3, the full misfit can be assimilated to several field-effect transistors stacked periodically along the z-axis of the MLC. This configuration is achieved by replacing the rocksalt with a uniformly positive charged gate. The gate's charge is set to match the amount of charge transferred from the rocksalt to the TMD in the considered misfit. In this way, the TMD is doped as it is in the misfit.

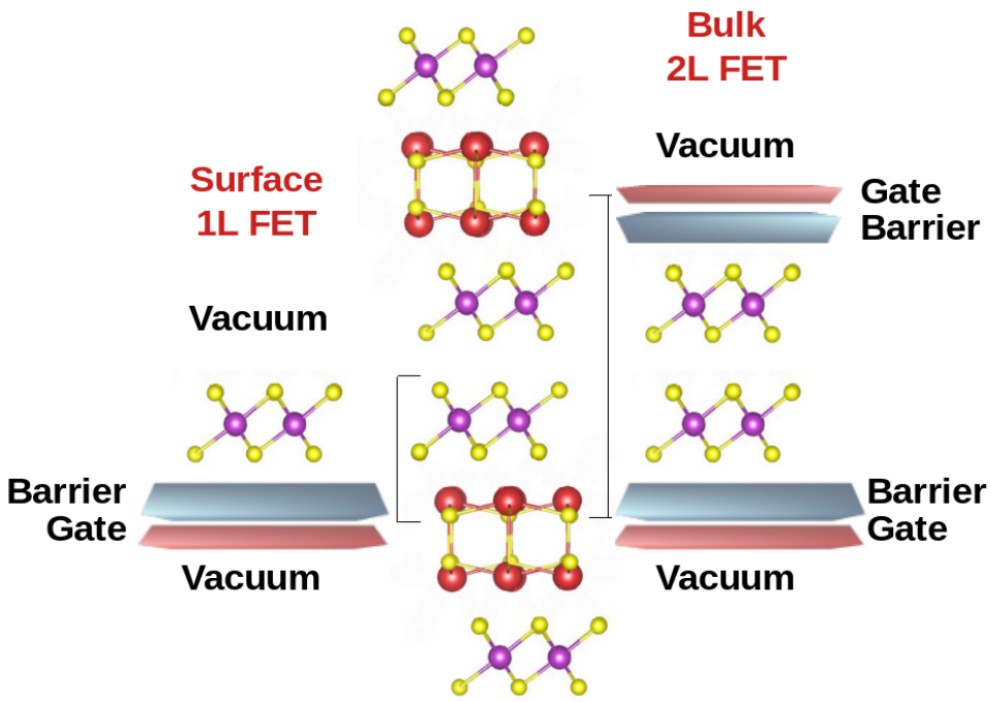

Figure 4.3: The field-effect modeling scheme for misfit layer compounds with m=2. In this scheme, MLC surfaces can be modeled in a single layer field effect transistor setup (1L FET) by replacing the rocksalt with a positively charged gate; a negatively charged monolayer TMD then corresponds to the misfit surface termination layer. Bulk MLCs can be modeled in a double layer field effect transistor setup (2L FET) by replacing the rocksalt with two positively charged gates sandwiching a negatively charged bilayer TMD. To confine the atoms in the region in between the charged plates, positive potential barriers are added. Vacuum space prevents periodic replicas from interacting with each other.

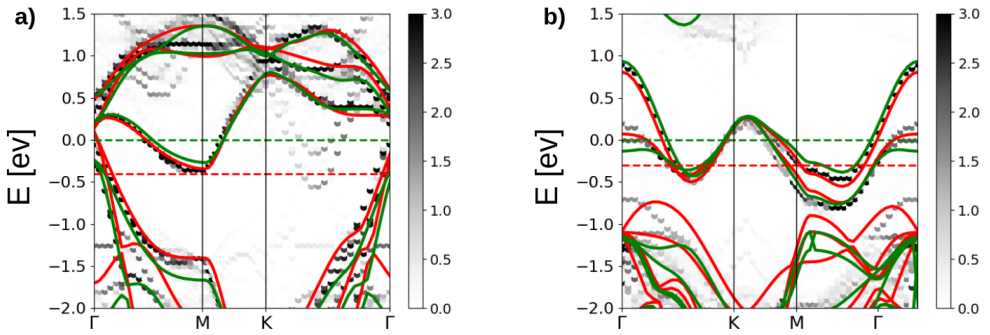

Figure 4.4: Example of FET applied to simulate misfit layer compounds surface and bulk. a) Band unfolding (grey) of $(LaSe)_{1.18}(TiSe_2)_2$ misfit surface supercell onto the hexagonal primitive Brillouin Zone (BZ) of single layer $TiSe_2$ (the zero energy is set to the Fermi level, dashed green line). The superimposed solid lines are the band structure of an isolated single layer $TiSe_2$ (red), and of a single layer $TiSe_2$ doped in a single FET setup as in $(LaSe)_{1.18}(TiSe_2)_2$ by 0.5 electrons per Ti atoms (green), respectively. b) Band unfolding (grey) of $(LaSe)_{1.15}(NbSe_2)_2$ misfit bulk supercell onto the hexagonal primitive Brillouin Zone (BZ) of bilayer $NbSe_2$ (the zero energy is set to the Fermi level, dashed green line). The superimposed solid lines are the band structure of an isolated bilayer layer $NbSe_2$ (red), and of a bilayer layer $NbSe_2$ doped in a double FET setup as in $(LaSe)_{1.15}(NbSe_2)_2$ by 0.6 electrons per Nb atoms (green), respectively. Darker regions in the colormap represent the most relevant projection of the misfit eigenvalues of the band structure in the $TiSe_2$ ($NbSe_2$) first BZ (band unfolding).

As we can see in Fig. 4.3, it is possible to model both the surface and the bulk MLCs within the FET setup. In particular, we used this scheme to model misfit layer compounds with m=2. A MLC surface can be modeled in a single layer field effect transistor setup (1L FET). In this case, the rocksalt is replaced with a positively charged gate, while the TMD is a negatively charged monolayer corresponding to the misfit surface termination layer. Bulk MLCs can be modeled in a double layer field effect transistor setup (2L FET) by replacing the rocksalt with two positively charged gates sandwiching a negatively charged bilayer TMD. To confine the atoms in the region in between the charged plates, positive potential barriers are added, as explained in the previous section. Vacuum space prevents periodic replicas from interacting with each other, and must be sufficient to place the system in the physical region of the FET setup. As an example, we show in Fig. 4.4 FET setup applied to the electronic structure of misfits surface and bulk. We consider specifically the unfolded band structure of (a) the surface of $(LaSe)_{1.18}(TiSe_2)_2$ and (b) the bulk of $(LaSe)_{1.15}(NbSe_2)_2$. First, we calculate the amount of charge transferred from the RS to the TMD, as detailed in Chapter 3. Then, we model the surface (bulk) in the single (double) FET setup (see Fig. 4.3) by replacing the rocksalt units with the appropriate charged plates. In the first case, we unfold the band structure of $(LaSe)_{1.18}(TiSe_2)_2$ misft surface onto the hexagonal primitive Brillouin Zone (BZ) of single layer $TiSe_2$. The superimposed solid lines are the band structure of an isolated single layer $TiSe_2$ (red), and of a single layer $TiSe_2$ doped in a single FET setup (see Fig. 4.3) as in

$(LaSe)_{1.18}(TiSe_2)_2$ by 0.5 electrons per Ti atoms (green), respectively. In the second case we unfold $(LaSe)_{1.15}(NbSe_2)_2$ misfit bulk supercell onto the hexagonal primitive Brillouin Zone (BZ) of bilayer $NbSe_2$ (the zero energy is set to the Fermi level, dashed green line). The superimposed solid lines are the band structure of an isolated bilayer layer $NbSe_2$ (red), and of a bilayer layer $NbSe_2$ doped in a double FET setup as in $(LaSe)_{1.15}(NbSe_2)_2$ by 0.6 electrons per Nb atoms (green), respectively. As can be seen, the calculation is in good agreement with the one for the MLC surface (bulk).

In our work [81], we apply the FET setup to the misfit layer compound $(LaSe)_{1.27}(SnSe_2)_2$ where, as shown in Chapter 3, there is substantial band distortion of the s-band of Sn with respect to the isolated single layer (see Fig. 3.5(c)). Technical details of these calculations can be found in Appendix A.3. From the the electronic band structure of the misfit surface, unfolded onto that of a single layer $SnSe_2$, we extracted the amount of charge transfer between the LaSe and the $SnSe_2$ (0.77 e^-/Sn atoms, or $n_e \approx 6 \times 10^{14}$ cm^{-2}). In Chapter 3, we discussed how this huge charge transfer causes the distortion of the Sn s-band at the Fermi level of the misfit. Indeed, as shown in Fig. 4.5, we compare the MLC surface electronic structure with the one of an isolated layer (red line). The substantial band distortion with respect to the isolated single layer is evident in the figure.

A better description of the surface electronic structure is obtained by replacing the LaSe layer with a uniformly positive charged potential barrier, as in a single gate field effect transistor setup by using the method developed in Ref. [100, 101]. Green line in Fig. 4.3 corresponds to the electronic structure of an isolated $SnSe_2$ layer under this approximation. As can be seen, the calculation agrees perfectly with the one for the entire MLC surface, both in terms of band bending at the Fermi level (some deviations are seen in the empty states near to the zone center) and the position of the valence band top. As discussed in Chapter 3, we attribute the band bending occurring at the K high-symmetry point to a modification of the intralayer spacing between Sn and Se in $SnSe_2$ due to the charging of the monolayer.

To further validate our hypothesis, we can separate the contribution of each subunit to the density of states (DOS) of $(LaSe)_{1.27}(SnSe_2)_2$ and then compare it with the one of a single layer $SnSe_2$ doped in a single FET setup. This calculation is shown in Fig. 4.5. We calculate the total DOS per $SnSe_2$ formula unit of $(LaSe)_{1.27}(SnSe_2)_2$ (yellow line). We then project the density of states over atomic orbitals of the LaSe layers (purple) and of the $SnSe_2$ layers (blue), respectively. Finally, we compare it with the green line, which is the DOS of a single layer $SnSe_2$ doped in a single FET setup of 0.7 electrons per Sn atom. As seen in Chapter 3, the amount of LaSe electrons is low at the Fermi level. In addition, we can see that the FET setup recovers the behaviour of the total DOS at the Fermi level, indicating once again, that the FET modeling is in perfect agreement with the complete calculation of the MLC surface. Finally, a comparison of the interlayer spacing d_z between Sn and Se in $SnSe_2$ is shown in Fig. 4.6. The charge transfer exerted by LaSe in $(LaSe)_{1.27}(SnSe_2)_2$ modifies the out-of-plane spacing (d_z) in monolayer $SnSe_2$. The intralayer spacing between the two Se atoms increases

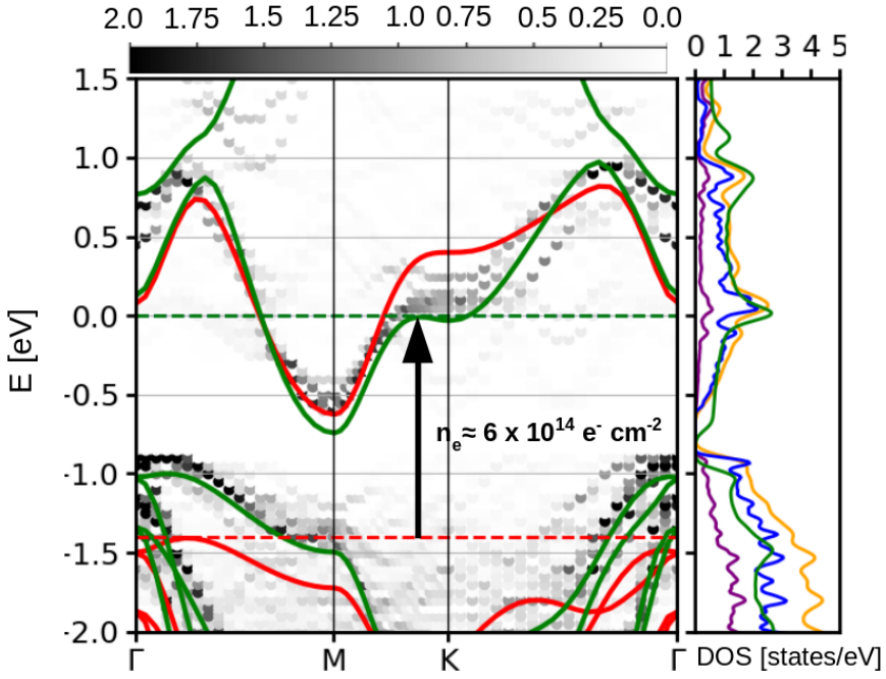

Figure 4.5: Band unfolding (grey) of $(LaSe)_{1.27}(SnSe_2)_2$ misfit supercell onto the hexagonal primitive Brillouin Zone (BZ) of single layer $SnSe_2$ (the zero energy is set to the Fermi level, dashed green line) . The superimposed solid lines are the band structure of an isolated single layer $SnSe_2$ (red), and of a single layer $SnSe_2$ doped in a single FET setup as in $(LaSe)_{1.27}(SnSe_2)_2$ by 0.7 electrons per Sn atoms (green), respectively. Darker regions in the colormap represent the most relevant projection of the misfit eigenvalues of the band structure in the $SnSe_2$ first BZ (band unfolding). In the adjacent panel we plot the total DOS per $SnSe_2$ formula unit of $(LaSe)_{1.27}(SnSe_2)_2$ (yellow) and the projected density of states over atomic orbitals of the LaSe layers (purple) and of the $SnSe_2$ layers (blue), respectively. The green line is the DOS of a single layer $SnSe_2$ doped in a single FET setup of 0.7 electrons per Sn atoms.

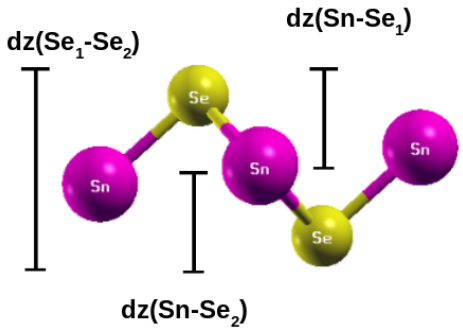

dz (Å)	Misfit	1L-FET	1L
$dz(Se_1\text{-}Se_2)$	3.34	3.37	3.19
$dz(Sn\text{-}Se_1)$	1.78	1.79	1.59
$dz(Sn\text{-}Se_2)$	1.56	1.58	1.59

Figure 4.6: Intralayer spacing (d_z) between Sn and Se in $SnSe_2$. Comparison between values of d_z in isolated monolayer (1L), monolayer in the MLC $(LaSe)_{1.27}(SnSe_2)_2$ (misfit), and single-gate doped monolayer (1L-FET) with 0.7 e^-/Sn.

by ∼5% in the misfit, with respect to that of an isolated monolayer $SnSe_2$ (1L). While the Sn-Se interatomic distances in the out-of-plane axis (d_z(Sn-Se_x), with x=1, 2) of an isolated monolayer $SnSe_2$ are equal, due to the effect of the LaSe doping substrate, their value differs in the misfit. The structural optimization in a FET setup recovers this geometrical behavior with an interlayer spacing within the ∼ 0.8% with that of the misfit, thus being in excellent agreement with the complete MLC structural optimization.
These findings demonstrate that FET modeling is a reliable tool for tackling the electronic structure of misfit layer compounds.

4.3 Doping-induced superconductivity in misfit layer compound $(LaSe)_{1.27}(SnSe_2)_2$ in the FET setup

After achieving complete knowledge of the charge transfer in MLCs, we now demonstrate how to design a misfit superconductor starting from its constituents. In particular, we show that non-superconducting pristine RS and TMD compounds can lead to a misfit superconductor via charge transfer control (emergent superconductivity). We specialize our discussion to misfit layer compound $(LaSe)_{1.27}(SnSe_2)_2$ whose electronic and geometrical properties are reported in Chapter 3 and 4. As superconductivity is a bulk property, we must simulate the complete 3D crystal. The calculation of the vibrational properties and electron-phonon coupling for the complete MLC is, however, a very cumbersome task due to the large number of atoms.
We then proceed differently, namely we consider a $SnSe_2$ bilayer in a field effect configuration as in Fig. 4.3 with a +0.7 charge on each of the two plates (double gate configuration). In order to prevent the ions from moving too close to the gate electrodes, a potential barrier is placed before the gates, and the total charge of the system is maintained equal to zero [101].
We then calculate the phonon dispersion ($\omega_{\mathbf{q}\nu}$) and the electron-phonon coupling (in Chapter 5, we will go into more details on the requirements for superconductivity calculations) $\lambda_{\mathbf{q}\nu}$ (see Eq. 5.11) for each mode ν of phonon crystal momentum $\mathbf{q}$ in double gate geometry. From these quantities we obtain the Eliashberg function $\alpha^2F(\omega)$ (see Eq. 5.10). These quantities are plotted in Fig. 4.7. As detailed in Appendix A.3, these calculations have been performed within EPI*q* (Electron-Phonon Interpolation over q- and k-points), an open-source in-house software [103]. Our results show that the average electron-phonon coupling of the system is $\lambda = 0.6$.
Approximately 30% of the coupling arises from the Einstein optical modes at $\approx 45 - 50$ cm^{-1}, while the rest of the coupling is uniformly distributed throughout the other modes. The phonon density of states (not shown) is very similar to the Eliashberg function.
We calculate the superconducting critical temperature by solving the anisotropic Migdal-Eliashberg equations [104], as implemented in the EPIq software [102, 103,

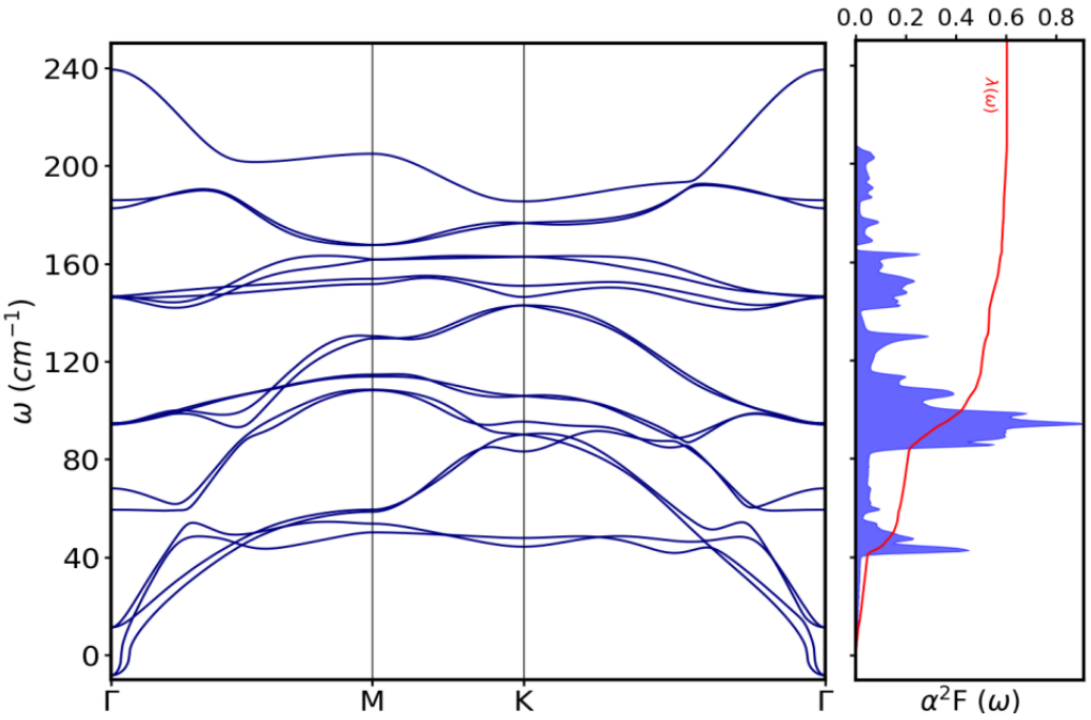

Figure 4.7: Dynamical properties and electron-phonon coupling of $(LaSe)_{1.27}(SnSe_2)_2$ modeled by a bilayer $SnSe_2$ in a double FET setup. The phonon dispersion is shown in the first panel while, in the adjacent panel, the Eliashberg function $\alpha^2F(\omega)$ (filled blue curve) and the total electron-phonon coupling $\lambda(\omega)$ (red) are depicted.

105], and by assuming $\mu^* = 0.1$. We obtain a predicted critical temperature of $T_c = 3.5$ K.
This result matches well with the $T_c = 4.8$ K detected in ultrathin Li-intercalated $SnSe_2$ via field effect gating and demonstrates that superconductivity can emerge in MLC from pristine components that are not superconducting.
In conclusion, we identify a strategy to design emergent superconductivity and demonstrate its applicability in $(LaSe)_{1.27}(SnSe_2)_2$ by FET modeling.

4.4 Vibrational properties of misfit layer compounds

In this section, we demonstrate how to predict the vibrational properties of misfit layer compounds based on that of their subunits, namely the rocksalts and the TMDs. This can be accomplished with appropriate field-effect doping.
In our work [106], we focus on the specific case of misfit layer compound $(LaSe)_{1.14}(NbSe_2)_2$. This heterostructure is composed of two subsystems, namely bilayers $NbSe_2$ (subsystem 1) and LaSe rocksalt subunits (subsystem 2) with different symmetries and periodicity [87] (see Fig. 3.1). The lattice parameter's mismatch along one of the in-plane direction of ratio $|\mathbf{a_2}|/|\mathbf{a_1}| = 6/3.437$ ($\approx 7/4$) makes $(LaSe)_{1.14}(NbSe_2)_2$ an incommensurate compound.
In Chapter 3, we already presented the geometrical properties of this compound. We now focus on one of the two subsystem of this misfit : the TMD $NbSe_2$. Bulk $NbSe_2$ displays competition between charge density wave (CDW) and superconducting order. An incommensurate CDW transition at 33 K occurs in bulk 2H-$NbSe_2$ [25–27]. Superconductivity (SC) emerges below 7.2 K and coexists with the CDW state [24]. Recent experiments [107, 108] demonstrate that CDW survives in the two-dimensional (2D) limit for $NbSe_2$ bi and single layers.
Achieving a complete control of CDW order in these systems could lead to a better understanding of the interplay between SC and CDW. To this aim, external parameters that can be tuned are doping, pressure, strain and sample thickness. However, each one of these control knobs leads to different effects.
For example, applying pressure to bulk $NbSe_2$ leads to a suppression of the CDW at ≈ 4.4 GPa and an increase of the superconducting T_c [109], but no change in the ordering vector occurs.
In the bulk, electron doping can be achieved via chemical intercalation [110] paving the way to a tunability of the ordering vector. Exfoliation of 2D TMDs and ionic-liquid based field-effect transistors has led to the possibility of setting the doping electrochemically by tuning the voltage drop at the capacitor plates to generate an electrical-double layer in the proximity of the 2D dichalcogenide [111].
Experiments show that the CDW phase in bilayer $NbSe_2$ is weakened by electron doping [7]. This suggests that it could be possible to observe a CDW collapse at high voltages. Unfortunately, the amount of doping required to observe a collapse of the CDW phase exceeds the largest carrier chargings accessible via field effect gating ($n_e \approx 3 \times 10^{14}$ e^- cm^{-2}). Other approaches are thus needed to achieve

higher doping.
As shown in Chapter 3, misfit layer compounds are an intriguing alternative for achieving nearly perfectly integrated 2D TMDs with massive doping.
In this particular case, quasiparticle interference measurements (QPIs) and angle-resolved photoemission spectroscopy (ARPES) show that each monolayer of $NbSe_2$ inside the $(LaSe)_{1.14}(NbSe_2)_2$ MLC is strongly electron-doped with a large Fermi level shift of +0.3 eV, (corresponding to $n_e \approx 6 \times 10^{14}$ e^- cm^{-2}) [6].
Furthermore, scanning tunneling microscopy (STM) and magneto-transport measurements demonstrate that bulk $(LaSe)_{1.14}(NbSe_2)_2$ is superconducting at 5.7 K with a critical field in the TMD plane that strongly violates the Pauli limit due to an efficient Ising protection, as in the monolayer case [9].
Although superconductivity in $(LaSe)_{1.14}(NbSe_2)_2$ has been clearly demonstrated, the occurrence of CDW is still under debate. STM topography detected the presence of a short-range 2×2 modulation disappearing above 105 K [6].
However, the 2×2 modulation observed in $(LaSe)_{1.14}(NbSe_2)_2$ by STM could be ascribed to a non-uniform doping on the cleaved surface. Up to our work, no bulk sensitive probes have demonstrated the presence or absence of a CDW in $(LaSe)_{1.14}(NbSe_2)_2$. Our work [106], based on the combination of our first-principles calculations and Raman measurements carried out by the group of Marie-Aude Méasson at the Néel Institut in Grenoble, aims to investigate the vibrational properties of $(LaSe)_{1.14}(NbSe_2)_2$. As we will detailed in the following, our analyses emphasize the 2D character of the TMD's lattice dynamics inside the misfit 3D structure.

4.4.1 Modeling bulk $(LaSe)_{1.14}(NbSe_2)_2$

Given the incommensurability of the misfit layer compounds along one of the in-plane directions, a (3+1)D superspace group could be adopted to label the crystal structures [4]. However, the commensurate approximant of the $(LaSe)_{1.14}(NbSe_2)_2$ compound crystallizes in the $P1$ space group.
The number of expected phonons is large, virtually infinite due to the incommensurability. From the symmetry analysis deriving from the $P1$ symmetry, all modes are both Raman (R) and Infrared (IR) active. However, many of the potentially Raman active modes have very low intensity as (i) the symmetry of the subunits closely resemble the one of the isolated counterparts and (ii) the P1 group arises from the need of matching the rocksalt and TMD space groups.
In order to gain a better understanding of the Raman active phonon modes, we first consider the two sub-structures as separated, namely a rocksalt bilayer of LaSe and a bilayer of 2H-$NbSe_2$ (2L-$NbSe_2$). Along the c axis, one bilayer of $NbSe_2$ corresponds to one unit cell of 2H-$NbSe_2$.
In the presence of mirror symmetry with respect to the Nb plane (i.e. isolated $NbSe_2$ bilayer in the absence of an external electric field), the 2L-$NbSe_2$ sub-structure belongs to the space group $P\bar{3}m1$ (#164, D^3_{3d} point group). Each bilayer has 6 atoms per unit cell. The Wyckoff positions of the two Nb atoms are 2c (with z= 3.13Å), while the four Se are in 2d (with z= 1.47Å) and 2d (with z= 4.84Å), respectively.

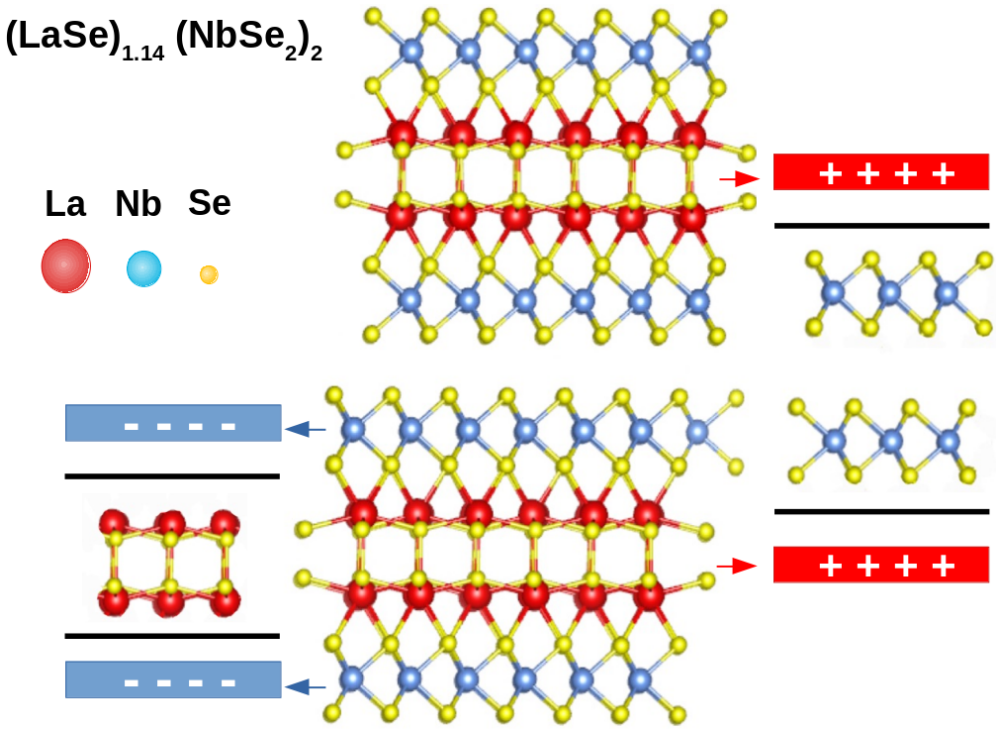

Figure 4.8: Crystal structure of $(LaSe)_{1.14}(NbSe_2)_2$ (center) composed of LaSe bilayers (red and yellow) and $NbSe_2$ bilayers (blue and yellow). Each LaSe bilayer donates ≈ 0.6 electrons/Nb to each $NbSe_2$ layer. The $NbSe_2$ bilayer is modeled in a field effect transistor set up (right) in which each LaSe bilayer is replaced by a charged plate having a positive charge of 0.6 electrons per Nb atom. The LaSe bilayer is modeled in a field effect transistor setup, replacing each $NbSe_2$ bilayer by a negatively charged plate of 0.6 electrons per Nb. To confine the atoms in the region in between the charged plates, positive potential barriers are added (black lines).

Bulk LaSe crystallizes in the Fm$\bar{3}$m (#225) space group with two atoms per cell. However, we choose to label the atomic positions of the isolated LaSe bilayer by using the Cmm2 space group (#35, C_{2v} point group), which is suitable for the orthorhombic lattice of LaSe within the misfit.
The LaSe bilayer is an alternation of La and Se with a total of 8 atoms per unit cell. The 4 atoms composing the first layer have Wyckoff positions 2a (with z= -0.077Å) for Se and 2b (with z= -0.076Å) for La. The 4 atoms composing the second layer have Wyckoff positions 2a (with z= 0.076Å) for La and 2b (with z= 0.077Å) for Se.
In our calculations, the in-plane lattice parameter of all the considered structures is fixed as the one of each sub-system in the bulk $(LaSe)_{1.14}(NbSe_2)_2$, namely, $a_1 = 3.437$ Å and $a_2 = 6$ Å [6].
Bulk $(LaSe)_{1.14}(NbSe_2)_2$ is a periodic arrangement of LaSe and $NbSe_2$ subunits along the stacking direction (see Fig. 3.1 in Chapter 3). The lattice parameter mismatch in one of the in-plane directions makes the misfit cell incommensurate. As detailed in Chapter 1, it is possible to simulate an approximate commensurate cell [6] by considering the ratio $|\mathbf{a_2}|/|\mathbf{a_1}| = 6/3.437$ ($\approx 7/4$), and thus m $=7|\mathbf{a_1}| \approx 4|\mathbf{a_2}|$. This periodic approximant has been used to calculate the electronic structure [6], however it is still formed by too many atoms for the calculation of the vibrational properties.
In order to reduce the computational effort, we approximate the 7/4 mismatch ratio by 8/4, corresponding to a 2/1 ratio. This is done by applying 14.6% tensile strain to the rocksalt subunit, increasing the lattice parameter to $a_2 = 6.875$ Å. The $NbSe_2$ in-plane parameter is, on the contrary, kept the same as in the misfit ($a_1 = 3.437$ Å).
Consequently, the two subunit cells in the 2×1 periodic approximant of bulk $(LaSe)_{1.14}(NbSe_2)_2$ are listed below. The $NbSe_2$ sublattice has an orthorhombic cell with in-plane lattice vectors $a_1 = 3.437$ Å and $b_1 = 6$ Å, while the LaSe sublattice has an orthorhombic cell with in-plane lattice vectors $a_2 = 6.875$ Å and $b_2 = 6$ Å.
The resulting misfit crystal has an orthorhombic cell with lattice parameters a $= |\mathbf{b_1}| = |\mathbf{b_2}| = 6$ Å, b $= 2|\mathbf{a_1}| \approx 1|\mathbf{a_2}|$=6.875 Å and c= 18.25 Å. The structure has a P1 symmetry and includes 32 atoms in the cell (atomic positions are reported in the Tab. A.4 in Appendix A.4).
Inside the misfit, the LaSe subunit acts as a donor, losing ≈ 1.2 electrons and donating ≈ 0.6 electrons per Nb atom to each monolayer of the $NbSe_2$ bilayer subunit [6].
By means of the field effect transistor setup developed in Ref. [100, 101], it is then possible to model the effect of the misfit structure onto the $NbSe_2$ bilayer by using a bilayer TMD sandwiched between two uniformly positive charged gates (see Fig. 4.8). Each charged gate replaces the RS subunit and has a positive charge per Nb corresponding to 0.6 times the modulus of the electronic charge. As shown in the previous section, this approach is efficiently carried out to estimate the misfit electronic structure in Ref. [81].
The field-effect scheme can also be employed by considering an RS subunit sand-

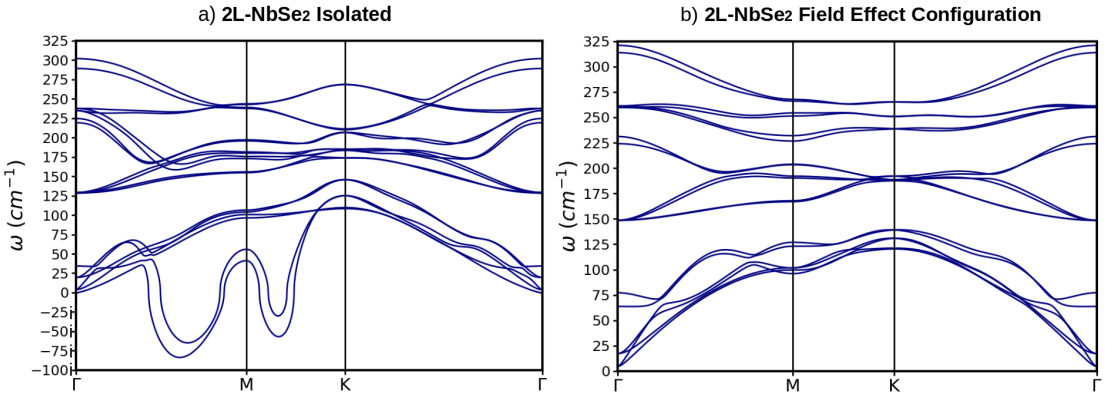

Figure 4.9: Calculated phonon dispersion along the Γ-M-K-Γ path of a) an isolated 2L-$NbSe_2$ and b) a field effect doped 2L-$NbSe_2$. In panel b) the charge-density-wave instability is clearly removed by electron doping.

wiched between two uniformly negative charged gates (see Fig. 4.8). In this case the goal is to determine the effect of the misfit structure onto the LaSe bilayer subunit so that the charged plates are now negatively charged. A detailed description of the computational parameters employed for these simulations are reported in Appendix A.4.

4.4.2 Charge density wave collapse of $NbSe_2$ in the $(LaSe)_{1.14}(NbSe_2)_2$ misfit layer compound

In Fig. 4.9 we calculate the harmonic phonon dispersion of an isolated neutral $NbSe_2$ bilayer (panel a) and of a $NbSe_2$ bilayer in field-effect configuration with a charging corresponding to 0.6 electrons per niobium atom (panel b). The charge density wave instability occurring in the isolated $NbSe_2$ bilayer is showcased by the presence of an imaginary phonon band with the most imaginary value at $\mathbf{q} \approx 2/3\mathbf{\Gamma M}$. Anharmonic effects do not qualitatively alter this behaviour, since the instability is reduced, but its wave vector is preserved [112].
In the FET charged $NbSe_2$ bilayer (panel b) the CDW instability is completely removed for charge transfers similar to those in the misfit. We thus expect that the CDW should collapse once the $NbSe_2$ subunit is inserted in the misfit. We will see that this estimation is confirmed by Raman data.
We believe that our FET simulation can accurately recreate CDW behaviour as a function of misfit doping level. Indeed, in the first place, it has been demonstrated that the misfit generally behaves as a periodic arrangement of tunable field effect transistors [81]. In addition, in the specific case of $(LaSe)_{1.14}(NbSe_2)_2$, the electronic band structure of the misfit can be assimilated as that of a rigidly doped $NbSe_2$ single layer [6]. Second, because the CDW in $NbSe_2$ originates from the in-plane modes, FET modeling is appropriate for characterising its physics.
Finally, we conclude by noting that, if the charged plates mimicking the charge transfer by the LaSe subunits are removed and the FET charging is replaced by a uniform background doping, the results are completely different as they show an

instability at the M point, in qualitative disagreement with experiments (see for example supplemental materials of Ref. [6]). The reason is that in the misfit, as in a field-effect transistor, the charge transfer to the $NbSe_2$ bilayer is not uniformly distributed along the $c-$axis. For this reason, the uniform background doping approximation is inappropriate.

Raman spectroscopy offers a direct probe of charge-density-wave signatures in the bulk [114,115], and in few-layer systems [107]. Two types of new Raman active modes arise as a fingerprint of the CDW.

The first one is a soft phonon called the amplitude mode, that gradually hardens when cooling down and that arises from the phonon branch which softens at the CDW wavevector. This mode has been detected in bulk 2H-$NbSe_2$ at ≈ 40 cm^{-1} (triangle in Fig. 4.10, panel (c)) [116, 117].

The second type of new peaks are zone-folded modes that arise from other phonon bands at the CDW wavevector. These modes are folded into Γ by the effect of the CDW modulation and are therefore detectable (Cf. stars in Fig. 4.10, panel (c)). Figs. 4.10 (a) and (b) show the Raman response of $(LaSe)_{1.14}(NbSe_2)_2$ in crossed and parallel polarisations for temperatures ranging from 8 to 200 K. In both polarizations, a substantial increase of the overall intensity is measured when cooling down. Narrow phonon modes are reported up to 350 cm^{-1}. The modes above 350 cm^{-1} are broader and are most likely due to double phonon excitations.

Globally, the phonon modes harden when cooling down, as it is generally expected from anharmonic effect. No new modes appear at low temperatures, neither across the temperature range where STM was detecting small patches with short range 2×2 modulation (100K) [6], nor across the temperature range at which the CDW is detected in bulk samples (35 K). The large-range electronic response does not present any signature of electronic gap opening that is sometimes measured in the CDW state [118, 119].

The last possible fingerprint of the presence of a CDW is a two-phonon Raman feature from the soft phonon branch at $\mathbf{Q}_{CDW}$, i.e. the phonon momentum related to the CDW instability. In bulk 2H-$NbSe_2$, it is visible in Fig. 4.10(c) as indicated by the arrow. The only candidate for this experimental Raman feature is the broad mode in the low energy range around 100 cm^{-1} which is detected in both polarization configurations. However, the temperature dependence of this mode is peculiar and in stark contradiction with the behaviour of the double phonon mode in $NbSe_2$. Indeed, as shown Fig. 4.10(c), in bulk 2H-$NbSe_2$ the double phonon feature loses intensity in both A_{1g} and E_{2g} symmetries and softens with decreasing temperature. Conversely, in the case of our $(LaSe)_{1.14}(NbSe_2)_2$, the large spectral weight bump always remains in the same energy range, and its intensity largely grows when cooling down as shown in Fig. 4.10. So even if this part of the spectra could be partially due to two phonon scattering, it does not evidence a softening of the branch and, thus, it is not related to a CDW.

A comparison with DFT calculations suggests that the nature of the broad mode in the misfit can be attributed to the presence of a dense population of LaSe modes that overlap with a few low energy $NbSe_2$ frequencies. Overall, these measurements suggest that no amplitude modes or CDW related modes occur down

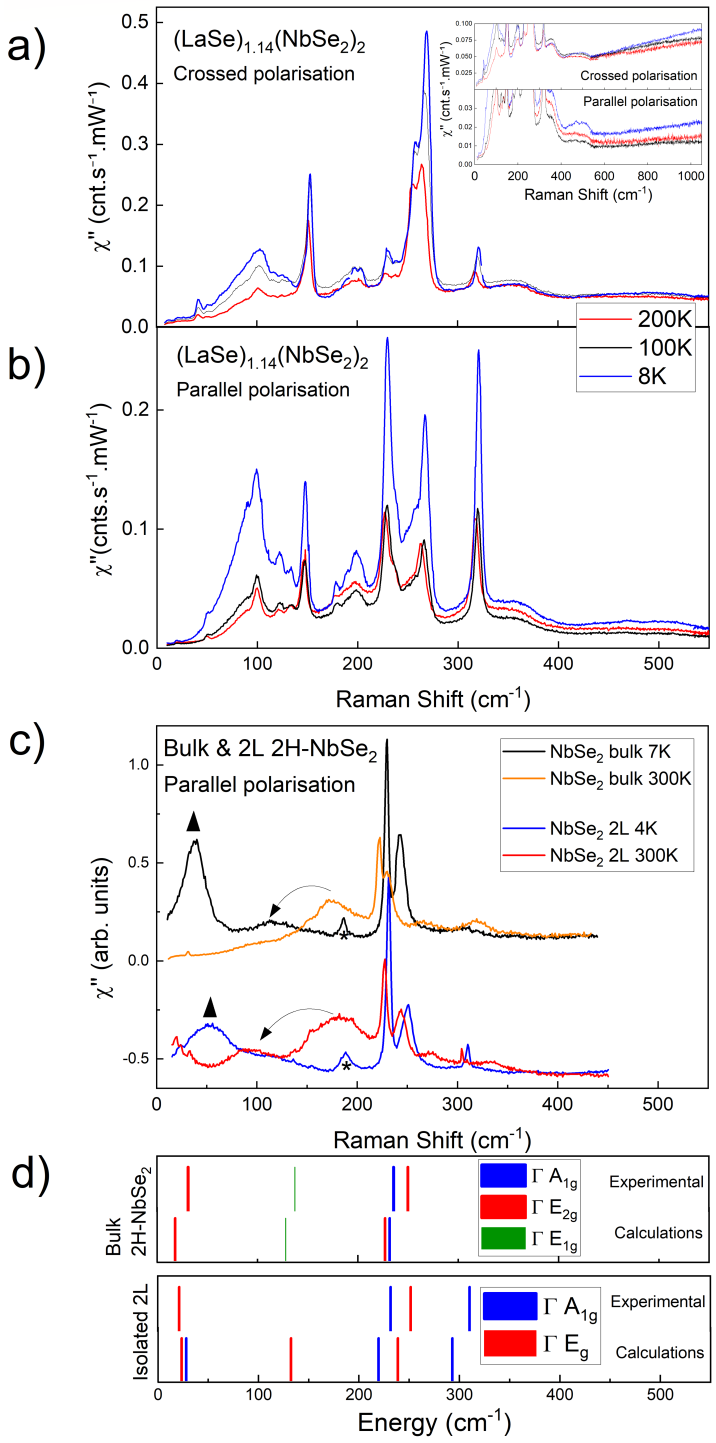

Figure 4.10: Temperature dependence of the Raman response of $(LaSe)_{1.14}(NbSe_2)_2$ with (ab)-plane crossed (a) and parallel (b) polarisation configurations. Inset: large energy-range electronic Raman response. c) Raman response of bulk 2H-$NbSe_2$ and isolated 2L-$NbSe_2$ [113] at 300 K and ∼5K, in the CDW state. The stars, triangles stands for the Brillouin-zone folded phonons and amplitudons, respectively. The arrows indicate the double phonon modes related to the soft phonon branches of the CDW. (d) Raman active phonons energies from experiments and from theory.

to 8 K.
We comment here on the CDW signatures observed by STM at the cleaved $(LaSe)_{1.14}(NbSe_2)_2$ surface while no signature in the bulk could be detected by Raman spectroscopy. Investigation of the Raman response of 2H-$NbSe_2$ as a function of quality of the samples, as stated by the residual resistivity ratio (RRR= 50 for good samples and 6 for the worst samples), clearly shows that the main CDW signature observed by Raman spectroscopy, namely the amplitudon, becomes extremely weak intensity in low quality samples [120].
A first hypothesis would be that the CDW would exist in the bulk but with a very short coherence length of ≈ 2 nm, as suggested by the STM experiment. In this case, the situation would be somehow analogous to the one observed in the normal state of 2H-$NbSe_2$, where it is reported that short range CDW modulations are observed by STM near the defects much above the bulk CDW critical temperature [121–123], while no Raman signatures are detected in this temperature regime.
A second hypothesis would be that a surface peculiar behaviour would stabilize and enhance a surface CDW, while its bulk counterpart would develop at much lower temperature and with lower amplitude and coherence length, or even not form at all. There have been reports of such complicated and different surface versus bulk CDW properties in well-known quasi-one dimensional materials such as $NbSe_3$ or the blue bronze [124–126].

4.4.3 Raman scattering and mode attribution of bulk $(LaSe)_{1.14}(NbSe_2)_2$

In Fig. 4.11 we show the Raman spectra of $(LaSe)_{1.14}(NbSe_2)_2$ at 8 K in both parallel and crossed polarizations. There is a substantial difference among the two spectra, supporting a strong dependence of the signal on the symmetry of the modes. In Tab. 4.1 we report the most intense modes together with their Raman active channels.
By comparing with the experimental Raman spectra in the bulk and in the 2L-$NbSe_2$ in Fig. 4.10(c) and (d), we notice a striking resemblance on the symmetry of the most intense modes, especially at high energy. Notably in the 2L system, in addition to the expected 3 modes of the bulk 2H-$NbSe_2$, namely one $E_{(2)g}$ interlayer mode at $\sim$30 cm^{-1}, one A_{1g} and one $E_{(2)g}$ mode at $\sim$ 250 cm^{-1}, Lin et al. [113] report one additional mode due to the few-layer structures, namely an A_{1g} mode at high energy 310 cm^{-1}. A mode at $\sim$ 155 cm^{-1} is possibly measured by Lin et al., but would require some confirmation. Importantly, these modes, even if measured at low temperature, are not due to the CDW ordering. As shown Fig. 4.10 (d), the energy and symmetry of the modes are well reproduced by our calculations for both systems, with a general tendency to underestimate their energy compared to the experimental results. As a straightforward interpretation of the spectra, we then tentatively assigned the most intense modes in the misfit to the modes of the same symmetry in the 2 layer structure. As shown Table 4.1, there is a good correspondence with 4 modes, in terms of energy and symmetry.

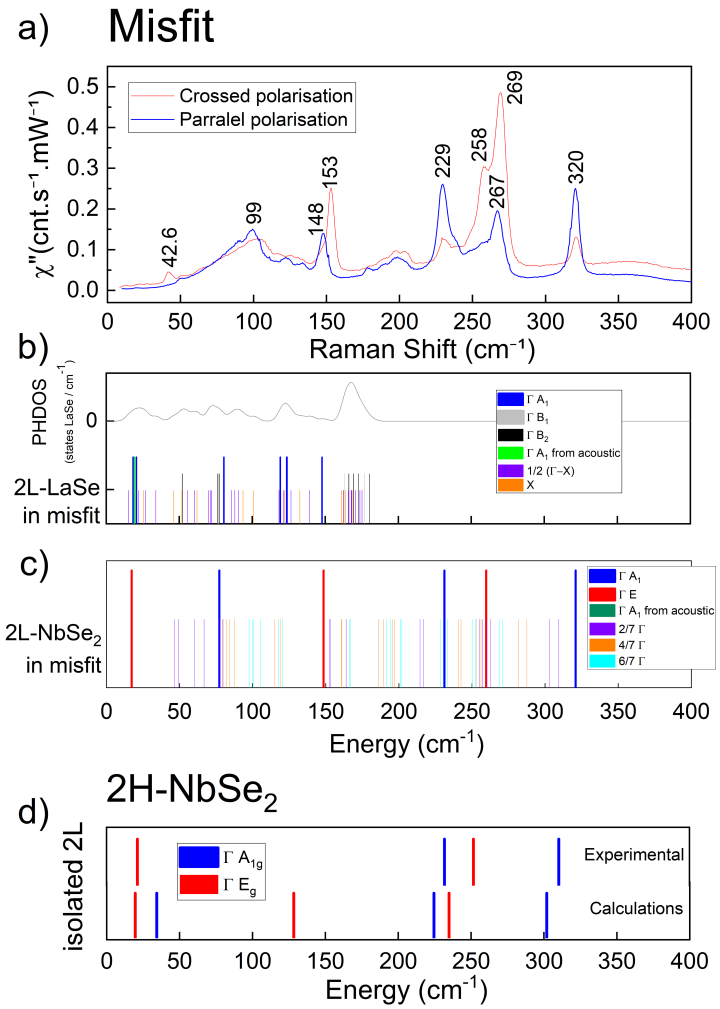

Figure 4.11: a) Raman spectra of $(LaSe)_{1.14}(NbSe_2)_2$ at 8 K in crossed and parallel polarizations in the (ab)-plane. b) and c) Theoretical calculations of Raman active modes of $(LaSe)_{1.14}(NbSe_2)_2$ obtained from those of the two subsystems, namely LaSe (panel b)) and $NbSe_2$ (panel c)), electron doped by means of the FET setup. The original modes from Γ of the 1×1 cell (long bars) and their subsequent BZ folding (short bars) modes are indicated (Cf. text). Original modes from Γ of the 1×1 cell are classified by symmetries. The phonon density of states of LaSe is shown in the upper part of panel b). d) Comparison between experimental [113] and theoretical zone center modes of isolated 2L-$NbSe_2$. Here, the $NbSe_2$ lattice parameter is the one in the misfit, namely a=3.437 Å.

In order to further corroborate our analysis and perform a full assignment of the modes, we consider here the two subunits of the compounds, namely LaSe and $NbSe_2$, as well as their interplay.
As the space group of the bulk misfit compound is P_1, all vibrational modes are Raman active. Thus, in the absence of a charge density wave instability, besides the zone center modes related to the LaSe and $NbSe_2$ subunit cells, one expects (i) $NbSe_2$ modes at in-plane phonon momenta that are not at zone center in the $NbSe_2$ bilayer Brillouin zone but are backfolded at zone center in the misfit Brillouin zone due to the 7×1 $NbSe_2$ periodicity occurring in $(LaSe)_{1.14}(NbSe_2)_2$, (ii) LaSe modes at in-plane phonon momenta that are not at zone center in the LaSe bilayer Brillouin zone but are backfolded at zone center in the misfit Brillouin zone due to the the 4×1 LaSe periodicity occurring in $(LaSe)_{1.14}(NbSe_2)_2$, (iii) modes arising from the presence of two inequivalent $(LaSe)_{1.14}(NbSe_2)_2$ units along the $c-$axis of the misfit unit cell (see Fig. 4.8) and, finally, (iv) modes that cannot be interpreted as pure LaSe or $NbSe_2$ modes.
As we will see later from phonon density of states (PHDOS) calculations of the whole misfit, practically all modes can be interpreted as modes of the two separated subunits. Thus, the occurrence of phonon modes that are mixed modes of the LaSe and $NbSe_2$ subunits can be excluded and point (iv) can be neglected. The splitting of phonon frequencies due to the presence of two inequivalent $(LaSe)_{1.14}(NbSe_2)_2$ units along the c-axis, i.e. point (iii), is also expected to be negligible as the $(LaSe)_{1.14}(NbSe_2)_2$ units are weakly interacting along the c-axis. It then follows that an attempt of interpreting the Raman response in terms of the backfolded modes of the $NbSe_2$ and LaSe subunits should lead to a clear understanding of the Raman spectra. Thus, we proceed to a more detailed analysis based on the Raman activity of the isolated and charged LaSe and $NbSe_2$ bilayers.
The LaSe rock salt subunit (#35, C_{2v} point group), has 24 Γ-point frequencies:

$$\Gamma_{\mathrm{LaSe}} = 8A_1 + 8B_1 + 8B_2. \tag{4.19}$$

From symmetry, we expect B_1 and B_2 modes being Raman active, since there is no inversion center. Even so, B_1 and B_2 modes are not expected to be measured in the configuration of measurement (with Poynting vector along c axis). On the contrary, the 8 A_1 modes are Raman active and mainly in the parallel configuration since they have a $(a-b)^2$ response in crossed polarization leading to small intensities. To summarize, the only modes that can be identified in parallel polarization, expected from the pure rocksalt subsystem, have A_1 symmetry.
For the $NbSe_2$ bilayer having $P\bar{3}m1$ space group (#164, D^3_{3d} point group), the behaviour of the modes is the following. We have 18 Γ-point frequencies as:

$$\Gamma_{\mathrm{NbSe_2}} = 3A_{1g} + 3E_g + 3A_{2u} + 3E_u. \tag{4.20}$$

The 3 completely symmetric A_{1g} modes are all Raman active only in parallel polarization. The 3 double degenerate E_g modes can be detected in both crossed and parallel polarizations. Finally, the A_{2u} and E_u are not Raman active. The

Intense Modes of $(LaSe)_{1.14}(NbSe_2)_2$ (in cm^{-1})	Raman activity $\perp$ or $\parallel$	Experimental modes in 2L $NbSe_2$	Calculated modes energy/symmetry from 2L-$NbSe_2$ at Γ	Calculated modes from splitted E_g in misfit	Calculated modes energy/symmetry from LaSe at Γ
42.6	$\perp$	$21/E_g$	$17.3/E_g$		
99.0	$\parallel$		$77.2/A_{1g}$		or $120.1/A_1$
148	$\parallel$				$148.9/A_1$
153	$\perp$	154 [a]	$148.5/E_g$		
229	$\parallel$	$232/A_{1g}$	$231.2/A_{1g}$		
258	$\perp$	$251.5/E_g$	$259.7/E_g$	$251.5/E_g$	
267	$\parallel$		X		X
269	$\perp$			$258.7/E_g$	
320	$\parallel$	$310.5/A_{1g}$	$320.9/A_{1g}$		

[a] Xi Xiaoxiang, private communication: This mode at 154 cm^{-1} may require experimental confirmation.

Table 4.1: Intense Raman active modes measured in $(LaSe)_{1.14}(NbSe_2)_2$ at 8 K with polarizations in the (ab) plane. The labels $\perp$ and $\parallel$ stand for crossed and parallel polarizations, respectively. The 3^{rd} column reports the experimental data in an isolated 2L-$NbSe_2$ [113]. Calculated phonon modes in the misfit structure originating from the Γ point of the unfolded Brillouin Zone and from subunits of $NbSe_2$ and LaSe in the 4^{th} and 6^{th} columns, respectively. In the 5^{th} column, the splitted E_g modes of the 8/4 misfit cell which correspond to the former E_g of $NbSe_2$ subunit (in blue). The label X marks the single intense mode that we could not assign from the two subunits (Cf. text).

symmetry of the Γ modes, as well as their activity in different polarization configurations, are reported in Tab. 4.1, in the 4^{th} and 6^{th} column.

In the table, we assign the calculated Γ frequencies to the most intense mode in the Raman spectra. As it can be seen, only one of the most intense modes can be ascribed to LaSe. A second one at 99 cm^{-1} could be either assigned to LaSe or $NbSe_2$ since both subunits present a parallel-active mode in this range of energy. The other peaks are all derived from the 2L-$NbSe_2$ subsystem. The physics of the Raman spectra at 8 K reveals that the lattice dynamics of $(LaSe)_{1.14}(NbSe_2)_2$ can be described in terms of that of its individual constituents.

To strengthen this statement, we can look at the PHDOS calculation on the $8/4 = 2/1$ periodic approximant of the full misfit is shown in Fig. 4.12. The results are compared in Fig. 4.12 with the phonon density of states of the two separated subunits as well as with their sum in the presence of a field effect charging mimicking the charge transfer among the LaSe and $NbSe_2$ subunits. As depicted in Fig. 4.12, almost all features in the misfit PHDOS are fairly well explained in terms of the sum of the PHDOS of the two (field-effect charged) separated subunits. The only feature present in the misfit PHDOS, but not in the PHDOS of the two subunits, is a peak at ≈ 150 cm^{-1}. This peak is at slightly higher energies $\approx 165 - 170$ cm^{-1} in the LaSe subunit. The difference is due to the strain applied to the LaSe subunit inside the misfit to obtain the 2/1 periodic approximant (14% strain), while the field-effect transistor (FET) charged LaSe bilayer is unstrained and has the same lattice parameters as in the bulk misfit. Overall, we can state that the vibrational properties of the $(LaSe)_{1.14}(NbSe_2)_2$ are entirely determined by those of the two separated subunits with an appropriate amount of charging.

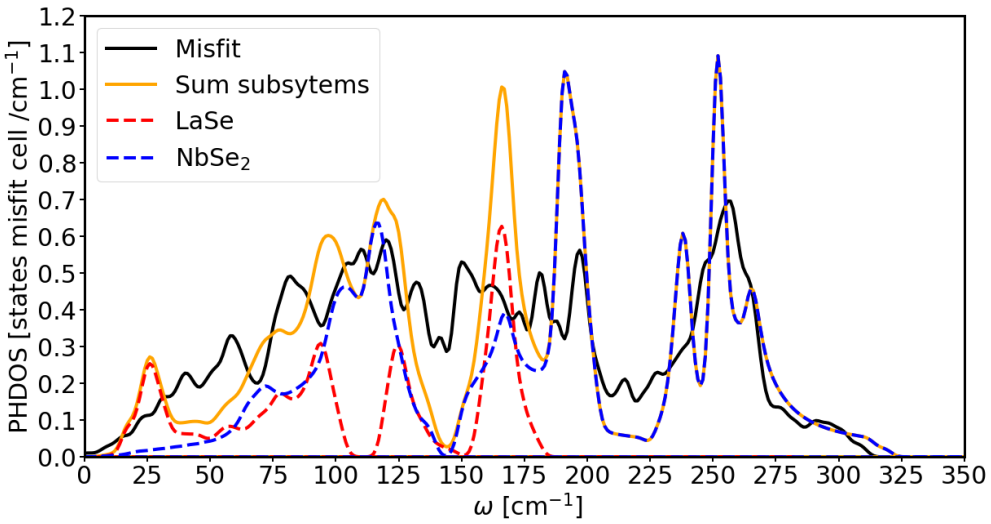

Figure 4.12: Phonon density of states (PHDOS) per misfit formula unit of bulk $(LaSe)_{1.14}(NbSe_2)_2$ (black solid line). Comparison with the PHDOS of the individual subsystems: (red dashed line) LaSe subunit doped of 1.2 electrons per unit cell in the FET setup, (blue dashed line) $NbSe_2$ bilayer doped of 0.6 electrons per Nb atom in the FET setup, respectively, and with their sum (orange solid line).

From Fig. 4.12 it is also clear that, due to the heavy La mass, the phonon modes of the RS subunit are mostly concentrated in the low energy part of the spectrum (below 175 cm^{-1}), while those of the $NbSe_2$ bilayer occurs at all energies.
As summarized in Tab. 4.1 only two of the most intense Raman peak, namely the one at 269 cm^{-1} in crossed polarization and 267 cm^{-1} in parallel polarization, are not directly deducible from 2L-$NbSe_2$'s modes. We are able to assign the highly intense mode at 269 cm^{-1} in crossed polarization to the former double-degenerate high energy E_g mode of 2L-$NbSe_2$ at 259 cm^{-1} that splits in the misfit.
In order to perform this assignment we consider the full misfit calculation employing the $8/4 = 2/1$ periodic approximant (4.12), where the two distinct peaks can be clearly identified in this energy range. In order to check if these peaks originate from the E_g mode of the isolated FET-doped 2L-$NbSe_2$, we project all the full misfit phonon eigenvectors onto the ones corresponding to the doubly degenerate E_g mode at 259 cm^{-1} in the isoated FET-doped 2L-$NbSe_2$. We find that the highest E_g character is present in two modes at 251.5 and 258.7 cm^{-1} (see Tab. 4.1, 5th column).
Note that we also evaluated the effect of the slight non-hexagonality of 2L-$NbSe_2$ within the misfit [6], which is just a very small $\sim$ 1 cm^{-1} splitting that cannot account for our experimental results (see Appendix A.4).
Finally, only the intense mode at 267 cm^{-1} in parallel polarization is not captured by our DFT calculations. This one is most probably a hybrid mode of the system as a whole, caused by the bonding between the TMD and the RS subunits that we neglected in our calculations.
In conclusion, our work [106] provides a complete description of the vibrational properties of the misfit layer compound $(LaSe)_{1.14}(NbSe_2)_2$. We identify all the

main phonon modes and their symmetry and demonstrate that, similarly to what happens for the electronic properties, the vibrational properties can be understood in terms of the two subunits (LaSe and $NbSe_2$ bilayers) in a field effect configuration, where the charging of the gates is directly determined by the charge transfer in the misfit structure.
Notably, the lattice dynamics of the TMD has a strong 2D character in this 3D misfit structure. Finally, our theoretical understanding is supported by the Raman results, particularly by the charge density wave collapse in the misfit due to the large charge transfer from the LaSe subunit. Our work is relevant beyond the case of $(LaSe)_{1.14}(NbSe_2)_2$. Indeed, it sets a reference scheme for the interpretation of vibrational properties of misfit layer compounds that can be extended to other compounds of the same family.

4.5 Summary

In Chapter 4, we explain how to model misfit layer compounds as a collection of field effect transistors.
First of all, we discuss the field effect transistor setup (FET setup) as developed in Ref. [100,101] for the study of gated two-dimensional materials. We then detail how, within the FET setup, the full misfit can be assimilated to several field-effect transistors stacked periodically along the z-axis.
We present our results on the misfit layer compound $(LaSe)_{1.27}(SnSe_2)_2$, showing that FET modeling is a reliable tool for tackling the electronic structure and the geometrical behavior of misfit layer compounds [81].
Most important, we show how to design a misfit superconductor starting from its constituents. In particular, we show that non-superconducting pristine RS and TMD compounds can lead to a misfit superconductor via charge transfer control (emergent superconductivity) [81].
Finally, we demonstrate how to predict the vibrational properties of misfit layer compounds based on that of their subunits, namely the rocksalts and the TMDs. We provide a complete experimental and theoretical description of the lattice dynamics of the misfit compound $(LaSe)_{1.14}(NbSe_2)_2$ [106].
We show that the vibrational properties are obtained from those of the two subunits, namely the LaSe unit and the $NbSe_2$ bilayer, in the presence of a suitable field-effect doping. In particular, we demonstrate the $NbSe_2$'s charge density wave collapse in the misfit due to the large charge transfer from the LaSe subunit.
Our work shows that the lattice dynamics of the TMD have a strong 2D character in this 3D misfit structure, setting a reference scheme beyond this particular case for the interpretation of vibrational and structural properties of misfit layer compounds.

Chapter 5

Superconductivity in misfit layer compounds

5.1 First principles calculations of superconducting properties

We briefly discuss the recipe for ab initio superconductivity calculations before applying it to misfit layer compounds. We need to calculate three main ingredients: the electronic structure, the vibrational properties, and the electron-phonon coupling of the system.
First and foremost, we need to find the ground state (GS) of our system that can be obtained by means of standard DFT calculations. By solving the Kohn-Sham equations, we can extract the GS eigenvalues $\epsilon_{\mathbf{k}n}$ and eigenstates $|\mathbf{k}n\rangle$ of the system, where n is the band index and $\mathbf{k}$ is the wavevector. The value of the Fermi energy ϵ_F is also known from the electronic structure of the system.
Second, we need to have access to the phonon frequencies $\omega_{\mathbf{q},\nu}$ and phonon eigenvectors $e_{\mathbf{q},\nu}$ for each mode ν and phonon momentum $\mathbf{q}$. In the harmonic approximation, we can define the force constant matrix as the second derivative of the Born-Oppenheimer energy surface E with respect to the phonon displacement $u_{LA\alpha}$:

$$C_{A\alpha,B\beta}(\mathbf{R}_L,\mathbf{R}_M)=\frac{\partial^2 E}{\partial u_{LA\alpha}\partial u_{MB\beta}} \tag{5.1}$$

where A,B labels the atomic positions within a cell, $\alpha,\beta=x,y,z$ are the labels for Cartesian coordinates of the ions and $\mathbf{R}_L,\mathbf{R}_M$ are the positions of the L-th M-th unit cells. In a crystal, discrete translational invariance grantees that $C_{A\alpha,B\beta}(\mathbf{R}_L,\mathbf{R}_M)=C_{A\alpha,B\beta}(\mathbf{R}_L-\mathbf{R}_M)$. The Fourier transform of the force constant matrix is defined as $C_{A\alpha,B\beta}(\mathbf{q})=\sum_L C_{A\alpha,B\beta}(\mathbf{R}_L)e^{-i\mathbf{q}\cdot\mathbf{R}_L}$.
We can thus define the dynamical matrix as:

$$D_{A\alpha,B\beta}(\mathbf{R}_L-\mathbf{R}_M)=\frac{C_{A\alpha,B\beta}(\mathbf{R}_L-\mathbf{R}_M)}{\sqrt{M_A M_B}}. \tag{5.2}$$

where M_A, M_B are the masses of atoms A and B. Finally, diagonalizing the dynamical matrix in reciprocal space $D_{A\alpha,B\beta}(\mathbf{q}) = C_{A\alpha,B\beta}(\mathbf{q})/\sqrt{M_A M_B}$, we can obtain its eigenvalues ($\omega_{\mathbf{q},\nu}$) and eigenvectors ($e_{\mathbf{q},\nu}$):

$$det|D_{A\alpha,B\beta}(\mathbf{q}) - \omega^2_{\mathbf{q},\nu}\delta_{A\alpha,B\beta}| = 0 \tag{5.3}$$

for each mode ν and momentum $\mathbf{q}$, where phonon eigenvectors are:

$$e_{\mathbf{q},\nu} = \sum_{A\alpha} M_A \sqrt{2\omega_{\mathbf{q},\nu}} e^{A\alpha}_{\mathbf{q},\nu} u_{\mathbf{q}A\alpha}, \tag{5.4}$$

where $e^{A\alpha}_{\mathbf{q},\nu}$ are the cartesian components of the phonon eigenvectors. This can be done by using a q-points discrete phonon momentum grid in the DFPT framework [105, 127].
Third, we need to calculate the electron-phonon coupling. The linear electron-phonon matrix elements in a DFPT framework represent the scattering of an electron from a state with momentum $\mathbf{k}$ to a state with momentum $\mathbf{k}+\mathbf{q}$ through absorption of a phonon of momentum $\mathbf{q}$ and frequency $\omega_{\mathbf{q},\nu}$ and describe the interaction strength between electrons and phonons. They are defined as:

$$g^{\nu}_{\mathbf{k}n,\mathbf{k}+\mathbf{q}m} = \langle \mathbf{k}n| \frac{\delta V_{KS}}{\delta e_{\mathbf{q},\nu}} |\mathbf{k}+\mathbf{q}m\rangle \tag{5.5}$$

where $\delta V_{KS}/\delta e_{\mathbf{q},\nu}$ is the derivative of the Kohn-Sham potential V_{KS} with respect to the phonon eigenvector $e_{\mathbf{q},\nu}$ that can be calculated in the DFPT framework [128]. The Fermi "golden rule" gives a formula for the electron-phonon contribution to the phonon linewidth (FWHM) at lowest order:

$$\gamma_{\mathbf{q},\nu} = \frac{4\pi}{N_k} \sum_{\mathbf{k},n,m} |g^{\nu}_{\mathbf{k}n,\mathbf{k}+\mathbf{q}m}|^2 (f_{\mathbf{k}n} - f_{\mathbf{k}+\mathbf{q}m}) \delta(\epsilon_{\mathbf{k}+\mathbf{q}m} - \epsilon_{\mathbf{k}n} - \omega_{\mathbf{q}\nu}) \tag{5.6}$$

where $f_{\mathbf{k}n}$ is the Fermi occupation of the band $\epsilon_{\mathbf{k}n}$ and N_k is an electron momentum k-point mesh in the Brillouin zone. At temperatures such that $k_B T >> \omega_{\mathbf{q},\nu}$ or in the case of a temperature independent $\gamma_{\mathbf{q},\nu}$, by using the δ-function condition $\delta(\epsilon_{\mathbf{k}+\mathbf{q}m} - \epsilon_{\mathbf{k}n} - \omega_{\mathbf{q}\nu})$ in Eq. 5.6 one can substitute in Eq. 5.6,

$$\omega_{\mathbf{q}\nu} \frac{f_{\mathbf{k}+\mathbf{q}m} - f_{\mathbf{k}n}}{\omega_{\mathbf{q}\nu}} \longrightarrow \omega_{\mathbf{q}\nu} \left.\frac{\partial f}{\partial \epsilon}\right|_{\epsilon=\epsilon_{\mathbf{k}n}}. \tag{5.7}$$

If the temperature dependence in equation 5.6 is weak, then the Fermi functions can be considered as step functions. In actual calculations, it is also customary to neglect the frequency dependence in the δ function in Eq. 5.6 so that:

$$\gamma_{\mathbf{q},\nu} = \frac{4\pi\omega_{\mathbf{q}\nu}}{N_k} \sum_{\mathbf{k},n,m} |g^{\nu}_{\mathbf{k}n,\mathbf{k}+\mathbf{q}m}|^2 \delta(\epsilon_{\mathbf{k}n} - \epsilon_F) \delta(\epsilon_{\mathbf{k}+\mathbf{q}m} - \epsilon_F). \tag{5.8}$$

This approximation has been discussed in details in Ref. [129–131].
The mode-resolved electron-phonon coupling constant $\lambda_{\mathbf{q}\nu}$ is related to the phonon linewidth from the Allen formula [129, 130]:

$$\lambda_{\mathbf{q}\nu} = \frac{\gamma_{\mathbf{q}\nu}}{2\pi N(\epsilon_F)\omega^2_{\mathbf{q}\nu}} \tag{5.9}$$

where $\gamma_{\mathbf{q}\nu}$ is obtained from Eq. 5.8 and $N(\epsilon_F)$ is the density of states at the Fermi level. The knowledge of these quantities allows the evaluation of the average electron-phonon coupling constant λ and of the Eliashberg spectral function $\alpha^2F(\omega)$ via the relations:

$$\alpha^2F(\omega) = \frac{1}{2N_q}\sum_{\mathbf{q}\nu}\lambda_{\mathbf{q}\nu}\omega_{\mathbf{q}\nu}\delta(\omega-\omega_{\mathbf{q}\nu}), \tag{5.10}$$

$$\lambda = \frac{1}{N_q}\sum_{\mathbf{q}\nu}\lambda_{\mathbf{q}\nu}, \tag{5.11}$$

where N_q is the number of phonon-momentum point of the grid on which $\lambda_{\mathbf{q}\nu}$ is calculated. Then, it is possible to calculate the superconducting critical temperature by the Allen and Dynes semi-empirical formula [132]:

$$T_c = \frac{\langle\omega\rangle_{log}}{1.2}\exp\left[-\frac{1.04(1+\lambda)}{\lambda-\mu^*(1+0.62\lambda)}\right]. \tag{5.12}$$

Eq. 5.12 gives critical temperature T_c as function of electron-phonon coupling parameter λ. The parameter μ^* is the effective Coulomb pseudopotential and represents the screened Coulomb repulsion between electrons in a superconductor. The value of μ^* typically ranges from 0.10 to 0.15 for most conventional superconductors. The logarithmic average of the phonon frequencies $\langle\omega\rangle_{log}$ to be used in the Allen and Dynes formula is:

$$\langle\omega\rangle_{\log} = \exp[\frac{2}{\lambda}\int_0^{+\infty}\alpha^2F(\omega)\log(\omega)/\omega\, d\omega]. \tag{5.13}$$

To address the role of the different vibrations in determining the electron-phonon coupling it is possible to decompose the electron-phonon coupling into selected atomic vibrations, using the relation [133, 134]:

$$\lambda = \sum_{i,j}\Lambda_{i,j} = \sum_{A,B}\left[\sum_{\alpha,\beta}\frac{1}{N_q}\sum_{\mathbf{q}}[G_{\mathbf{q}}]_{A\alpha,B\beta}[{C_{\mathbf{q}}}^{-1}]_{B\beta,A\alpha}\right] \tag{5.14}$$

where A,α (B,β) indicates the displacement of the $A^{\text{th}}(B^{th})$ atom in $\alpha(\beta)$ Cartesian direction, $[G_q]_{A\alpha,B\beta} = \sum_{\mathbf{k},n,m} 4\tilde{g}^*_{A\alpha}\tilde{g}_{B\beta}\delta(\epsilon_{\mathbf{k}n})\delta(\epsilon_{\mathbf{k}+\mathbf{q}m})/[N(\epsilon_F)N_k]$, and $\tilde{g}_{A\alpha} = \langle\mathbf{k}n|\delta V_{KS}/\delta u_{\mathbf{q}A\alpha}|\mathbf{k}+\mathbf{q}m\rangle/\sqrt{2}$, $u_{\mathbf{q}A\alpha}$ being the Fourier transform of the α component of the phonon displacement of the atom A in the unit cell. The $C_{\mathbf{q}}$ matrix is the Fourier transform of the force constant matrix.
We can also write $\alpha^2F(\omega)$ as:

$$\alpha^2F(\omega) = \sum_{A,B}\alpha^2_{A,B}F(\omega) = \sum_{A\alpha,B\beta}\left[\frac{1}{N_{\mathbf{q}}}\sum_{\mathbf{q}}\frac{[G_{\mathbf{q}}]_{A\alpha,B\beta}[L_{\mathbf{q}}]_{B\beta,A\alpha}}{2\sqrt{M_AM_B}}\right], \tag{5.15}$$

where

$$[L_{\mathbf{q}}]_{B\beta,A\alpha} = \sum_{\rho} e^{A\alpha}_{\mathbf{q}\rho}\frac{\delta(\omega-\omega_{\mathbf{q},\rho})}{\omega_{\mathbf{q},\rho}}(e^{B\beta}_{\mathbf{q}\rho})^*, \tag{5.16}$$

TMD	a_1 [Å]	b_1 [Å]	RS	a_2 [Å]	b_2 [Å]
$NbSe_2$	3.437	6.0191	LaSe	6.875 (14.6% tensile strain)	6.0191
$NbSe_2$	3.437	6.0148	BiSe	6.874 (14.1% tensile strain)	6.0148
$NbSe_2$	3.44	5.99	PbSe	6.879 (14.1% tensile strain)	5.99
$NbSe_2$	3.44	5.92	SnSe	6.879 (16.1% tensile strain)	5.92

Table 5.1: In-plane lattice parameters of each subsystem: a_1 and b_1 for the TMDs (cyan) and a_2 and b_2 for rocksalts (red) used to build misfit supercells. The amount of tensile strain applied to each rocksalt is reported.

where $e^{A\alpha}_{\mathbf{q}\rho}$ are the components of $\mathbf{q}\rho$ phonon eigenvector normalized on the unit cell.
In conclusion, we have now all of the elements necessary to calculate the superconducting properties of misfit layer compounds. In Chapters 3 and 4, we discussed how to calculate the electronic structure and vibrational properties of MLCs. In the next part, we will demonstrate how to calculate electron-phonon coupling with practical examples of MLCs.

5.2 Superconductivity of bulk $(RQ)_{1+\delta}(NbSe_2)$ misfit series

After achieving complete knowledge of the charge transfer in MLCs, and showing how to characterize their electronic and vibrational properties, we present our ab initio calculations of superconducting properties of misfit layer compounds. As detailed in Chapter 1, misfit layer compounds exhibit a range of emergent properties that arise from the interaction between the individual constituents. Among them, superconductivity is experimentally measured in different compounds (see discussion in Chapter 1, Fig. 1.13). Here we present our first principle calculations of superconducting properties of the bulk $(RQ)_{1+\delta}(NbSe_2)$ misfit series.
The specific choice of this family of misfits stems from the fact that superconductivity has previously been experimentally measured in almost all of the materials in the series.

5.2.1 Modeling bulk $(RQ)_{1+\delta}(NbSe_2)$

We focus here on a particular misfit layer compound family. Misfits of this type are composed of single layers of $NbSe_2$ alternated with different rocksalt units as building blocks and sharing comparable mismatching ratios very close to 7/4 (these compounds belong to the ninth column in Fig. 1.6 in Chapter 2). We specifically consider the $(RQ)_{1+\delta}(NbSe_2)$ misfit series, where we fix the TMD as $NbSe_2$, and we change the rocksalt with RQ= LaSe, BiSe, PbSe, and SnSe.
In Chapter 4, we discuss how to derive the vibrational properties of bulk misfits. We pointed out that the periodic approximant of the misfit cell with mismatch

Mismatch ratio	Misfit	a [Å]	b [Å]	c [Å]
2/1 (8/4)	$(LaSe)_{1.15}(NbSe_2)$	6.875	6.0191	11.5
2/1 (8/4)	$(BiSe)_{1.14}(NbSe_2)$	6.874	6.0148	11.5
2/1 (8/4)	$(PbSe)_{1.14}(NbSe_2)$	6.879	5.99	11.5
2/1 (8/4)	$(SnSe)_{1.16}(NbSe_2)$	6.879	5.92	11.5

Table 5.2: Mismatch ratios and lattice parameters, summarized for each misfit supercell under consideration.

ratio 7/4 contains too many atoms for this task.
In this chapter, we try to calculate the electron-phonon coupling of bulk misfits. This type of computation would need even more extensive linear response computations on denser q-point grids.
In order to reduce the computational effort, we approximate the 7/4 mismatch ratio by 8/4, corresponding to a 2/1 ratio. This is done by applying a certain percentage of tensile strain to the rocksalt subunits, increasing their lattice parameter along the mismatch axis. On the contrary, the $NbSe_2$ in-plane parameter is left unchanged, kept as in the misfit. As we will see in the following, this choice weakly affects the charge transfer from the rocksalt to the TMD. Furthermore, because superconductivity originates mostly from $NbSe_2$, we intend to maintain the stability of this subunit. In Fig. 5.1, an example of the 2/1 commensurate approximant supercell of bulk misfit is shown.
By examining the $(RQ)_{1+\delta}(NbSe_2)$ misfit series, we have access to a vast range of doping of $NbSe_2$. Thus, we can explore how the effect of doping inside the misfit structure modifies the superconducting properties of $NbSe_2$.
We now briefly illustrate how the 2/1 misfit approximant of bulk misfit is built. For all the considered structures, we first optimize each subsystem separately. Then, we assemble the misfit bulks by stacking the subsystems in a periodic arrangement of TMD monolayers and rocksalt bilayers along the c-axis. Finally, we perform geometrical optimization of the misfit crystal.
We adopt the convention of using the value of δ as obtained from the lattice parameters a_1 and a_2 of the pristine TMD and RS respectively, before assembling them in a MLC structure, as reported in the tables in Fig. 1.4 and 1.5 in Chapter 1. In order to build commensurate misfit supercells, from these analysis we extract the approximant that will be used in the calculations (see Fig. 1.6).
For the $NbSe_2$ part, we use orthohorombic cells with the transition metal atom in trigonal coordination. We optimize the in-plane lattice parameters to match that of the chosen rocksalt for each corresponding mismatch ratio. Then, starting from these cells, we build supercells according to the misfit proportions, namely a 2×1 cell of monolayer $NbSe_2$.
For the rocksalt part, we use centered orthohorombic cells and optimize the in-plane lattice parameters in order to obtain commensurability with the considered TMD according to the 2/1 mismatch ratio. Then, starting from these cells, we build supercells according to the misfit proportions, namely a 1×1 of LaSe, BiSe,

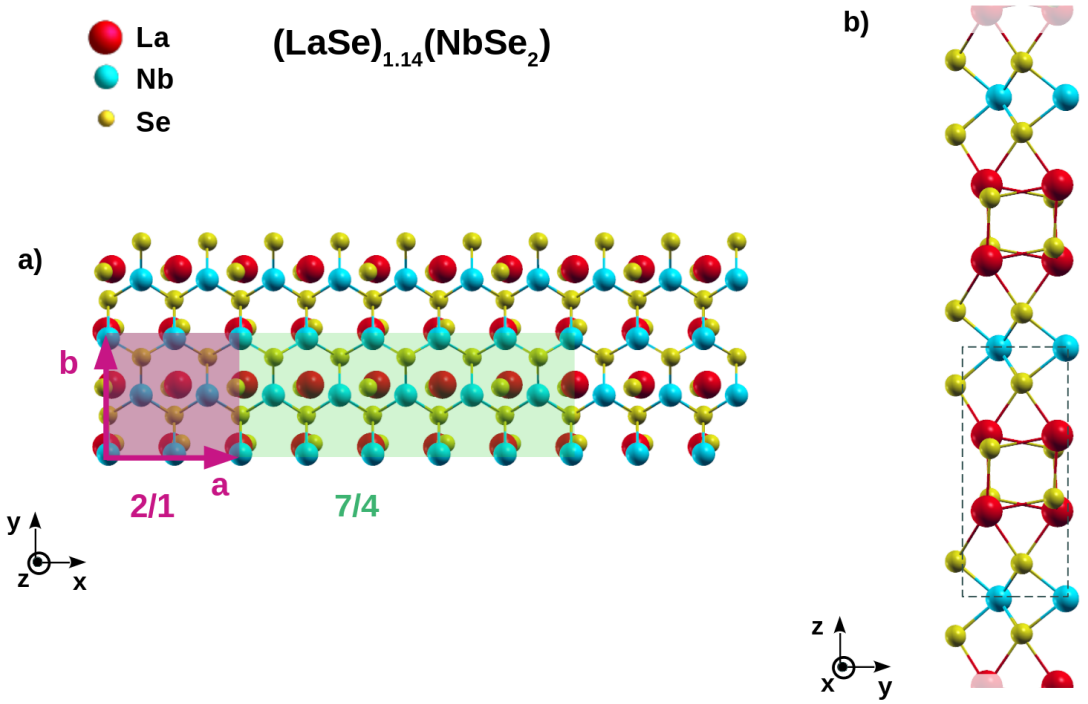

Figure 5.1: An example of the 2/1 commensurate approximant supercell of misfit bulk. a) The in-plane cell of the misfit layer compound $LaSe_{1.15}NbSe_2$. The shaded green region corresponds to the 7/4 commensurate approximant of the misfit cell, while shaded violet region corresponds to the reduced 2/1 cell. b) Side view of the $LaSe_{1.15}NbSe_2$ crystal. The stacking sequence is depicted, with black dashed lines corresponding to the misfit unit cell.

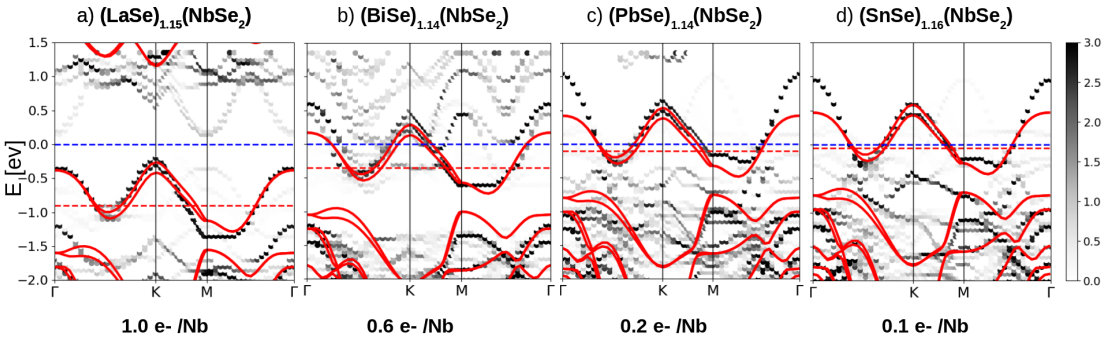

Figure 5.2: Band unfolding onto the $NbSe_2$ single layer Brillouin zone for the $NbSe_2$ misfit series with different rocksalt Q-layers having comparable mismatching ratio close to 2/1. (a) $(LaSe)_{1.15}(NbSe_2)$, (b) $(BiSe)_{1.14}(NbSe_2)$, (c) $(PbSe)_{1.14}(NbSe_2)$, (d) $(SnSe)_{1.16}(NbSe_2)$. The band structure for the isolated single layer $NbSe_2$ (red line) is superimposed and aligned to the Nb d-band in the misfit. The blue dashed line corresponds to the Fermi level E_F of the misfit compound, while the red one to the Fermi level of the isolated $NbSe_2$ layer.

PbSe and SnSe to match with each $NbSe_2$ cell.
Tab. 5.1 summarizes the lattice parameters for each individual subunit. In this process of refinement, lattice parameters of the rocksalts in the mismatch direction are increased in order to build a commensurate misfit structure. The amount of tensile strain applied to each rocksalt is detailed in the 5th column of Tab. 5.1. Finally, the common part is composed by stacking the TMD monolayer and rocksalt supercells. The resulting misfit crystal has an orthorhombic cell. Tab. 5.2 summarizes each examined misfit supercell, including its mismatch ratio, compound name, and lattice parameters.
Finally, we perform geometry optimization of each misfit supercell. The final misfit bulks have a P1 symmetry and includes 20 atoms in the cell (atomic positions are reported in the Tabs. A.5, A.6, A.7 and A.8 in Appendix A.5).

5.2.2 Electronic properties of bulk $(RQ)_{1+\delta}(NbSe_2)$ misfit series

We present here our band structure calculations of bulk misfit layer compounds $(RQ)_{1+\delta}(NbSe_2)$, with RQ= LaSe, BiSe, PbSe and SnSe. We unfold the band structure of the misfit supercell onto the primitive cell of the isolated $NbSe_2$ monolayer.
To carefully take into account the spin orbit coupling (SOC) of $NbSe_2$, which splits the two degenerate bands at the Fermi level, SOC is included in all the electronic structure calculations. The results of band unfolding are shown in Fig. 5.2.
As can be seen in Fig. 5.2, the $NbSe_2$ electronic structure in going from $(SnSe)_{1.14}(Nb_2)_2$ to $(LaSe)_{1.15}(Nb_2)_2$ is n-doped. The charge transfer induces a Fermi level up-shift, from 0.0 to 0.5 eV. The amount of charge transfer in e^-/Nb atoms is reported in Fig. 5.2. We can do a comparison with the $(RQ)_{1+\delta}(NbSe_2)_m$ series with m=2 presented in Chapter 3 (see Fig. 3.7). In the current example,

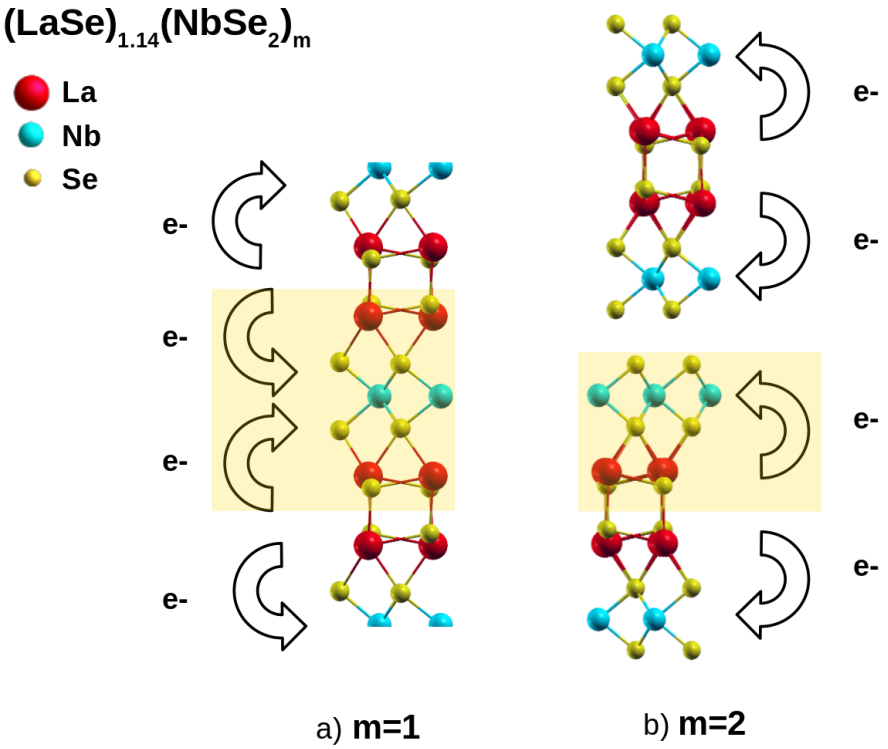

Figure 5.3: Sketch of misfit layer compound belonging to the family $(RQ)_{1+\delta}(NbSe_2)_m$. The example shows $(LaSe)_{1+\delta}(NbSe_2)_m$ misfit bulk with a) m=1 and b) m=2. The arrows indicate the electron (e^-) charge transfer from the rocksalt to the $NbSe_2$ single layers in both cases. Yellow shaded regions highlight the region of the charge transfer per $NbSe_2$ single layer.

with m=1, $NbSe_2$ is more doped by each individual rocksalt than in the previous case. This effect is related to the number of rocksalt atoms per $NbSe_2$ layer. As seen in Fig. 5.3, in cases with m=1, there is the equivalent of a whole rocksalt bilayer per $NbSe_2$ single layer, while in cases of m=2, each $NbSe_2$ single layer is bounded with just half of the rocksalt bilayer.
We note that as in the case with m=1, the behavior of the misfit $NbSe_2$ series is almost completely characterized by the work function differences, as expected from the analyses discussed in Chapter 2.
The metallic rocksalt compounds, namely LaSe and BiSe, transfer a large amount of electrons. In particular LaSe transfers an entire electron to $NbSe_2$. Instead, in the insulating compounds with PbSe and SnSe transfer less electrons.
We now comment on the shape of the Nb d-band at the Fermi level of monolayer $NbSe_2$ in each misfit of the series. This is modified due mainly two factors: the large doping and the strain applied to the rocksalt subunit to reduce the cell to the 2/1 commensurate approximant. However, this last effect does not hinder the calculated amount of charge transferred from the rocksalt to $NbSe_2$. To show that, we can take the compound with LaSe as an example. Fig. 5.4 shows the comparison of the unfolded band structure of $(LaSe)_{1.15}(NbSe_2)$ onto the $NbSe_2$ single layer BZ for the case of a) the 7/4 (taken from Ref. [135]) and b) 2/1 (this

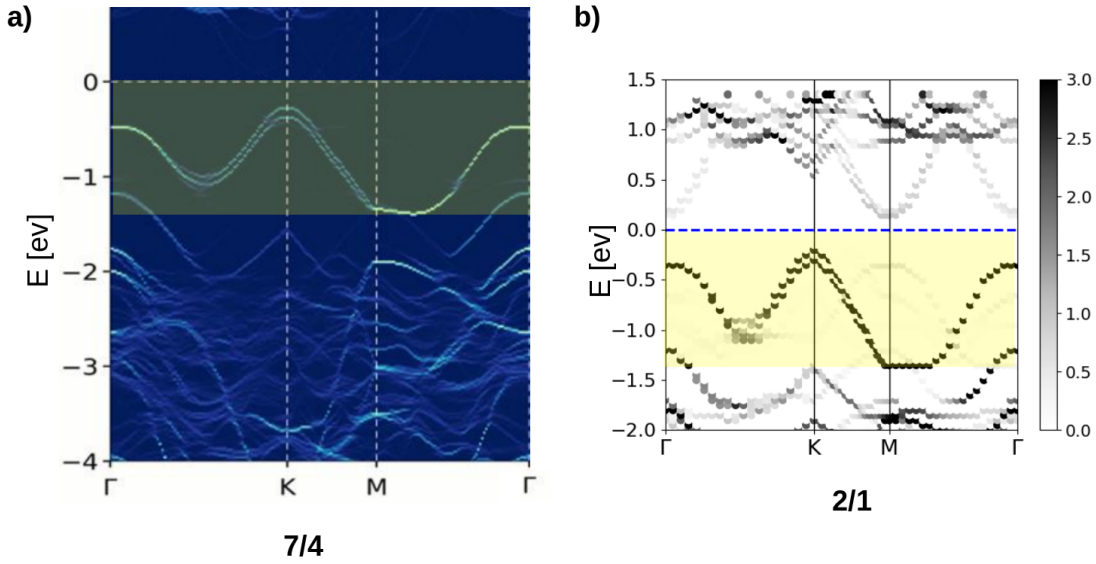

Figure 5.4: Band unfolding onto the $NbSe_2$ single layer Brillouin zone for the $(LaSe)_{1.15}(NbSe_2)$ compound. a) Image adapted from Ref. [135] showing the band unfolding of the 7/4 commensurate approximant of the misfit cell. b) Image from this work showing the band unfolding of the 2/1 commensurate approximant of the misfit cell. In both figures, the yellow-shaded area represents the energy range going from the misfit Fermi level to the bottom of the Nb d-band.

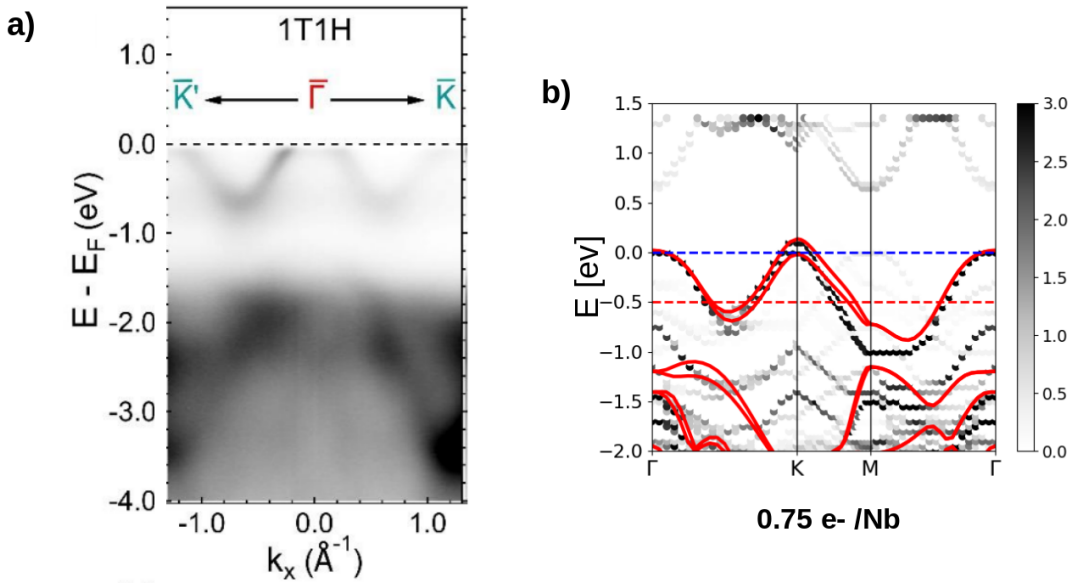

Figure 5.5: a) ARPES map of $(LaSe)_{1.15}(NbSe_2)$ adapted from Ref. [135]. The sample has 11.1% of La vacancies, corresponding to a charge transfer of 0.75 e^-/Nb atoms b) Band unfolding onto the $NbSe_2$ single layer Brillouin zone for the 2/1 commensurate approximant of the $(LaSe)_{1.15}(NbSe_2)$ cell (this work). To match the experimental value of La vacancies, the compound is rigidly doped.

Misfit	λ	λ_{NbSe_2}	λ_{RS}	ω_{log} [meV]	T_c [K]	T_c^{Exp} [K]
$(LaSe)_{1.15}(NbSe_2)$	0.34	0.23	0.11	16.86	0.0	1.23 [135]
$(BiSe)_{1.14}(NbSe_2)$	0.78	0.28	0.50	8.31	3.0	2.7 [58]
$(PbSe)_{1.14}(NbSe_2)$	0.89	0.57	0.32	10.66	5.2	5.6 [56]
$(SnSe)_{1.16}(NbSe_2)$	1.58	0.60	0.98	5.50	6.6	3.4 [57]

Table 5.3: Summary of the calculated superconducting properties of the $(RQ)_{1+\delta}(NbSe_2)$ misfit series.

work) commensurate approximant of the misfit cell. In this picture, the yellow shaded regions represent the energy region going from the misfit Fermi level to the bottom of the Nb d-band. As can be seen, these calculations give the same amount of charge transferred to the $NbSe_2$ single layer, corresponding to 1.0 e^-/Nb atoms. Thus, even if the 2/1 alters the geometry of the system, nothing changes in terms of the amount of charge transfer.
As the subunits experience mutual modulation during the relaxation of the whole misfit, strain in the rocksalt subunit affect the intralayer distances of $NbSe_2$. This is what clearly happens for the case of PbSe and SnSe, where the doping experienced by $NbSe_2$ is low, but the intralayer distances of $NbSe_2$ are compressed by $\sim$ 2% with respect to the experimental value of bulk $NbSe_2$ [88]. Because the d_z orbitals at Γ represent the majority of the niobium's d orbitals, reducing the intralayer lengths of the $NbSe_2$ monolayer causes the Nb d-bands to stretch at the Γ point. However, the amount of calculated charge transfer is recovered, being in agreement with experimental work on these compounds [56, 136].
Lastly, since we are interested in calculating the superconducting properties of the $(RQ)_{1+\delta}(NbSe_2)$ misfit series with the aim of comparing our result to the available experimental data, we have to correct the band structure of the compound containing LaSe. Indeed, since LaSe donates an entire electron to $NbSe_2$, the Fermi level up-shift exceeds the Nb d-bands, reaching a gap region, thus suppressing superconductivity. However, experimental ARPES from Ref. [135] shows that the Fermi level is still in the $NbSe_2$ band and Hall effect measurements show that carriers are hole like. This is explained by the fact that there are about 15% of La vacancies, as confirmed by precise measurements of the chemical compositions by X-ray diffusion; thus, this compound is superconducting thanks to the presence of La vacancies. In particular, the sample with 11.1% exhibits superconductivity with a critical temperature of 1.23 K. To match this experimental result, we p-doped the 2/1 commensurate approximant of the misfit cell of 12.5% La vacancies with a uniform background doping. This amount is comparable to the experimentally estimated value, as shown in Ref. [135]. In this way, within the compound, the $NbSe_2$ is n-doped of 0.75 e^-/Nb atoms that matches the experimental value of Ref. [135] (see Fig. 5.5).

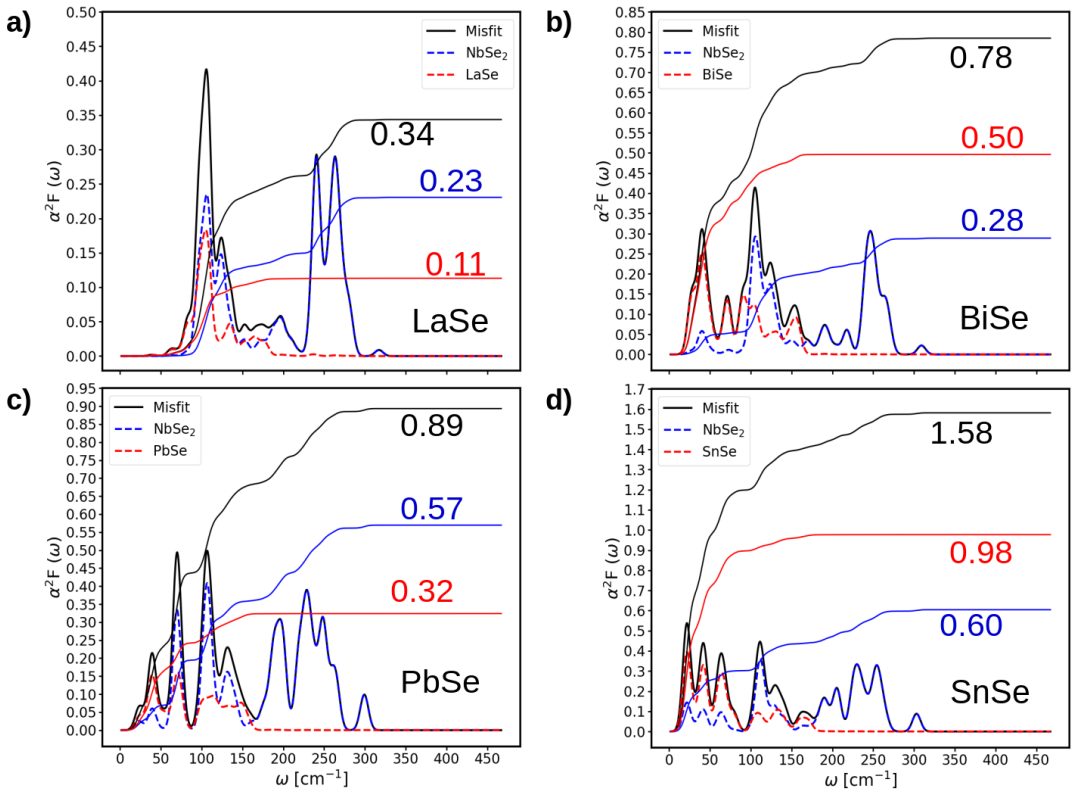

Figure 5.6: Superconducting properties of bulk $(RQ)_{1+\delta}(NbSe_2)$ misfit series. (a) $(LaSe)_{1.15}(NbSe_2)$, (b) $(BiSe)_{1.14}(NbSe_2)$, (c) $(PbSe)_{1.14}(NbSe_2)$, (d) $(SnSe)_{1.16}(NbSe_2)$. The total Eliashberg function $\alpha^2F(\omega)$ and the total average electron-phonon coupling λ are plotted in a black solid curve. The partial contribution to the $\alpha^2F(\omega)$ from each subsystem is also plotted (blue dashed line for $NbSe_2$ and red dashed line for each different rocksalt), together with their partial average electron-phonon coupling λ (blue solid line for $NbSe_2$ and red solid line for each different rocksalt).

5.2.3 Ab initio superconducting properties of bulk $(RQ)_{1+\delta}(NbSe_2)$ misfit series

After determining their structure and electronic properties, we finally provide our ab initio calculations of superconducting properties of bulk $(RQ)_{1+\delta}(NbSe_2)$ misfit series.

Last column of Tab. 5.3 provides a summary of experimental results for the critical temperatures of the superconducting transition of each compound in the $(RQ)_{1+\delta}(NbSe_2)$ misfit series.

As already mentioned, the calculation of vibrational properties and electron-phonon coupling for the complete MLC is a very computationally heavy task due to the large number of atoms in the 7/4 supercell. However, we are able to estimate the superconducting properties of the $(RQ)_{1+\delta}(NbSe_2)$ misfit series by using the 2/1 commensurate approximant.

We then calculate the electron-phonon coupling for each mode ν at the Γ point. Given the large amount of atoms, only the Γ point calculation was affordable, we will discuss the accuracy of this approach in the following. From these quantities we obtain the Eliashberg function $\alpha^2F(\omega)$ that is plotted in solid black curves in Fig. 5.6. Then, we obtained the average electron-phonon coupling λ for each of the considered system (black lines in Fig. 5.6). Detail of these calculations can be found in Appendix A.5.

We decompose the Eliashberg function to evaluate the contribution of each of the two subsystems to the misfit's electron-phonon coupling (see Eq. 5.15). In Fig. 5.6, we plot the decomposition of $\alpha^2F(\omega)$ into vibrations of $NbSe_2$ (blue dashed lines) and of each different rocksalt (red dashed lines). We also calculate the contribution of each misfit' subsystem to the average electron-phonon coupling λ (blue solid lines for $NbSe_2$ and red solid lines for each rocksalt).

As it can be seen in Fig. 5.6, in all the considered cases, the contribution of the highest energy modes (180-350 cm^{-1}) is essentially due to vibrations of $NbSe_2$ decoupled from the rocksalt's ones. The rocksalts' modes are instead present in the low energy part of the Eliashberg function. In this region, also low energy modes of $NbSe_2$ appear, therefore we may deduce that the contribution of the lower energy modes (0-180 cm^{-1}) to $\alpha^2F(\omega)$ of the misfit is a mixture of the modes of the two subsystems.

We can further identify two scenarios. In the cases of LaSe (Fig. 5.6 (a)) and PbSe (Fig. 5.6 (c)), the predominant contribution to the electron-phonon coupling comes from $NbSe_2$, with the contribution of the rocksalts being half that of the TMD. In the case of BiSe (Fig. 5.6 (b)) and SnSe (Fig. 5.6 (d)), the existence of rocksalt modes in the lowest frequency range (0-70 cm^{-1}) amplifies the contribution of the rocksalts to the electron-phonon coupling.

In the case of BiSe, we may attribute the significant contribution of the rocksalt layers to the misfit's electron-phonon coupling to band alignment. Our ab initio calculations of the electronic properties of the $(BiSe)_{1.14}(NbSe_2)$ misfit layer compound (see Fig. 5.2 panel (b)) reveal the existence of BiSe bands at the Fermi level, which contributes to electron-phonon coupling.

In the case of SnSe, the explanation is more challenging. The CDW of $NbSe_2$

may be inherited by the bulk due to its low doping inside the $(SnSe)_{1.16}(NbSe_2)$ misfit. This impact cannot be accounted for with a Γ-only grid and would require a considerably denser one, which is currently beyond our computing capabilities. Furthermore, during the construction of the 2/1 commensurate approximant of the misfit cell, the rocksalt SnSe is the most strained in the mismatch direction to match $NbSe_2$, decreasing some low energy modes that would be higher in frequency if the larger 7/4 ratio was used.
A summary of the contribution of $NbSe_2$ and the respective rocksalt to the misfit's electron-phonon coupling is shown in Tab. 5.3 for each case.
We then calculate the superconducting critical temperature by the Allen and Dynes semi-empirical formula (Eq. 5.12). In this work we assume $\mu^* = 0.15$. We choose this value as the electronic states at the Fermi level are poorly screened in $NbSe_2$ [137]. Moreover, because of a different orbital character, these states weakly interact with those far from the Fermi level, yielding a weak reduction of the Coulomb pseudopotential (high μ^*) [137, 138].
Tab. 5.3 summarizes the estimated critical temperatures for each compound of the series in comparison with the experimental values.
As can be seen, our calculations show that the critical temperature increases with decreasing doping of $NbSe_2$ in the misfit. This linear trend is confirmed by the comparison with the experimental measurements of the compounds of this series (T_c^{Exp} in the last column of Tab. 5.3). For the case of $(LaSe)_{1.15}(NbSe_2)$, we estimate the value of the T_c within ≈ 1 K in comparison with the experimental work of reference [135]. For the case of $(BiSe)_{1.14}(NbSe_2)$, we calculate a critical temperature of 3.0 K. The comparison is done with the available experimental data on the compound $(BiSe)_{1.10}(NbSe_2)$, where the percentage of BiSe within the misfit is slightly lower, but still comparable with our considered system [58]. In the case of $(PbSe)_{1.14}(NbSe_2)$, we estimate the critical temperature of the system to be $T_c = 5.2$ K. This value is consistent (within $\sim 7\%$) with the experimental results in Ref. [56]. The sole exception is $(SnSe)_{1.16}(NbSe_2)$, where our expected value for the T_c is $\sim 50\%$ of that of the experimental study in Ref. [57]. This system corresponds to the lowest doping of $NbSe_2$ within the series. As previously noted, at this low doping level, the existence of the CDW of $NbSe_2$, which cannot be described in our approximations, can significantly alter electron-phonon coupling, competing with superconductivity.

Finally, we wanted to address the role of the z-axis in the calculation of the electron-phonon coupling. In Fig. 5.7, we show the misfit calculations using a k-point grid for the electron-phonon coupling of $N_k = 12 \times 12 \times 12$, which corresponds to the grid we used in our simulations provided in Fig. 5.6. We compare our results with a k-points grid of $N_k = 12 \times 12 \times 1$ excluding the effect of the kz-axis. Our plot in Fig. 5.7 shows that the contribution of kz to the electron phonon coupling is essentially negligible, since the shape of the first (black solid curve) and the second (lilac solid curve) $\alpha^2F(\omega)$ is almost identical. When further inspecting the average electron-phonon coupling λ for the two grids, we can see that it is identical for LaSe, while it varies in a short range of $5 - 12\%$ with decreasing doping.

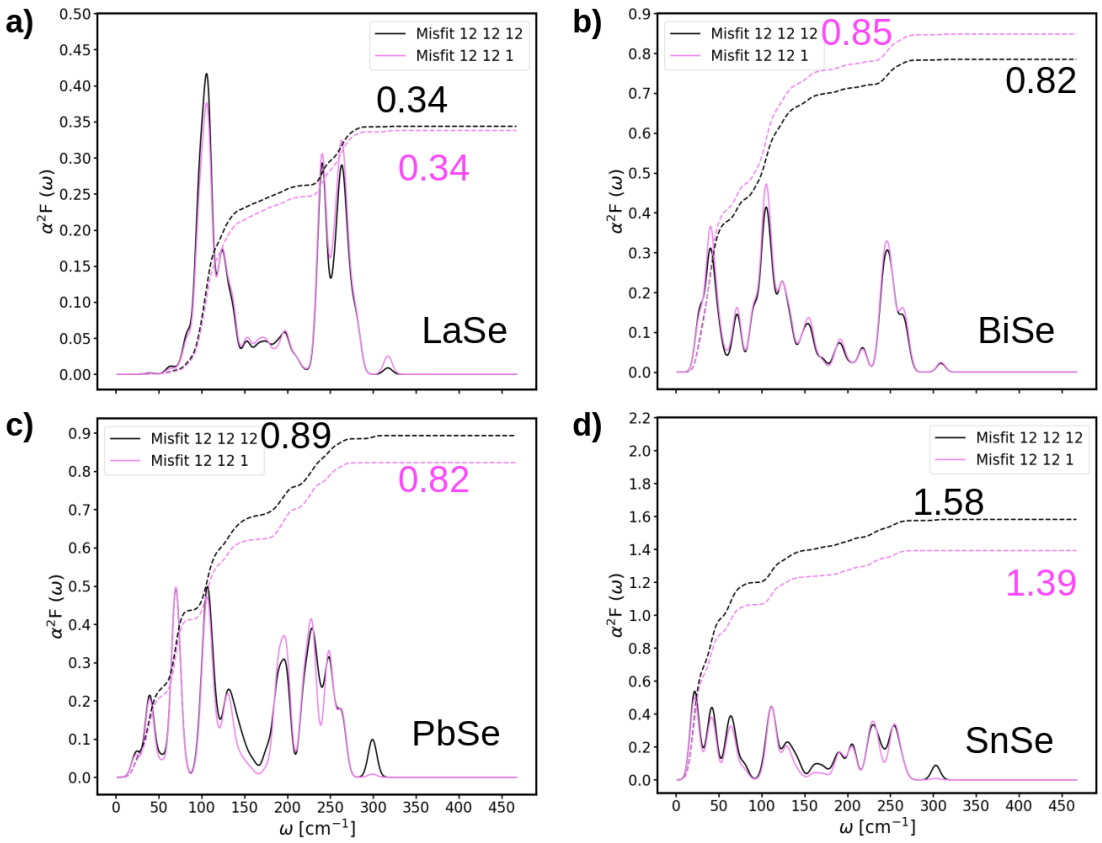

Figure 5.7: Superconducting properties of bulk $(RQ)_{1+\delta}(NbSe_2)$ misfit series. (a) $(LaSe)_{1.15}(NbSe_2)$, (b) $(BiSe)_{1.14}(NbSe_2)$, (c) $(PbSe)_{1.14}(NbSe_2)$, (d) $(SnSe)_{1.16}(NbSe_2)$. The total Eliashberg function $\alpha^2F(\omega)$ and the average electron-phonon coupling λ are plotted in a black solid and dashed curve for a k-point grid for the electron-phonon coupling of $N_k = 12 \times 12 \times 12$. The total Eliashberg function $\alpha^2F(\omega)$ and the average electron-phonon coupling λ are plotted in a lilac solid and dashed curve for a k-point grid for the electron-phonon coupling of $N_k = 12 \times 12 \times 1$, neglecting the kz-axis contribution.

In conclusion, our calculations represent a first step towards the theoretical understanding of the superconducting properties of bulk $(RQ)_{1+\delta}(NbSe_2)$ misfit series. A potential improvement of our results could involve using the anisotropic Migdal-Eliashberg equations to calculate the superconducting gap of $NbSe_2$ within the misfit. The methodology applied is relevant beyond the considered family and can be further applied to other misfit layer compounds.

5.3 Summary

In Chapter 5, we present our study of the superconducting properties of misfit layer compounds. First of all, we introduce the electron-phonon coupling theory. Then we show a method to reduce the computational effort of modeling bulk misfit layer compounds to compute superconducting properties. This method consists in considering the smallest commensurate approximant of the misfit cell by straining the rocksalt bilayers.
We specifically consider the $(RQ)_{1+\delta}(NbSe_2)$ misfit series, where we fix the TMD as $NbSe_2$, and we change the rocksalt with RQ= LaSe, BiSe, PbSe, and SnSe. We approximate the 7/4 mismatch ratio by 8/4, corresponding to a 2/1 ratio. With this reduced cell, we are able to reproduce the correct charge transfer from the rocksalt to the TMD, as shown with the electronic properties of the $(RQ)_{1+\delta}(NbSe_2)$ misfit series.
Then, we perform the electron-phonon coupling calculations of the full misfit. The estimated critical temperatures are in good agreement with the available experimental values. Our findings are useful beyond the examples studied because they establish a baseline for the ab initio investigation of superconductivity in misfit layer compounds.

Conclusions

Misfit layer compounds are a family of heterostructures built by stacking rocksalt units with few layers of transition metal dichalcogenides. Aside from their relevance for crystallography, these heterostructures have lately sparked a lot of attention in the condensed matter physics due to recent measurements indicating the occurrence of a plethora of emergent phenomena, such as superconductivity, charge density waves, and many others. However, the research in the field of misfits has focused on specific compounds, mostly through experimental synthesis and measurements, without a global, clear physical picture that is needed as a guide to exploit the potential of these heterostructures. In this thesis, we provided a fresh perspective for the study of misfit layer compounds by addressing most of the unanswered questions on these heterostructures. Specifically, this Thesis focused on deriving the properties of misfit layer compounds from those of their individual building blocks. Within our approach, we are able to fully characterize misfit layer compounds with the aim of designing these heterostructures with desired emergent properties for future device applications.

We first outlined the theoretical and experimental background in which our research has been carried on. We placed particular emphasis on the distinct subsystems that are the baseline for building misfit heterostructures, namely rocksalts and transition metal dichalcogenides. We then gave an overview of the composition of the misfit crystals and of the state-of-the-art emergent properties discovered in misfit layer compounds. This initial perspective not only introduced the composition and underlying physics of this family of heterostructures but also brought to light the significant challenges that define and drive advancements in this field.

Then, we solved the crucial problem of explaining the charge transfer mechanism occurring in these heterostructures. We detailed our approach, which is based on determining the work function of each separate rocksalt and TMD units in order to acquire a basic knowledge of the charge transfer process between misfit constituents. We showed that the work function of rocksalt units is always lower than that of TMDs, indicating a favorable path for electron transfer in misfit layer compounds: from the RS (electron donor) to the TMD (electron acceptor). By performing ab initio calculations of the work functions and band edges we were able to build the band alignement plot between each considered RS and TMD that offers in one picture a qualitatively and quantitatively predictions of the

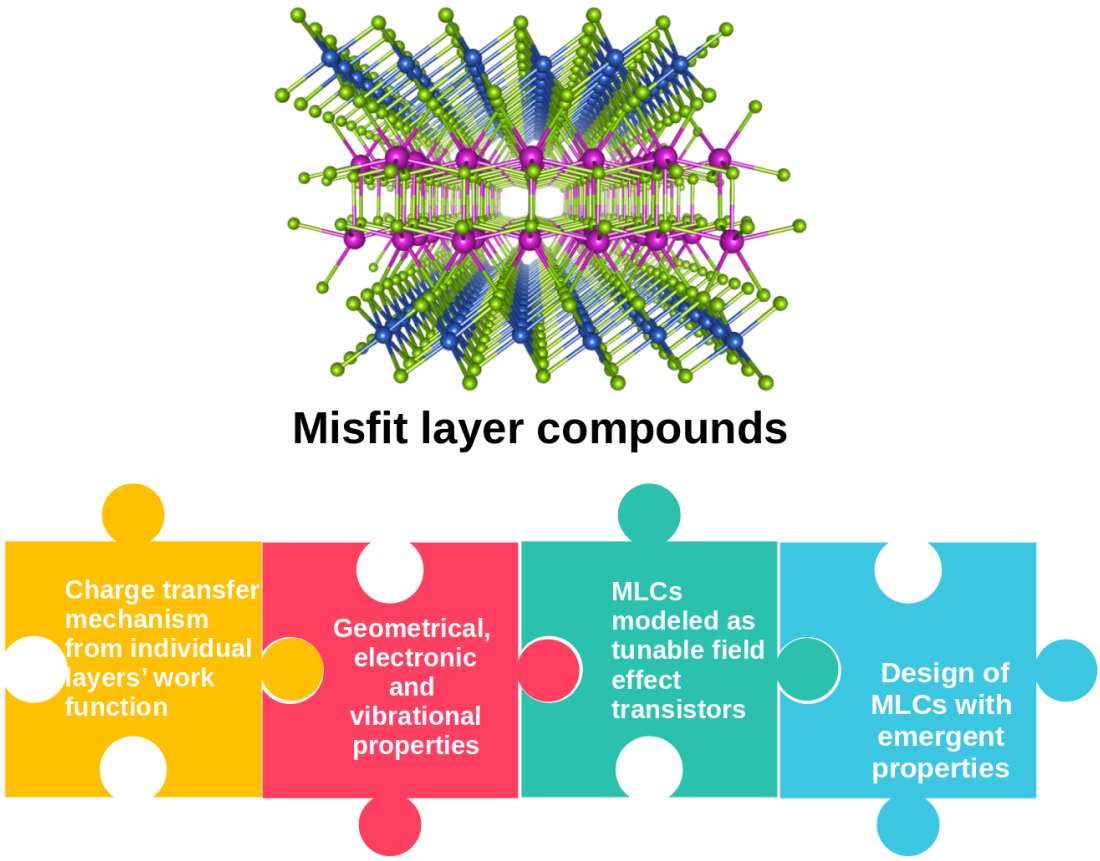

charge transfer in these structures. These findings serve as a guide for selecting the suitable RS/TMD couple to build a misfit layer compound, avoiding heavy calculations, and also provide significant information for experimental synthesis.

After established the key process ruling the charge transfer in these materials, we validated our method based on the work function determination. At this aim, we performed extensive geometrical optimization and electronic structure first-principle calculations of misfit layer compounds. In particular, we used the band unfolding technique to evidence the TMD features within the band structure of the misfit. We found that our method based on the work function determination and the band alignment plot produces reliable predictions of the charge transfer mechanism in agreement with our full misfit calculations and the available experimental data. We found that, in most of the cases, misfits behave as rigidly doped transition metal dichalcogenides. The electron density that can be injected in the TMD layers can be as high as 6×10^{14} e^{-} cm^{-2}, sensibly larger than in ordinary field-effect transistors. In addition, we proposed a efficient way to tune the amount of charge transferred from the RS to the TMD within the misfit. We showed that the charging of the TMD layers can be efficiently controlled by chemical insight without the introduction of any external parameters via alloying in the rocksalt. These results are crucial for the engineering of new misfit layer compounds with a high tunability of carrier concentration injected into TMD layers [81].

Our results based on electronic properties calculations show that misfits behave

essentially as highly doped TMDs, with doping controlled by the chemistry of the rocksalts that serve as electron reservoirs. We thus demonstrated that a misfit can be assimilated to a collection of ultratunable field effect transistor with an unequaled charging of the TMD layers. Based on this conceptualization, we were able to design a model for misfit layer compounds by means of the field effect transistor (FET) setup. The model consist in replacing each RS units with a charged plate and a barrier. With this method we showed that the surface of the misfit layer compound behaves as a single gated field-effect transistor while the bulk can be seen as a periodic arrangement of a double-gated field effect transistors. This model highly reduces the computational effort of simulating huge misfit supercells. We demonstrated the applicability of our model by showing that the electronic properties of misfits are well reproduced within the FET setup. Furthermore, we proposed to use our method for evaluating the vibrational properties of misfit layer compounds, a task that would be otherwise unfeasible without applying linear response theory to larger misfit supercells. As a practical demonstration, we showed how to reproduce the experimental Raman spectra of misfit layer compound $(LaSe)_{1.14}(NbSe_2)_2$. Our model was able to assign the most intense Raman peaks by analyzing the Raman active modes of each individual subsystem. More specifically, we showed that the vibrational properties are obtained from those of the two subunits, namely the LaSe unit and the $NbSe_2$ bilayer, in the presence of a suitable field-effect doping within our model. Our first-principles calculations predicted that $NbSe_2$ undergoes a doping-driven collapse of the CDW ordering within the misfit [106]. Our predictions are confirmed by polarized Raman spectroscopy measurements in which no signature of the CDW is detected down to 8 K. Interestingly, our model in comparison with experimental results highlights the 2D nature of the lattice dynamics of $NbSe_2$ within the $(LaSe)_{1.14}(NbSe_2)_2$ 3D structure. These results are relevant beyond the specific considered case as it sets a roadmap for the investigation of vibrational properties of misfit layer compounds. Lastly, we used the knowledge gained from the previous analysis to design a misfit with emergent superconductivity within the the FET setup. We showed that superconductivity can emerge in misfit layer compounds formed by assembling non-superconducting RS and TMDs. As a practical application, we were able to predict a doping-induced insulator-to-metal transition of $SnSe_2$ in misfit layer compound $(LaSe)_{1.27}(SnSe_2)_2$. By chemical alloying in the rocksalt, it is possible to reach a region corresponding to the Van Hoove singularity. We predicted by means of the anisotropic Migdal-Eliashberg theory a critical temperature of 3.5 K, demonstrating that doping-driven superconductivity can arise as an emergent property in misfit layer compounds.

Finally, we exploited the insights obtained from our modeling to estimate superconductivity in misfit layer compounds in comparison with the promising experimental results already achieved. We explain how to obtain a reduced misfit supercell by applying strain to the rocksalt unit. We demonstrate that this approximation doesn't hinder the electronic charge transfer in the misfit, reproducing the electronic properties of the full supercell. With this reduced cell we were able to calculate the electron-phonon coupling at the Brillouin Zone cen-

ter of the $(RQ)_{1+\delta}(NbSe_2)$ misfit series, estimating their superconducting critical temperatures. We deeply investigated the composition of the Eliashberg function, isolating the contribution of the different rocksalts and of $NbSe_2$, showing that the modes of each individual rocksalt contribute at the low frequency range of the coupling, while the high energy range is completely due to the vibrations of $NbSe_2$. Our results are in good agreement with the state-of-the-art experimental data of the $(RQ)_{1+\delta}(NbSe_2)$ misfit series, indicating that our technique may be further extended to study superconductivity in other compounds of the family.

Our work provides an original modeling of misfit layer compounds based on chemical and physical insights that can be applied as a general tool for those families of materials. In addition, the methodology developed in this Thesis could be relevant beyond the misfit case to be employed for other heterostructures of two-dimensional materials. For example, it has the potential to be used for other materials such as TMDs/graphene (or hBN) or TMDs/2D perovskites to construct tunable heterostructures for electronics and thermoelectric applications. The potential impact of this Thesis resides in the possibility of being used as guidance for future experimental synthesis of misfit layer compounds with tailored physical properties for future device applications.

Bibliography

[1] K. Novoselov, A. Geim, S. Morozov, Da Jiang, Yanshui Zhang, S. Dubonos, Irina Grigorieva, and A. Firsov. Electric field effect in atomically thin carbon films. *Nat. Mater.*, 6, 01 2004.

[2] A. K. Geim and I. V. Grigorieva. Van der Waals heterostructures. *Nature*, 499(7459):419–425, Jul 2013.

[3] K. S. Novoselov, A. Mishchenko, A. Carvalho, and A. H. Castro Neto. 2D materials and van der waals heterostructures. *Science*, 353(6298):aac9439, 2016.

[4] G.A Wiegers. Misfit layer compounds: Structures and physical properties. *Progress in Solid State Chemistry*, 24(1):1–139, 1996.

[5] J. Rouxel, A. Meerschaut, and G.A. Wiegers. Chalcogenide misfit layer compounds. *Journal of Alloys and Compounds*, 229(1):144–157, 1995.

[6] Raphaël T. Leriche, Alexandra Palacio-Morales, Marco Campetella, Cesare Tresca, Shunsuke Sasaki, Christophe Brun, François Debontridder, Pascal David, Imad Arfaoui, Ondrej Šofranko, Tomas Samuely, Geoffroy Kremer, Claude Monney, Thomas Jaouen, Laurent Cario, Matteo Calandra, and Tristan Cren. Misfit layer compounds: A platform for heavily doped 2D transition metal dichalcogenides. *Advanced Functional Materials*, 31(6):2007706, 2021.

[7] Xiaoxiang Xi, Helmuth Berger, László Forró, Jie Shan, and Kin Fai Mak. Gate Tuning of Electronic Phase Transitions in Two-Dimensional $NbSe_2$. *Physical Review Letters*, 117(10):106801, August 2016.

[8] Yecun Wu, Danfeng Li, Chun-Lan Wu, Harold Y. Hwang, and Yi Cui. Electrostatic gating and intercalation in 2D materials. *Nature Reviews Materials*, 8(1):41–53, Jan 2023.

[9] P. Samuely, P. Szabó, J. Kačmarčík, A. Meerschaut, L. Cario, A. G. M. Jansen, T. Cren, M. Kuzmiak, O. Šofranko, and T. Samuely. Extreme in-plane upper critical magnetic fields of heavily doped quasi-two-dimensional transition metal dichalcogenides. *Phys. Rev. B*, 104:224507, Dec 2021.

[10] N. Giang, Q. Xu, Y. S. Hor, A. J. Williams, S. E. Dutton, H. W. Zandbergen, and R. J. Cava. Superconductivity at 2.3 K in the misfit compound $(PbSe)_{1.16}(TiSe_2)_2$. *Phys. Rev. B*, 82:024503, Jul 2010.

[11] Jin Hee Kim, Jae Hyun Yun, Yoo Jang Song, and Jong-Soo Rhyee. Anisotropic thermoelectric and superconducting properties of the bulk misfit-layered $(SnSe)_{1.17}(TaSe_2)$ compound. *Current Applied Physics*, 28:1–6, 2021.

[12] Xiaohui Yang, Jiang Ma, Baijiang Lv, Hanxian Hu, Tulai Sun, Miaocong Li, Lei Qiao, Siqi Wu, Qian Tao, Guang-Han Cao, and Zhu-An Xu. Enhanced superconductivity in a misfit compound $(PbSe)_{1.12}(TaSe_2)_2$ with double $TaSe_2$ layers. *Europhysics Letters*, 128(1):17004, nov 2019.

[13] Corinna Grosse, Matti B. Alemayehu, Matthias Falmbigl, Anna Mogilatenko, Olivio Chiatti, David C. Johnson, and Saskia F. Fischer. Superconducting ferecrystals: turbostratically disordered atomic-scale layered $(PbSe)_{1.14}(NbSe)_n$ thin films. *Scientific Reports*, 6(1):33457, Sep 2016.

[14] Benjamin A. Trump, Kenneth J.T. Livi, and Tyrel M. McQueen. The new misfit compound $(BiSe)_{1.15}(TiSe_2)_2$ and the role of dimensionality in the $Cu_x(BiSe)_{1+\delta}(TiSe_2)_n$ series. *Journal of Solid State Chemistry*, 209:6–12, 2014.

[15] M. Falmbigl, D. Putzky, J. Ditto, and D.C. Johnson. Influence of interstitial V on structure and properties of ferecrystalline $([SnSe]_{1.15})_1(V_{1+x}Se_2)_n$ for n=1,2,3,4,5, and 6. *Journal of Solid State Chemistry*, 231:101–107, 2015.

[16] Ryan Atkins, Sabrina Disch, Zachary Jones, Ines Haeusler, Corinna Grosse, Saskia F. Fischer, Wolfgang Neumann, Paul Zschack, and David C. Johnson. Synthesis, structure and electrical properties of a new tin vanadium selenide. *Journal of Solid State Chemistry*, 202:128–133, 2013.

[17] Huixia Luo, Kai Yan, Ivo's Pletikosic, Weiwei Xie, Brendan F. Phelan, Tonica Valla, and Robert J. Cava. Superconductivity in a misfit phase that combines the topological crystalline insulator $Pb_{1-x}Sn_xSe$ with the cdw-bearing transition metal dichalcogenide $TiSe_2$. *Journal of the Physical Society of Japan*, 85(6):064705, 2016.

[18] Sajedeh Manzeli, Dmitry Ovchinnikov, Diego Pasquier, Oleg V. Yazyev, and Andras Kis. 2D transition metal dichalcogenides. *Nature Reviews Materials*, 2(8):17033, Jun 2017.

[19] Qiang Fu, Jiecai Han, Xianjie Wang, Ping Xu, Tai Yao, Jun Zhong, Wenwu Zhong, Shengwei Liu, Tangling Gao, Zhihua Zhang, Lingling Xu, and Bo Song. 2D transition metal dichalcogenides: Design, modulation, and challenges in electrocatalysis. *Advanced Materials*, 33(6):1907818, 2021.

[20] Hui Chen, Jiwei Zhang, Dongxiao Kan, Jiabei He, Mengshan Song, Jianhua Pang, Songrui Wei, and Kaiyun Chen. The recent progress of two-

dimensional transition metal dichalcogenides and their phase transition. *Crystals*, 12(10), 2022.

[21] Saju Joseph, Jainy Mohan, Seetha Lakshmy, Simil Thomas, Brahmananda Chakraborty, Sabu Thomas, and Nandakumar Kalarikkal. A review of the synthesis, properties, and applications of 2D transition metal dichalcogenides and their heterostructures. *Materials Chemistry and Physics*, 297:127332, 2023.

[22] Y J Zhang, M Yoshida, R Suzuki, and Y Iwasa. 2D crystals of transition metal dichalcogenide and their iontronic functionalities. *2D Materials*, 2(4):044004, oct 2015.

[23] Jong Hun Kim, Hayeong Sung, and Gwan-Hyoung Lee. Phase engineering of two-dimensional transition metal dichalcogenides. *Small Science*, 4(1):2300093, 2024.

[24] E. Revolinsky, G.A. Spiering, and D.J. Beerntsen. Superconductivity in the Niobium-Selenium system. *Journal of Physics and Chemistry of Solids*, 26(6):1029–1034, June 1965.

[25] J.A. Wilson, F.J. Di Salvo, and S. Mahajan. Charge-density waves and superlattices in the metallic layered transition metal dichalcogenides. *Advances in Physics*, 24(2):117–201, March 1975.

[26] D. E. Moncton, J. D. Axe, and F. J. DiSalvo. Neutron scattering study of the charge-density wave transitions in 2H-$TaSe_2$ and 2H-$NbSe_2$. *Physical Review B*, 16(2):801–819, July 1977.

[27] Christos D. Malliakas and Mercouri G. Kanatzidis. Nb–Nb Interactions Define the Charge Density Wave Structure of 2H-$NbSe_2$. *Journal of the American Chemical Society*, 135(5):1719–1722, February 2013.

[28] Kuang-Chung Wang, Teodor K. Stanev, Daniel Valencia, James Charles, Alex Henning, Vinod K. Sangwan, Aritra Lahiri, Daniel Mejia, Prasad Sarangapani, Michael Povolotskyi, Aryan Afzalian, Jesse Maassen, Gerhard Klimeck, Mark C. Hersam, Lincoln J. Lauhon, Nathaniel P. Stern, and Tillmann Kubis. Control of interlayer physics in 2H transition metal dichalcogenides. *Journal of Applied Physics*, 122(22):224302, 12 2017.

[29] Xuefei Li, Xinhang Shi, Damiano Marian, David Soriano, Teresa Cusati, Giuseppe Iannaccone, Gianluca Fiori, Qi Guo, Wenjie Zhao, and Yanqing Wu. Rhombohedral-stacked bilayer transition metal dichalcogenides for high-performance atomically thin CMOS devices. *Sci Adv*, 9(7):eade5706, February 2023.

[30] Eunbin Son, Sangjin Lee, Jihyung Seo, Ungsoo Kim, Sang Heon Kim, Jeong Min Baik, Young-Kyu Han, and Hyesung Park. Engineering the local atomic configuration in 2H TMDs for efficient electrocatalytic hydrogen evolution. *ACS Nano*, 17(11):10817–10826, Jun 2023.

[31] Mohammad Salavati and Timon Rabczuk. Application of highly stretchable and conductive two-dimensional 1T VS_2 and VSe_2 as anode materials for Li-, Na- and Ca-ion storage. *Computational Materials Science*, 160:360–367, 2019.

[32] P. Chen, Y.-H. Chan, X.-Y. Fang, Y. Zhang, M. Y. Chou, S.-K. Mo, Z. Hussain, A.-V. Fedorov, and T.-C. Chiang. Charge density wave transition in single-layer titanium diselenide. *Nature Communications*, 6(1):8943, Nov 2015.

[33] Zhuangchai Lai, Qiyuan He, Thu Ha Tran, D. V. Maheswar Repaka, Dong-Dong Zhou, Ying Sun, Shibo Xi, Yongxin Li, Apoorva Chaturvedi, Chaoliang Tan, Bo Chen, Gwang-Hyeon Nam, Bing Li, Chongyi Ling, Wei Zhai, Zhenyu Shi, Dianyi Hu, Vinay Sharma, Zhaoning Hu, Ye Chen, Zhicheng Zhang, Yifu Yu, Xiao Renshaw Wang, Raju V. Ramanujan, Yanming Ma, Kedar Hippalgaonkar, and Hua Zhang. Metastable 1T'-phase group VIb transition metal dichalcogenide crystals. *Nature Materials*, 20(8):1113–1120, Aug 2021.

[34] Anthony R. West. *Basic solid state chemistry.* Wiley, 1988.

[35] Neeraj Mishra and Guy Makov. A novel interstitial site in binary rock-salt compounds. *Materials*, 15(17), 2022.

[36] Yan Sun, Zhicheng Zhong, Tomonori Shirakawa, Cesare Franchini, Dianzhong Li, Yiyi Li, Seiji Yunoki, and Xing-Qiu Chen. Rocksalt SnS and SnSe: Native topological crystalline insulators. *Phys. Rev. B*, 88:235122, Dec 2013.

[37] Paolo Barone, Tomá š Rauch, Domenico Di Sante, Jürgen Henk, Ingrid Mertig, and Silvia Picozzi. Pressure-induced topological phase transitions in rocksalt chalcogenides. *Phys. Rev. B*, 88:045207, Jul 2013.

[38] Chongjian Zhou, Yong Kyu Lee, Yuan Yu, Sejin Byun, Zhong-Zhen Luo, Hyungseok Lee, Bangzhi Ge, Yea-Lee Lee, Xinqi Chen, Ji Yeong Lee, Oana Cojocaru-Mirédin, Hyunju Chang, Jino Im, Sung-Pyo Cho, Matthias Wuttig, Vinayak P. Dravid, Mercouri G. Kanatzidis, and In Chung. Polycrystalline SnSe with a thermoelectric figure of merit greater than the single crystal. *Nature Materials*, 20(10):1378–1384, Oct 2021.

[39] Nicholas Ng and Tyrel M. McQueen. Misfit layered compounds: Unique, tunable heterostructured materials with untapped properties. *APL Materials*, 10(10):100901, 10 2022.

[40] Sander van Smaalen. Symmetry of composite crystals. *Phys. Rev. B*, 43:11330–11341, May 1991.

[41] A. Yamamoto. Unified setting and symbols of superspace groups for composite crystals. *Acta Crystallographica Section A*, 48(4):476–483, Jul 1992.

[42] K. Kato and M. Onoda. Strukturverfeinerung des Kompositkristalls im mehrdimensionalen Raum: Kommensurabler Kompositkristall. *Acta Crystallographica Section A*, 47(1):55–56, Jan 1991.

[43] Michael Binnewies, Robert Glaum, Marcus Schmidt, and Peer Schmidt. *Chemical vapor transport reactions*. Walter de Gruyter, 2012.

[44] Dongya Wang, Fei Luo, Min Lu, Xiaoji Xie, Ling Huang, and Wei Huang. Chemical vapor transport reactions for synthesizing layered materials and their 2D counterparts. *Small*, 15(40):1804404, 2019.

[45] J M Jasinski, B S Meyerson, and B A Scott. Mechanistic studies of chemical vapor deposition. *Annual Review of Physical Chemistry*, 38(Volume 38,):109–140, 1987.

[46] Donald M Mattox. *Handbook of physical vapor deposition (PVD) processing*. William Andrew, 2010.

[47] John R Arthur. Molecular beam epitaxy. *Surface science*, 500(1-3):189–217, 2002.

[48] Atsushi Koma, Kazumasa Sunouchi, and Takao Miyajima. Fabrication and characterization of heterostructures with subnanometer thickness. *Microelectronic Engineering*, 2:129–136, 1984.

[49] E Wisotzki, A Klein, and W Jaegermann. Quasi van der waals epitaxy of ZnSe on the layered chalcogenides InSe and GaSe. *Thin Solid Films*, 380(1):263–265, 2000.

[50] Haruhiko Tanaka. Thermal analysis and kinetics of solid state reactions. *Thermochimica acta*, 267:29–44, 1995.

[51] S-H Feng and G-H Li. Hydrothermal and solvothermal syntheses. In *Modern inorganic synthetic chemistry*, pages 73–104. Elsevier, 2017.

[52] Yoshio Waseda, Eiichiro Matsubara, and Kozo Shinoda. *X-ray diffraction crystallography: introduction, examples and solved problems*. Springer Science & Business Media, 2011.

[53] Xin Zhang, Qing-Hai Tan, Jiang-Bin Wu, Wei Shi, and Ping-Heng Tan. Review on the raman spectroscopy of different types of layered materials. *Nanoscale*, 8(12):6435–6450, 2016.

[54] Paul F. Sullivan and G. Seidel. Steady-state, ac-temperature calorimetry. *Phys. Rev.*, 173:679–685, Sep 1968.

[55] J. Kačmarčík, Z. Pribulová, V. Pal'uchová, P. Szabó, P. Husaníková, G. Karapetrov, and P. Samuely. Heat capacity of single-crystal Cu_xTiSe_2 superconductors. *Phys. Rev. B*, 88:020507, Jul 2013.

[56] Haoyuan Zhong, Hongyun Zhang, Haoxiong Zhang, Ting Bao, Kenan Zhang, Shengnan Xu, Laipeng Luo, Awabaikeli Rousuli, Wei Yao,

Jonathan D. Denlinger, Yaobo Huang, Yang Wu, Yong Xu, Wenhui Duan, and Shuyun Zhou. Revealing the two-dimensional electronic structure and anisotropic superconductivity in a natural van der waals superlattice $(PbSe)_{1.14}NbSe_2$. *Phys. Rev. Mater.*, 7:L041801, Apr 2023.

[57] Hua Bai, Xiaohui Yang, Yi Liu, Meng Zhang, Mengmeng Wang, Yupeng Li, Jiang Ma, Qian Tao, Yanwu Xie, Guang-Han Cao, and Zhu-An Xu. Superconductivity in a misfit layered compound $(SnSe)_{1.16}(NbSe_2)$. *Journal of Physics: Condensed Matter*, 30(35):355701, aug 2018.

[58] S Matsuzawa, S Pyon, and T Tamegai. Characterizations of anisotropic superconductivity in $(BiSe)_{1+\delta}NbSe_2$. *Journal of Physics: Conference Series*, 2323(1):012008, aug 2022.

[59] Xiaohui Yang, Mengmeng Wang, Yupeng Li, Hua Bai, Jiang Ma, Xikang Sun, Qian Tao, Cheng Dong, and Zhu-An Xu. Superconductivity in a misfit compound $(PbSe)_{1.12}(TaSe_2)$. *Superconductor Science and Technology*, 31(12):125010, nov 2018.

[60] E. Morosan, H. W. Zandbergen, B. S. Dennis, J. W. G. Bos, Y. Onose, T. Klimczuk, A. P. Ramirez, N. P. Ong, and R. J. Cava. Superconductivity in Cu_xTiSe_2. *Nature Physics*, 2(8):544–550, Aug 2006.

[61] Yoo Jang Song, Min Jae Kim, Wan Gil Jung, Bong-Joong Kim, and Jong-Soo Rhyee. Superconducting properties of the misfit-layer compound $(SnSe)_{1.18}(TiSe_2)_2$. *physica status solidi (b)*, 253(8):1517–1522, 2016.

[62] Fabian Göhler, Shrinidhi Ramasubramanian, Sanam Kumari Rajak, Niels Rösch, Adrian Schütze, Susanne Wolff, Dmitri Leo Mesoza Cordova, David C. Johnson, and Thomas Seyller. Modulation doping and charge density wave transition in layered PbSe–VSe_2 ferecrystal heterostructures. *Nanoscale*, 14:10143–10154, 2022.

[63] Kazuya Suzuki, Tetsuo Kondo, Makoto Iwasaki, and Toshiaki Enoki. Variety of magnetism in incommensurate misfit layer compounds $(RES)_xTS_2$ (RE=rare earths, T=Ta, V, Ti, Cr). *Japanese Journal of Applied Physics*, 32(S3):341, jan 1993.

[64] L. Cario, B. Corraze, A. Meerschaut, Y. Moelo, and O. Chauvet. Electronic properties of the $(LaS)_{1.18}VS_2$ incommensurate misfit compound. *Synthetic Metals*, 103(1):2640–2643, 1999. International Conference on Science and Technology of Synthetic Metals.

[65] O Leynaud, A Lafond, K Poduska, and A Meerschaut. Magnetic properties of misfit layer compounds $[(Pb,M)S)_{1.5}]_{1+x}NbS_2$; M=Fe or (Mn,Nb). *Journal of Magnetism and Magnetic Materials*, 231(2):185–190, 2001.

[66] Aleksandr V Sotnikov, Priyanka Jood, and Michihiro Ohta. Enhancing the thermoelectric properties of misfit layered sulfides $(MS)_{1.2q}(NbS_2)_n$ (m =

gd and dy) through structural evolution and compositional tuning. *ACS Omega*, 5(22):13006–13013, June 2020.

[67] Devin R. Merrill, Daniel B. Moore, Sage R. Bauers, Matthias Falmbigl, and David C. Johnson. Misfit layer compounds and ferecrystals: Model systems for thermoelectric nanocomposites. *Materials*, 8(4):2000–2029, 2015.

[68] Herbert B. Michaelson. The work function of the elements and its periodicity. *Journal of Applied Physics*, 48(11):4729–4733, 11 1977.

[69] Antoine Kahn. Fermi level, work function and vacuum level. *Mater. Horiz.*, 3:7–10, 2016.

[70] F. G. Allen and G. W. Gobeli. Work function, photoelectric threshold, and surface states of atomically clean silicon. *Phys. Rev.*, 127:150–158, Jul 1962.

[71] Lin Lin, Ryan Jacobs, Tianyu Ma, Dongzheng Chen, John Booske, and Dane Morgan. Work function: Fundamentals, measurement, calculation, engineering, and applications. *Phys. Rev. Appl.*, 19:037001, Mar 2023.

[72] O.C. Olawole, D.K. De, O.F. Olawole, R. Lamba, E.S. Joel, S.O. Oyedepo, A.A. Ajayi, O.A. Adegbite, F.I. Ezema, S. Naghdi, T.D. Olawole, O.O. Obembe, and K.O. Oguniran. Progress in the experimental and computational methods of work function evaluation of materials: A review. *Heliyon*, 8(10):e11030, 2022.

[73] Zhen Zhang and John T. Jr. Yates. Band Bending in Semiconductors: Chemical and Physical Consequences at Surfaces and Interfaces. *Chemical Reviews*, 112(10):5520–5551, 2012.

[74] W. Schottky. Halbleitertheorie der Sperrschicht. *Naturwissenschaften*, 26(52):843–843, Dec 1938.

[75] N. F. Mott. Note on the contact between a metal and an insulator or semi-conductor. *Mathematical Proceedings of the Cambridge Philosophical Society*, 34(4):568–572, 1938.

[76] Alfonso Franciosi and Chris G. Van de Walle. Heterojunction band offset engineering. *Surface Science Reports*, 25(1):1–140, 1996.

[77] Alfonso Baldereschi, Stefano Baroni, and Raffaele Resta. Band offsets in lattice-matched heterojunctions: A model and first-principles calculations for GaAs/AlAs. *Phys. Rev. Lett.*, 61:734–737, Aug 1988.

[78] M Peressi, N Binggeli, and A Baldereschi. Band engineering at interfaces: theory and numerical experiments. 31(11):1273, jun 1998.

[79] L. Weston, H. Tailor, K. Krishnaswamy, L. Bjaalie, and C.G. Van de Walle. Accurate and efficient band-offset calculations from density functional theory. *Computational Materials Science*, 151:174–180, 2018.

[80] C J Fall, N Binggeli, and A Baldereschi. Deriving accurate work functions from thin-slab calculations. *Journal of Physics: Condensed Matter*, 11(13):2689, apr 1999.

[81] Ludovica Zullo, Giovanni Marini, Tristan Cren, and Matteo Calandra. Misfit layer compounds as ultratunable field effect transistors: From charge transfer control to emergent superconductivity. *Nano Letters*, 23(14):6658–6663, Jul 2023.

[82] Han-gyu Kim and Hyoung Joon Choi. Thickness dependence of work function, ionization energy, and electron affinity of Mo and W dichalcogenides from DFT and GW calculations. *Phys. Rev. B*, 103:085404, Feb 2021.

[83] John P. Perdew, Kieron Burke, and Matthias Ernzerhof. Generalized gradient approximation made simple. *Physical Review Letters*, 77(18):3865–3868, oct 1996.

[84] Paolo Giannozzi, Oscar Baseggio, Pietro Bonfà, Davide Brunato, Roberto Car, Ivan Carnimeo, Carlo Cavazzoni, Stefano de Gironcoli, Pietro Delugas, Fabrizio Ferrari Ruffino, Andrea Ferretti, Nicola Marzari, Iurii Timrov, Andrea Urru, and Stefano Baroni. Quantum espresso toward the exascale. *The Journal of Chemical Physics*, 152(15):154105, 2020.

[85] Hendrik J. Monkhorst and James D. Pack. Special points for brillouin-zone integrations. *Phys. Rev. B*, 13:5188–5192, Jun 1976.

[86] Jochen Heyd, Gustavo E. Scuseria, and Matthias Ernzerhof. Hybrid functionals based on a screened Coulomb potential. *The Journal of Chemical Physics*, 118(18):8207–8215, 05 2003.

[87] R. Roesky, A. Meerschaut, J. Rouxel, and J. Chen. Structure and electronic transport properties of the misfit layer compound $(LaSe)_{1.14}(NbSe_2)_2$, $LaNb_2Se_5$. *Zeitschrift für anorganische und allgemeine Chemie*, 619(1):117–122, 1993.

[88] B. E. Brown and D. J. Beerntsen. Layer structure polytypism among niobium and tantalum selenides. *Acta Crystallographica*, 18(1):31–36, Jan 1965.

[89] Paulo V. C. Medeiros, Sven Stafström, and Jonas Björk. Effects of extrinsic and intrinsic perturbations on the electronic structure of graphene: Retaining an effective primitive cell band structure by band unfolding. *Phys. Rev. B*, 89:041407, Jan 2014.

[90] Voicu Popescu and Alex Zunger. Extracting e versus $\vec{k}$ effective band structure from supercell calculations on alloys and impurities. *Phys. Rev. B*, 85:085201, Feb 2012.

[91] G. V. Lashkarev, L. A. Ivanchenko, V. A. Obolonchik, T. M. Mikhlina, and V. I. Lazorenko. *Monochalcogenides of the Rare-Earth Elements and Their Alloys Having Semiconductor Conductivity*, pages 39–44. Springer US, New York, NY, 1972.

[92] Matteo Cococcioni and Stefano de Gironcoli. Linear response approach to the calculation of the effective interaction parameters in the LDA + U method. *Phys. Rev. B*, 71:035105, Jan 2005.

[93] Burak Himmetoglu, Andrea Floris, Stefano de Gironcoli, and Matteo Cococcioni. Hubbard-corrected DFT energy functionals: The LDA+U description of correlated systems. *International Journal of Quantum Chemistry*, 114(1):14–49, 2014.

[94] Raffaello Bianco, Matteo Calandra, and Francesco Mauri. Electronic and vibrational properties of $TiSe_2$ in the charge-density-wave phase from first principles. *Phys. Rev. B*, 92:094107, Sep 2015.

[95] Jiatian Fu, Liyun Zhao, Liang Zhou, Kang Wu, Jiaxing Du, Xiangzhuo Wang, Jiepeng Song, Lijie Zhu, Fan Zhou, Yahuan Huan, Lihong Bao, Rongming Wang, Qing Zhang, and Yanfeng Zhang. Controllable synthesis of atomically thin 1T-$SnSe_2$ flakes and its linear second harmonic generation with layer thickness. *Advanced Materials Interfaces*, 9(11):2102376, 2022.

[96] Laurent Cario, Dirk Johrendt, Alain Lafond, Claudia Felser, Alain Meerschaut, and Jean Rouxel. Stability and charge transfer in the misfit compound $(LaS)(SrS)_{0.2}(CrS)_2$: Ab initio band-structure calculations. *Phys. Rev. B*, 55:9409–9414, Apr 1997.

[97] Sadhu Kolekar, Manuel Bonilla, Yujing Ma, Horacio Coy Diaz, and Matthias Batzill. Layer- and substrate-dependent charge density wave criticality in 1T-$TiSe_2$. *2D Materials*, 5(1):015006, 2018.

[98] Hong Wang, Yu Chen, Martial Duchamp, Qingsheng Zeng, Xuewen Wang, Siu Hon Tsang, Hongling Li, Lin Jing, Ting Yu, Edwin Hang Tong Teo, and Zheng Liu. Large-area atomic layers of the charge-density-wave conductor $TiSe_2$. *Advanced Materials*, 30(8):1704382, feb 2018.

[99] Xin-Yue Fang, Hawoong Hong, Peng Chen, and T.-C. Chiang. X-ray study of the charge-density-wave transition in single-layer $TiSe_2$. *Phys. Rev. B*, 95:201409, May 2017.

[100] Thomas Brumme, Matteo Calandra, and Francesco Mauri. First-principles theory of field-effect doping in transition-metal dichalcogenides: Structural properties, electronic structure, hall coefficient, and electrical conductivity. *Phys. Rev. B*, 91:155436, Apr 2015.

[101] Thibault Sohier, Matteo Calandra, and Francesco Mauri. Density functional perturbation theory for gated two-dimensional heterostructures: Theoretical developments and application to flexural phonons in graphene. *Phys. Rev. B*, 96:075448, Aug 2017.

[102] Giovanni Marini and Matteo Calandra. Phonon mediated superconductivity in field-effect doped molybdenum dichalcogenides. *2D Materials*, 10(1):015013, nov 2022.

[103] Giovanni Marini, Guglielmo Marchese, Gianni Profeta, Jelena Sjakste, Francesco Macheda, Nathalie Vast, Francesco Mauri, and Matteo Calandra. epiq: An open-source software for the calculation of electron-phonon interaction related properties. *Computer Physics Communications*, 295:108950, 2024.

[104] Philip B. Allen and Božidar Mitrović. Theory of superconducting tc. In Henry Ehrenreich, Frederick Seitz, and David Turnbull, editors, *Solid State Physics*, volume 37, pages 1–92. Academic Press, 1983.

[105] Matteo Calandra, Gianni Profeta, and Francesco Mauri. Adiabatic and nonadiabatic phonon dispersion in a wannier function approach. *Phys. Rev. B*, 82:165111, Oct 2010.

[106] Ludovica Zullo, Grégory Setnikar, Amit Pawbake, Tristan Cren, Christophe Brun, Justine Cordiez, Shunsuke Sasaki, Laurent Cario, Giovanni Marini, Matteo Calandra, and Marie-Aude Méasson. Charge density wave collapse of $NbSe_2$ in the $(LaSe)_{1.14}(NbSe_2)_2$ misfit layer compound. *Phys. Rev. B*, 110:075430, Aug 2024.

[107] Xiaoxiang Xi, Liang Zhao, Zefang Wang, Helmuth Berger, László Forró, Jie Shan, and Kin Fai Mak. Strongly enhanced charge-density-wave order in monolayer $NbSe_2$. *Nature Nanotechnology*, 10(9):765–769, September 2015.

[108] Miguel M. Ugeda, Aaron J. Bradley, Yi Zhang, Seita Onishi, Yi Chen, Wei Ruan, Claudia Ojeda-Aristizabal, Hyejin Ryu, Mark T. Edmonds, Hsin-Zon Tsai, Alexander Riss, Sung-Kwan Mo, Dunghai Lee, Alex Zettl, Zahid Hussain, Zhi-Xun Shen, and Michael F. Crommie. Characterization of collective ground states in single-layer $NbSe_2$. *Nature Physics*, 12(1):92–97, jan 2016.

[109] Owen Moulding, Israel Osmond, Felix Flicker, Takaki Muramatsu, and Sven Friedemann. Absence of superconducting dome at the charge-density-wave quantum phase transition in 2H-$NbSe_2$. *Physical Review Research*, 2(4):043392, December 2020.

[110] Ziying Wang, Runlai Li, Chenliang Su, and Kian Ping Loh. Intercalated phases of transition metal dichalcogenides. *SmartMat*, 1(1):e1013, December 2020.

[111] K. S. Novoselov, D. Jiang, F. Schedin, T. J. Booth, V. V. Khotkevich, S. V. Morozov, and A. K. Geim. Two-dimensional atomic crystals. *Proceedings of the National Academy of Sciences*, 102(30):10451–10453, July 2005.

[112] Raffaello Bianco, Lorenzo Monacelli, Matteo Calandra, Francesco Mauri, and Ion Errea. Weak Dimensionality Dependence and Dominant Role of Ionic Fluctuations in the Charge-Density-Wave Transition of $NbSe_2$. *Physical Review Letters*, 125(10):106101, September 2020.

[113] Dongjing Lin, Shichao Li, Jinsheng Wen, Helmuth Berger, László Forró, Huibin Zhou, Shuang Jia, Takashi Taniguchi, Kenji Watanabe, Xiaoxi-

ang Xi, and Mohammad Saeed Bahramy. Patterns and driving forces of dimensionality-dependent charge density waves in 2H-type transition metal dichalcogenides. *Nature Communications*, 11(1):2406, May 2020.

[114] S. Sugai, K. Murase, S. Uchida, and S. Tanaka. Comparison of the soft modes in tantalum dichalcogenides. *Physica B+C*, 105(1-3):405–409, May 1981.

[115] J. C. Tsang, J. E. Smith, and M. W. Shafer. Raman Spectroscopy of Soft Modes at the Charge-Density-Wave Phase Transition in 2 H - $NbSe_2$. *Physical Review Letters*, 37(21):1407–1410, November 1976.

[116] M.-A. Méasson, Y. Gallais, M. Cazayous, B. Clair, P. Rodière, L. Cario, and A. Sacuto. Amplitude Higgs mode in the 2H-$NbSe_2$ superconductor. *Physical Review B*, 89(6):060503, February 2014.

[117] Romain Grasset, Tommaso Cea, Yann Gallais, Maximilien Cazayous, Alain Sacuto, Laurent Cario, Lara Benfatto, and Marie-Aude Méasson. Higgs-mode radiance and charge-density-wave order in 2H-$NbSe_2$. *Physical Review B*, 97(9):094502, March 2018.

[118] Romain Grasset, Yann Gallais, Alain Sacuto, Maximilien Cazayous, Samuel Mañas-Valero, Eugenio Coronado, and Marie-Aude Méasson. Pressure-Induced Collapse of the Charge Density Wave and Higgs Mode Visibility in 2 H-TaS_2. *Physical Review Letters*, 122(12):127001, March 2019.

[119] Ge He, Leander Peis, Emma Frances Cuddy, Zhen Zhao, Dong Li, Yuhang Zhang, Romona Stumberger, Brian Moritz, Haitao Yang, Hongjun Gao, Thomas Peter Devereaux, and Rudi Hackl. Anharmonic strong-coupling effects at the origin of the charge density wave in CsV_3Sb_5. *Nature Communications*, 15(1):1895, March 2024.

[120] R. Sooryakumar, M. V. Klein, and R. F. Frindt. Effect of nonmagnetic impurities on the Raman spectra of the superconductor niobium diselenide. *Physical Review B*, 23(7):3222–3229, April 1981.

[121] C. J. Arguello, S. P. Chockalingam, E. P. Rosenthal, L. Zhao, C. Gutiérrez, J. H. Kang, W. C. Chung, R. M. Fernandes, S. Jia, A. J. Millis, R. J. Cava, and A. N. Pasupathy. Visualizing the charge density wave transition in 2H-$NbSe_2$ in real space. *Physical Review B*, 89(23), June 2014.

[122] Eunseok Oh, Gyeongcheol Gye, and Han Woong Yeom. Defect-Selective Charge-Density-Wave Condensation in 2H-$NbSe_2$. *Physical Review Letters*, 125(3):036804, July 2020.

[123] Utkalika P. Sahoo, Anamitra Mukherjee, and Pratap K. Sahoo. Short-Range Charge Density Wave and Bandgap Modulation by Au-Implanted Defects in $TiSe_2$. *ACS Applied Electronic Materials*, 4(7):3428–3434, July 2022.

[124] Christophe Brun, Zhao-Zhong Wang, Pierre Monceau, and Serguei Brazovskii. Surface Charge Density Wave Phase Transition in NbS_3. *Physical Review Letters*, 104(25):256403, June 2010.

[125] E. Machado-Charry, P. Ordejón, E. Canadell, C. Brun, and Z. Z. Wang. Analysis of scanning tunneling microscopy images of the charge-density-wave phase in quasi-one-dimensional $Rb_{0.3}MoO_3$. *Physical Review B*, 74(15):155123, October 2006.

[126] C Brun, E Machado-Charry, P Ordejón, E Canadell, and Z Z Wang. Inhomogenities of the CDW vector at the (-201) surface of Quasi-1D blue bronze $Rb_{0.3}MoO_3$. *Journal of Physics: Conference Series*, 61:140–146, March 2007.

[127] Stefano Baroni, Stefano de Gironcoli, Andrea Dal Corso, and Paolo Giannozzi. Phonons and related crystal properties from density-functional perturbation theory. *Reviews of Modern Physics*, 73(2):515–562, July 2001.

[128] Francesco Mauri, Oleg Zakharov, Stefano de Gironcoli, Steven G. Louie, and Marvin L. Cohen. Phonon softening and superconductivity in tellurium under pressure. *Phys. Rev. Lett.*, 77:1151–1154, Aug 1996.

[129] Philip B. Allen. Neutron spectroscopy of superconductors. *Phys. Rev. B*, 6:2577–2579, Oct 1972.

[130] Philip B. Allen and Richard Silberglitt. Some effects of phonon dynamics on electron lifetime, mass renormalization, and superconducting transition temperature. *Phys. Rev. B*, 9:4733–4741, Jun 1974.

[131] Matteo Calandra and Francesco Mauri. Electron-phonon coupling and phonon self-energy in MgB_2: Interpretation of MgB_2 raman spectra. *Phys. Rev. B*, 71:064501, Feb 2005.

[132] P. B. Allen and R. C. Dynes. Transition temperature of strong-coupled superconductors reanalyzed. *Phys. Rev. B*, 12:905–922, Aug 1975.

[133] Matteo Calandra and Francesco Mauri. Theoretical explanation of superconductivity in C_6Ca. *Phys. Rev. Lett.*, 95:237002, Nov 2005.

[134] Matteo Calandra and Francesco Mauri. High-T_c superconductivity in superhard diamondlike BC_5. *Phys. Rev. Lett.*, 101:016401, Jun 2008.

[135] Tomas Samuely, Darshana Wickramaratne, Martin Gmitra, Thomas Jaouen, Ondrej Šofranko, Dominik Volavka, Marek Kuzmiak, Jozef Haniš, Pavol Szabó, Claude Monney, Geoffroy Kremer, Patrick Le Fèvre, Fran çois Bertran, Tristan Cren, Shunsuke Sasaki, Laurent Cario, Matteo Calandra, Igor I. Mazin, and Peter Samuely. Protection of ising spin-orbit coupling in bulk misfit superconductors. *Phys. Rev. B*, 108:L220501, Dec 2023.

[136] G.A. Wiegers and W.Y. Zhou. The misfit layer compound $(SnSe)_{1.16}NbSe_2$. *Materials Research Bulletin*, 26(9):879–885, 1991.

[137] Antonio Sanna, Camilla Pellegrini, Eva Liebhaber, Kai Rossnagel, Katharina J. Franke, and E. K. U. Gross. Real-space anisotropy of the superconducting gap in the charge-density wave material 2H-$NbSe_2$. *npj Quantum Materials*, 7(1):6, Jan 2022.

[138] P. Morel and P. W. Anderson. Calculation of the superconducting state parameters with retarded electron-phonon interaction. *Phys. Rev.*, 125:1263–1271, Feb 1962.

[139] David Vanderbilt. Soft self-consistent pseudopotentials in a generalized eigenvalue formalism. *Phys. Rev. B*, 41:7892–7895, Apr 1990.

[140] Andrea Dal Corso. Pseudopotentials periodic table: From h to pu. *Computational Materials Science*, 95:337–350, 2014.

[141] Stefano Baroni, Stefano de Gironcoli, Andrea Dal Corso, and Paolo Giannozzi. Phonons and related crystal properties from density-functional perturbation theory. *Rev. Mod. Phys.*, 73:515–562, Jul 2001.

[142] Giovanni Pizzi, Valerio Vitale, Ryotaro Arita, Stefan Blügel, Frank Freimuth, Guillaume Géranton, Marco Gibertini, Dominik Gresch, Charles Johnson, Takashi Koretsune, Julen Ibañez-Azpiroz, Hyungjun Lee, Jae-Mo Lihm, Daniel Marchand, Antimo Marrazzo, Yuriy Mokrousov, Jamal I Mustafa, Yoshiro Nohara, Yusuke Nomura, Lorenzo Paulatto, Samuel Poncé, Thomas Ponweiser, Junfeng Qiao, Florian Thöle, Stepan S Tsirkin, Małgorzata Wierzbowska, Nicola Marzari, David Vanderbilt, Ivo Souza, Arash A Mostofi, and Jonathan R Yates. Wannier90 as a community code: new features and applications. *Journal of Physics: Condensed Matter*, 32(16):165902, jan 2020.

[143] H. J. Vidberg and J. W. Serene. Solving the eliashberg equations by means of n-point padé approximants. *Journal of Low Temperature Physics*, 29(3):179–192, Nov 1977.

[144] P. Morel and P. W. Anderson. Calculation of the superconducting state parameters with retarded electron-phonon interaction. *Phys. Rev.*, 125:1263–1271, Feb 1962.

[145] Paolo Giannozzi, Oscar Baseggio, Pietro Bonfà, Davide Brunato, Roberto Car, Ivan Carnimeo, Carlo Cavazzoni, Stefano De Gironcoli, Pietro Delugas, Fabrizio Ferrari Ruffino, Andrea Ferretti, Nicola Marzari, Iurii Timrov, Andrea Urru, and Stefano Baroni. QUANTUM ESPRESSO toward the exascale. *The Journal of Chemical Physics*, 152(15):154105, April 2020.

[146] John P. Perdew, Kieron Burke, and Matthias Ernzerhof. Generalized Gradient Approximation Made Simple. *Physical Review Letters*, 77(18):3865–3868, October 1996.

[147] Stefan Grimme, Stephan Ehrlich, and Lars Goerigk. Effect of the damping function in dispersion corrected density functional theory. *Journal of Computational Chemistry*, 32(7):1456–1465, May 2011.

[148] David Vanderbilt. Soft self-consistent pseudopotentials in a generalized eigenvalue formalism. *Physical Review B*, 41(11):7892–7895, April 1990.

Appendix A

Computational details

A.1 Geometrical optimization of misfit surfaces

In Chapter 3, we discuss the surfaces construction and geometrical properties of misfit layer compounds with m= 2. In this appendix, the convergence parameters of DFT calculations for all the investigated misfit surfaces are reported, while details of each specific considered system follows. We employ a $2 \times 8 \times 1$ a Monkhorst-Pack k-points grid and a Gaussian smearing of 0.025 Ry for Brillouin Zone (BZ) sampling. We use the generalized gradient approximation in the Perdew–Burke–Ernzerhof [83] parametrization for the exchange-correlation functional. In the calculation of surface properties, as the interaction among transition metal dichalcogenides layers is missing and only covalent bonds among the rocksalt and the transition metal dichalcogenides are present, we did not consider any Van der Waals correction. We consider the pseudopotential configurations taken from the Vanderbilt [139] and PSlibrary [140] distributions. The values of kinetic energy cutoff for plane-wave basis set is set to 50 Ry and for charge density 600 Ry respectively for all misfits. The atomic position of the slab are relaxed, by means of the Broyden-Fletcher-Goldfarb-Shanno (BFGS) algorithm, with a convergence threshold of 10^{-4} Ry on the total energy difference between consecutive structural optimisation steps and of 10^{-3} Ry/Bohr on all forces components.

A.1.1 Misfit surfaces with $TiSe_2$ and $SnSe_2$

We detail the procedure that we use to build misfit cells, specifically considering two cases: misfits with single layers $TiSe_2$ and $SnSe_2$, both found in the 1T phase, stacked with bilayers LaSe, and misfits belonging to the $(RQ)_{1+\delta}(NbSe_2)_2$ series with $NbSe_2$ in the 1H phase stacked with different rocksalts, namely RQ=LaSe, BiSe, PbSe and SnSe. For the first case, we start by considering the orthorhombic $TiSe_2$ and $SnSe_2$ cells with octahedral coordination of the transition metal atom (see Fig. 1.9 in the Chapter 1), and optimize their lattice parameters. We keep the **a** axis as the mismatch direction to build the misfit supercell. The mismatch ratio for the cases of $TiSe_2$/LaSe (5/3) and $SnSe_2$/LaSe (3/2) misfits, respectively

are extracted from Fig. 1.6. Lattice parameters in the mismatch direction are slightly strained in order to build a commensurate misfit structure. We obtain a_{TiSe_2}=3.6 Å (tensile strain of ≈ 2%, exp. value a_{TiSe_2}=3.54 Å) and a_{SnSe_2}=3.8 Å (compressive strain of ≈ 0.3%, exp. value a_{SnSe_2}=3.81 Å), respectively. In the other in-plane direction, we find b_{TiSe_2}=6.0191 Å and b_{SnSe_2}=6.5818 Å, respectively.
Starting from this cell, a supercell is built according to the misfit proportions (5×1 and a 3×1 supercell for the cases of $TiSe_2$/LaSe and $SnSe_2$/LaSe misfits, respectively).
Regarding the Q-layer rocksalt, we optimized LaSe with centered orthorhombic cell and slightly strained in-plane lattice parameter in order to obtain some commensurability with the considered TMD. A 3×1 LaSe supercell with in-plane lattice parameters $a_{LaSe} \approx b_{LaSe}$=6 Å (tensile strain of ≈ 0.5%, exp. value $a_{LaSe} \approx b_{LaSe}$=5.97 Å) is considered in order to match with $TiSe_2$, and a $2 \times 1 \times 1$ with lattice parameter a_{LaSe}=5.7 Å (compressive strain of ≈ 4%, exp. value a_{LaSe}=5.97 Å) and b_{LaSe}=6.5818 Å (tensile strain of ≈ 10%, exp. value a_{LaSe}=5.97 Å) is considered in order to match with $SnSe_2$.
Starting from this cell, a supercell is built according to the misfit proportions (3×1 and a 2×1 supercell for the cases of $TiSe_2$/LaSe and $SnSe_2$/LaSe misfits, respectively).
The two cells (one for the TMD and one for the rocksalt) are then appropriately assembled to build the slab system, which possesses a P1 symmetry. The supercell is composed of a Q-layer LaSe sandwiched between two $TiSe_2$ (or $SnSe_2$) single layers. The final $(LaSe)_{1.18}(TiSe_2)_2$ cell is orthorhombic, composed of 84 atoms, the mismatch ratio is a_2/a_1 =(6 Å)/(3.6 Å) = 1.66 ≃ 5/3, leading to lattice parameter of the misfit supercell equal to a = 18Å. Instead, $(LaSe)_{1.27}(SnSe_2)_2$ is orthorhombic, composed of 52 atoms, the mismatch ratio is a_2/a_1 =(5.7 Å)/(3.8 Å) = 1.57 ≃ 3/2, leading to lattice parameter of the misfit supercell equal to a = 11.4 Å.
The lattice parameters of the misfit cells are summarized in Tab. 3.3. In the tables Tab. A.1 and Tab. A.2, we report the optimized atomic positions expressed in crystalline coordinates of $(LaSe)_{1.27}(SnSe_2)_2$ and $(LaSe)_{1.18}(TiSe_2)_2$, respectively.

A.1.2 Misfit surfaces with $NbSe_2$ and RQ=LaSe, BiSe, PbSe, SnSe

In the second case, we start by considering the orthorhombic $NbSe_2$ cell with trigonal coordination of the transition metal atom (see Fig. 1.9 in Chapter 1). We keep the **a** axis as the mismatch direction to build the misfit supercell. For all the $NbSe_2$/RQ cases, the mismatch ratio is 7/4, extracted from Fig. 1.6. We obtain $a_{NbSe_2/LaSe}$=3.437 Å, $a_{NbSe_2/BiSe}$=3.434 Å and $a_{NbSe_2/PbSe}$=3.439 Å. Only $a_{NbSe_2/SnSe}$=3.38 Å have a compressive strain of ≈ 1.3%, with respect to its experimental value a_{NbSe_2}=3.43 Å. In the other in-plane direction, we find $b_{NbSe_2/LaSe}$=6.0191 Å, $b_{NbSe_2/BiSe}$=6.0102 Å, $b_{NbSe_2/PbSe}$=5.99 Å, and $b_{NbSe_2/SnSe}$= 5.94 Å, respectively. Starting from this cell, a supercell 7×1 is built according to

the misfit proportions.
For the Q-layer rocksalt, we optimized all the rocksalts with centered orthorhombic cell and slightly strained in-plane lattice parameter in order to obtain some commensurability with $NbSe_2$ as detailed in the following.
A 4×1 LaSe supercell with in-plane lattice parameters $a_{LaSe} \approx b_{LaSe}$=6 Å (tensile strain of $\approx 0.5\%$, exp. value $a_{LaSe} \approx b_{LaSe}$=5.97 Å) is considered in order to match with $NbSe_2$.
A 4×1 BiSe supercell with in-plane lattice parameters $a_{BiSe} \approx b_{BiSe}$=6 Å (tensile strain of $\approx 0.5\%$, exp. value $a_{BiSe} \approx b_{BiSe}$=6.026 Å) is considered in order to match with $NbSe_2$.
A 4×1 PbSe supercell with in-plane lattice parameters a_{PbSe}= 6.02 Å and b_{PbSe}=5.99 Å (tensile strain of $\approx 0.2\%$ and $\approx 0.7\%$, exp. value $a_{PbSe} \approx b_{PbSe}$=6.028 Å) is considered in order to match with $NbSe_2$.
A 4×1 SnSe supercell with in-plane lattice parameters a_{SnSe}= 6.02 Å and b_{SnSe}=5.99 Å (tensile strain of $\approx 0.1\%$ and $\approx 0.2\%$, exp. value $a_{SnSe} \approx b_{SnSe}$=5.927 Å) is considered in order to match with $NbSe_2$.
The two cells (one for the TMD and one for the rocksalt) are then appropriately assembled to build the slab system, which possesses a P1 symmetry. The supercell is composed of a Q-layer with RQ = LaSe, BiSe, PbSe, SnSe sandwiched between two $NbSe_2$ single layers. The final cells are orthorhombic, composed of 116 atoms, with lattice parameters summarized in Tab. 3.3. As an example, we report in Tab. A.3 the optimized atomic positions expressed in crystalline coordinates of the compound $(LaSe)_{1.15}(NbSe_2)_2$.

A.2 Electronic properties of misfit surfaces

We provide the convergence parameters of DFT computations used to determine the band structure of the misfits' surface.
We use the generalized gradient approximation in the Perdew–Burke–Ernzerhof [83] parametrization for the exchange-correlation functional.
We consider the following pseudopotential configurations taken from the Vanderbilt [139] and PSlibrary [140] distributions. (i) For Se, norm-conserving pseudopotentials from the PSlibrary distributions. (ii) For Ti, ultrasoft pseudopotentials from Vanderbilt distribution. (iii) For La, ultrasoft pseudopotentials from the Vanderbilt distributions. (iv) For Sn, Optimized Norm-Conserving Vanderbilt Pseudopotential. (v) For Pb, ultrasoft pseudopotentials from the PSlibrary distributions. (vi) For Nb, ultrasoft pseudopotentials from the PSlibrary distributions. (vii) For Bi, norm-conserving pseudopotentials from the PSlibrary distributions.
We employ a $2 \times 8 \times 1$ a Monkhorst-Pack k-points grid and a kinetic energy cutoff for plane-wave basis set of 50 Ry and of 600 Ry for charge density respectively for misfits with $SnSe_2$ and $TiSe_2$. We optimize the computations for the largest supercells (with a mismatch ratio of 7/4) containing $NbSe_2$ using a Monkhorst-Pack k-points grid of $1 \times 4 \times 1$ and a kinetic energy cutoff for plane-wave basis set to 48 Ry and 480 Ry for charge density, respectively. A Gaussian smearing of 0.025 Ry for Brillouin Zone (BZ) sampling is used in all the calculations. Each misfit slab

Sn	-0.0350	-0.0839	-0.0356	Se	0.0358	0.5066	0.2033
Se	-0.0403	0.2573	0.0234	La	0.2870	0.4629	0.2271
Se	0.1215	0.0782	-0.0947	Se	0.2838	0.0119	0.1986
Sn	0.1330	0.4172	-0.0421	La	0.0352	0.0046	0.4629
Se	0.1382	0.7528	0.0193	Se	0.5366	0.5134	0.2031
Se	-0.0430	0.5889	-0.0900	La	0.7872	0.5377	0.2318
Sn	0.2992	-0.0781	-0.0471	Se	0.7834	0.0034	0.2037
Se	0.3008	0.2404	0.0151	La	0.5303	0.0218	0.2270
Se	0.4744	0.0779	-0.0959	Sn	-0.0339	0.0935	0.3713
Sn	0.4640	0.4187	-0.0440	Se	-0.0236	0.4344	0.4232
Se	0.4551	0.7486	0.0194	Se	0.1369	0.2524	0.3042
Se	0.2968	0.5791	-0.0978	Sn	0.1332	0.5962	0.3634
Sn	0.6313	-0.0837	-0.0360	Se	0.1440	0.9264	0.4182
Se	0.6350	0.2599	0.0231	Se	-0.0429	0.7642	0.3077
Se	0.8000	0.0909	-0.0883	Sn	0.3008	0.0971	0.3620
Sn	0.7987	0.4153	-0.0346	Se	0.3022	0.4217	0.4156
Se	0.8034	0.7542	0.0239	Se	0.4616	0.2553	0.3038
Se	0.6420	0.5863	-0.0908	Sn	0.4669	0.5965	0.3629
Se	0.0363	-0.0017	0.1241	Se	0.4592	0.9234	0.4173
La	0.2869	0.0253	0.0954	Se	0.3064	0.7583	0.3033
Se	0.2838	0.5086	0.1235	Sn	0.6351	0.0953	0.3692
La	0.0307	0.5326	0.1003	Se	0.6236	0.4342	0.4219
Se	0.5356	0.0039	0.1240	Se	0.8032	0.2717	0.3119
La	0.7867	0.0496	0.1001	Sn	0.8014	0.5905	0.3743
Se	0.7841	0.5003	0.1286	Se	0.7986	0.9333	0.4251
La	0.5357	0.5108	0.1003	Se	0.6399	0.7592	0.3079

Table A.1: Optimized atomic positions of the surface of MLC $(LaSe)_{1.27}(SnSe_2)_2$ in crystal coordinates. The lattice parameters in Å are summarized in the main text (see Tab. 3.3).

Ti	-0.0053	-0.0730	-0.0370	Se	0.0011	0.5178	0.2028
Se	-0.0061	0.2531	0.0162	La	0.1680	0.4935	0.2276
Se	0.0952	0.0878	-0.0862	Se	0.1674	-0.0009	0.2034
Ti	0.0942	0.4255	-0.0349	La	0.0006	0.0269	0.2277
Se	0.0923	0.7603	0.0192	Se	0.3343	0.5035	0.2034
Se	-0.0054	0.5863	-0.0862	La	0.5006	0.5267	0.2276
Ti	0.1943	-0.0773	-0.0354	Se	0.5011	0.0176	0.2028
Se	0.1954	0.2608	0.0176	La	0.3345	0.0022	0.2265
Se	0.2940	0.0857	-0.0858	Se	0.6674	0.4988	0.2034
Ti	0.2943	0.4233	-0.0349	La	0.8345	0.5024	0.2265
Se	0.2929	0.7615	0.0182	Se	0.8343	0.0037	0.2034
Se	0.1947	0.5848	-0.0858	La	0.6679	-0.0063	0.2275
Ti	0.3942	-0.0740	-0.0351	Ti	-0.0066	0.0913	0.3634
Se	0.3974	0.2588	0.0189	Se	-0.0068	0.4291	0.4133
Se	0.4943	0.0863	-0.0861	Se	0.0935	0.2509	0.3083
Ti	0.4944	0.4272	-0.0370	Ti	0.0939	0.5882	0.3624
Se	0.4938	0.7532	0.0162	Se	0.0926	0.9255	0.4139
Se	0.3935	0.5878	-0.0861	Se	-0.0066	0.7526	0.3107
Ti	0.5943	-0.0745	-0.0348	Ti	0.1932	0.0858	0.3642
Se	0.5924	0.2605	0.0192	Se	0.1932	0.4260	0.4137
Se	0.6947	0.0845	-0.0857	Se	0.2897	0.2565	0.3094
Ti	0.6945	0.4227	-0.0354	Ti	0.29348	0.5859	0.3634
Se	0.6956	0.7609	0.0175	Se	0.2941	0.9253	0.4135
Se	0.5952	0.5877	-0.0862	Se	0.1955	0.7586	0.3106
Ti	0.7946	-0.0769	-0.0351	Ti	0.3929	0.0888	0.3619
Se	0.7930	0.2615	0.0181	Se	0.3938	0.4255	0.4134
Se	0.8937	0.0874	-0.0862	Se	0.4933	0.2522	0.3107
Ti	0.8946	0.4259	-0.0353	Ti	0.4934	0.5909	0.3633
Se	0.8977	0.7585	0.0188	Se	0.4931	0.9288	0.4131
Se	0.7941	0.5854	-0.0859	Se	0.3945	0.7502	0.3082
Se	0.0007	0.0174	0.1243	Ti	0.5939	0.0880	0.3623
La	0.1680	-0.0080	0.1007	Se	0.5926	0.4254	0.4137
Se	0.1671	0.4986	0.1245	Se	0.6957	0.2584	0.3106
La	0.0005	0.5253	0.0991	Ti	0.6934	0.5857	0.3642
Se	0.3342	0.0024	0.1241	Se	0.6932	0.9261	0.4137
La	0.5005	0.0254	0.0991	Se	0.5936	0.7508	0.3082
Se	0.5007	0.5172	0.1242	Ti	0.7937	0.0861	0.3634
La	0.3332	0.4985	0.1010	Se	0.7941	0.4255	0.4136
Se	0.6670	-0.0012	0.1244	Se	0.8945	0.2505	0.3083
La	0.8333	-0.0014	0.1009	Ti	0.8931	0.5889	0.3621
Se	0.8343	0.5024	0.1240	Se	0.8939	0.9257	0.4135
La	0.6680	0.4920	0.1006	Se	0.7899	0.7566	0.3095

Table A.2: Optimized atomic positions of the surface of MLC $(LaSe)_{1.18}(TiSe_2)_2$ in crystal coordinates. The lattice parameters in Å are summarized in the main text (see Tab. 3.3).

Nb	0.4872	0.0889	0.5871	Se	0.1578	0.4838	0.9620	Nb	0.9886	0.8749	0.5872
Nb	-0.0085	0.1278	0.9160	Se	0.1633	0.5166	0.6327	Nb	0.4888	0.9124	0.9166
Se	0.1567	0.0884	0.5415	Se	0.1540	0.4833	0.8701	Se	0.6553	0.8736	0.5422
Se	0.1578	0.0562	0.9610	Nb	0.9879	0.4453	0.5879	Se	0.6617	0.8728	0.6331
Se	0.1546	0.0888	0.6341	Nb	0.4896	0.4852	0.9165	Se	0.6564	0.9844	0.9613
Se	0.1535	0.0569	0.8693	Se	0.6573	0.4457	0.5425	Se	0.6597	0.9813	0.8694
Nb	0.9920	0.0172	0.5869	Se	0.6583	0.4478	0.6349	La	0.4030	0.1044	-0.2997
Nb	0.4894	0.0549	0.9155	Se	0.6565	0.5559	0.9623	Se	-0.0928	0.1043	-0.2801
Se	0.6558	0.0169	0.5420	Se	0.6603	0.5587	0.8705	La	-0.1005	0.1033	-0.1958
Se	0.6568	0.0171	0.6320	Nb	0.4924	0.6595	0.5882	Se	0.4058	0.1036	-0.2157
Se	0.6568	0.1263	0.9610	Nb	-0.0124	0.6981	0.9168	La	-0.0664	0.0206	-0.3014
Se	0.6558	0.1269	0.8704	Se	0.1575	0.6605	0.5432	Se	0.4231	0.0211	-0.2810
Nb	0.4879	0.2320	0.5875	Se	0.1553	0.6269	0.9623	La	0.4172	0.0221	-0.1967
Nb	-0.0102	0.2700	0.9173	Se	0.1566	0.6605	0.6335	Se	-0.0837	0.0205	-0.2167
Se	0.1569	0.2316	0.5422	Se	0.1625	0.6253	0.8716	La	0.3981	0.1465	-0.3008
Se	0.1571	0.1981	0.9620	Nb	0.9881	0.5886	0.5881	Se	-0.0934	0.1461	-0.2804
Se	0.1593	0.2282	0.6343	Nb	0.4890	0.6278	0.9174	La	-0.0709	0.1443	-0.1961
Se	0.1569	0.2008	0.8694	Se	0.6579	0.5888	0.5425	Se	0.4190	0.1461	-0.2163
Nb	0.9894	0.1595	0.5868	Se	0.6568	0.5870	0.6351	La	-0.0801	0.2722	-0.2991
Nb	0.4873	0.1983	0.9165	Se	0.6572	0.6991	0.9624	Se	0.4145	0.2707	-0.2794
Se	0.6555	0.1606	0.5419	Se	0.6540	0.6985	0.8699	La	0.3955	0.2709	-0.1949
Se	0.6628	0.1609	0.6323	Nb	0.4883	0.8022	0.5877	Se	-0.0953	0.2712	-0.2150
Se	0.6555	0.2697	0.9622	Nb	-0.0126	0.8419	0.9164	La	0.4276	0.3943	-0.2997
Se	0.6630	0.2703	0.8720	Se	0.1565	0.8027	0.5425	Se	-0.0791	0.3963	-0.2795
Nb	0.4916	0.3749	0.5881	Se	0.1559	0.7703	0.9617	La	-0.0695	0.3977	-0.1948
Nb	-0.0079	0.4123	0.9169	Se	0.1608	0.8062	0.6342	Se	0.4219	0.3959	-0.2153
Se	0.1573	0.3737	0.5430	Se	0.1567	0.7697	0.8718	La	-0.1044	0.5209	-0.3002
Se	0.1571	0.3414	0.9624	Nb	0.9897	0.7323	0.5885	Se	0.4043	0.5209	-0.2801
Se	0.1560	0.3733	0.6338	Nb	0.4920	0.7701	0.9169	La	0.4146	0.5205	-0.1961
Se	0.1575	0.3397	0.8699	Se	0.6583	0.7308	0.5430	Se	-0.0879	0.5214	-0.2158
Nb	0.9903	0.3019	0.5882	Se	0.6540	0.7307	0.6349	La	0.4317	0.6476	-0.3000
Nb	0.4877	0.3416	0.9170	Se	0.6569	0.8416	0.9619	Se	-0.0790	0.6460	-0.2795
Se	0.6580	0.3036	0.5428	Se	0.6539	0.8413	0.8694	La	-0.0976	0.6458	-0.1953
Se	0.6545	0.3036	0.6344	Nb	0.4873	0.9452	0.5874	Se	0.4089	0.6458	-0.2154
Se	0.6572	0.4134	0.9619	Nb	-0.0121	0.9850	0.9160	La	-0.0864	0.7703	-0.2992
Se	0.6564	0.4135	0.8715	Se	0.1569	0.9457	0.5418	Se	0.4144	0.7713	-0.2792
Nb	0.4900	0.5173	0.5874	Se	0.1553	0.9135	0.9616	La	0.4337	0.7709	-0.1945
Nb	-0.0119	0.5551	0.9170	Se	0.1537	0.9462	0.6343	Se	-0.0770	0.7710	-0.2150
Se	0.1558	0.5171	0.5425	Se	0.1620	0.9141	0.8710				

Table A.3: Optimized atomic positions of the surface of MLC $(LaSe)_{1.15}(NbSe_2)_2$ in crystal coordinates. The lattice parameters in Å are summarized in the main text (see Tab. 3.3).

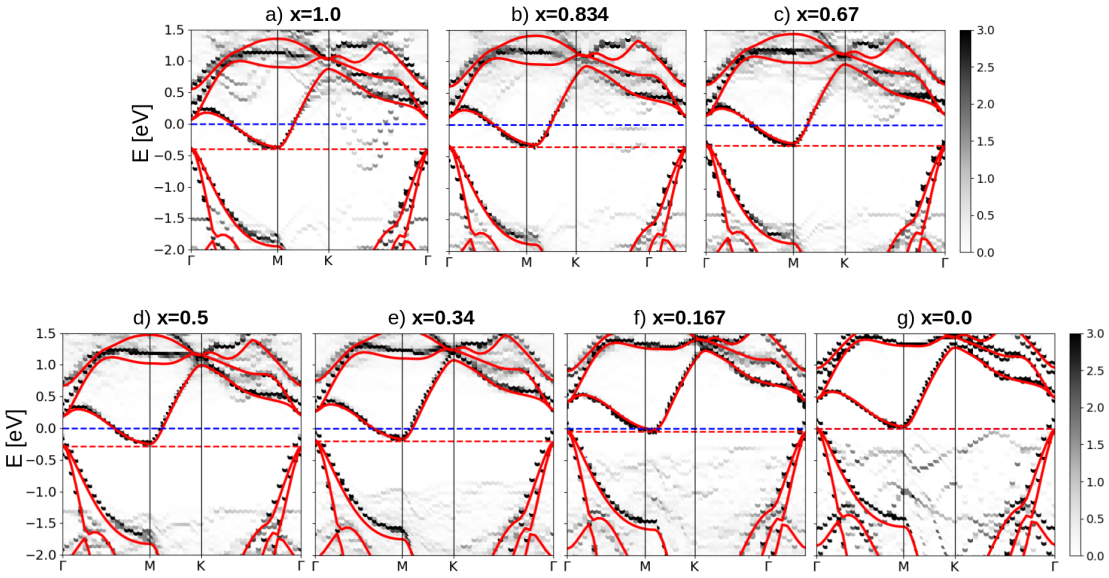

Figure A.1: Band unfolding onto the hexagonal Brillouin Zone (BZ) of a single layer $TiSe_2$ in the PBE+U scheme of misfit supercell $(La_xPb_{1-x}Se)_{1.18}(TiSe_2)_2$, with $x =$ (a) 1.0, (b) 0.834, (c) 0.67, (d) 0.5, (e) 0.34, (f) 0.167, (g) 0.0. Darker regions in the colormap represent the most relevant eigenvalues of the misfit band structure along the $TiSe_2$ first BZ. In red isolated single layer $TiSe_2$ band structure is superimposed onto the unfolded one. Blue (red) dashed line corresponds to the Fermi level E_F of the misfit (single layer $TiSe_2$).

comprises vacuum space (optimized form 15 to 18 Å, depending on the system) to prevent interactions between periodic replicas.

In case of $TiSe_2$ compounds, we calculate the band structure shown in Fig. 3.5 and 3.9 within the PBE+U method and with the inclusion of SOC. However, we verified that relativistic effects are negligible for the electronic properties of $(La_xPb_{1-x}Se)_{1.18}(TiSe_2)_2$ family of compounds. We report here the full calculation of $(LaSe)_{1.18}(TiSe_2)_2$ with partial substitution of Pb atoms ($(La_xPb_{1-x}Se)_{1.18}(TiSe_2)_2$ with $x = 1.0, 0.834, 0.67, 0.5, 0.34, 0.167, 0.0$) in the PBE+U, without SOC in Fig. A.1. In Fig. A.2, we also show the same calculations of $(La_xPb_{1-x}Se)_{1.18}(TiSe_2)_2$ in the PBE scheme for $x = 1.0, 0.67, 0.5, 0.34, 0.0$, without taking into account the Hubbard correction. The main difference between these two approaches resides in the energy dispersion around the Fermi level, especially the overlap/gap between the Se-4p valence band in Γ and the Ti-3d conduction band in M. Indeed, as shown in Ref. [94] the introduction of Hubbard interaction, where U is set to U= 3.25 eV, leads to a better comparison with ARPES experiments in which shows that monolayer 1T-$TiSe_2$ is a perfectly compensated semimetal.

Spin orbit coupling is included in all the electronic structure calculations concerning $NbSe_2$. In Fig. A.3, the calculation of the band structure of the $(RQ)_{1+\delta}(NbSe_2)_2$ series (with RQ=LaSe, BiSe, PbSe, and SnSe) without the introduction of the SOC is shown. As we can see, the main difference between the

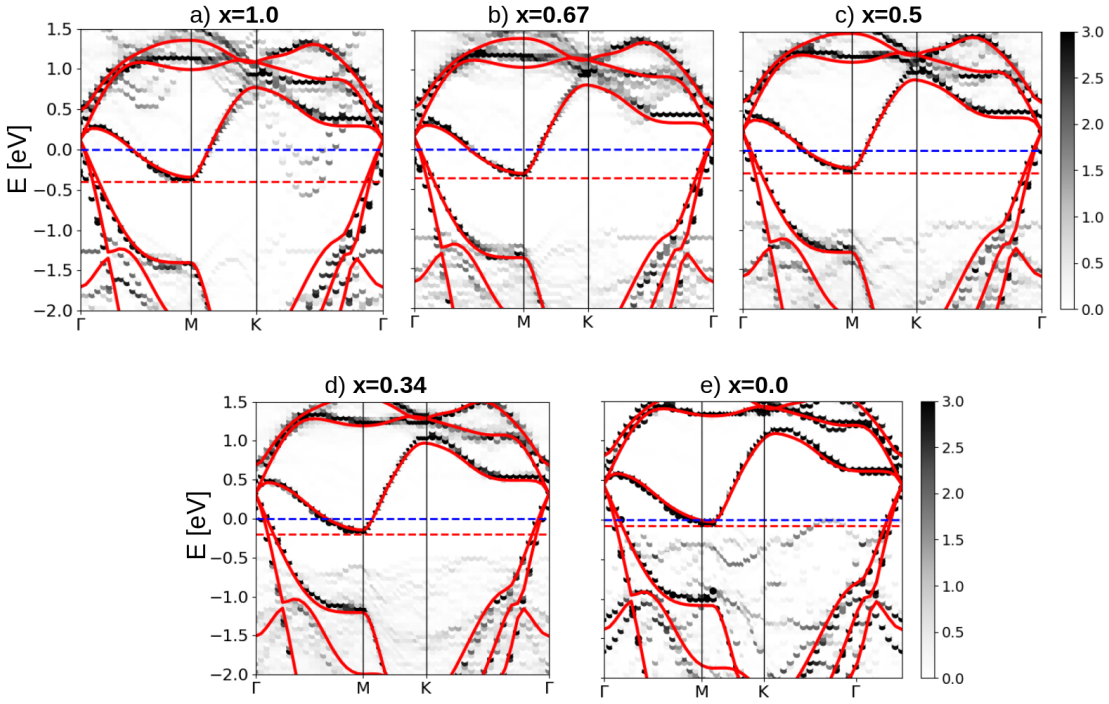

Figure A.2: Band unfolding in the PBE scheme of misfit supercell $(La_xPb_{1-x}Se)_{1.18}(TiSe_2)_2$, with x = (a) 1.0, (b) 0.67, (c) 0.5, (d) 0.34, (e) 0.0, onto the hexagonal BZ of a single layer $TiSe_2$. Darker regions in the colormap represent the most relevant eigenvalues of the misfit band structure along the $TiSe_2$ IBZ. In red isolated single layer $TiSe_2$ band structure is superimposed onto the unfolded one. Blue (red) dashed line corresponds to the Fermi level E_F of the misfit (single layer $TiSe_2$).

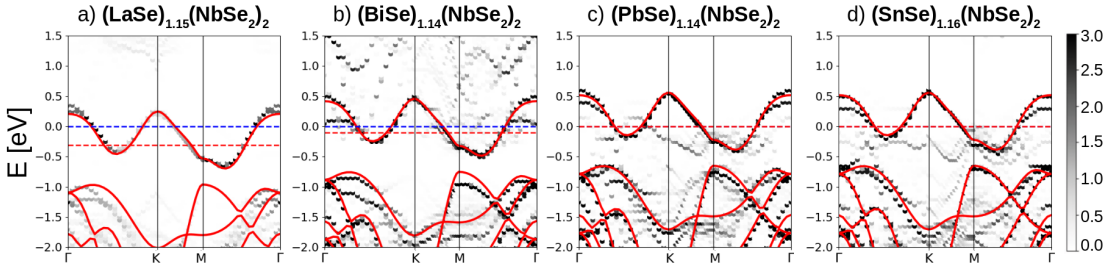

Figure A.3: Band unfolding onto the $NbSe_2$ single layer Brillouin zone for the $NbSe_2$ misfit series with different rocksalt Q-layers having comparable mismatching ratio close to 7/4. (a) $(LaSe)_{1.15}(NbSe_2)_2$, (b) $(BiSe)_{1.14}(NbSe_2)_2$, (c) $(PbSe)_{1.14}(NbSe_2)_2$, (d) $(SnSe)_{1.16}(NbSe_2)_2$. In this calculation, SOC is neglected. The band structure of the isolated single layer $NbSe_2$ (red line) is superimposed and aligned to the Nb d-band in the misfit. The blue dashed line corresponds to the Fermi level E_F of the misfit compound, while the red one to the Fermi level of the isolated $NbSe_2$ layer. In the last two panels the dashed red line is superimposed to the dashed blue one.

calculations with SOC presented in Chapter 3 (see 3.7) resides in the SOC splitting of the Nb d-bands of $NbSe_2$. The amount of charge transfer, however, is not affected by the presence of SOC.

A.3 Doping-induced superconductivity in misfit layer compound $(LaSe)_{1.27}(SnSe_2)_2$

As detailed in Chapter 4, in order to recover the $(LaSe)_{1.27}(SnSe_2)_2$ surface and bulk behaviour, we used the 2D material FET setup [101] to precisely dope $SnSe_2$ as it is inside the misfit.
A Coulomb long range interaction cutoff is placed at $l_z = c/2$ with c being the unit-cell size in the direction perpendicular to the 2D plane: c is set opportunely for single and double layer $SnSe_2$ at 16.14Å and 25.83Å, respectively.
For $SnSe_2$ monolayer we use a single gate setup, placing charged plate modelling a single gate electrode at $z_{bot} = -0.25c$ with a charge of +0.7, equal and opposite to the one of the single layer $SnSe_2$ to ensure charge neutrality. For $SnSe_2$ bilayer we use a double gate configuration, with the bilayer sandwiched between two charged plates at $z_{bot} = -0.266c$ and $z_{top} = +0.266c$ each with a charge of ρ=+(-)0.7, such that $\rho_{tot} = \rho_{2L} + \rho_{bot} + \rho_{top} = 0$.
For all systems, potential barriers V with a height of $V_H = 2.5$ Ry are placed before the gates at $z_V = z_{bot} + 0.1$ ($z_V = z_{top} - 0.1$) in order to prevent the ions from moving too close to the gate electrodes.
The harmonic phonon frequencies are evaluated within density-functional perturbation theory [141] on a 7×7×1 phonon momentum grid (q-grid) and 21×21×1 electron-momentum grid (k-grid). The slightly imaginary acoustic phonons (order of 8 cm^{-1}) observable in the phonon dispersion are an artifact linked to the acoustic sum rule breaking in linear response. To avoid spurious effects, we did not impose the acoustic sum rule manually since it has been shown that in field-effect gated 2D system one of the three acoustic modes remains finite at Γ (see [101]).
The correct evaluation of the electron-phonon coupling properties of doped $SnSe_2$ requires a precise knowledge of electron-phonon matrix elements for very dense electron and phonon momentum grids. Since the direct calculation of electron-phonon matrix elements over a ultradense q- and k-point grids is very time consuming in linear response, we perform a Wannier interpolation of the electron-phonon coupling as described in Ref. [105].
We used the Wannier90 [142] code to obtain the Bloch to Wannier transformation. We use as starting guess of the Maximally Localized Wannier Function procedure three *p*-like orbitals at every chalcogen site and 5 *d*-like orbitals at any molybdenum site. Within this approach, the electron-phonon matrix elements are first calculated on a coarse 7×7×1 q grid and 21×21×1 k-grid, and then Wannier interpolated to 96×96×1 q- and k- grids in order to evaluate the electron-phonon coupling parameter λ and the isotropic Eliashberg function $\alpha^2F(\omega)$. We employ a Gaussian smearing of 0.001 Ry for k- and q- summations in λ.
The superconducting gap is evaluated by solving the Migdal-Eliashberg equa-

tions [104]in the Wannier basis over the imaginary frequency axis and then by performing analytic continuation to the real axis using N-point Padé approximants [143]. In order to perform the k- and $\mathbf{k}+\mathbf{q}$- summations to solve the Migdal-Eliashberg equations on the imaginary axis, we generate random electron momenta on the Brillouin zone, and select 2048 of them having at least one eigenvalue within 0.2 eV of the Fermi surface. The Matsubara summation was truncated at 128 frequencies, where convergence is reached. The superconducting critical temperature is then evaluated by determining the temperature where the superconducting gap becomes zero. We use a Morel-Anderson pseudopotential [144] $\mu^* = 0.1$ to parameterize the Coulomb repulsion in the superconducting state.
The Wannier interpolation of the electron-phonon matrix elements, as well as the solution of the Migdal-Eliashberg equations have been performed within EPI*q* (Electron-Phonon Interpolation over q- and k-points), an open-source in-house software [103].

A.4 Modeling bulk $(LaSe)_{1.14}(NbSe_2)_2$ as a collection of field effect transistors

A.4.1 2×1 periodic approximant of bulk $(LaSe)_{1.14}(NbSe_2)_2$

As reported in Chapter 4, we needed to simulate vibrational properties of bulk $(LaSe)_{1.14}(NbSe_2)_2$. It is possible to simulate an approximate commensurate cell [6] by considering the ratio $|\mathbf{a_2}|/|\mathbf{a_1}| = 6/3.437$ ($\approx 7/4$), and thus m $=7|\mathbf{a_1}| \approx 4|\mathbf{a_2}|$. This periodic approximant has been used to calculate the electronic structure [6], however it is still formed by too many atoms for the calculation of the vibrational properties. In order to reduce the computational effort, we approximate the 7/4 mismatch ratio by 8/4, corresponding to a 2/1 ratio. This is done by applying 14.6% tensile strain to the rocksalt subunit, increasing the lattice parameter to $a_2 = 6.875$ Å. The $NbSe_2$ in-plane parameter is, on the contrary, kept the same as in the misfit ($a_1 = 3.437$ Å). The atomic positions in crystal coordinates are summarized in Tab. A.4.
We calculate the vibrational properties of bulk $(LaSe)_{1.14}(NbSe_2)_2$ by means of density functional perturbation theory (DFPT) as implemented in the QUANTUM ESPRESSO (QE) code [127, 145]. We choose to employ the optimized ultrasoft pseudopotentials from pslibrary to reduce the computational effort. The kinetic energy cutoff is set to 40 Ry and the Brillouin zone (BZ) integration is carried out over a 4×4×2 electron-momentum Monkhorst-Pack grid and by using a Gaussian smearing of 0.01 Ry. The PBE [146] exchange and correlation functional is used in the calculations.
The atomic positions are fully optimised by means of the Broyden-Fletcher-Goldfarb-Shannon (BFGS) algorithm, with a convergence threshold of 10^{-4} Ry on the total energy difference between consecutive structural optimisation steps and of 10^{-3} Ry/Bohr on all forces components. During the relaxation procedure, we use the Van der Waals corrections Grimme-D3 [147] to reproduce the interaction

among adjacent $NbSe_2$ layers.
We compute the dynamical matrix of bulk $(LaSe)_{1.14}(NbSe_2)_2$ at the Γ point. The phonon density of states (PHDOS) is obtained by Fourier interpolation over a $10 \times 10 \times 1$ phonon-momentum grid and by using a Gaussian smearing of 3 cm^{-1} (see Fig. 4.12).
We note that in our calculations, the shearing mode along the axis with the lattice mismatch among the $NbSe_2$ and LaSe units goes slightly imaginary; nevertheless, this is an artifact caused by the tensile strain applied to the LaSe subunit.

A.4.2 Field-effect transistor setup modeling

The field-effect modeling is carried out by using density functional theory (DFT) as implemented in the QUANTUM ESPRESSO (QE) [145] package using the PBE exchange and correlation functional [146]. We employ ultrasoft pseudopotentials from the Vanderbilt distribution for La and Nb, including semi-core states for Nb atoms [148], while for Se we use norm-conserving pseudopotentials with empty d-states in valence.
The kinetic energy cutoff for plane-wave basis set of $NbSe_2$ (LaSe) is set to 50 (48) Ry. The Brillouin zone (BZ) integration is performed with a Monkhorst-Pack grid of 21×21×1 (14×14×1) k-points and a Gaussian smearing of 0.01 (0.015) Ry. The smearing value of 0.01 Ry is proven to ensure the convergence of the phonon frequencies of $NbSe_2$ within 1 cm^{-1}.
A Coulomb long range interaction cutoff is placed at $z_{cut} = c/2$ with c being the unit-cell size in the direction perpendicular to the plane: c is set opportunely for each of the different systems to 20 Å for LaSe and 25 Å for $NbSe_2$. Each of the two subsystems is centred around z=0.
For 2L-$NbSe_2$ (LaSe) we use a double gate configuration, with two charged plates at $z_{bot} = -0.266c$ ($z_{bot} = -0.221c$) and $z_{top} = +0.266c$ ($z_{top} = +0.221c$) each with a charge of ρ=+0.6 (ρ=-0.6) times the modulus of the electronic charge, such that $\rho_{tot} = \rho_{2L} + \rho_{bot} + \rho_{top} = 0$.
For each system a potential barriers V of height 2.5 Ry is placed before the gates at $z_V = z_{bot} + 0.1$ ($z_V = z_{top} - 0.1$) in order to confine the atoms between the gate electrodes.
The Raman active phonon frequencies are calculated using density functional perturbation theory (DFPT) in the linear response regime [127]. In order to fulfill the 7/4 lattice mismatch ratio of the best periodic approximant, the dynamical matrices are calculated on uniform 7×7×1 and 4×4×1 phonon-momentum grids and then Fourier interpolated in the full Brillouin zone.
For the DOS at zone center in Fig. 4.11 panel (b), we use only the phonon frequencies obtained from the dynamical matrices on a 4×1×1 phonon momentum grid.
The individual phonon densities of states (PHDOS) in Fig. 4.12 are obtained by Fourier interpolation over a $40 \times 40 \times 1$ and $70 \times 70 \times 1$ phonon-momentum grid for LaSe and $NbSe_2$ respectively, and by using a Gaussian smearing of 3 cm^{-1}.
Vibrational properties of isolated neutral 2L-$NbSe_2$ are calculated using DFPT in the linear response regime on uniform 8×8×1 phonon-momentum grids. The

Nb	0.0310	0.0062	1.1843	Se	0.2537	0.4995	1.9301
Nb	0.0279	0.5056	1.1843	Se	0.7547	0.7548	1.9307
Nb	0.5260	0.2495	1.1840	Se	0.7540	0.2546	1.9302
Nb	0.5290	0.7496	1.1844	Se	0.4768	0.0716	-0.5506
Nb	-0.0789	0.0052	1.8389	La	0.4735	0.6448	-0.5895
Nb	-0.0815	0.5063	1.8389	Se	0.4714	0.5722	-0.4263
Nb	0.4204	0.2485	1.8388	Se	0.1995	0.2619	1.2789
Nb	0.4232	0.7489	1.8393	Se	0.1956	0.7582	1.2782
La	-0.0182	0.0735	-0.5905	Se	0.6999	0.4935	1.2773
Se	-0.0230	0.1472	-0.4267	Se	0.6965	-0.0014	1.2768
La	-0.0335	0.5729	-0.3863	Se	0.2495	-0.0073	1.7460
Se	0.1943	0.2547	1.0925	Se	0.2528	0.4978	1.7465
Se	0.1955	0.7546	1.0929	Se	0.7499	0.7616	1.7444
Se	0.6953	0.5008	1.0928	Se	0.7537	0.2578	1.7451
Se	0.6958	0.0004	1.0929	La	0.4747	0.1452	-0.3874
Se	0.2539	-0.0002	1.9305	Se	-0.0288	0.6480	-0.5501

Table A.4: Optimized atomic positions of the 2×1 periodic approximant of bulk $(LaSe)_{1.14}(NbSe_2)_2$ in crystal coordinates.

Brillouin zone integration is performed with a Monkhorst-Pack grid of 30×30×1 k-points and a Methfessel-Paxton smearing of 0.005 Ry.

A.4.3 Effect of the non-hexagonality of 2L-$NbSe_2$ within $(LaSe)_{1.14}(NbSe_2)_2$

In our DFT calculations we neglected the effect of the slightly non-hexagonal lattice of 2L-$NbSe_2$ within $(LaSe)_{1.14}(NbSe_2)_2$. Indeed, the angle of 60 °along the misfit direction is compressed to 59.6 ° [6] as an effect of the lattice mismatch.
By accounting this effect, all the modes in a non-hexagonal 2L-$NbSe_2$ at the zone center become Raman active and non-degenerate, as a result of the breaking of the hexagonal symmetry (the space group becomes P_{-1}).
The main consequence is that the Eg modes will be no longer degenerate. Thus, we considered the non-hexagonality as a possible explanation for the splitting of the high energy Eg modes observed in the Raman spectra of $(LaSe)_{1.14}(NbSe_2)_2$ (see Tab. 4.1 in Chapter 4).
To test this possibility, we include the non-hexagonality in our field-effect doped 2L-$NbSe_2$ calculation by setting $a_1 \neq b_1$ with $a_1 = 3.457$ Å and $b_1 = 3.437$ respectively. The resulting phonon modes at Γ in the 1×1 cell are shown in green bars in Fig.[A.4] panel a).
However, as we can see from Fig.[A.4] panel b), the splitting of former degenerate Eg modes caused by the non-hexagonality appears to be of the order of 1 cm^{-1} (red bars). This splitting is 10 times smaller than the one measured in the misfit, thus we infer that this argument is not sufficient to match experimental data. The explanation of the splitting in the misfit is given in the main text by accounting

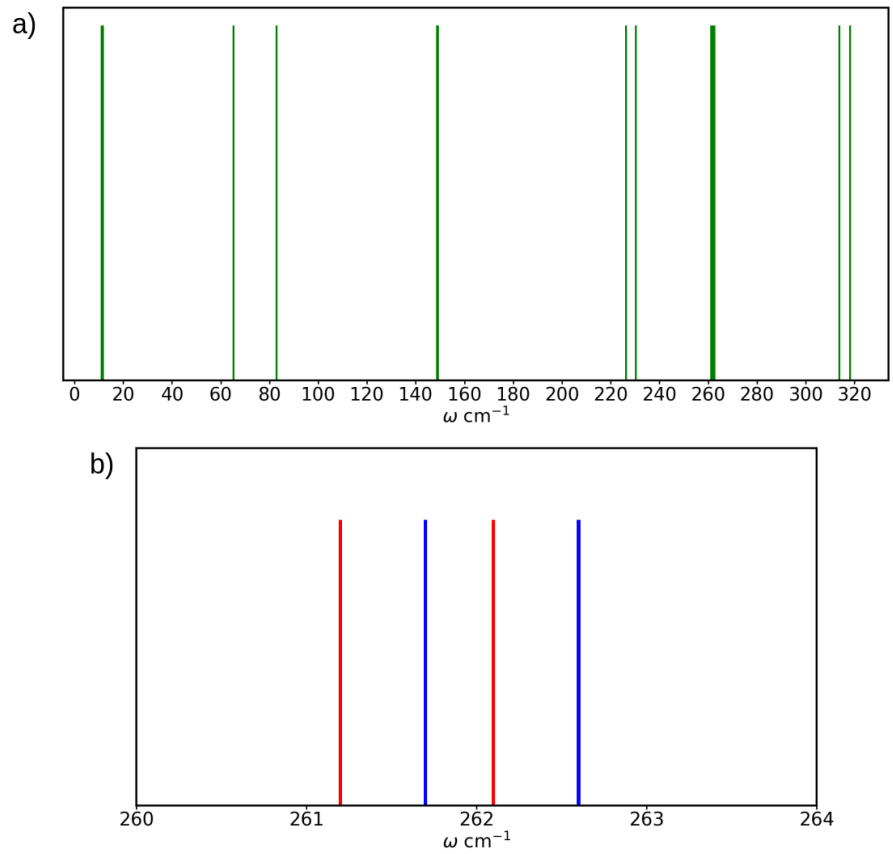

Figure A.4: a) Theoretical calculation of Raman active modes of non-hexagonal 2L-$NbSe_2$. The system is electron doped by means of the FET setup. Green bars represent the Γ modes of the 1×1 cell of the system. b) Zoom of the frequency range $260 - 265$ cm^{-1}. Red bars correspond to the splitted high energy E_g modes, while blue bars correspond to the splitted high energy E_u modes.

the projection of the misfit modes onto the Eg modes of 2L-$NbSe_2$.

A.5 Superconducting properties of bulk $(RQ)_{1+\delta}(NbSe_2)$ misfit series

We specifically consider the $(RQ)_{1+\delta}(NbSe_2)$ misfit series, where we fix the TMD as $NbSe_2$, and we change the rocksalt with RQ= LaSe, BiSe, PbSe, and SnSe. As detailed in Chapter 5, we approximate the 7/4 mismatch ratio by 8/4, corresponding to a 2/1 ratio. We calculate the electronic and geometrical properties of bulk $(RQ)_{1+\delta}(NbSe_2)$ misfit series by means of density functional theory (DFT) and the vibrational properties by means of density functional perturbation theory (DFPT), as implemented in the QUANTUM ESPRESSO (QE) code [127,145]. We choose to employ the optimized ultrasoft pseudopotentials from PSlibrary [140] to reduce the computational effort. For each of the considered misfit, the kinetic energy cutoff is set to 40 Ry, the Brillouin zone (BZ) sampling is carried out over a 8×8×4 k-points grid and by using a Methfessel-Paxton smearing of 0.005 Ry.

Nb	0.4864	0.3612	-0.0040
Nb	0.9958	0.1129	-0.0055
Nb	0.4863	0.8612	-0.0045
Nb	0.9958	0.6129	-0.0029
Se	0.1582	0.3667	0.8445
Se	0.6557	0.1128	0.8551
Se	0.1571	0.8599	0.8496
Se	0.6663	0.6090	0.8563
Se	0.1571	0.3599	0.1418
Se	0.6663	0.1090	0.1351
Se	0.1582	0.8666	0.1469
Se	0.6557	0.6128	0.1362
La	-0.0676	0.0985	0.6466
Se	0.4194	0.0755	0.5946
La	0.3947	0.1390	0.3443
Se	-0.0958	0.1640	0.3964
La	0.3949	0.6395	0.6471
Se	-0.0957	0.6644	0.5949
La	-0.0677	0.5980	0.3449
Se	0.4193	0.5752	0.3968

Table A.5: Optimized atomic positions of the 2×1 periodic approximant of bulk $(LaSe)_{1.15}(NbSe_2)$ in crystal coordinates.

The PBE [146] exchange and correlation functional is used in the calculations.
The atomic positions are fully optimised by means of the Broyden-Fletcher-Goldfarb-Shannon (BFGS) algorithm, with a convergence threshold of 10^{-4} Ry on the total energy difference between consecutive structural optimisation steps and of 10^{-3} Ry/Bohr on all forces components. The final misfit bulks have a P1 symmetry and includes 20 atoms in the cell. Atomic positions after the relaxation procedure are summarized in Tabs. A.5, A.6, A.7 and A.8 for each of the considered compounds.
The harmonic phonon frequencies are evaluated within density-functional perturbation theory [141] on a Γ-only q-grid. A denser 12×12×12 k-grid is employed to evaluate the electron-phonon coupling parameter λ and the isotropic Eliashberg function $\alpha^2F(\omega)$, with a Gaussian smearing of 0.015 Ry for k-summation in λ.
We use the Allen-Dynes semi-empirical formula to evaluate the superconducting critical temperatures of each considered misfit, with a Morel-Anderson pseudopotential [144] $\mu^* = 0.15$ to parameterize the Coulomb repulsion in the superconducting state.

Nb	0.4924	0.3656	-0.0051
Nb	0.9900	0.1146	-0.0034
Nb	0.4923	0.8656	-0.0034
Nb	0.9900	0.6148	-0.0049
Se	0.1586	0.3674	0.8494
Se	0.6580	0.1146	0.8528
Se	0.1605	0.8618	0.8515
Se	0.6587	0.6158	0.8512
Se	0.1606	0.3616	0.1399
Se	0.6586	0.1157	0.1401
Se	0.1587	0.8674	0.1423
Se	0.6579	0.6146	0.1386
Bi	-0.0370	0.1034	0.6437
Se	0.4249	0.0413	0.5941
Bi	0.3621	0.1280	0.3579
Se	-0.0945	0.1893	0.4060
Bi	0.3605	0.6256	0.6337
Se	-0.0945	0.6891	0.5852
Bi	-0.0377	0.6026	0.3475
Se	0.4254	0.5414	0.3973

Table A.6: Optimized atomic positions of the 2×1 periodic approximant of bulk $(BiSe)_{1.14}(NbSe_2)$ in crystal coordinates.

Nb	0.5034	0.3176	-0.0043
Nb	1.0123	0.0753	-0.0044
Nb	0.5034	0.8177	-0.0042
Nb	1.0123	0.5753	-0.0041
Se	0.1752	0.3273	0.8483
Se	0.6735	0.0684	0.8542
Se	0.1719	0.8241	0.8516
Se	0.6768	0.5659	0.8515
Se	0.1719	0.3242	0.1397
Se	0.6769	0.0659	0.1397
Se	0.1751	0.8272	0.1430
Se	0.6735	0.5684	0.1371
Pb	-0.0980	0.1763	0.6195
Se	0.3895	0.1040	0.6101
Pb	0.3958	0.1820	0.3714
Se	-0.1134	0.2553	0.3809
Pb	0.3966	0.6832	0.6200
Se	-0.1129	0.7564	0.6104
Pb	-0.0969	0.6751	0.3719
Se	0.3900	0.6029	0.3816

Table A.7: Optimized atomic positions of the 2×1 periodic approximant of bulk $(PbSe)_{1.14}(NbSe_2)$ in crystal coordinates.

Nb	0.5035	0.3610	-0.0056
Nb	1.0071	0.1122	-0.0024
Nb	0.5035	0.8607	-0.0027
Nb	1.0071	0.6123	-0.0058
Se	0.1699	0.3610	0.8464
Se	0.6716	0.1101	0.8527
Se	0.1708	0.8626	0.8504
Se	0.6695	0.6115	0.8512
Se	0.1708	0.3626	0.1411
Se	0.6694	0.1115	0.1402
Se	0.1698	0.8610	0.1451
Se	0.6718	0.6101	0.1390
Sn	-0.0675	0.0797	0.6235
Se	0.4191	0.0591	0.5931
Sn	0.3806	0.1615	0.3652
Se	-0.0931	0.1774	0.3954
Sn	0.3791	0.6617	0.6266
Se	-0.0938	0.6781	0.5950
Sn	-0.0631	0.5794	0.3670
Se	0.4204	0.5589	0.3989

Table A.8: Optimized atomic positions of the 2×1 periodic approximant of bulk $(SnSe)_{1.16}(NbSe_2)$ in crystal coordinates.